

Oxidative coupling of methane: Resolution of the surface and gas phase contributions to the mechanism of the oxidative coupling of methane at Na₂WO₄-Mn-SiO₂-catalyst

vorgelegt von
Diplom-Ingenieur
Vinzenz Fleischer
geb. in Berlin

Von der Fakultät II - Mathematik und Naturwissenschaften
der Technischen Universität Berlin
zur Erlangung des akademischen Grades

Doktor der Ingenieurwissenschaften
- Dr.-Ing. -

genehmigte Dissertation

Promotionsausschuss:

Vorsitzender: Prof. Dr. Nediljko Budisa, TU Berlin

Gutachter: Prof. Dr. rer. nat. Reinhard Schomäcker, TU Berlin

Gutachter: Prof. Dr. rer. nat. Robert Schlögl, FHI der MPG Berlin & Mühlheim an der Ruhr

Gutachter: Prof. Dr.-Ing. Ulrich Nieken, Universität Stuttgart

Tag der wissenschaftlichen Aussprache: 21.12.2016

Berlin 2017

Acknowledgements

The present thesis was performed and issued at the Technical Chemistry Department of the Chemistry Institute at the Technische Universität Berlin, in the framework of “Unicat” (Unifying Concepts in Catalysis) project as a part of the subproject D1/E1, “Activation of Methane”.

First of all, I would like to thank my supervisor Prof. Dr. Reinhard Schomäcker, for admitting me into his research group, for the supervision of my work and giving me the chance to achieve this milestone. I would also like to thank Prof. Dr. Robert Schlögl for the second supervision. I thank Prof. Dr.-Ing. Ulrich Nieken as my external examiner.

I thank also Dr. Patrick Littlewood and Samira Parishan for great discussions about the development of the setup, the OCM and also experimental techniques in general. Further I like to thank all colleagues in the research group of Prof. Dr. R. Schomäcker, especially:

Dr. Benjamin Beck

Dr. Torsten Otremba

Dr. Marc Schröder

Maximilian Neumann

Arno Zimmermann

Lukas Thum

Marcel Schmidt

Tobias Pogrzeba

Dr. Michael Schwarze

I would also thank all students who support me during this period, especially Rolf Steuer, Maika Stöbe, Trung Ngo Thanh and Maik Rudolf. I am also grateful for the support from Gabriele Vetter and Christa Löhr.

Also I have to thank the international Max Planck research school (IMPRS) and all of its members, for the initial financial support of my PhD and great discussions. I have learned a lot about fundamental research techniques. Furthermore that school gave me the opportunity to collaborate with other people, who work also in the OCM field.

I would like to thank Ulla Simon and Maria Gracia Colmenares for the preparation, characterization of several catalyst materials and the close collaboration. I would cordially like to thank Dr. H.R. Godini for the discussions about the OCM and the process engineering aspects.

I would like to thank the Deutsche Forschungsgemeinschaft (DFG) for funding the Excellence Cluster “Unicat” (Unifying Concepts in Catalysis).

Foremost I want to thank my parents Brigitte and Klemens for their support of my development during the last years and all my life before. The same is true for my girlfriend Lea, who supported me in all difficult situations. She was always there for me and I would give also a special Acknowledgement to my beloved daughter and son.

Abstract

Nowadays, ethene is produced through steam cracking of naptha, which is a fraction of crude oil obtained after its distillation. Ethene is an important basic chemical for the chemical industry, but due to decreasing reserves of crude oil an alternative feedstock is required. The oxidative coupling of methane (OCM) is a promising reaction for ethene production. Natural gas, which contains high amounts of methane, offers a new feedstock for the chemical industry. Further methane containing gases, such as shale or bio gas, can be utilized for that process, too. Many catalysts have been investigated so far, but due to several reasons a technical realization on an industrial scale is hard to realize. On the one hand a highly active, selective and stable catalyst is needed. On the other hand there is a strong contribution of gas phase side reactions, due to co-feeding of methane and oxygen at high temperatures, which requires an adequate reactor concept to achieve high ethene yields.

In the presented thesis, OCM reactions were carried out on $\text{Na}_2\text{WO}_4/\text{Mn}/\text{SiO}_2$ catalysts in absence of gas phase oxygen to clarify the surface reaction network. Temperature programmed surface reaction (TPSR) experiments with methane, ethane, and ethene were carried out to study their interaction with the catalyst material. Furthermore an activation energy for the selective methane activation was calculated using the Redhead method. Dynamic experiments at constant reaction temperature indicate that for the $\text{Na}_2\text{WO}_4/\text{Mn}/\text{SiO}_2$ catalyst strongly bound oxygen is involved in the OCM process, which can survive several hours under OCM conditions at the catalyst surface. Based on these results a chemical looping setup was constructed, which allows to dose the reactants separately in defined amounts. In our studies, we found that the OCM yield is limited to 25 %, which is caused by the catalyst material itself. Further investigations of differently loaded $\text{Na}_2\text{WO}_4/\text{Mn}/\text{SiO}_2$ catalysts by repetitive pulse experiments reveal a correlation between the stored amount of oxygen and the manganese content. For the chemical looping concept we found operation conditions which enable to convert methane more efficiently than in the classical co-feed mode. Additionally to the kinetic investigations an upscaling concept was proposed.

Erklärung

Ich erkläre hiermit, dass ich bislang an keiner anderen Hochschule oder Fakultät meine Promotionsabsicht beantragt habe.

Die vorliegende Dissertation wurde bereits in Form von wissenschaftlichen Publikationen veröffentlicht. Bei den entsprechenden Veröffentlichungen handelt es sich um folgende Publikationen:

Paper 1: Thermal Reaction Analysis of Oxidative Coupling of Methane

Hamid Reza Godini, Vinzenz Fleischer, Oliver Görke, Stanislav Jaso, Reinhard Schomäcker and Günter Wozny

Chemie Ingenieur Technik, 2014, 86(2), 1906-1915, DOI: [10.1002/cite.201400080](https://doi.org/10.1002/cite.201400080)

Eigenanteil: Ich bin Erstautor zusammen mit Hamid Reza Godini. In dieser Arbeit wurde der Einfluss des Sauerstoffpartialdrucks in der oxidativen Kupplung von Methan (OCM) durch Simulation eines Reaktionsnetzwerkes für Gasphasen-Reaktionen und der Implementierung eines einfachen Katalysatorberflächenreaktionsnetzwerkes von mir untersucht. Die Simulationen habe ich in *Chemkin (ReactionDesign)* für verschiedene Reaktormodelle (PFTR, CSTR) durchgeführt. Anhand der Simulationsergebnisse wurde von mir eine optimierte Sauerstoff-Dosierungsstrategie und die Auswirkung einer Hot-Spot Ausbildung auf die OCM diskutiert.

Paper 2: Oxidative coupling of methane — A complex surface/gas phase mechanism with strong impact on the reaction engineering

Benjamin Beck, Vinzenz Fleischer, Sebastian Arndt, Miguel González Hevia, Atsushi Urakawa, Peter Hugo and Reinhard Schomäcker

Catalysis Today, 2014, 228, 212-218, DOI: [10.1016/j.cattod.2013.11.059](https://doi.org/10.1016/j.cattod.2013.11.059)

Eigenanteil: Der Reaktionsverlauf der OCM Reaktion unter Verwendung eines $\text{Na}_2\text{WO}_4/\text{Mn}/\text{SiO}_2$ Katalysators wurde von mir in einem Hochdruckversuchsstand untersucht. Aus den gewonnenen Ergebnissen (dargestellt in Abbildung 2) konnte ich schließen, dass höhere Absolutdrücke die Performance der OCM Reaktion in einem Festbettreaktor verbessern.

Paper 3: Investigation of the surface reaction network of the oxidative coupling of methane over $\text{Na}_2\text{WO}_4/\text{Mn}/\text{SiO}_2$ catalyst by temperature programmed and dynamic experiments

Vinzenz Fleischer, Rolf Steuer, Samira Parishan and Reinhard Schomäcker

Journal of Catalysis, 2016, 341, 91-103, DOI: [10.1016/j.jcat.2016.06.014](https://doi.org/10.1016/j.jcat.2016.06.014)

Eigenanteil: Ich bin Erstautor. Die OCM Reaktion wurde von mir unter Verwendung eines $\text{Na}_2\text{WO}_4/\text{Mn}/\text{SiO}_2$ Katalysators mit Hilfe von temperatur-programmierten und dynamischen Experimenten untersucht und diskutiert. Aus den Ergebnissen wurde von mir ein Reaktionsnetzwerk für die Oberflächenreaktionen der OCM an einem $\text{Na}_2\text{WO}_4/\text{Mn}/\text{SiO}_2$

Katalysators von mir aufgestellt. Ferner wurden die Sauerstoffspeicherkapazität des Katalysators und deren Stabilität unter OCM Bedingungen von mir untersucht und diskutiert.

Paper 4: Chemical looping as reactor concept for the oxidative coupling of methane over a $\text{Na}_2\text{WO}_4/\text{Mn}/\text{SiO}_2$ catalyst

Vinzenz Fleischer, Patrick Littlewood, Samira Parishan, and Reinhard Schomäcker

Chemical Engineering Journal, 2016, 306, 646-654, DOI: [10.1016/j.cej.2016.07.094](https://doi.org/10.1016/j.cej.2016.07.094)

Eigenanteil: Ich bin Erstautor. Mit Hilfe der gewonnenen Erkenntnissen aus **Paper 3** wurde ein „Simulated Chemical Looping“-Versuchsstand konzipiert und konstruiert. Mit Hilfe dieses Reaktionsführungskonzeptes wurden von mir Untersuchungen zur C_2 Ausbeute Maximierung durchgeführt. Ebenso führte ich Stabilitätstests für den $\text{Na}_2\text{WO}_4/\text{Mn}/\text{SiO}_2$ Katalysator in Chemical-Looping Experimenten unter OCM Bedingungen durch. Aus den gewonnenen Ergebnissen wurden von mir bestehende Prozesskonzepte und deren Anwendung auf das Chemical Looping diskutiert. Weiterhin folgte ein Vergleich zwischen stationären und dynamischen Experimenten, der ebenfalls ausführlich diskutiert wurde.

Paper 5: Investigation of the role of the $\text{Na}_2\text{WO}_4/\text{Mn}/\text{SiO}_2$ catalyst composition in the oxidative coupling of methane by chemical looping experiments

Vinzenz Fleischer, Maria Garcia Colmenares, Samira Parishan, Ulla Simon, Oliver Görke, Aleksander Gurlo and Reinhard Schomäcker

Journal of catalysis, to be submitted

Eigenanteil: Ich bin Erstautor. In dieser Arbeit wurden verschiedene, von Maria Gracia Colmenares zur Verfügung gestellte, $\text{Na}_2\text{WO}_4/\text{Mn}/\text{SiO}_2$ Katalysatoren hinsichtlich ihrer Sauerstoffspeicher-eigenschaften von mir untersucht. Hierfür wurde von mir das „Simulated Chemical Looping“-Konzept und repetitive Puls-Experimente verwendet. Die repetitiven Puls-Experimente wurde von mir modelliert und es wurden Simulationen durchgeführt zur Untersuchung des Sauerstoffverbauchs. Aus den Ergebnissen wurde von mir eine Korrelation zwischen Sauerstoffspeicherkapazität und Mangangehalt und Filmdicke hergeleitet. Ferner wurde ein Schema zur Funktionsweise des $\text{Na}_2\text{WO}_4/\text{Mn}/\text{SiO}_2$ Katalysators in dynamischen Experimenten von mir aufgestellt.

Jeweils ein Exemplar der Publikation ist dieser Dissertation beigelegt.

Ort, Datum

Vinzenz Fleischer

Table of contents

1	Introduction.....	1
1.1	Motivation	1
1.2	Mechanistic aspects	1
1.2.1	Gas phase reaction network.....	1
1.2.2	Catalyst materials	3
1.2.3	Reaction network and kinetic models.....	5
1.3	Engineering aspects.....	6
1.3.1	Process engineering aspects	6
1.3.2	The chemical looping process concept.....	8
1.4	Outline of this thesis	10
2	Methods and materials.....	11
2.1	Simulation of the OCM gas phase reactions and catalyst surface reactions.....	11
2.2	Catalyst preparation	12
2.3	Nitrogen adsorption	12
2.4	High pressure experiments	12
2.5	Mass spectrometry	13
2.6	Temperature programmed surface reactions.....	14
2.7	Dynamic experiments.....	15
2.8	Simulated chemical looping	16
2.9	Residence time analyses of the simulated chemical looping setup	18
3	Results and discussion.....	20
3.1	Contribution of gas phase reactions to the OCM reaction	20
3.2	Pressure variation during the OCM reaction	22
3.3	Temperature programmed surface reaction experiments	24
3.4	Dynamic experiments.....	28
3.5	Development of a simulated chemical looping setup.....	30
3.5.1	Setup construction.....	30
3.5.2	Residence time analyses of the simulated chemical looping setup	32
3.6	Process parameter studies in simulated chemical looping experiments	35
3.6.1	Influence of flowrate and temperature on the OCM reaction	35
3.6.2	Continuous operation of the chemical looping process and comparison with steady state process mode	37
3.7	Investigation of the role of the catalyst composition in simulated chemical looping experiments and repetitive pulse experiments	41
3.7.1	Variation of the surface concentration of Na_2WO_4 and Mn on COK-12 support.....	41
3.7.2	Variation of the manganese loading on COK-12 support	44
3.7.3	Variation of the support material	47
4	Conclusions.....	51
5	List of References.....	56

Nomenclature

List of Abbreviations

Abbreviations	Description
CLC	Chemical looping combustion
CLR	Chemical looping reforming
CSTR	Continuous stirred tank reactor
DFT	Density functional theory
EPR	Electron paramagnetic resonance
FTIR	Fourier transform infrared spectroscopy
MFC	Mass flow controller
MS	Mass spectrometer
PFTR	Plug flow tube reactor
OCM	Oxidative coupling of methane
PV	Pulse valve
SSA	Specific surface area
STY	Space time yield
TCD	Thermal conductivity detector
Td	Transducer
TPSR	Temperature programmed surface reaction
XAFS	X-ray absorption fine structure
XPS	X-ray photoelectron spectroscopy
XRD	X-ray diffraction spectroscopy

List of symbols

Symbol	Description	Unit
A	Peak area	%·s
A_{spec}	Specific surface area	m ² /g
c	Concentration	mole/ml
D	Diffusion coefficient	m ² /s
d	Diameter	m
d₃₂	Sauter mean diameter	m
D_{ax}	Axial dispersion coefficient	m ² /s
d_h	Hydraulic diameter	m
d_R	Reactor diameter	m
E(t)	Residence time distribution function	1/s
E_A	Activation energy	kJ/mole
k_b	Boltzmann constant	J/K
k_{oo}	Pre-factor	1/(s·m ^{3(x-1)} ·mole ^(x-1))
L	Length	m
M	Molar mass	g/mole
m	Mass	kg
n	Amount of substance	mole
N	Number of segments	-
p	Pressure	Pa

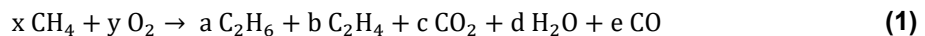
Symbol	Description	Unit
P_e	Peclet number	-
R	Universal gas constant	J/(mole·K)
Re	Reynolds number	-
R_o	Oxygen transport capability	-
S	Selectivity	-
Sc	Schmidt number	-
T	Temperature	K
t	Time	s
t_{delay}	Time duration since gas pulse reaches the reactor inlet	s
t_{dosing}	Time duration since the gas pulse is completely dosed	s
t_{pulse}	Pulse contact time	s/m
u	Flow velocity	m/s
V	Volume	m ³
V*	Vacancy on the catalyst surface	-
⋮	Flowrate	Nml/min
w	Mean free path length of a gas molecule	m
X	Conversion	-
O*	Oxygen species bound on the catalyst surface	-
Y	Yield	-
z	Spatial coordinate	m
Δ_RH	Reaction enthalpy	kJ/mole
ε	Void fraction	-
ζ	Drag coefficient	-
η	Viscosity	Pa·s
ρ	Density	Kg/m ³

1 Introduction

1.1 Motivation

According to the forecast by Owen et al., the demand for crude oil will raise during the next decades by about 40 Bill. barrels. [1] Concurrently, the remaining and newly discovered oil reserves can cover the demand until the end of this century. The main utilization of crude oil is energy generation (93 %) and minor amounts (7 %) are used for the production of chemicals. [2] Most of our daily used products are based on these chemicals. Especially plastics, lacquers, surfactants and basic chemicals, which are further converted to pharmaceuticals, fertilizers and textile-pulps contribute to the daily life in our highly technologized society. One of the most important plastics is polyethylene, which is widely used for films, pipes, and for wire or cable insulations. [3] The preferred production of the monomer ethylene is carried out by the steam cracking process. [4] Therefore, an alternative production route based on a new feedstock seems to be necessary to overcome the high dependence on crude oil, covering further ethene request in the future.

Methane is the main compound in natural gas, which is widely used for energy production, nowadays. [5] One promising reaction to convert methane into C₂ building blocks is the oxidative coupling of methane (OCM) which was first published by Keller and Bhasin in 1982. [6] The overall reaction is given in equation (1).



The reaction requires methane, which is converted by a catalyst into methyl radicals. These radicals can couple to ethane, which can be further dehydrogenated to ethene. [7] Thus, the oxidative coupling of methane is a promising route to convert natural gas into valuable compounds for chemical industry, which is independent from crude oil.

1.2 Mechanistic aspects

1.2.1 Gas phase reaction network

The thermal coupling process of methane is thermodynamically limited, because of its highly endothermic nature in absence of oxidizing agents. The use of oxidizing agents leads to an exothermal reaction enthalpy, which does not limit the methane conversion by thermodynamics anymore. [8] The methane molecule itself has the strongest C-H bond strength in comparison with other alkanes, which means that a high activation barrier has to be overcome for methane activation. Therefore the OCM reaction is typically performed above 700 °C. [9] Unfortunately, these high temperatures cause unselective reactions of methane and oxygen, forming deep oxidation products. Those side reactions are strongly exothermic and decrease the selectivity of C₂ compounds in several ways as shown in Table 1. The use of oxygen as oxidizing agent has the consequence that not only methane is converted into CO_x. Also the C₂ products are affected

by consecutive oxidation reactions which lead to the formation of further deep oxidation products and strong heat generation. Further, it has to be considered that there is a competition between methane molecule activation on the catalyst surface and in gas phase caused through the harsh reaction conditions. Therefore not only the catalyst contributes to the conversion of methane.

Table 1: Reaction enthalpies of important reactions in the OCM process [10]

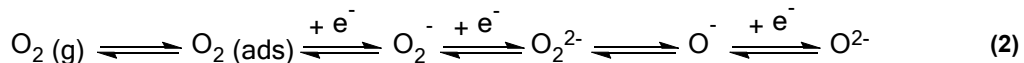
No.	Reaction	$\Delta_R H$ (kJ/mole)
1	$\text{CH}_4 + \frac{1}{2} \text{O}_2 \rightarrow \text{C}_2\text{H}_6 + \text{H}_2\text{O}$	-177
2	$\text{CH}_4 + 2 \text{O}_2 \rightarrow \text{CO}_2 + 2 \text{H}_2\text{O}$	-803
3	$\text{C}_2\text{H}_6 + \frac{1}{2} \text{O}_2 \rightarrow \text{C}_2\text{H}_4 + \text{H}_2\text{O}$	-103
4	$\text{C}_2\text{H}_6 + \frac{7}{2} \text{O}_2 \rightarrow 2 \text{CO}_2 + 3 \text{H}_2\text{O}$	-1429
5	$\text{C}_2\text{H}_4 + 3 \text{O}_2 \rightarrow 2 \text{CO}_2 + 2 \text{H}_2\text{O}$	-1323

As mentioned before, the primary role of the catalyst material is the cleavage of a C-H bond in the methane molecules. These radicals are highly active and couple to ethane molecules. Other radical intermediates formed by activation of different molecules in gas phase or on the catalyst surface are also involved. Dooley and Coworkers published a mechanism for manifold gas phase reactions, considering around 1600 reactions and 280 intermediates. [11] Their reaction mechanism was verified by Schwarz et al. in a profile reactor which allowed to study the local gas composition of the gas feed by a sampling capillary. [12] A sensitivity analysis of that reaction network was carried out by Mavlyankariev. [13] He found that the initiating gas phase reaction steps are induced by the reactions between methane and oxygen which form methyl and hydroperoxyl radicals. Hydroperoxyl radicals and similar oxygen radicals contribute to further unselective reactions by activation of alkanes or alkenes or their radical intermediates. Especially ethane and ethene molecules are highly sensitive for further oxidation reactions. Zanthonoff and Baerns pointed out that a scavenger material for $\text{HO}_2\bullet$, $\text{OH}\bullet$ and O_2^\bullet radicals seem to be necessary to prevent total oxidation routes in gas phase after successful coupling of methyl radicals. [14] Another important intermediate is formaldehyde which is highly active for further radical formation by its decomposition into $\text{H}\bullet$ and $\text{HCO}\bullet$ radicals. These radicals contribute to other radical reaction steps, which preferably lead to deep oxidation product formation. The origin of H_2CO is basically the coupling process of methyl radicals with different oxygen species. However, these gas phase reactions contribute to the limitation of the C_2 yield, which was presented by Zavyalova et al. for several catalyst materials. [15] For the application of the OCM process in chemical industry, a C_2 yield about 30 % is necessary for economical ethene production. [16,17] It has to be noted that such cost estimations are strongly dependent on the current market prices of methane and ethene.

1.2.2 Catalyst materials

A large number of active materials for the OCM reaction was presented by Bhasin and Keller, later reviewed by Baerns and Hutchings et al. [18–20] They suggested as most promising material MgO. One important factor, besides catalytic activity for the OCM process, is the long time stability of the catalyst material. It was demonstrated that several highly active materials, performing the OCM reaction under harsh conditions, tend to deactivate in time on stream experiments. [21] One well-known catalyst material is the Li/MgO system, which was reviewed in detail by Arndt et al. [8] That catalyst material tends to loose Li in time on stream experiments and its catalytic activity correlates with the number of steps or edges. [22] Therefore the OCM activity of this material has a strong sensitivity on its morphology. A proposed mechanism is the methane adsorption and coordination at a dehydroxylated step. The methane molecule is than polarized and the C-H bond is cleaved by an O₂ molecule from gas phase, which forms an HO₂• radical. [23] One important aspect is that the knowledge about the MgO material provides the opportunity of Density Functional Theory (DFT) calculations for a mechanistically understanding of the OCM process. Kwapien et al. presented a model for a MgO cluster, which involves several oxygen species on the catalyst surface for methane activation. [24] That fact indicates that simplified kinetic models, as Langmuir Hinshelwood or Eley Rideal, for that material are not able to predict the reaction progress in different reactor systems. This is because the oxygen dosing strategy of the feed and the reactants dispersion may influence the presence of these species. Therefore the contribution of the catalyst material to the OCM reaction may differ, because the nature of different oxygen ions or radical species is very different. That will be discussed later. Unfortunately, Korf et al. demonstrated that the Li/MgO catalyst is not stable in time on stream experiments. [25]

Another well-known catalyst material is La₂O₃. To reach high catalytic activity, lanthan-oxy-carbonates have to be formed by the adsorption of CO₂ on the catalyst surface. The insertion of CO₂ molecules dopes the top layer structure of the catalyst material. That was proven in experimental studies by Fourier transform infrared spectroscopy (FTIR). [26,27] However, there is a debate about the involvement of several oxygen species on the catalyst surface, which contribute to the OCM surface reaction network for that material, too. The first discussion about methane interaction with different oxygen intermediates was presented by Kaliaguine et al. [28] All discussed oxygen species on the catalyst surface are presented in equation (2).



For lanthanum oxide it was proposed that superoxide species (O₂⁻) are responsible for selective methane activation. [29] Lacombe et al. discussed the contribution of the “working surface” for the La₂O₃ catalyst. [30] They concluded that especially the formation of deep oxidation products is highly sensitive for low coordinated surface sites. The origin of low coordinated surface sites is the selective activation of methane. Therefore a selective activation of methane creates the active site for the unselective reaction. Palmer et al. demonstrated by DFT calculations for a lanthanum oxide cluster that O⁻ is the most active oxygen species for selective methane

activation. [31] Unfortunately, O^- is hard to detect in Electron Paramagnetic Resonance (EPR) spectroscopy studies, because of its unstable nature in comparison to the superoxo- and peroxy-intermediates. [32] Ferreira et al. demonstrated by doping of the lanthanum oxide with ceria that the activity and selectivity is enhanced in comparison to the standard lanthanum oxide. In their X-ray photoelectron spectroscopy (XPS) studies they proposed that O^- is responsible for such findings. It has to be noted, that the O^- species is preferably bound close to the ceria ions. [33] A similar enhancement effect was observed by doping of the MgO catalyst with iron ions. [34] It was demonstrated through an experimental and theoretical study that the oxygen adsorption on doped surface areas of CaO with molybdenum follows the reaction pathways according to equation (2). [35] Thus, the involvement of several oxygen species on the catalyst surface of various active materials in the OCM reaction is an important aspect. Although the La_2O_3 system allows for a stable performance in time on stream experiments, the C_2 yield is limited. [36]

Another well-known high performance catalyst material for the OCM reaction is the $Na_2WO_4/Mn/SiO_2$ system. The active phase contains Na_2WO_4/Mn and is deposited on a silica support material. That system was first presented by Fang et al. [37] It was reported by different groups that the material has a stable performance for several hundred hours in time on stream experiments. [38–41] Furthermore, a material benchmark was carried out in an OCM mini-plant, performed in a fluidized bed reactor, with different doped lanthanum oxide systems and the $Na_2WO_4/Mn/SiO_2$ catalyst. [42] In that study it was reported that the $Na_2WO_4/Mn/SiO_2$ catalyst showed the best overall performance. This catalyst is mostly prepared by incipient wetness impregnation methods, because of less experimental effort compared to the sol-gel and the mixed slurry method. All preparation methods showed comparable catalytic performance and stability. Major phases, found in X-ray diffraction spectroscopy (XRD), are Mn_2O_3 , Na_2WO_4 and α -cristobalite (SiO_2). [43] Unfortunately, this catalyst has several complex material properties and tremendous dependency on compound composition. It was reported that the phase transition of the support material into α -cristobalite is induced by Na^+ ions, which is absolutely necessary for a high performance of this catalyst material. [44] As consequence there is a dramatic shrinkage of the specific surface area (SSA). Furthermore, the active phase (Na_2WO_4/Mn) undergoes surface reconstruction and has strong interactions between the support and the transient metal oxide. [45] The highest catalytic performance was reported for a composition of 5 wt-% Na_2WO_4 and 2 wt-% Mn(II). [39,45,46] Kou et al. studied this catalyst with X-ray absorption fine structure (XAFS) and XPS. [47] They reported that the surface of the fresh catalyst material, enriched by oxygen during a calcination procedure, exists as an amorphous phase which contains dispersed tungstate and manganese oxides. Their findings were confirmed by Gholipour et al., who carried out a variation of the sodium ion by different alkali metal ions. [48] They concluded that the alkali ion enables the structural flexibility of the active phase on the catalyst surface, which is highly active and selective. Nipan calculated a theoretical phase diagram, which considers several phases of the $Na_2O-WO_3-Mn_2O_3-SiO_2$ system and its ability to form a quasi-liquid active surface on the support material. [49] This

aspect enables the ability of an oxygen spillover reaction between Mn_2O_3 and Na_2WO_4 . In principle, that reaction is a redox mechanism between Mn(III+) and W(VI+). [50,51] Such spillover effect enhances the OCM activity of the $\text{Na}_2\text{WO}_4/\text{Mn}/\text{SiO}_2$ system more than three times compared to the $\text{Na}_2\text{WO}_4/\text{SiO}_2$ system, which cannot perform such a reaction. The oxygen-spillover effect is very sensitive to the manganese oxide oxidation state, which shows also the highest activity in comparison with other transient metal ions. [52] It was reported that also a high dispersion of Na_2WO_4 and Mn on the support material enhance the catalytic activity. [53] A better distribution of these compounds could improve the reaction rate of the oxygen-spillover reaction.

1.2.3 Reaction network and kinetic models

Lunsford and Coworkers proved that the ethane formation process undergoes methyl radical coupling and many groups contributed to the development of a surface reaction networks with big effort for several catalyst materials. [54] One of the first mechanisms for selective methane activation was postulated by Lunsford and Coworkers for the Li/MgO catalyst. [55] They adapted the assumption of Ito et al., who proposed (Li^+O^-) as active centers. [56] The center is involved in the hydrogen abstraction reaction of a methane molecule, which is then converted into $2(\text{Li}^+\text{O}^-)\text{H}$ and finally reduced to Li^+O^{2-} . Thereafter, it is reoxidized by gas phase oxygen. Sinev discussed several mechanisms for C-H bond cleavage on the catalyst surface [57] and he discussed the reoxidation process of the active sites in detail. He proposed that the oxidative dehydrogenation in steady state experiments of the formed hydroxyl groups is the dominant reoxidation step. Korf et al. suggested the participation of surface carbonates, which contribute to the selective activation of methane. [25] Hutchings and Coworkers studied MgO, Li/MgO and Ag/ Al_2O_3 catalysts materials by use of different oxidant agents. [58] They suggested that O^- radical ions are the oxygen species for selective methane activation, but due to a very short life time under OCM conditions the analytical prove of this species is difficult. Furthermore, they could show that two active oxygen species on the Li/MgO surface contribute to selective and unselective methane activation. [59]

As discussed above, the contribution of gas phase reactions and the presence of several oxygen intermediates on the catalyst surface increase the experimental effort and complicate the calculations of reliable kinetic data. Based on the available data a variety of surface reaction networks and kinetic models have been developed. [60–65] One well-known micro kinetic network was presented by Sun and Thybaut for a Li/MgO catalyst, which considers gas phase reactions and reactions on the catalyst surface. [66] A comparable model was presented by Lee et al. for the $\text{Na}_2\text{WO}_4/\text{Mn}/\text{SiO}_2$ catalyst. [67] Both surface reaction models are presented in Table 2. It is shown that both networks follow similar reaction pathways despite the different nature of the catalyst materials. Gas phase oxygen is adsorbed by dissociation on a free active site (V^*) of the catalyst surface and is converted into an active oxygen species (O^*). Methane is activated by C-H bond cleavage by that oxygen species and methyl radicals are produced. Further alkanes and alkanes are activated in a similar reaction step, which produces radical intermediates. Methyl radicals and CO are further oxidized to alkoxides and CO_2 .

Table 2: Comparison of reaction networks on the catalyst surface of Li/MgO and Na₂WO₄/Mn/SiO₂ catalyst

No.	Lee et al. [67]	Sun et al. [66]
1	O ₂ + 2 * V ⇌ 2 O *	O ₂ + 2 V ⇌ 2 O *
2	CH ₄ + O * ⇌ CH ₃ · + OH *	CH ₄ + O * ⇌ CH ₃ · + OH *
3	C ₂ H ₄ + O * ⇌ C ₂ H ₃ · + OH *	C ₂ H ₄ + O * ⇌ C ₂ H ₃ · + OH *
4	C ₂ H ₆ + O * ⇌ C ₂ H ₅ · + OH *	C ₂ H ₆ + O * ⇌ C ₂ H ₅ · + OH *
5		2 OH * ⇌ H ₂ O * + O *
6		CH ₃ · + O * ⇌ CH ₃ O · *
7	CH ₃ · + 3 O * ⇌ HCO · · + 2 OH *	{ CH ₃ O · · + O * ⇌ CH ₂ O * + OH *
8		CH ₂ O * + O * ⇌ HCO · · + OH *
9	HCO · · + O * ⇌ CO * + OH *	HCO · · + O * ⇌ CO * + OH *
10	CO * + O * ⇌ CO ₂ * + V *	CO * + O * ⇌ CO ₂ * + V *
11		CO * + * ⇌ CO *
12		CO ₂ * + * ⇌ CO ₂ *
13	2 OH * ⇌ H ₂ O + O * + V *	4 HO ₂ · → 3 O ₂ + 2 H ₂

However, the contribution of several oxygen intermediates on the catalyst surface was proposed in recent experimental works, by use of different oxidizing agent (O₂ and N₂O). [68,69] It was demonstrated by use of different oxidizing agents, which were nitrous oxide and molecular oxygen that the catalytic activity is decreased but C₂ selectivity is drastically increased. In dynamic experiments, the use of CO₂ as oxidant for the Na₂WO₄/Mn/SiO₂ catalyst also shows extremely high C₂ selectivity of about 95 % at 5 % methane conversion. [70] Comparable effects were shown by Takanabe and Iglesia, who co-fed water to the reactant mixture at the reactor inlet. [71] They pointed out that also OH· radicals contribute as selective oxidants to the selective methane activation on the catalyst surface. Beck et al. demonstrated in temporal analysis of products (TAP) experiments that weakly adsorbed oxygen intermediates contribute to the unselective activation of methane on MgO and Na₂WO₄/Mn/SiO₂ catalysts, while a strongly bound oxygen species is responsible for the selective methane activation. [72]

The contribution of several oxygen intermediates to the catalyst activity is well-known for systems as formaldehyde or ethylene oxide production. [73,74], but not for the OCM reaction. Therefore, experimental methods are required to investigate the contribution of all oxygen species on the catalyst surface. Furthermore, it is necessary to understand how all these species are formed and interact with other compounds during the OCM reaction.

1.3 Engineering aspects

1.3.1 Process engineering aspects

As mentioned in the last section, one important aspect of the OCM reaction is the strong exothermic reaction enthalpy and the contribution of gas phase reactions which leads to the formations of hotspots. Several experimental techniques exist to avoid hot spot formation or handle the hotspot temperature during OCM reaction. Kooh et al. optimized the steady state conditions for C₂ yield maximization with a La₂O₃ catalyst, dealing with hot spot formation. [75]

They found that high linear space velocities and high temperatures are beneficial for the OCM reaction. Such conditions avoid back mixing of C₂ products to the catalyst bed, which can activate these products again. Further oxidation reactions would lead to the formation of deep oxidation products. Furthermore, ethane should be quickly dehydrogenated to ethene, because in comparison to ethane it is more resistant against oxidation reactions. Wolf et al. demonstrated that also the heat conductivity of the catalyst bed is essential to remove the reaction heat from the catalyst zone. [76] The complex interplay of gas phase and catalyst surface reactions is highly influenced by the temperature profile in the OCM reaction. Therefore, an up-scaling of an OCM reactor is very challenging. However, there are several publications which present process engineering aspects such as modeling of reactor concepts and up-scaling. [40,77–79] Furthermore, large amounts of the catalyst are needed for an industrial relevant scale. An up scaled synthesis method for large batches of Na₂WO₄/Mn/SiO₂ catalysts was presented by Simon et al. [41] The catalyst was made by sprayed impregnation in a fluidized bed reactor and showed stable performance in time on stream experiments. The cluster of excellence “Unifying concepts in catalysis” (UNICAT) presented the successful development and operation of an OCM mini-plant. [80] The OCM reaction was performed in a fluidized bed reactor with Na₂WO₄/Mn/SiO₂ and La₂O₃/CaO catalysts achieving a C₂ yield of 19 %. [42]

Another important aspect of the OCM reaction is the separation process of the product stream. Godini et al. analyzed different separation concepts and made cost estimations of a hypothetical plant which produces 240 000 tons ethylene/year. [81] One of the most costly operations is the separation of ethylene from ethane, which is caused by energy intensive cryogenic rectification. Several separation processes were discussed to separate the unconverted methane and deep oxidation products first. That would reduce the amount of the total product stream for cryogenic rectification dramatically. Also the adsorption of methane, hydrogen and CO directly after the OCM reactor improves the operation of that plant, with decreasing of the operation costs. Another idea for the separation of ethylene is a chemical reaction to convert it directly to polymers or to Ethylbenzene, which was presented as the ACRO or OXCO process. [82,83]

Besides these aspects, different types of reactor concepts were tested to overcome the limitations of the C₂ yield. Kruglow and Coworkers presented the operation of a countercurrent moving bed reactor. [84] The idea of this concept is to remove C₂ products from the feed stream during increase of methane conversion. That was carried out by reaction columns and separation columns. In the first stage small amounts of methane were converted and C₂ products were separated in the separation column. The rest of the feed was send to the next reaction column, which proceeds the conversion of methane. The C₂ products of that run were separated again and the rest of the feed was send to the next stage and so on. They were able to reach methane conversions of 75 % with a C₂ yield of 55 %. Hu et al. presented a dual catalyst, fixed bed reactor for a simultaneous production of ethene and syngas. [85] The yield for CO + C₂H₄ was 18.5 %. Godini et al. presented a membrane reactor concept for the OCM reaction. [86] Oxygen is dosed in small amounts through a porous ceramic reactor wall to the

catalyst fixed bed section, which is constantly fed with methane. That technique allows encountering gas phase reactions, induced by gas phase oxygen, and 25.5 % C₂ yield were reported.

Recently, Siluria Technologies presented a full operational plant, which is aimed to convert natural gas into liquid hydrocarbons economically, performing the OCM reaction even with limited C₂ yield. [87] However, their process concept depends strongly on very cheap methane prices.

1.3.2 The chemical looping process concept

The first publication about chemical looping was reported by Hurst in 1939. [88] The Messerschmitt Wasserstoffgas-Generator was the pioneer setup to produce hydrogen by use of steam and iron by that concept. Further development of that technology offers several types of application. The main research fields are chemical looping combustion (CLC) and Chemical looping reforming (CLR). [89] The general process concept is presented in Figure 1. A reduced oxygen carrier material Me_XO_{Y-1}, typically a transition metal oxide, is oxidized by air in the first reactor (Me_XO_Y). The oxidized metal oxide is then used in a second reactor to oxidize a reactant. The reduced oxygen carrier is recycled back to the first reactor, where it is oxidized again. There are modified reactor concepts, which handle different problems during application. [90] Typical configurations are two interconnected moving or fluidized bed reactors, alternating fixed bed, fluidized bed reactors or rotating reactors.

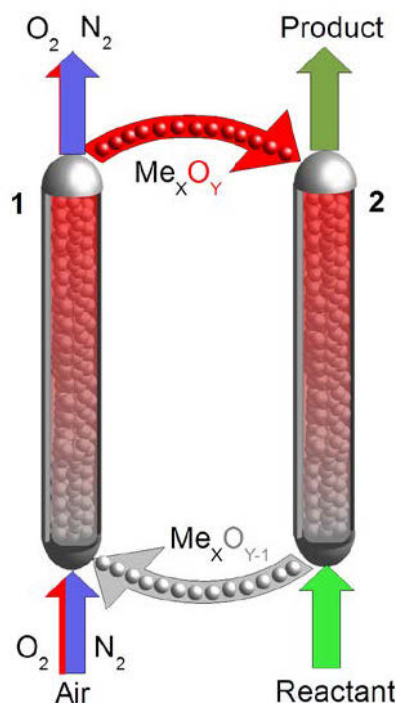


Figure 1: Scheme of the chemical looping process concept

The CLC focusses on energy production by complete methane combustion to CO₂. The advantage of that technology, compared to standard co-feed of methane and oxygen, is the capture of CO₂ without further separation processes after the combustion reactor. Furthermore, NO_x emissions are drastically reduced, because no nitrogen is present in the combustion reactor. Unfortunately, the investment cost of a CLC plant is 71 % higher, compared to a classical natural gas power plant. [91] The biggest CLC plant is operated by the Technische Universität Darmstadt with a nominal power of 1 MW_{th}. [92] The CLR deals with the oxidation of methane to syngas. The main advantage of such application is the heat balance, because the oxidation reaction of the oxygen carrier is exothermic and the reforming process endothermic. [93] The energy of the oxidation reaction is stored mostly in the oxygen carrier and transported to the reforming reactor, which allows a good energy integration concept.

One of the most important parameters in chemical looping systems is the amount of stored oxygen, which is transported by the oxygen carrier. The oxygen transport capability R_O is described by equation (3), where m_o is the mass of the oxidized carrier material and m_r is the mass of the reduced one. The higher that value is the more oxygen can be stored in the oxygen carrier material. Common oxygen carrier materials were reviewed and discussed by Adanez et al. and Li et al. [89,94] A high specific surface area (SSA) is required to provide enough adsorption sites for gas phase oxygen. Furthermore, the oxidation and reduction rate should be high for sufficient residence times in both reactors. In Addition, a high availability, low toxicity, good mechanical strength and suitable heat capacity of the oxygen carrier are also necessary. [95]

$$R_O = \frac{m_o - m_r}{m_o} \quad (3)$$

The most relevant oxygen carrier systems and their oxygen transport capability are presented in Table 3. It has to be noted that the R_O and the redox properties are strongly influenced by the support materials. [96]

Table 3: Most relevant oxygen carrier materials and their oxygen transport capability in chemical looping experiments [89]

Redox system	R _O (-)
NiO / Ni	0.210
Mn ₂ O ₃ / MnO	0.100
Mn ₂ O ₃ / Mn ₃ O ₄	0.034
Mn ₃ O ₄ / MnO	0.070
Fe ₂ O ₃ / Fe ₃ O ₄	0.034
Co ₃ O ₄ / CoO	0.067
CuO / Cu	0.200

Another important aspect is the suppression of coke formation on the carrier particles. Typically the origin of coke is the disproportion of CO, according to the Boudouard reaction in equation (4).



Ishida et al. demonstrated that a very low concentration of water vapor in the reactant feed can completely suppress the formation of carbon coke in CLC. [97] The reason is the water gas shift reaction (Equation (5)), which act as a co-oxidant for the CO oxidation.



Besides the production of deep oxidation products and energy or hydrogen, other groups applied the chemical looping concept for partial oxidation reactions successfully. The challenging situation in the production of ethylene oxide is the presence of several oxygen species on the catalyst surface, comparable to the OCM surface reaction network, as discussed in the previous section. [74] Park and Coworkers demonstrated that the cyclic operation improves the selectivity to ethylene oxide dramatically. [98] In another work the periodic operation was applied for the production of maleic acid from butadiene. [99] Similar selectivity improvements for maleic acid were reported by Lang et al. [100]

The cyclic operation of the oxidative dehydrogenation of propane was presented by Creaser et al. [101] They could demonstrate that the dynamic operation of the reactor for propene formation enhances the yield significantly. On the one hand that is caused by the avoidance of any gas phase reactions, induced by oxygen. On the other hand unselective site reactions on the catalyst material were minimized. [102] Their experiments were verified by Ballaniri et al. who prepared a variety of supported vanadia catalysts for this reaction, enhancing the propene yield by a factor two. [103] Therefore, the chemical looping system seems to be a suitable reactor concept for the oxidative coupling of methane, too.

1.4 Outline of this thesis

As discussed before, the contribution of gas phase oxygen and several surface oxygen species to the production of ethylene in the OCM reaction decrease the C₂ yield. Such challenge could be encountered by transient and cyclic operation experiments. The Na₂WO₄/Mn/SiO₂ catalyst is a well-known system, which provides long time stability and high activity. Furthermore, it can be produced in large scales batch. Finally, manganese oxide is well-known for its oxygen storage capacity in different chemical looping studies and results from earlier presented transient experiments of the Na₂WO₄/Mn/SiO₂ catalyst show promising activity and superior C₂ selectivity in comparison with co-feed experiments. [104] It should be noted that the catalyst material has to fulfill two roles. On the one hand, it serves as oxygen carrier material, similar as in the CLC and CLR processes. On the other hand, it fulfills the role as a catalyst material, because stored oxygen on the catalyst surface is converted to water by methane activation, to form methyl radicals.

[**Paper 1**](#) analyses the thermal reaction sensitivity of the OCM reaction in case of hot spot formation during steady state experiments. Furthermore, the influence of gas phase and surface reactions in different experimental and theoretical steady state reactors were investigated.

[**Paper 2**](#) deals with the experimental investigation of the Na₂WO₄/Mn/SiO₂ catalyst material in temporal analysis of products (TAP) experiments in absence of gas phase oxygen. Further, the catalyst activity was studied in steady state experiments at pressures up to 10 bar and calculations about reaction engineering aspects of the OCM reaction in a steady state fixed bed reactor were carried out.

[**Paper 3**](#) deals with temperature programmed and dynamic experiments to study the interactions between OCM reactants such as CH₄, C₂H₆ and C₂H₄ in absence of gas phase oxygen with the Na₂WO₄/Mn/SiO₂ catalyst surface. Additionally, the ability to store and provide strongly bound oxygen for the OCM reaction under non-steady state conditions was investigated.

[**Paper 4**](#) describes the development and operation of a lab scale simulated chemical looping setup for the OCM process. Yield boundary studies in chemical looping experiments were carried out and compared with standard steady state experiments. Based on these results a design proposal was made for a hypothetical chemical looping OCM plant.

[**Paper 5**](#) investigates the role of the catalyst compounds of the Na₂WO₄/Mn/SiO₂ material. The focus is the finding of a correlation between the active compounds and the oxygen storage capacity. Furthermore, the influence of the catalyst's SSA on the OCM reaction in chemical looping experiments was studied.

2 Methods and materials

2.1 Simulation of the OCM gas phase reactions and catalyst surface reactions

The simulation of the OCM reaction was performed in Chemkin (Reaction Design/Ansys). For the gas phase reaction mechanism the Dooley mechanism was used. [11] One of the key steps in OCM reaction on the catalyst surface is the C-H bond cleavage of methane, which is the origin for methyl radicals that by coupling form ethane. The simplest approach to implement a chemical reaction, induced by a catalyst material, is presented in

Table 4. A vacancy (V*) on the catalyst surface is filled by dissociative adsorption of gas phase oxygen. Methane is activated in the selective way by methyl radical formation. Finally, the formed OH group on the catalyst surface is removed by the formation and desorption of water molecules. Through lack of reliable micro kinetic data for the Na₂WO₄/Mn/SiO₂ catalyst, the kinetic parameters were set to the generally accepted fact, of fast catalyst reoxidation and the methane activation as rate limiting step. The strong impact of gas phase activity on product selectivity was investigated by the selection of different ideal reactors as the plug flow tube reactor (PFTR) with no back mixing effects and the continuous stirred tank reactor (CSTR), which is completely mixed. A detailed implementation to Reaction Design Chemkin was presented in the model-based analysis part of [Paper 1](#).

Table 4: Semi-empirical catalyst reaction network of the OCM reaction ([Paper 1](#))

No.	Reaction step	k_{oo} (1/s)	E_A (kJ/mole)
1	$\text{O}_2 + 2 \text{V}^* \rightleftharpoons 2 \text{O}^*$	$3 \cdot 10^6$	40
2	$\text{CH}_4 + \text{O}^* \rightleftharpoons \text{CH}_3 \cdot + \text{OH}^*$	$3 \cdot 10^5$	120
3	$2 \text{OH}^* \rightleftharpoons \text{H}_2\text{O} + \text{O}^* + \text{V}^*$	$3 \cdot 10^6$	40

2.2 Catalyst preparation

The reference $\text{Na}_2\text{WO}_4/\text{Mn}/\text{SiO}_2$ catalyst was synthesized and characterized by Dr.-Ing. Ulla Simon (Groupleader: Prof. Aleksander Gurlo). The experimental methods are described in [41]. The final catalyst had a composition of 5 wt-% Na_2WO_4 and 2 wt-% Mn(II) ions. The SSA was $1.86 \text{ m}^2/\text{g}$ and the particle size was $150 - 350 \mu\text{m}$. This catalyst was used in all of our experiments which are presented [Paper 1](#)-[Paper 4](#), and also as reference catalyst material in [Paper 5](#).

All other presented $\text{Na}_2\text{WO}_4/\text{Mn}/\text{SiO}_2$ catalysts, supported on COK-12, in [Paper 5](#) were synthesized and characterized by Maria Gracia Colmenares (Groupleader: Prof. Aleksander Gurlo). The XRD characterization of the spent catalysts were carried out by Dr.-Ing. Ulla Simon. It has to be noted that COK-12 is a mesoporous silica material.

2.3 Nitrogen adsorption

Nitrogen adsorption at 77 K is a well-known technique to determine the SSA of solid materials, according to the theory of Brunauer, Emmet, and Teller (BET) [105]. The catalysts were degassed at 120°C and 0.15 mbar for 60 minutes. Thereafter, they were analyzed by a Micromeritics Gemini III 2375 Surface Area Analyzer.

2.4 High pressure experiments

A scheme of the high pressure reactor is presented in Figure 2. The catalyst (100 mg) was placed on an inert bed of quartz granules inside of a corundum inlay. The inlay was surrounded by a steel jacket to operate at pressure up to 10 bar. The feed was 95 vol.-% methane and 5 vol% oxygen with an overall gas flow rate between 50 to 500 Nml/min and a constant residence time of 0.16 s in each run. The reaction temperature was between $700 - 800^\circ\text{C}$ and the products were analyzed with a gas chromatograph GC-2014 by Shimadzu. More details are given in the experimental part of [Paper 2](#).

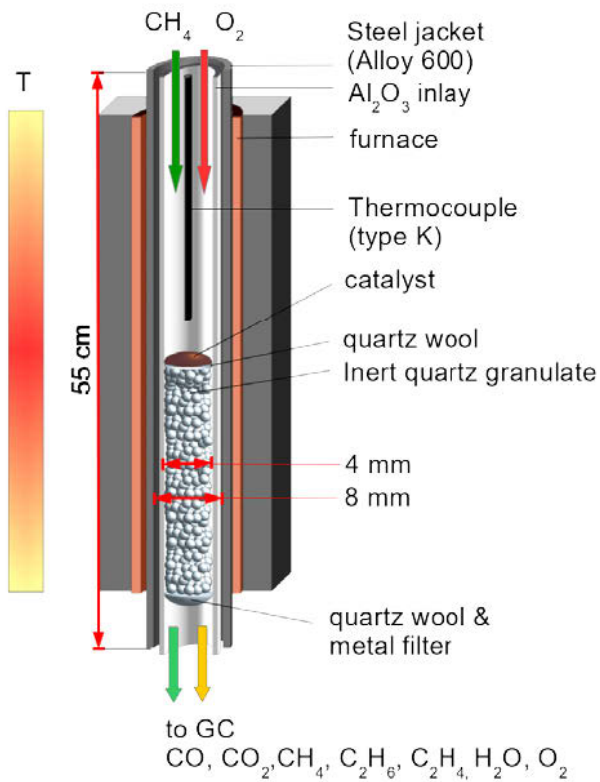


Figure 2: Scheme of the high pressure reactor

2.5 Mass spectrometry

A scheme of the mass spectrometer (InProcess Instruments, GAM 200) is presented in Figure 3. The gas mixture from the reactor outlet was send to Inlet 1 of the mass spectrometer (MS). A small amount of the gas was send continuously through a capillary by a rotary vane pump, while the rest was sent to the vent. The gas sample was ionized by electron impact ionization, utilizing yttriated yttrium filament. A cascade of a turbomolecular pump, a diaphragm pump and an external rotary vane pump generates a pressure of 10^{-6} mbar. The ionized fragments passed a quadrupole, which deflects the fragments by their specific ratio of Lorentz force to inertial force. Finally a channeltron secondary electron multiplier (SEM, 1200 V) was used to enhance and analyze the composition of the fragments. The software for control of the MS and calculation of the compound concentration by balances of the fragment composition was provided by InProcess Instruments. The details about compound calibration and data recording are presented in the experimental section and in the supporting information of [Paper 3](#).

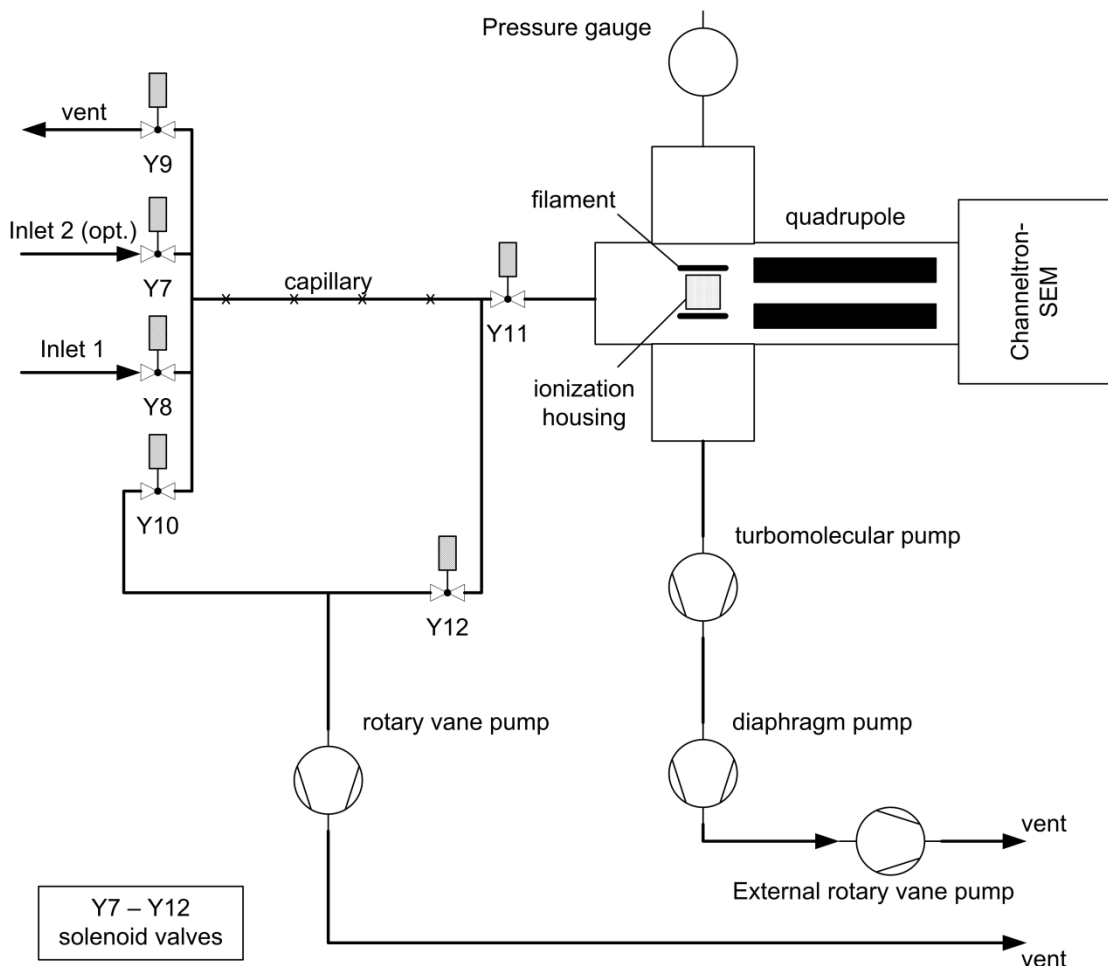


Figure 3: Scheme of the quadrupole mass spectrometer Model GAM 200 (InProcess Instruments)

2.6 Temperature programmed surface reactions

The experimental concept of a temperature programmed surface reaction (TPSR) is presented in Figure 4. In a first step the catalyst was heated up (10 K/min) under a flow of an oxidizing agent (e.g. synthetic air). After the oxidation treatment, the catalyst was cooled down again. The reactor was purged by an inert gas (e.g. N₂, He) to remove gas phase and weakly bound oxygen species. Thereafter, a reactant (e.g. hydrogen, methane...) was fed to the reactor, while the catalyst material was heated up with a defined temperature ramp (1-5 K/min). The composition at the outlet of the reactor was continuously recorded by a detector (e.g. thermal conductivity detector (TCD), MS). The exact procedure for all TPSR experiments and further information, e.g. temperature profile of the furnace, are given in [Paper 3](#) and [Paper 3-SI](#).

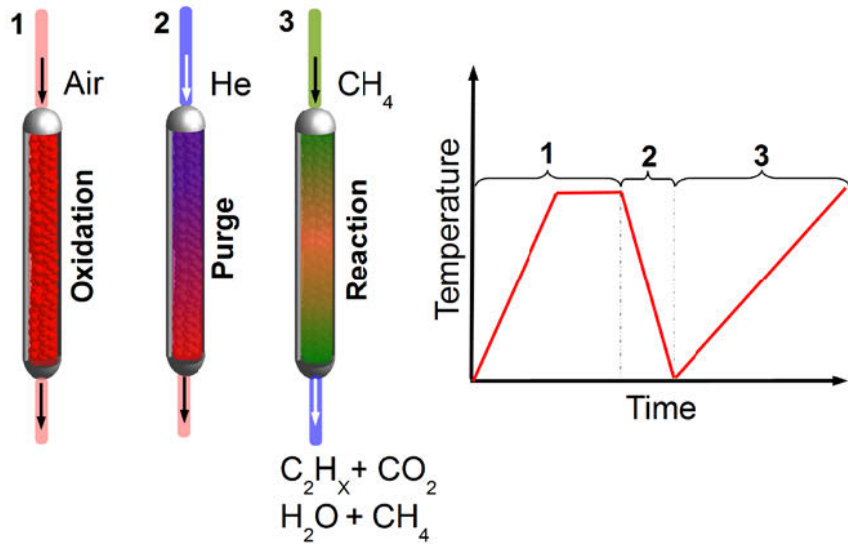


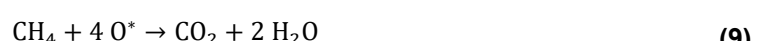
Figure 4: Experimental concept of temperature programmed surface reaction (TPSR) experiments

2.7 Dynamic experiments

Dynamic experiments follow a similar experimental concept as presented in the last subsection (2.6). The catalyst material (1 g) was heated up to reaction conditions in a flow of an oxidizing agent (e.g. synthetic air). After reaching the desired reaction temperature (700 – 800 °C), the reactor was purged by an inert gas (He) keeping the temperature constant. The reaction was carried out by an immediate replacement of the inert gas by the reactant gas (e.g. methane, ethane, ethene). That was realized by opening and closing of switching valves (Swagelok SS-41S2) in front of the gas supplies. Again, the composition at the outlet was continuously measured by MS. The experimental method and all parameters are presented in the experimental section of [Paper 3](#). The selectivity of the products was derived according to equation (6).

$$S_i = \frac{v_i \cdot A_{\text{Product},i}}{\sum(v_i \cdot A_{\text{Product},i})} \quad (6)$$

Furthermore, the converted amount of stored oxygen n_{O*} was derived according to the oxygen balances given in the rate equations (7) - (9) and finally by equation (10).



$$n_{\text{O}^*} = \frac{p \cdot \dot{V} \cdot \sum(v_{\text{O}^*,i} \cdot A_{i,\text{product}} [\% \cdot s])}{R \cdot T} \quad (10)$$

In addition, a molecule specific oxygen balance was calculated according to the reaction network presented in Figure 5 and the following assumptions:

- There is no mass transport effect for the stored amount of oxygen
- All reactions are second order
- The ratio of k₃/k₄ is between 2 and 7 according to the findings of Lunsford and coworkers [106,107]

For instance, for each detected ethene molecule, one O_{C₂H₆} and one O_{C₂H₄} were converted to water. Based on these assumptions the first four methane pulses in repetitive pulse experiments were fitted. Based on the fitting parameters (k₁ – k₄) the repetitive pulse experiment was simulated (15 methane pulses) and the amount of converted oxygen was determined ([Paper 5-SI](#))

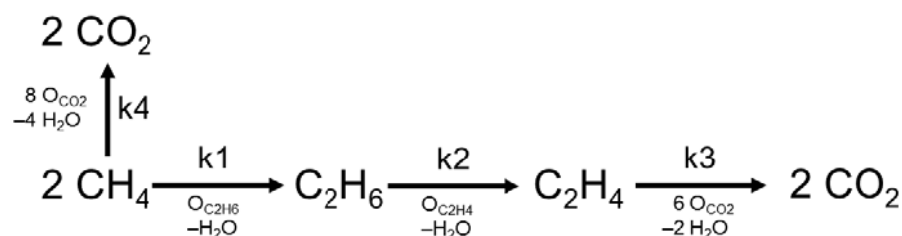


Figure 5: Assumed OCM surface reaction network of the Na₂WO₄/Mn/SiO₂ catalyst for molecule specific oxygen balance ([Paper 5](#))

2.8 Simulated chemical looping

The adaption of the chemical looping process concept to the OCM reaction with Na₂WO₄/Mn/SiO₂ catalysts was realized by two pneumatic six port valves. These valves allow the dosage of defined amounts (0.25 – 2 ml) of reactants to the catalyst fixed bed. The simulated chemical looping concept was chosen to prevent comminution or abrasion of the catalyst particles which is a significant problem in fluidized bed reactors. A fundamental process scheme is presented in Figure 6. Helium (15 - 60 Nml/min) was used as carrier gas to transport the reactant gasses from the sample loop to the reactor, through the catalyst fixed bed (0.5 – 1 g), and finally to the MS. In the first step, oxygen was dosed to the reactor for catalyst oxidation at reaction temperature, by pulse valve 1 (PV). After complete dosage, the position of the first pulse valve was set back to refill the sample loop with oxygen. The flow of the carrier gas was used to purge the reactor, removing gas phase and weakly adsorbed oxygen intermediates. A second PV was utilized to dose methane to the reactor. The filling procedure was carried out parallel to the dosing procedure of oxygen. Finally, non-converted methane was purged out by the carrier gas, to avoid an explosive mixture with the followed oxygen pulse.

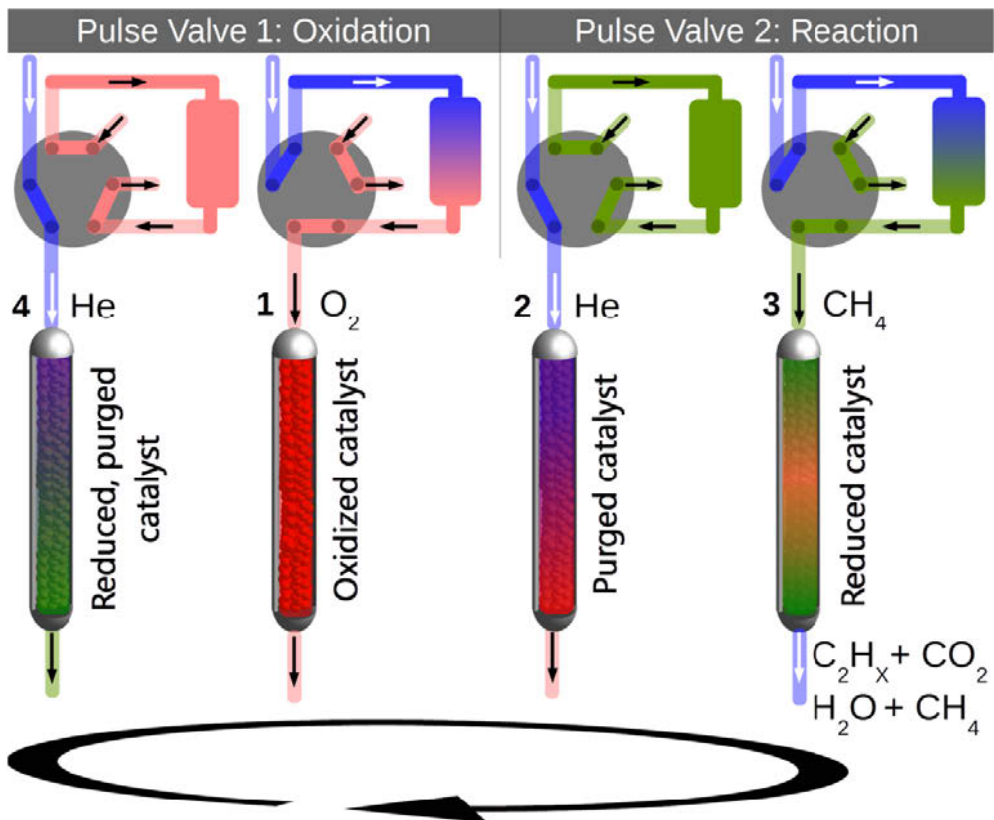


Figure 6: Simulated chemical looping concept for the oxidative coupling of methane ([Paper 4](#))

The construction plan of the chemical looping setup is given in [Paper 4](#). The control software for the pulse valves was developed in Microsoft Visual Basic 6. Further, the experimental parameters and operation conditions are also presented the experimental part of [Paper 4](#). The baseline corrected peaks were integrated and methane conversion (X_{CH_4}), the selectivities of detected compounds and the C_2 yield were derived according to equations (12), (6) and (11).

$$X_{CH_4} = \frac{\sum(v_i \cdot A_{\text{Reaction products}})}{\sum(v_i \cdot A_{\text{Reaction products}}) + A_{CH_4,\text{unconverted}}} \quad (12)$$

$$Y = X_{CH_4} \cdot S_{C_2H_6+C_2H_4} \quad (13)$$

A modification of that operation was the repetitive pulsing of methane. After oxidation (PV 1) of the catalyst material at 775 °C and 30 Nml/min, the reactor was purged by the carrier gas. Than the first methane pulse (via PV 2) was injected and after complete dosage the PV was set back to filling position, immediately. The oxidation procedure was spared out and the reactor was purged by the carrier gas to remove unconverted methane. Thereafter, an additional methane pulse was dosed to the reactor. That procedure was repeated similar to a titration experiment. The experiment ended, when no methane conversion was observed anymore, indicated by no detection of C_2 and deep oxidation products. All experimental parameters and conditions are presented in the experimental section of [Paper 5](#).

2.9 Residence time analyses of the simulated chemical looping setup

The residence time analysis was carried out by a series of pulse marking experiments, using PV 1 as injector for different tracer gases (0.5 - 2 ml pulse) and He as carrier gas. First the dosing behavior of the tracer pulse (Ar) by the pulse valve was analyzed at different flow rates of 20 – 60 Nml/min. A thermal conductivity detector (TCD) was mounted to the pulse valve pipe instead of the reactor inlet. This is presented in Figure 7 A. The TCD detected a signal each 0.5 s. The recorded peak area for each experiment was normalized to one and the results were fitted in Berkley Madonna by square pulse functions (Figure 7 C, left part). The fitting parameters were the delay time (t_{delay}) between detector and pulse valve, the pulse width (t_{dosing}) and pulse amplitude. The square pulse function ($\text{squarepulse}(t_{\text{dosing}}, t_{\text{delay}})$) in Berkley Madonna generates a rectangular signal with amplitude hight of one. That signal was multiplied by an amplitude parameter which was related to the experimental tracer dispersion. The finally fitted rectangular signals had peak areas of one, similar to the residence time distribution function $E(t)$ which is defined by equations (14) and (15).

$$E(t) = \dot{V} \cdot \frac{c(t)}{n_{\text{tracer}}} \quad (14)$$

$$\int E(t) dt = 1 \quad (15)$$

In the next experimental set the reactor, filled with catalyst (0 – 2g), was connected to the pipe of the pulse valve and the TCD was placed at the reactor outlet, which is shown in Figure 7 B. A series of pulse marking experiments were carried out where the reactor temperature was varied from 23 °C to 800 °C and the flow rate was varied between 20 – 60 Nml/min. Each experiment was carried out with Ar and repeated with N₂ as tracers to consider possible transport effects by diffusion.

The calculated parameters t_{delay} , t_{dosing} and amplitude of the squarepulse function were implemented to the axial dispersion model. That model describes the reactor as an ideal plug flow reactor with dispersion effects in axial direction. The material balance is shown in equation (16). The dispersion depends on an axial dispersion coefficient (D_{ax}), which is related to the Bodenstein number (Bo) according to equation (17) and the flow velocity (u).

$$\frac{dc}{dt} = -u \frac{dc}{dz} + D_{\text{ax}} \frac{d^2c}{dz^2} \quad (16)$$

$$D_{\text{ax}} = \frac{u \cdot L}{Bo} \quad (17)$$

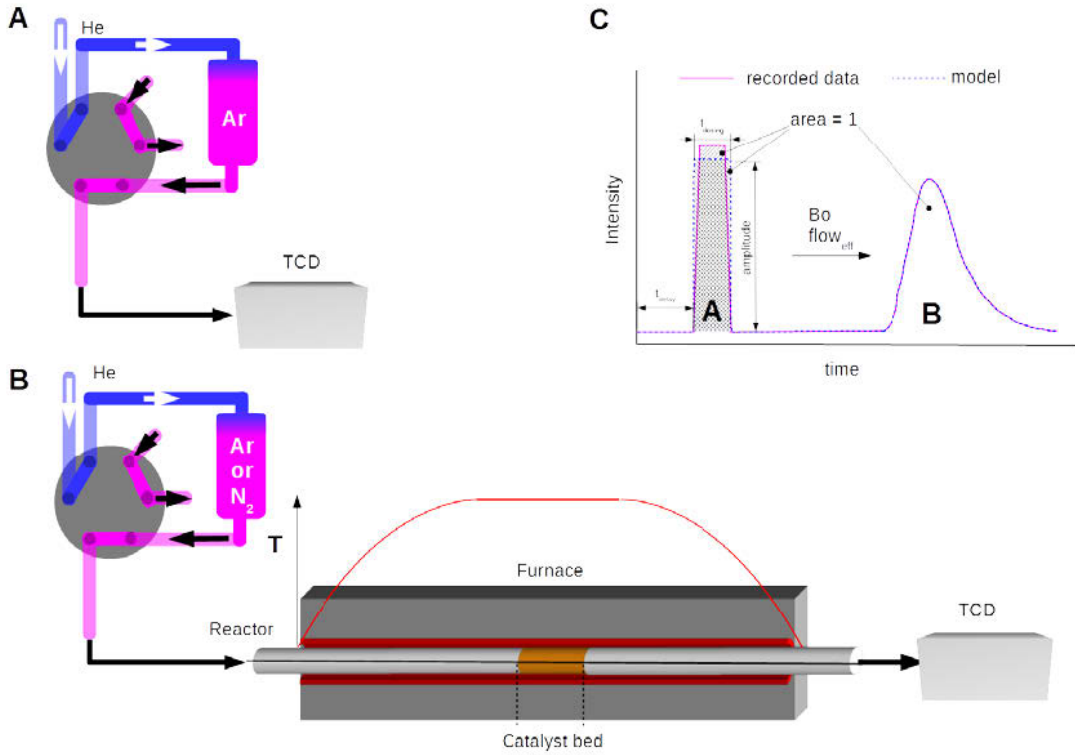


Figure 7: Scheme of residence time analyses experiments, **A:** Analyses of Pulse dosing behavior of the PV, **B:** Residence time analyses of the heated reactor, **C:** Scheme of the fitting procedure

The implementation of the dispersion model was carried out by the use of a high number of segments, where each segment represents a finitesimal part of the reactor. The flow of the tracer through the reactor, passing each segment, is affected by convection and dispersion, which is described according to equations (18) and (19). The parameter N is the total number of segments, which was set to 200 and L is the physical length of the reactor which was 55 cm. The implementation of the square-pulse signal to that model is shown in equation (20).

$$\frac{dc[1..N]}{dt} = -u \frac{(c[i+1] - c[i-1])}{2 \cdot L_i} + D_{ax} \frac{c[i+1] - 2 \cdot c[i] + c[i-1]}{(2 \cdot L_i)^2} \quad (18)$$

$$L_i = \frac{L}{N} \quad (19)$$

$$\frac{dc[0]}{dt} = -u \cdot \frac{(-\text{squarepulse}(t_{\text{dose}}, t_{\text{delay}}) \cdot \text{amplitude} + c[i+1])}{L_i} + D_{ax} \frac{c[i+1] - c[i]}{(L_i)^2} \quad (20)$$

The recorded data from the residence time analyses with heated reactor were fitted by this model. The fitting parameters were the Bodenstein number and the effective flowrate (Figure 7 C, right part). The effective flow rate averages the initial flow rate of the carrier gas and the contribution of gas expansion effects by the furnace temperature profile. The results of the reactor characterization are described in section 3.5.2.

3 Results and discussion

3.1 Contribution of gas phase reactions to the OCM reaction

In [Paper 1](#), three different reactor types were investigated in which the $\text{Na}_2\text{WO}_4/\text{Mn}/\text{SiO}_2$ catalyzed OCM reaction was performed: a fluidized bed reactor, a standard fixed bed reactor, and a membrane reactor. All experiments were carried out under steady state conditions but with different oxygen dosing strategies. The fluidized bed reactor was fed with oxygen and methane at the inlet. The strong back mixing behavior in the fluidized bed reactor distributed the oxygen quickly in the whole reactor chamber. The fixed bed reactor was fed similarly with the reactants, but dispersion effects and free gas space are lower than in the fluidized bed reactor. In the porous membrane reactor the oxygen was dosed constantly in small fractions through a ceramic membrane to the reactor chamber along the catalyst fixed bed. Stanislav Jaso and Hamid Godini found that the membrane reactor has a higher C_2 yield and a better C_2 selectivity in comparison to the fluidized bed reactor, despite similar initial conditions as the catalyst material, temperature and gas hour space velocity (Table 5). The C_2 selectivity of the fixed bed reactor was in between. Therefore, a strong influence by chemical reactions in the gas phase and heat transport effects, which also influences reaction rates, is assumed. To analyze this situation in more detail, the different oxygen dosing strategies were simulated by using of three different reactor models.

Table 5: Experimental and simulation results of the OCM reaction in a membrane, standard Co-fed fixed bed and fluidized bed reactor ([Paper 1](#))

Reactor	Parameter	Experimental result (with catalyst)	Simulation of gas phase reactions (Dooley Mech.)	Simulation of Gas phase + semi-emp. Mod.
Membrane reactor	$X(\text{CH}_4)$	0.33	≈ 0	≈ 0
	$S(\text{C}_2)$	0.65	0.45	0.99
	$S(\text{CO}_x)$	0.35	0.45	0.99
Fixed-bed reactor	$X(\text{CH}_4)$	0.32	0.01	0.34
	$S(\text{C}_2)$	0.53	0.99	0.56
	$S(\text{CO}_x)$	0.47	0.01	0.44
Fluidized bed reactor	$X(\text{CH}_4)$	0.35	0.29	0.30
	$S(\text{C}_2)$	0.40	0.14	0.12
	$S(\text{CO}_x)$	0.60	0.86	0.88

The fluidized bed reactor has a similar mixing behavior as the continuous stirred tank reactor (CSTR), while the plug flow tube reactor (PFTTR) has no axial back mixing behavior, which is comparable to the standard fixed bed reactor. It was demonstrated that the gas phase reaction network is active even in absence of the catalyst material (Table 5). The conversion of methane correlates with the free gas space and the oxygen dispersion of the reactor for empty reactor simulations. The membrane reactor shows no methane conversion, because of low oxygen partial pressure and no back mixing, while in the PFTTR the methane conversion is also very low. The CSTR shows high methane conversion, which demonstrates clearly that the oxygen

dosing strategy influences strongly the results of our experiments. To proof our hypothesis a simulation of a simplified surface reaction model for the catalyst material was realized, as presented in

Table 4 and in [Paper 1](#). In that model methane is only converted into methyl radicals on the catalyst surface and catalyst reoxidation steps were implemented. Such drastic simplification avoids a complex situation of deep oxidation product formation in gas phase and on the catalyst surface, which cannot clearly be distinguished.

The simulation results of gas-phase reaction and semi-empirical catalyst model (Table 5, last column) for the PFTR showed higher methane conversion and higher C₂ selectivity in comparison with the CSTR, which supports the hypothesis that an adequate oxygen dosing strategy improves the overall OCM performance in a reactor. High oxygen partial pressures and free gas space support the formation of deep oxidation products. On the one hand in the gas phase the molecular oxygen activates methane by the formation of peroxy and methyl radicals. The presence of other oxygen-species or intermediates may prevent the coupling process of methyl radicals and lead to the formation of deep oxidation products by coupling of methyl radicals with oxygen-species in the gas phase. The main reason is that the partial pressure of the oxygen species in the early stage of the reaction progress is much higher than the partial pressure of methyl radicals. Furthermore, even after successful methyl radical coupling, the ethane molecule can be more easily activated in the gas phase or on the catalyst surface because of its lower C-H bond strength. Therefore, low oxygen partial pressures may improve the OCM performance in the gas phase by suppressing side reactions. On the other hand there is a strong effect of heat formation. In the gas phase the heat removal is much slower in comparison to a solid material, because of the big difference in heat capacity and conductivity. Therefore, a conversion of methane in the gas phase generates higher temperatures in comparison to the same reaction on the catalyst particles. Such effect enhances all activation processes in the gas phase, which are mostly the origin of deep oxidation products. That effect can be seen in Figure 8, where at low methane conversion, less heat is generated and therefore the reactions on the catalyst surface and the coupling process of methyl radicals dominate the formation of products, namely ethane and ethene. If no heat is removed, the temperature raises more and more, while the C₂ selectivity decreases sharply. The heat formation lead to hot spot formation and the gas phase reaction network dominates the overall reaction progress. This can be seen by the sharp decrease of C₂ product formation and the simultaneous enhancement of deep oxidation product formation.

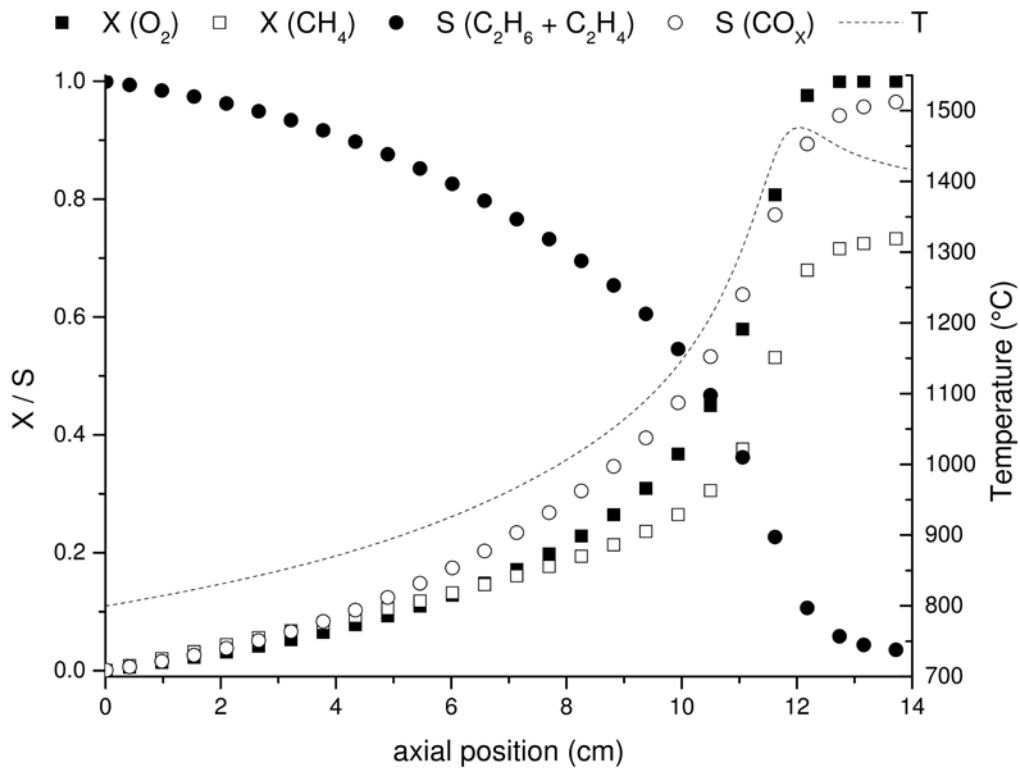


Figure 8: Simulated reaction progress of the fixed-bed reactor with the gas phase model and simple micro-kinetic surface model by solving the free energy equation (hot spot formation) with the initial temperature of 800°C (180 Nml/min N₂; 120 Nml/min CH₄; 60 Nml/min O₂; 3.5 g catalyst) ([Paper 5](#))

3.2 Pressure variation during the OCM reaction

In literature, the most OCM experiments were carried out at ambient pressure (1 atm). The absolute pressure seems to be a crucial parameter for the OCM reaction, because it influences the number of molecules in the gas phase and the transport effects to the catalyst surface.

[Paper 2](#) deals with the investigation of the OCM reaction in a broad range of absolute pressures. The results of the co-fed steady state experiments at high pressures are presented in Figure 9. In general, the methane conversion increases by an increase of the absolute pressure. For the experiments with an empty reactor the C₂ selectivity is below 0.1 and at 10 bar, no C₂ products were observed anymore. These results support the hypothesis discussed in section 3.1. The methane is activated by gas phase oxygen and a higher concentration accelerates the formation of deep oxidation products. When we performed the same experiment in a fixed bed filled with quartz granules, the C₂ selectivity was much higher. On the one hand, the quartz granules may contribute to the catalytic activity. On the other hand the inert bed decreases the free gas space significantly. Therefore, the thermal methane activation and coupling of methyl radicals in the gas phase became the major reaction route. That is because at low methane conversion the deep oxidation product formation might be preferred. That reaction route decreases the partial pressure of gas phase oxygen much faster because of the big difference in the stoichiometric factors of methyl radical formation and oxygen insertion reactions (Eq. (7) vs. (9)). By decreasing the oxygen partial pressure the

thermal coupling process of methyl radicals becomes the more dominant reaction step. At high methane conversion further oxidation processes in the gas phase are not possible because of the low oxygen concentration.

By the use of a catalyst fixed bed, the C₂ selectivity increases from 0.52 to 0.57 only slightly with pressure. The C₂ product formation benefits from two effects. Firstly the adsorption rates of methane and oxygen could be enhanced. Therefore the catalytic activity is enhanced and the reoxidation of the catalyst bed consumes the gas phase oxygen much faster than under atmospheric pressure. Secondly, the coupling process is more likely under higher pressures. This is caused by the effect that after successful C–H bond cleavage by the catalyst, the mean free pathway to the next methyl radical is decreased. Therefore it is more likely that two methyl radicals couple and form an ethane molecule.

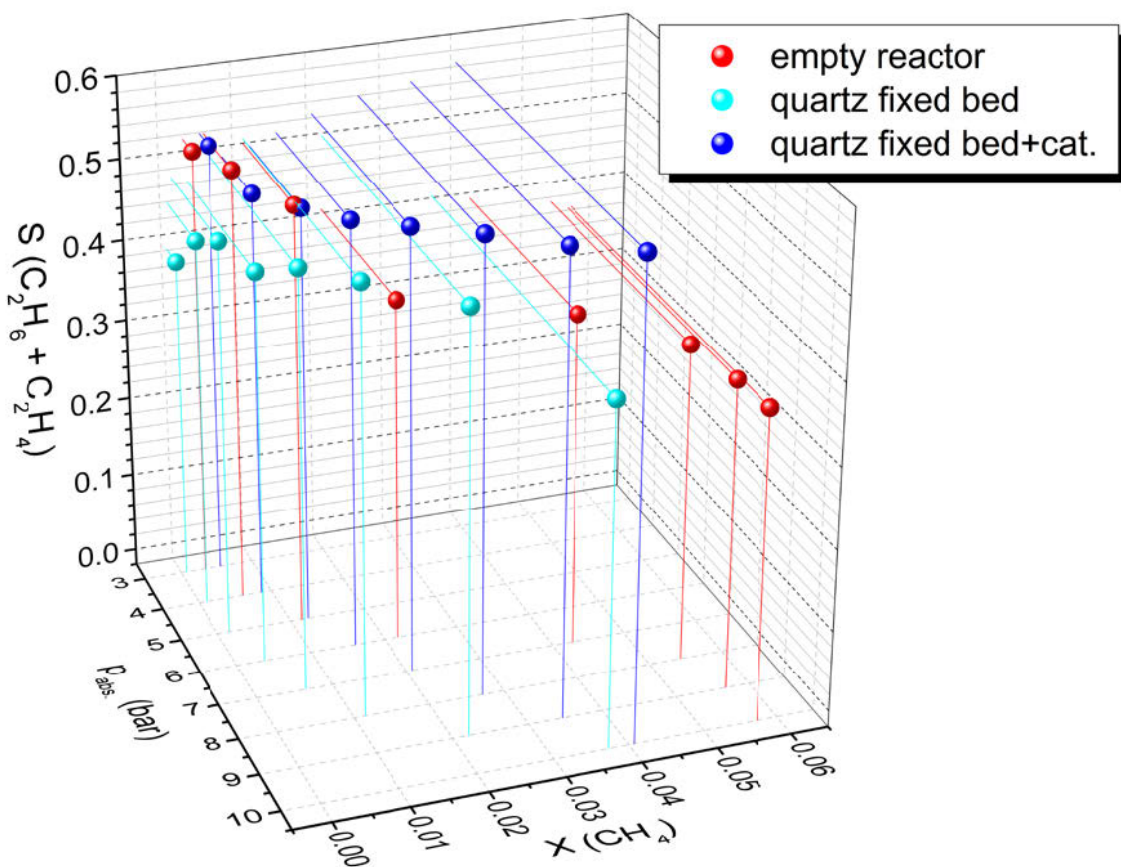


Figure 9: Influence of absolute pressure on C₂+ selectivity at constant residence time 0.16s, 100 mg catalyst, 700 °C, 50 – 500 Nml CH₄:O₂ (95:5) (converted from [Paper 2](#))

In addition a series of temporal analysis of products (TAP) experiments were carried out in [Paper 2](#) by Benjamin Beck. In such experiments, the absolute pressure is in the range of 1 – 100 mPa and the reactants are injected as gas pulses to the fixed bed reactor, simultaneously or delayed. A simultaneous injection of methane and oxygen simulates the steady state experiment at low pressures, while a delayed reactant injection separates the catalyst oxidation from the methane activation by the catalyst into two independent reaction steps. These reaction conditions are chosen close to the Knudsen-diffusion regime, where the collision of molecules

with each other is negligible and the collision between gas phase molecules and surfaces is dominating. Therefore the pressure was set higher, to allow for interactions in the gas phase. Otherwise the coupling process of methyl radicals would not be possible. In the case of simultaneous injection of the reactants, the methane conversion was 0.02 with a C₂ selectivity of 0.95 for the Na₂WO₄/Mn/SiO₂ catalyst. Such high selectivity indicates that the gas phase reactions, induced by the gas phase oxygen, is more or less inactive and only the coupling process of methyl radicals is relevant. In the second case, oxygen was first injected and the methane pulse was injected delayed in time. The delay time was between 0.1 – 1 s. It was observed that a constant amount of C₂ products was produced in each case, despite the delay time between the two reactant pulses. Contrary, the formation of deep oxidation products decreases by an increase of the time delay. We concluded from these experiments that two oxygen species are present on the catalyst surface at these conditions: A strongly and a weakly bound oxygen species. While the strongly bound species would remain on the catalyst surface and its life time would be long enough to interact with the delayed methane pulse to form similar amounts of C₂ products, the weakly bound oxygen species would desorb after the oxygen pulse left the reactor system. Therefore, it would be responsible for deep oxidation product formation. At longer delay times between the two reactant pulses, most of the weakly bound oxygen species would be desorbed and therefore less deep oxidation products are produced.

3.3 Temperature programmed surface reaction experiments

[Paper 3](#) deals with TPSR experiments to study the surface interactions of the OCM reactants in the absence of the gas phase and weakly bound oxygen on the Na₂WO₄/Mn/SiO₂ catalyst. Such technique follows the idea of the TAP experiments to separate the oxidation of the catalyst material from the activation reaction of methane by the catalyst material. The results of CH₄-TPSR experiments with different heating rates are presented in Figure 10 A - C. It was found that methane is converted into CO and ethane. Interestingly first ethane is formed and later CO, which indicates that two different active oxygen species contribute to methane activation. That was concluded by the fact that the oxidation reaction of methyl radicals would proceed immediately with surface bound oxygen species. Our results show that the CO formation starts at higher temperatures, which is a delay of several minutes, dependent on the heating rate. That time span is not in the range of methyl radical lifetimes. Therefore two different types of methane activation induced by different oxygen species were suggested. These results are in straight contradiction with the model of Lee et al., which was presented in the introduction section (Table 2), where only one oxygen species contributes to all activation reactions of alkanes [67].

The results of C₂H₆-TPSR experiments are shown in Figure 10 D – F. In [Paper 3](#) it was demonstrated that the reactivity of ethane is much higher than the methane one. Therefore it was expected that ethane activation would be observed at lower temperatures, but interestingly the product formation starts at higher temperatures in comparison with CH₄-TPSR experiments. Furthermore, the ethene formation starts in all experiments at the same temperature. That is

also different to CH₄-TPSR experiments, where the position of the ethane peak depends on the heating rate. We concluded that ethane is preferably activated in gas phase, which was validated in a blank experiment without the catalyst. The activation barrier in the gas phase has to be much higher in comparison to the catalytic ones. Otherwise no catalytic activity for C–H bond cleavage would be observed for methane, according to the C–H bond dissociation energies which are 439 kJ/mole for methane and 436 kJ/mole for ethane [9]. In addition we found the formation of water, which indicates an oxidative dehydrogenation reaction of ethane or the conversion of formed hydrogen by the catalyst material. That reactant could be formed by thermal dehydrogenation reaction of ethane to ethene. At higher temperatures in C₂H₆-TPSR experiments CO₂ and CH₄ were observed, which was interpreted as product formation by ethene conversion.

Figure 10 G – I present our findings of C₂H₄-TPSR experiments. We found in all experiments the formation of CO₂ and CH₄, starting at similar temperature ranges. In [Paper 3](#) we were unable to resolve the mechanism in detail for these reaction pathways. During the experimental procedure coke formation was observed, proven by catalyst reoxidation and simultaneous CO₂ formation. We concluded that both oxygen species on the catalyst surface may contribute to ethylene activation. On the one hand electrophilic oxygen could be inserting to the molecule by an attack of the ethene double bond. Such epoxide species would be very unstable at OCM conditions and decomposes immediately to deep oxidation products and in the absence of oxygen to carbon. On the other hand nucleophilic oxygen may attack one of the C–H bonds, which forms vinyl radicals. These are well-known as precursor in carbon coke formation [108].

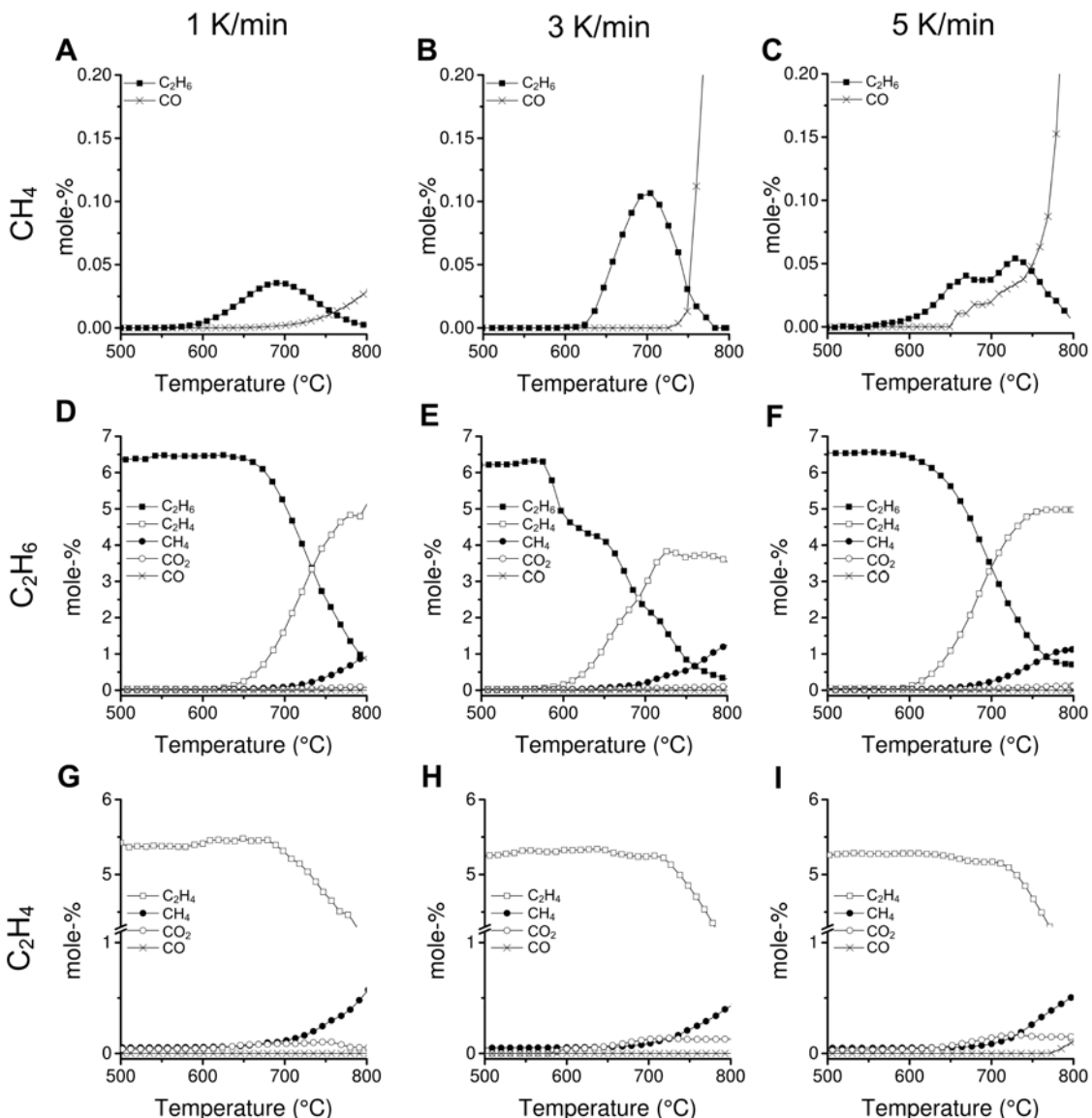


Figure 10: TPSR product formation peaks of methane, ethane and ethene TPSR experiments at heating rates from 1-5 K/min, 1 g Na₂WO₄/Mn/SiO₂, **A-C:** methane TPSR, **D-F:** ethane TPSR (He : C₂H₆, 95:5), **G-I:** ethene TPSR (He : C₂H₄, 95:5), 30 Nml/min ([Paper 3](#))

According to our findings by TPSR experiments we presented in [Paper 3](#) a reaction network, which was completed by the findings of Lunsford et al. and Beck et al. [54,72]. The reaction network is shown in Figure 11. Alkanes or Alkenes can be converted to deep oxidation products by an oxygen adsorption intermediate. The catalyst surface provides electrophilic and nucleophilic oxygen species. The electrophilic one activates methane by C–H bond cleavage to form methyl radicals. These can couple in the gas phase and form ethane. Besides, methane can be converted by nucleophilic oxygen species into deep oxidation products. Ethane is converted in the gas phase or on the catalyst surface into ethene. The formed hydrogen in gas phase is also converted by the catalyst material into water, when oxygen on the catalyst surface is available. Furthermore, ethene is converted on the catalyst surface to deep oxidation products, undergoing the formation of coke.

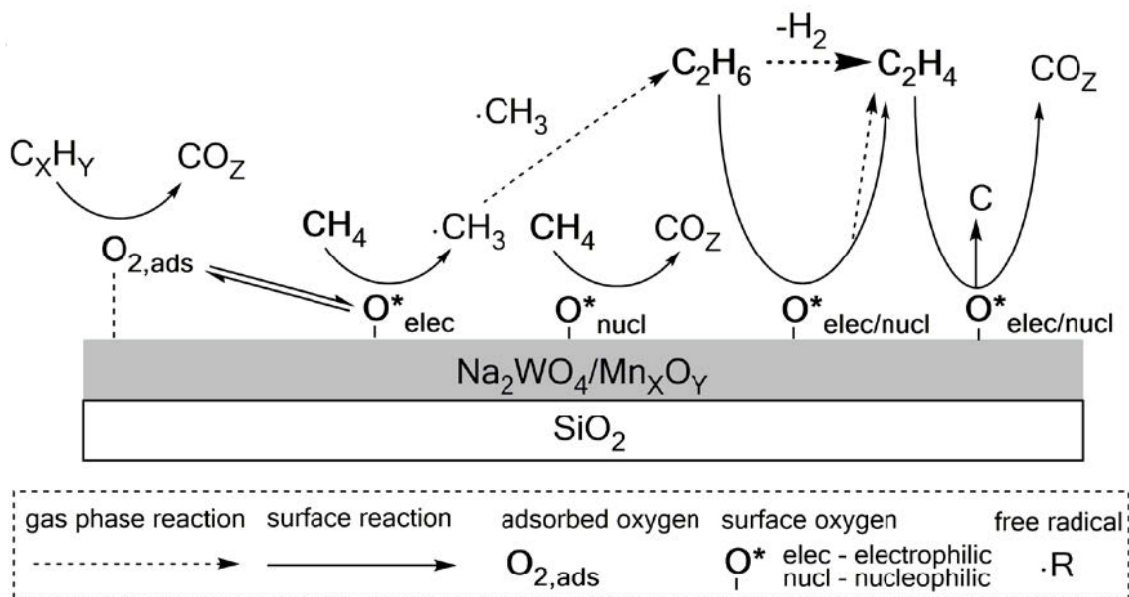


Figure 11: Proposed Reaction network by TPSR experiments [54,72] ([Paper 3](#))

According to the work by Redhead, the rate limiting step of a heterogeneous reaction of molecules from a gas phase on a catalyst surface is sensitive to the temperature ramp in TPSR experiments [109]. Typically, that step could be the adsorption of the gas molecule on the catalyst surface, the activation of the molecule, the formation of transition state or the desorption of the product. In OCM it is accepted that the C–H bond cleavage of methane is the rate determining step [67,110].

Therefore, the positions of the recorded ethane peaks in CH₄-TPSR experiments were fitted by an empirical function. According to the Redhead method we calculated an activation energy of 275 kJ/mole (E_{A,3}). Such high value reflects the nature of the strongly bound oxygen species, which may also involve the lattice oxygen. A possible energy profile for the OCM reaction on the Na₂WO₄/Mn/SiO₂ catalyst is presented in Figure 12. Molecular oxygen undergoes the formation of an adsorption intermediate (O_{2,ads}). That is converted into the strongly bound oxygen species (O_x*). We assume that the reaction rate of the adsorbed oxygen intermediate with methane is much faster in steady state experiments than the reaction rate of nucleophilic oxygen (not shown). Therefore, in steady state experiments E_{A,1} is measured for the unselective reaction pathway. The apparent activation energy (E_{A,2}) is observed in steady state experiments for selective methane activation because the interaction between O_{2,ads} and O_x* were not considered so far. However, there is a big deviation between our findings (E_{A,3}) and those ones from the literature (E_{A,1}). That was explained by the fact that the energy level of O* is much lower, compared to O₂, because the O* species undergoes adsorption and lattice insertion. Both reactions release energy and therefore much more energy is required to form the transition state for selective methane activation.

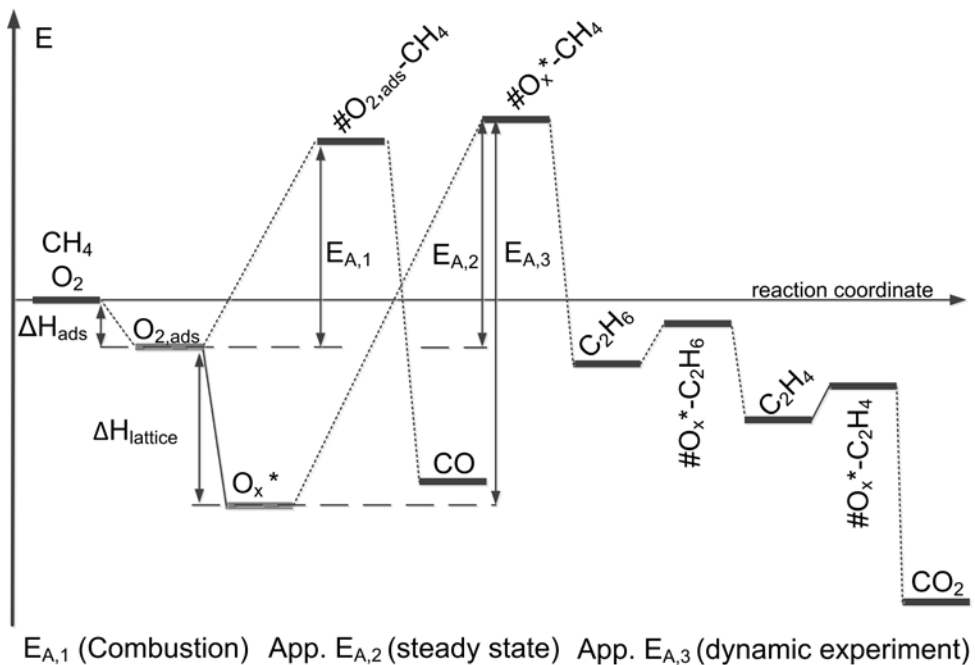


Figure 12: Proposed energy profile for the OCM reaction at the $\text{Na}_2\text{WO}_4/\text{Mn}/\text{SiO}_2$ catalyst at $800\text{ }^\circ\text{C}$ ([Paper 3](#))

3.4 Dynamic experiments

In [Paper 3](#), dynamic experiments at constant reaction temperature were carried out to investigate the oxygen storage capacity of the catalyst and the lifetime of the stored oxygen species. First the stability of the strongly bound oxygen was analyzed by increasing the purge time from 10 minutes to 300 minutes. The results are presented in Figure 13. In each experiment similar product distributions were observed. The overall C_2 selectivities are in the range of 0.9 and deep oxidation products are only formed in the first minutes of each experiment. Our results indicate that under OCM conditions the stored oxygen can remain on the surface of the $\text{Na}_2\text{WO}_4/\text{Mn}/\text{SiO}_2$ catalyst for hours. We concluded that the ability to store oxygen over that period of time may involve lattice oxygen of the $\text{Na}_2\text{WO}_4/\text{Mn}/\text{SiO}_2$ catalyst material. Therefore, a Mars van Krevelen type of mechanism may be applied for the OCM surface reaction network which is valid for both, nucleophilic and electrophilic oxygen species.

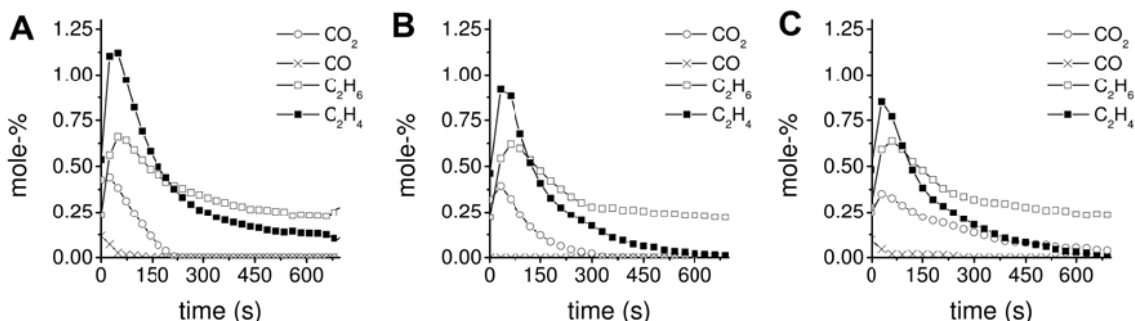


Figure 13: OCM product signals from dynamic experiments with methane for increasing purge duration at $750\text{ }^\circ\text{C}$, 20 Nml/min CH_4 for 10 min , 1 g $\text{Na}_2\text{WO}_4/\text{Mn}/\text{SiO}_2$, **A:** 10 min He purge, **B:** 180 min He purge, **C:** 300 min He purge ([Paper 3](#))

For each dynamic experiment an oxygen balance was calculated according to the material balances in section 2.7. The results are presented in Table 6. We found that the amount of consumed oxygen for the formation of deep oxidation products is more or less constant in all experiments. Furthermore, the amount of converted oxygen to form C₂ products is also almost constant. In additional series of dynamic experiments purge time was reduced to 15 s, which is the experimental limitation of the setup. Even such short purge intervals results in comparable C₂ selectivities as in the experiments before. These results confirm our previous hypotheses about the presence of two oxygen species which are strongly bound on the catalyst surface. The ratio of ethane to ethene is strongly affected by the flowrate, which supports our hypothesis from section 3.3 that ethane is preferably formed in the gas phase. Furthermore, a linear dependency between the partial pressure of methane and converted amount of oxygen was found. Our findings indicate that the Na₂WO₄/Mn/SiO₂ catalyst is a suitable oxygen carrier material for chemical looping experiments, because it fulfills all basic requirements:

- Stable redox properties under reaction conditions
- The stored amount of oxygen is stable bound under reaction conditions
- Short purge times allow adequate operation times

Table 6: Compound based oxygen balance for a broad range of purge times in dynamic experiments from 15 s to 18000 s, 1 g Na₂WO₄/Mn/SiO₂, 750 °C, 20 & 30 Nml/min CH₄ for 10 min ([Paper 3](#))

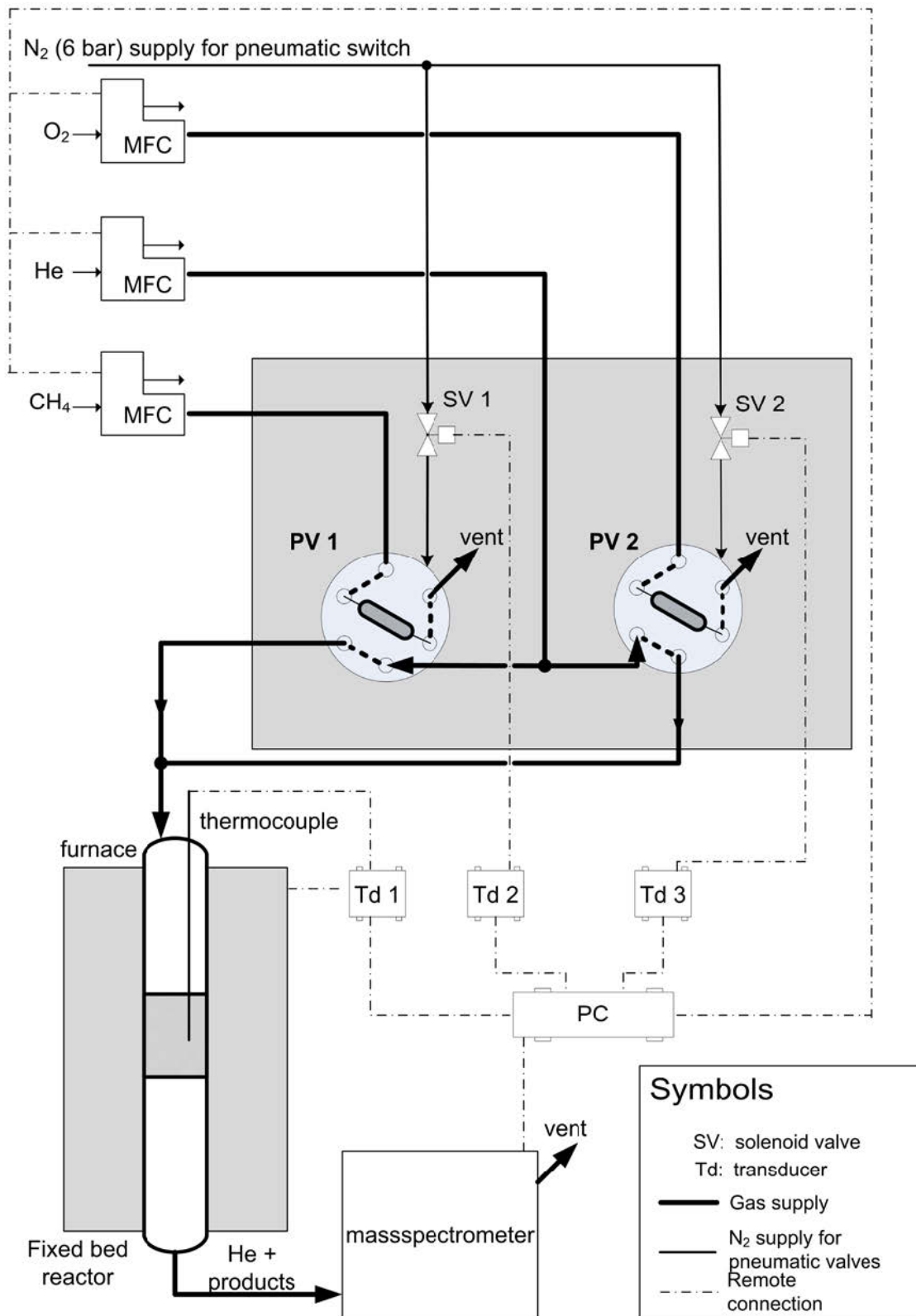
Purge time (s)	Flow rate (Nml/min)	CO ₂ (#O/nm ²)	CO (#O/nm ²)	C ₂ H ₆ (#O/nm ²)	C ₂ H ₄ (#O/nm ²)	Σ (#O/nm ²)
18,000	20	8.8	0.6	4.6	6.8	20.66
10,800	20	10.4	0.6	4.5	7.1	18.00
600	20	7.2	5.4	1.8	3.6	21.66
300	30	10.7	0	7.3	2.6	20.60
270	30	9.4	0	7.6	1.9	18.94
230	30	9.8	0	7.3	1.8	18.81
160	30	8.9	0	7.7	1.7	18.32
100	30	9.1	0	7.2	1.5	17.80
60	30	9.5	0	7.0	1.5	17.99
30	30	9.7	0	7.6	2.2	19.47
15	30	8.3	0	8.6	2.3	19.11

Calculation of the oxygen transport capability R_O for the Na₂WO₄/Mn/SiO₂ catalyst according to equation (3), considering as m_o only the weight of active compounds Na₂WO₄ and Mn gives 0.014. Including the support material in this calculation for R_O gives 1·10⁻³. These values are much lower in comparison to the materials listed in Table 3. The main drawback is the high molar mass of WO₄ and the high amount of silica, which offers only a small SSA (1.86 m²/g). The common range of the SSA of chemical looping particles is 3 – 100 m²/g. [95,111,112]

3.5 Development of a simulated chemical looping setup

3.5.1 Setup construction

Based on our findings in [Paper 3](#), a simulated chemical looping setup was constructed by the use of two six-port valves. The most important information of [Paper 3](#) was the amount of stored oxygen in order to dose adequate amounts of the reactant to reach high conversions. In [Paper 4](#) the detailed process concept is described and the final flow chart is presented in Figure 14. Mass flow controllers (MFC) were used to control the flow rates of carrier gas and reactant gases. The reactants were fed to the sample loops of the PV's, which have a volume of 0.25 - 2 ml. According to the operating principle of the PV's, which is presented in the supporting information of [Paper 4](#), the dosing and filling position was switched by a pneumatic system, which was controlled by solenoid valves (SV). Furnace temperature, the solenoid valves for the PV's and the operation of the MS was controlled by a computer via transducers (Td). The flow of carrier gas was split directly in front of the pulse valves and recombined at the outlet of the PV's. The overall flow, which transports the injected reactants, was send to the reactor. After passing the catalyst fixed bed the reactant pulses were analyzed by a MS.

**Figure 14:** Flow chart of the chemical looping setup (**Paper 4-SI**)

3.5.2 Residence time analyses of the simulated chemical looping setup

To analyze the dispersion of the gas pulses by the pulse valves and the dispersion effects of the reactor a wide series of residence time analyses experiments were carried out. Several effects contribute to the gas pulse dispersion as the amount of catalyst, the temperature profile of the furnace and the initial gas flow rate. Therefore a detailed study was required. The fitted parameters for the square-pulse signals are listed in Table 7. These parameters were implemented to the residence time model for the fixed bed reactor.

Table 7: Fitted square-pulse parameters for residence time analyses of gas pulses in Berkley Madonna

Flowrate (Nml/min)	Fitting parameter	Volume of sample loop (ml)		
		0.5	1	2
20	t_{delay} (s)	22	23	24
	t_{dosing} (s)	15	24	38
	amplitude (s^{-1})	0.066	0.042	0.026
30	t_{delay} (s)	14	16	15
	t_{dosing} (s)	10	20	31
	amplitude (s^{-1})	0.099	0.049	0.033
40	t_{delay} (s)	11	13	11
	t_{dosing} (s)	7	15	23
	amplitude (s^{-1})	0.135	0.066	0.044
50	t_{delay} (s)	9	10	9
	t_{dosing} (s)	6	12	18
	amplitude (s^{-1})	0.171	0.083	0.056
60	t_{delay} (s)	7	8	8
	t_{dosing} (s)	5	10	15
	amplitude (s^{-1})	0.207	0.0998	0.067

The fitted Bodenstein numbers of our pulse marking experiments with the fixed bed reactor for different amounts of catalysts, temperatures and initial flow rates are presented in Figure 15. It was found that the flow rate and the temperature have minor influences on the dispersion of the dosed pulses. We couldn't find deviations of the gas pulse shape by switching the tracer gas from Ar to N₂. Such results indicate that the mass transport is dominated by convection and dispersion and not by molecular diffusion. By increasing the flow rate or the amount of catalyst, the Bodenstein number increases. The opposite case is observed by increasing the temperature, which indicates that higher temperatures decrease the dispersion effects of the fixed bed reactor. These effects are well-known for gases, because of their strong dependence on the Peclet number (Pe).

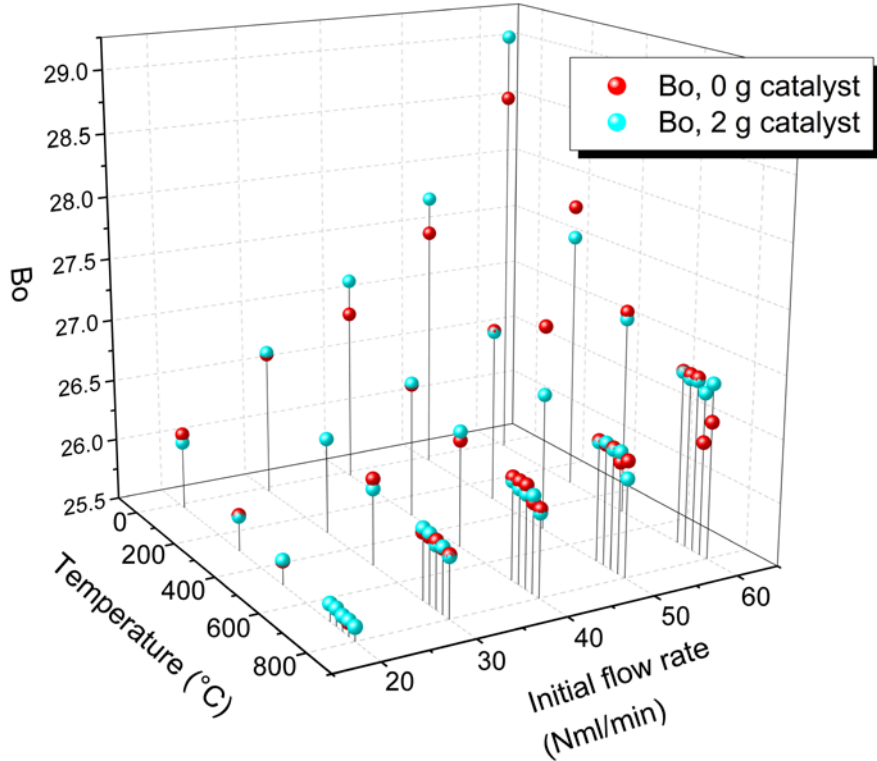


Figure 15: Results of fitted Bodenstein numbers for different temperatures and initial flowrates at different amounts of catalyst

The Peclet number is defined by equations (21) - (23).

$$Pe = Re \cdot Sc \quad (21)$$

$$Re = \frac{u \cdot d_R}{v} = \frac{\bar{u} \cdot d_{32} \cdot \rho}{\eta \cdot (1 - \epsilon)} \quad (22)$$

$$Sc = \frac{v}{D} \quad (23)$$

We assume a monodispersed fixed bed where the Sauter mean diameter (d_{32}) is equal to the mean diameter of a catalyst particle (250 µm).

$$d_{32} = d_{\text{particle}} \quad (24)$$

The density ρ of He at the highest temperature in the furnace (800 °C) was derived according to equation (25).

$$\rho = \frac{n \cdot M_{He} \cdot T_0}{V \cdot T_{max}} \quad (25)$$

The mean flowrate \bar{u} was calculated for an average feed stream, considering the highest temperature and a mean diameter with respect to the void fraction.

$$\bar{u} = \frac{T_{\text{fixed bed}} \cdot \dot{V}}{T_0 \cdot A \cdot \epsilon} \quad (26)$$

Finally the diffusion coefficient D was calculated by the fundamentals of the kinetic gas theory and the Chapman-Enskog equation for a mono atomic, ideal gas (equations (27) - (29)). The cross section σ for a He atom is 0.26 nm. [113]

$$D = \frac{1}{S} \cdot \Lambda \cdot w \quad (27)$$

$$\Lambda = \frac{(k_B \cdot T_{\text{fixed bed}})}{\sqrt{2 \cdot \pi \cdot \sigma^2 \cdot p}} \quad (28)$$

$$w = \sqrt{\frac{8 \cdot k_B \cdot T_{\text{fixed bed}}}{\pi \cdot m}} \quad (29)$$

The Peclet numbers for the experimental setup are in the range of 0.1 – 1. These low numbers indicate that the gas transport through the fixed bed reactor involves forced diffusion effects by convection. The results of Miyauchi and Kikuchi, who reviewed a broad number of residence time experiments, confirm our trends of the Bodenstein numbers [114].

The results of the fitting process for the effective flow rates are presented in Figure 16. For the blank reactor (Figure 16 A) the simulation of ideal gas law, considering the temperature profile, was an adequate approximation. When the reactor was operated with a catalyst fixed bed, pressure drop effects may occur. The pressure drop Δp was calculated according to equation (30).

$$\Delta p = \zeta \cdot \frac{\rho}{2} \cdot \bar{u}^2 \cdot \frac{L_{\text{fixed bed}}}{d_h} \quad (30)$$

The hydraulic diameter of the catalyst bed was derived by equation (31).

$$d_h = \frac{2}{3} \cdot \frac{\epsilon}{1 - \epsilon} \cdot d_{\text{particle}} \quad (31)$$

The drag coefficient ζ was derived by the Ergun equation (eq. (32)).

$$\zeta = \frac{150}{Re} + 1,75 \quad (32)$$

To calculate the dynamic viscosity η of He, the Hirschfelder equation (eq. (33)) was used, assuming that He is not compressible during the collision and therefore the collision integral Ω was set to one.

$$\eta = \frac{5}{16} \cdot \frac{\sqrt{\pi \cdot m_{\text{He}} \cdot k_b \cdot T_{\text{fixed bed}}}}{\pi \cdot \sigma^2 \cdot \Omega} \quad (33)$$

Unfortunately, our experimental parameters are not in the validity range of the Ergun equation. Therefore, in the case of 2 g catalyst the experimental pressure drop is higher than the simulated one (Figure 16 B).

Another approximation to calculate the pressure drop is the Kozeny–Carman equation (eq. (34)). That equation is highly sensitive to the void fraction. As mentioned in the introduction, the quasi liquid surface of the catalyst material tends to sinter the fixed bed and the void fraction changes under reaction conditions. Therefore, for simulations the use of the adjusted flow rate is required.

$$\Delta p = \frac{180 \cdot \eta \cdot (1 - \epsilon)^2 \cdot u}{\Phi_s^2 \cdot d_{\text{particle}}^2 \cdot \epsilon^3} \quad (34)$$

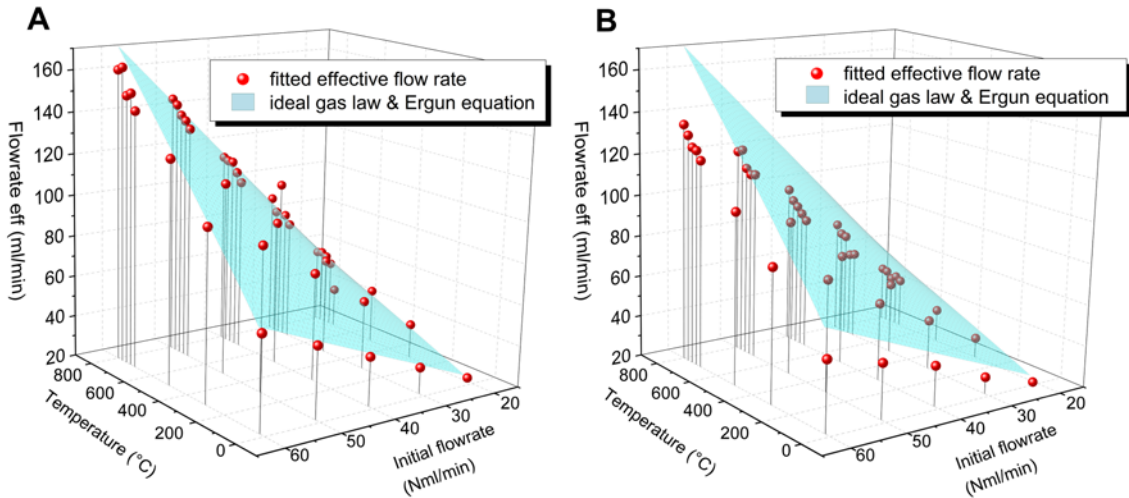


Figure 16: Results of the fitted effective flowrates for different temperatures and initial flowrates by the dispersion model and calculated flowrate by ideal gas law including pressure drop by Ergun equation **A:** empty tube reactor, **B:** 2 g catalyst in fixed bed reactor

3.6 Process parameter studies in simulated chemical looping experiments

3.6.1 Influence of flowrate and temperature on the OCM reaction

In [Paper 4](#), we compared several chemical looping experiments for which the calculation of the pulse contact time (t_{pulse} , calculated according to equation (35)) was necessary. This parameter is similar to the modified residence time. The higher t_{pulse} the longer the methane pulse remains in the catalyst bed. The main differences in our experiments were different amounts of catalyst and flowrates.

$$t_{\text{pulse}} = \frac{m_{\text{cat}} \cdot A_{\text{spec}}}{\dot{V}} \quad (35)$$

The experimental results of the temperature and flow rate variation are shown in Figure 17. In our experiments to study the yield boundary we observed a methane conversion range between 0.05 - 0.8 (Figure 17 A). Unfortunately, the correlation between methane conversion and C_2 selectivity is anti-proportional (Figure 17 B). At low methane conversion, high C_2 selectivities

were observed, while at high methane conversion less C₂ products were observed. Finally the calculation of the C₂ yield shows a maximum of 0.25 (Figure 17 C). Thus, not only the oxygen induced gas phase reactions contribute to the yield maximum in the OCM reaction. Also the catalyst itself contributes to an apparent C₂ yield maximum.

In our TPSR experiments in [Paper 3](#), we pointed out that two different oxygen species, electrophilic and nucleophilic oxygen, on the catalyst surface contribute to alkane and alkene activation. These species compete also in chemical looping experiments with each other to activate methane and other components. Both species are not removable during the purge step, because both are strongly bound on the catalyst surface, as demonstrated in our dynamic experiments in [Paper 3](#). We concluded that the presence of both oxygen species and their interactions with alkanes and alkenes are the origin of the C₂ yield maximum. This is because one selective reaction (methyl radical formation by electrophilic oxygen and methane) competes at least with three unselective reactions on the catalyst surface. These are the reaction of methane with nucleophilic oxygen and the consecutive reaction of ethene with both oxygen species.

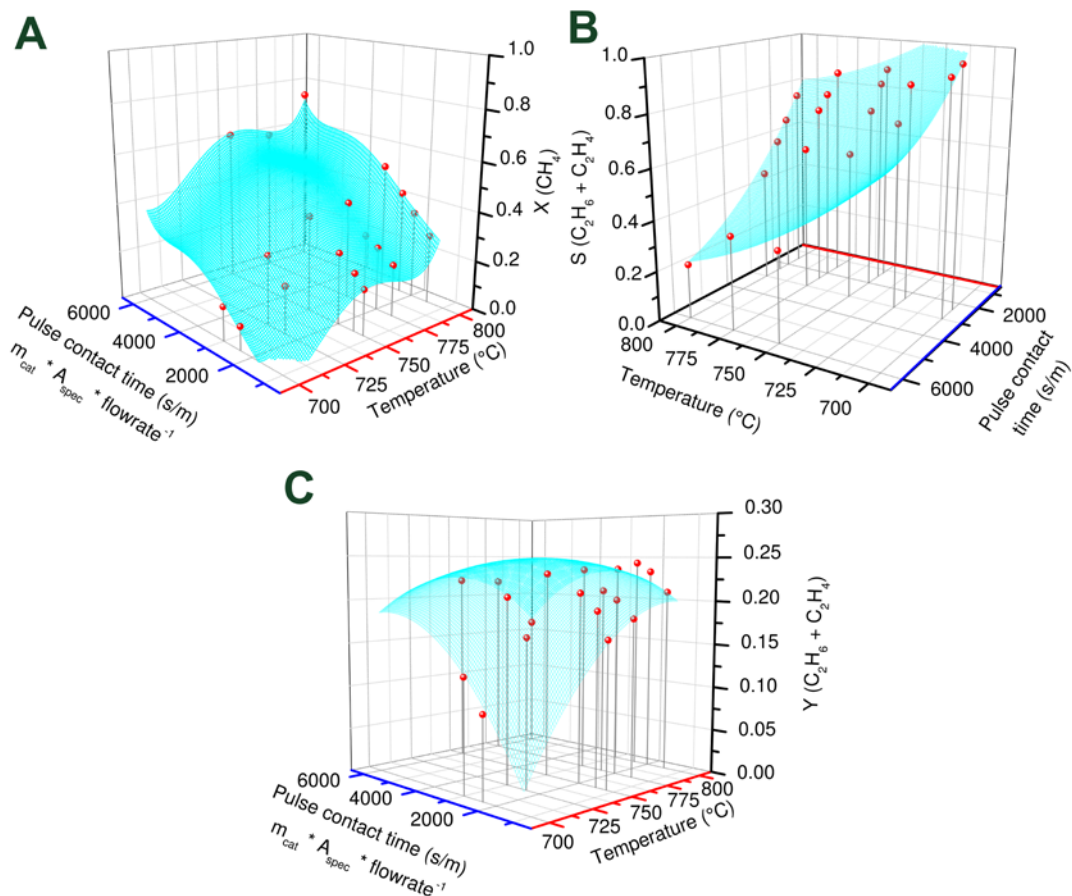


Figure 17: Results of yield studies, 2 g Na₂WO₄/Mn/SiO₂ catalyst, 15 - 50 Nml/min, 700-800 °C, 1 ml CH₄ pulse, **A:** methane conversion, **B:** C₂ selectivity, **C:** C₂ yield ([Paper 4](#))

3.6.2 Continuous operation of the chemical looping process and comparison with steady state process mode

We also present a continuous operation of the simulated chemical looping concept in [Paper 4](#), which is shown in Figure 18. The first oxygen pulse had a higher amplitude as the next one, because the catalyst was already oxidized. When the methane pulse was detected we observed simultaneously C₂ products and carbon dioxide. When the catalyst was reoxidized by the following oxygen pulse, water was removed from the catalyst surface. These results indicate that the redox properties of the Na₂WO₄/Mn/SiO₂ catalyst material are stable in dynamic experiments at reaction conditions for hours. Furthermore, the catalyst reoxidation reaction rate must be equal or faster than the OCM reaction rate, because during the experiment the methane conversion was constant which indicates that there is no decrease in the stored amount of oxygen. Otherwise the methane conversion should be decreased during the experimental progress.

Another aspect is the formation of water. It can be clearly seen that water is only removed from the catalyst surface by the oxygen pulse. Therefore, we conclude that water molecules or OH groups can remain, even under these hard conditions, on the catalyst surface. It is not clear, whether they contribute to the OCM reaction or are involved in the transport processes of the reactants.

In the continuous operation of the chemical looping experiment only one methane pulse was injected before the catalyst material was reoxidized. Therefore it is possible that even more methane pulses can be converted and utilize the available amount of stored oxygen, before the catalyst reoxidation is required. These repetitive pulse experiments will be discussed later.

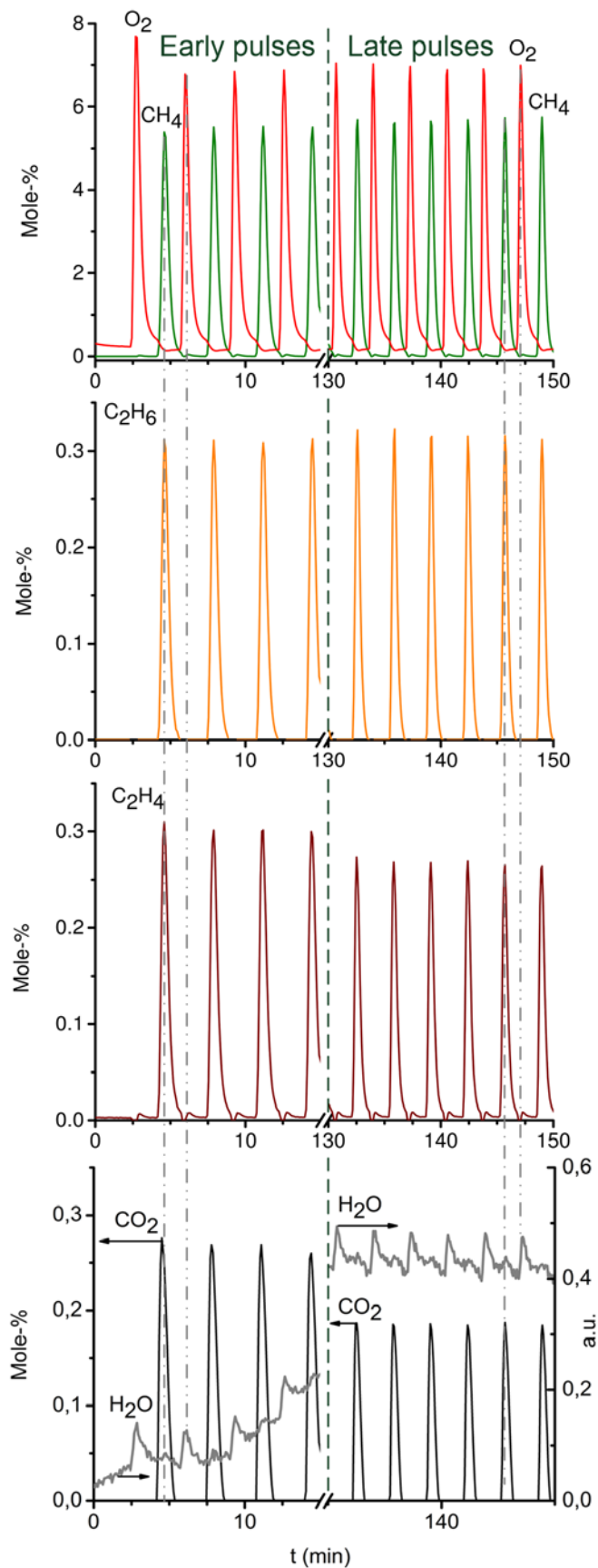


Figure 18: Early and late reactant and product peaks during continuous simulated chemical looping, 775 °C, 25 Nml/min, 2 g catalyst, pulses of 1 ml O_2 or 1 ml CH_4 ([Paper 4](#))

A comparison between a co-feed steady state and a simulated chemical looping experiment is also presented in [Paper 4](#), which is shown in Table 8. At similar methane conversion we observed for the simulated chemical looping experiment a higher C₂ yield. Comparing both experiments at a similar C₂ yield, the simulated chemical looping experiments converts less methane more selective.

Another important parameter which was compared is the space time yield (STY). The STY in our continuously operated simulated chemical looping experiments at 775 °C was 73 µmole(C₂)/(h·g_{cat}) and 83 µmole(C₂)/(h·g_{cat}) at 800°C, respectively. In both steady state experiments that parameter was much higher (529 and 970 µmole(C₂)/(h·g_{cat})). Such a big difference is caused by the fact that the simulated chemical looping setup had much free gas space (ca. 60 ml), because of constructive aspects from the piping system and the furnace geometry, which requires a long tubular reactor. The free gas space must be filled with the carrier gas and also the carrier gas is necessary to transport the reactants (1 ml) through the setup. Typically the difference between the dosed reactant volume and the reactor volume is much smaller and therefore the STY would be much higher in a large scale reactor.

Table 8: Comparison between steady state experiment (800 °C, 25 & 50 Nml/min, 250 mg catalyst) and simulated chemical looping (2 g catalyst, 1 ml CH₄ pulse) ([Paper 4](#))

Co-feed steady state experiment				
X (CH ₄)	X (O ₂)	S C ₂	Y	
0.29	1.00	0.63	0.18	
0.18	1.00	0.81	0.15	
Chemical looping – equal methane conversion				
X (CH ₄)	T (°C)	Flowrate (Nml/min)	S C ₂	Y
0.29	775	25	0.74	0.21
0.18	750	50	0.89	0.17
Chemical looping – equal C₂ yield				
X (CH ₄)	T (°C)	Flowrate (Nml/min)	S C ₂	Y
0.21	775	30	0.87	0.18
0.19	725	25	0.87	0.16

Based on our findings in [Paper 4](#), a concept for an OCM chemical looping process plant was proposed, which is shown in Figure 19. The catalyst oxidation reactor has a similar functionality as an air separation unit combined with the oxidizer reactor (Figure 1), because no nitrogen is transported to the OCM reactor. In parallel, water is also removed there and no condenser behind the OCM reactor is required. The other separation processes, like the CO₂ absorber, the CH₄ separator and the C₂ separator, were located according to the proposal of Godini et al. [80]. The catalyst oxidation and the OCM reaction could be performed in fluidized bed reactors, because the catalyst seems to be resistant against comminution or abrasion which shows stable operation in an OCM mini-plant [115]. Otherwise, four fixed bed reactors with alternating feeds have to be used, which is not shown here. As demonstrated before, the catalyst

reoxidation is very fast and therefore no temperature swing is required during the operation, which is also beneficial for a continuous operation.

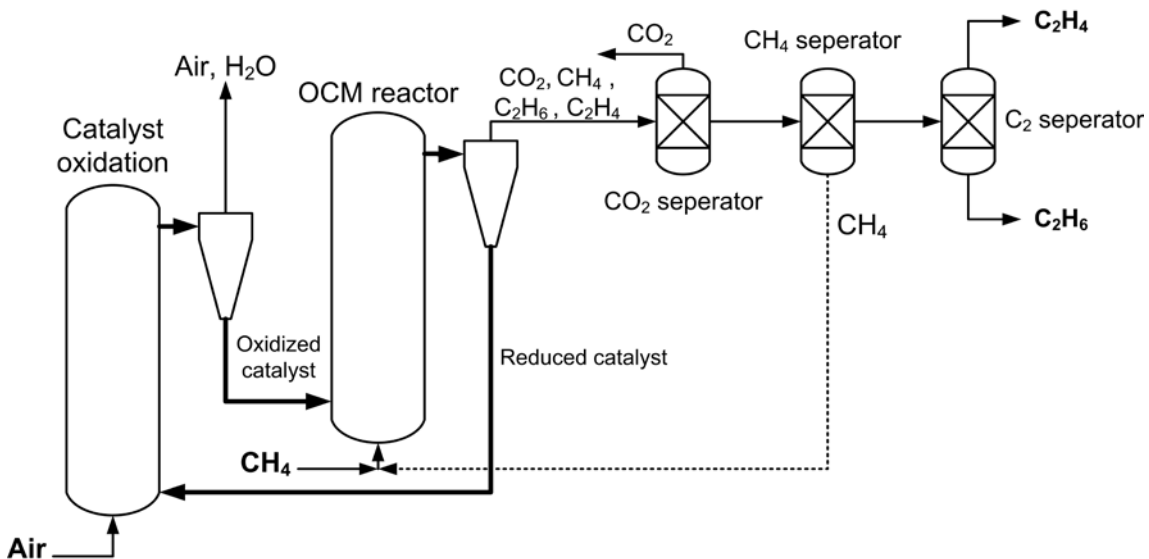


Figure 19: Scheme of chemical looping of two fluidized bed reactors [81] ([Paper 4](#))

In the case of fixed bed reactors with alternating feed, a purge gas is required to remove unconverted methane or oxygen, similar to the simulated chemical looping process. One attractive compound is carbon dioxide, because it could be more easily separated from the unconverted reactants, than nitrogen or other inert gases. Therefore, we switched the carried gas in the setup from He to CO₂. Because of the high partial pressure of CO₂, the calculation of the carbon balance was not sufficiently calculated. Thus, the peak areas of C₂ products were compared by the use of different carrier gases. That parameter is proportional to the amount of the corresponding compound. The results are presented in Figure 20. Under CO₂ atmosphere less C₂ products were observed. These results indicate that the catalyst material is less active or the C₂ products were converted in gas phase by CO₂ into H₂ and CO in a dry reforming reaction. Another alternative sweep gas would be water vapor.

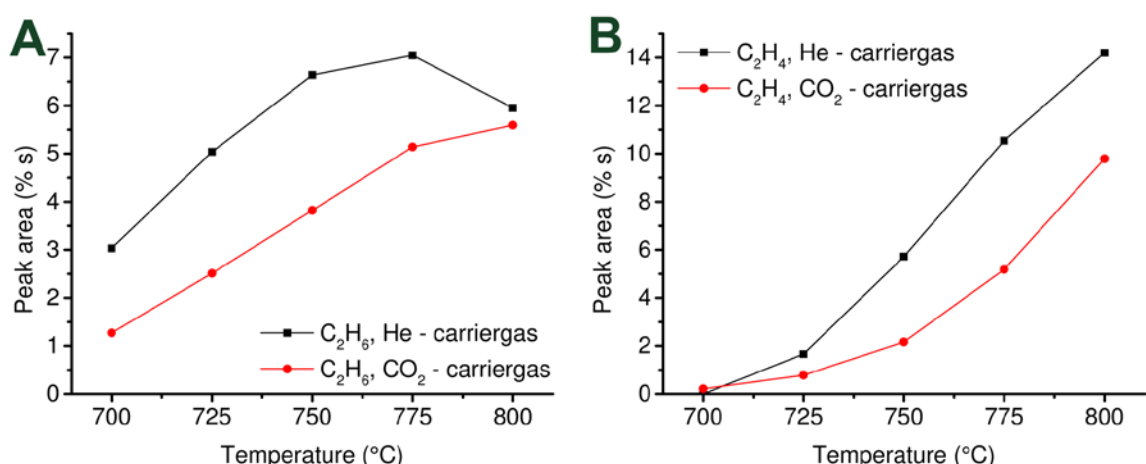


Figure 20: Effect of different carrier gases on C₂ production, 1 g catalyst, 20 Nml/min, 1 ml CH₄ pulse, **A:** Influence on C₂H₆ production, **B:** Influence on C₂H₄ production,

3.7 Investigation of the role of the catalyst composition in simulated chemical looping experiments and repetitive pulse experiments

In [Paper 5](#), the composition of the catalyst was systematically varied to understand the contribution of each part to the catalytic activity and selectivity. Furthermore, the origin of the two different oxygen species was investigated, as well as the two different functionalities of the material.

3.7.1 Variation of the surface concentration of Na_2WO_4 and Mn on COK-12 support

The first investigated parameter was the surface loading with Na_2WO_4 and Mn_2O_3 . Therefore, several catalysts were prepared, keeping the total weight loading of 5 wt-% Na_2WO_4 and 2 wt-% Mn(II) constant, supported on silica material (COK-12) which had different specific surface areas after calcination. The larger the SSA, the lower was the specific surface concentration of both compounds. The screening results at different temperatures are presented in Figure 21. By decreasing the specific surface concentration of the catalyst compounds an increase of catalytic activity was observed, but the C_2 selectivity decreases. At the lowest specific surface concentration, the catalytic activity decreases again. We calculated a specific surface concentration of 66 Mn/nm² and 33 W/nm², which had the highest catalytic activity. Such effect was explained by two related phenomena.

Firstly, it has to be considered that one of the compounds of the active film, the Mn_xO_y or Na_2WO_4 , must be related to the oxygen storage capacity. Further, such high loadings of both compounds indicate a multilayered active film on a silica support material, because the monolayer concentration of several transient metal oxides supported on silica is reached at around 1 atom/nm² [116]. Therefore, the film thickness of the active compounds seems to be important. The ratio of oxygen atoms which are available on the catalyst surface for methane activation ($\text{O}_{\text{surface}}$) and those ones which are stored in the film of the active compounds (O_{bulk}) is defined as $\text{O}_{\text{surface}}/\text{O}_{\text{bulk}}$. A thick film would result in a low ratio, while a thin film should increase that value. Therefore, thinner films lead to higher activity, because more oxygen atoms are available for methane activation, when the weight loadings were constant and the SSA was increased.

Secondly, the film thickness of the active compounds layer influences their crystallinity. A thin film leads to smaller crystal sizes. On the one hand smaller crystals can be reduced in temperature programmed desorption experiments more easily [43]. That means that oxygen atoms are less stable bound on thinner films, which may lead to a release into gas phase, without contribution to catalytic activity. In addition the catalyst performance depends strongly on the structural flexibility of that film [117,118]. A decrease of the crystal size would increase the interaction with the support material and the interaction between Mn_xO_y and Na_2WO_4 would decrease, which decreases catalytic activity.

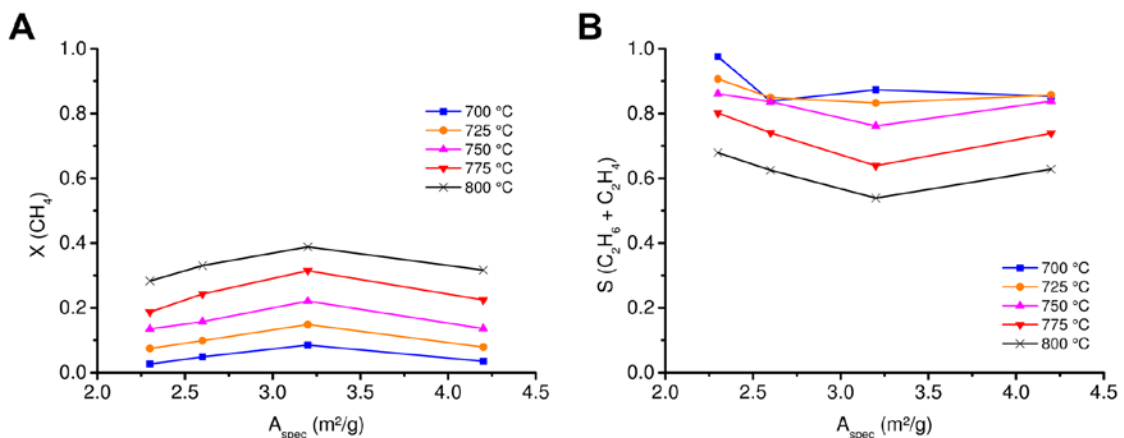


Figure 21: Results of single methane pulse experiments on $\text{Na}_2\text{WO}_4/\text{Mn}/\text{SiO}_2$ with different specific surface areas, 20 Nml/min, 0.6 g catalyst, 1 ml CH_4 pulse, **A:** methane conversion, **B:** C_2 selectivity ([Paper 5](#))

The results of our repetitive pulse experiments for $\text{Na}_2\text{WO}_4/\text{Mn}/\text{SiO}_2$ catalysts with different SSA are presented in Figure 22. In all cases high C_2 selectivities were observed and similar to the single pulse experiments, the higher the methane conversion the lower was the C_2 selectivity. We observed for the most active catalyst ($3.2 \text{ m}^2/\text{g}$) also the highest amount of converted oxygen (Figure 22 C). Such result validates our hypothesis about the correlation between activity and the film thickness as discussed before. According to the calculations of the molecule specific oxygen balance, we observed no big difference in the amount of oxygen atoms for ethene formation.

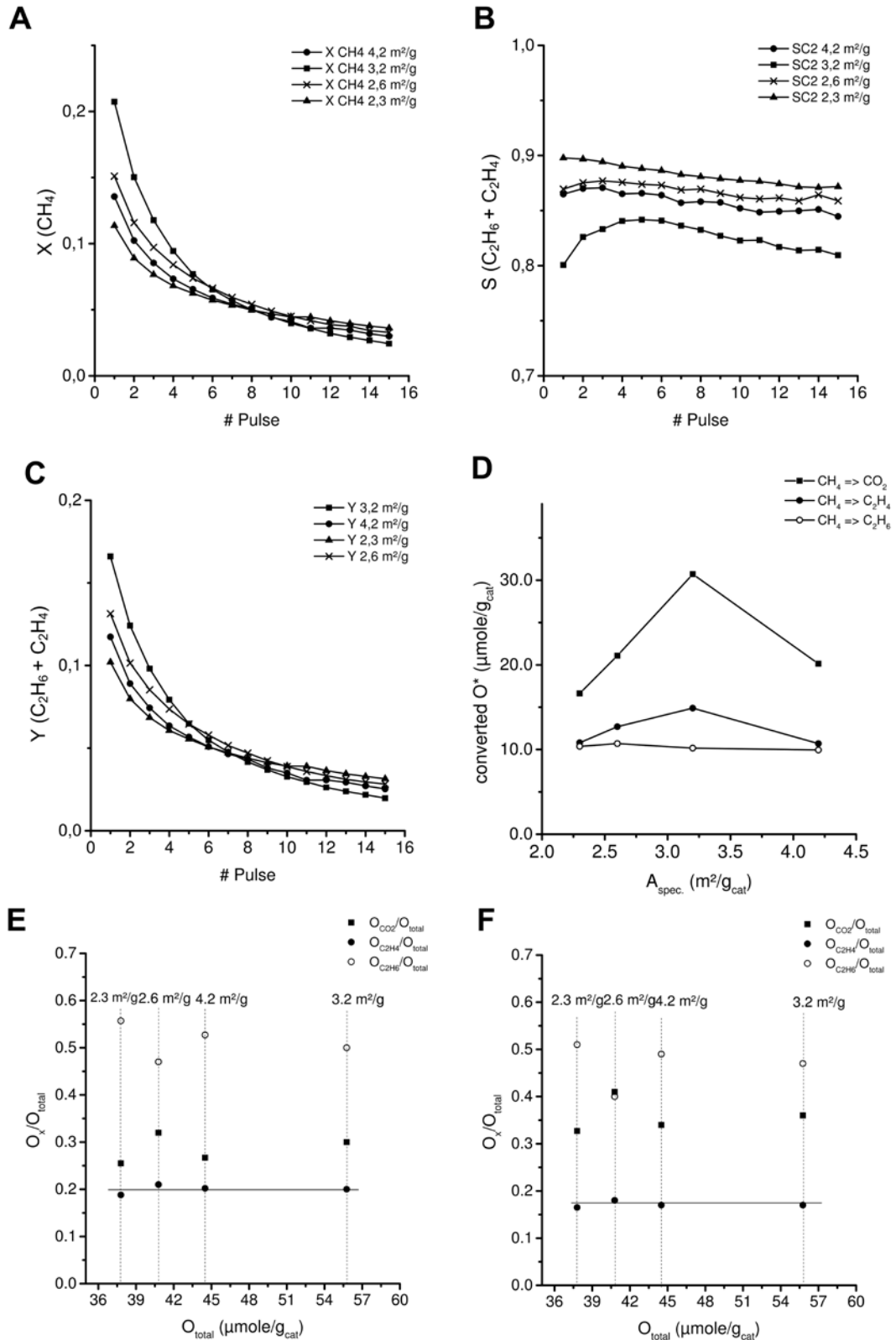


Figure 22: Results of repetitive methane pulse experiments on Na_2WO_4 (5 wt-%)/Mn (2 wt-%)/ SiO_2 at different specific surface areas, 30 Nml/min, 775 °C, 0.6 g catalyst; **A-C**: methane conversion, selectivity and C_2 yield for each pulse; **D**: oxygen balance (methane based), **E**: oxygen balance (molecule specific, $k_3/k_4 = 7$), **F**: oxygen balance (molecule specific, $k_3/k_4 = 2$) ([Paper 5](#))

3.7.2 Variation of the manganese loading on COK-12 support

Our results of single pulse experiments for catalysts with different manganese oxide loadings are presented in Figure 23. We observe an optimum between catalyst activity and manganese loading. Na_2WO_4 rich catalysts show high C_2 selectivities but low methane conversions. By increasing the manganese oxide loading the catalyst activity increases, but the C_2 selectivity decreases. The highest performance was observed for 5 wt-% Na_2WO_4 and 2 wt-% Mn, which is the classical composition for this catalyst. Further increase of the manganese oxide loading decreases the methane conversion and increases the C_2 selectivity again.

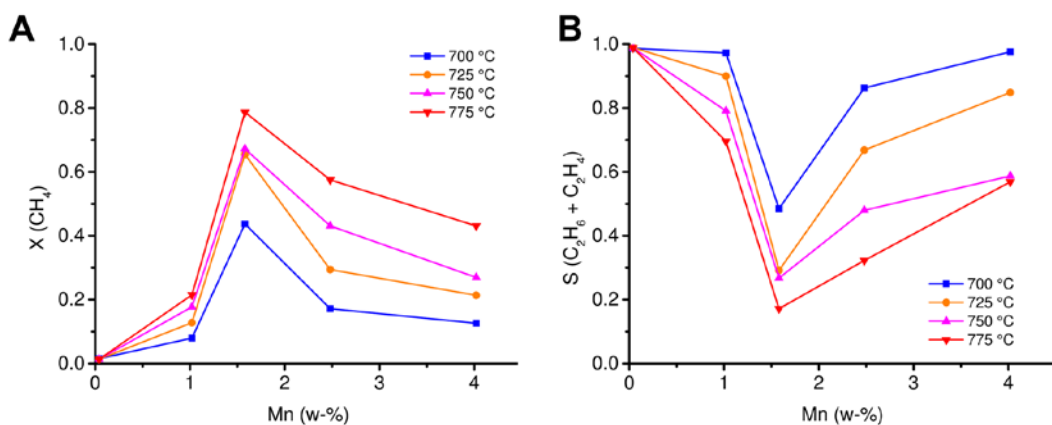


Figure 23: Results of chemical looping experiments on $\text{Na}_2\text{WO}_4/\text{Mn}/\text{SiO}_2$ catalysts at different Mn loadings and temperatures, 20 Nml/min, 1 g catalyst, 1 ml CH_4 pulse, **A:** methane conversion, **B:** C_2 selectivity ([Paper 5](#))

The results of our repetitive pulse experiments for the manganese oxide variation are presented in Figure 24. The stored oxygen amount of the most active catalyst (1.58 wt-% Mn) was completely converted after 12 methane pulses. Higher loadings need more pulses, while lower loadings of manganese oxide require only 8 methane pulses until no methane is converted. These results are based on the oxygen balances (Figure 24 C & D) showing that the manganese oxide seems to be responsible for the storage capacity of the $\text{Na}_2\text{WO}_4/\text{Mn}/\text{SiO}_2$ catalyst in chemical looping experiments. That was concluded from the fact that Na_2WO_4 rich catalysts have significantly lower activity and require less methane pulses to reach non-catalytic activity. The more manganese was loaded, the more methane pulses were required. The amount of stored oxygen differs by factor five.

We also observed no dependence for the amount of oxygen in the ethylene formation reaction. That indicates that the ethylene formation is independent from the catalyst. That was concluded because there is no influence on the formation rate neither by the overall surface concentration of the $\text{Na}_2\text{WO}_4/\text{Mn}$ phase nor by variation of the $\text{Na}_2\text{WO}_4/\text{Mn}$ ratio. Therefore, the formation of ethene seems to happen by gas phase reaction steps. During our pulse experiments, no stoichiometric amounts of hydrogen, corresponding to the amount of ethylene, were observed.

We assume that the hydrogen is quickly consumed by reduction of the catalyst, similar to temperature programmed reduction experiments with hydrogen.

By increasing the manganese oxide loading at constant tungstate loading, the film thickness is also influenced. The more manganese is deposited on the surface, the thicker is the film of the active compounds on the support material. Therefore much more methane pulses were required to reduce the highly loaded catalyst until no catalytic activity was observed. In section 3.7.1 we pointed out that the crystallinity of the active phase may contribute also to the catalyst activity. For supported manganese oxides such effect was found by different groups. Ji et al. found by Raman spectroscopy and XRD that at 2 wt-% Mn the Mn_2O_3 is formed preferably, where Mn is in oxidation state +III [46]. Increasing of the manganese loading forms also the mixed oxide $\text{MnMn}_6\text{O}_{12}$. That species stores less amounts of oxygen, which was also demonstrated by Stobbe et al. who performed TPSR experiments with different manganese oxide species [119]. They also found that different manganese oxides are reduced by methane to MnO . It has to be noted that Na_2WO_4 can also switch the oxidation state between W^{+6} to W^{+5} , according to the findings of Jiang et al., which may also contribute to the oxygen storage capacity [120]. In our repetitive pulse experiments such effect seems to be negligible, because the amount of stored oxygen increases by a factor of five but not the loading of the Na_2WO_4 . Therefore, a constant amount of stored oxygen would be expected.

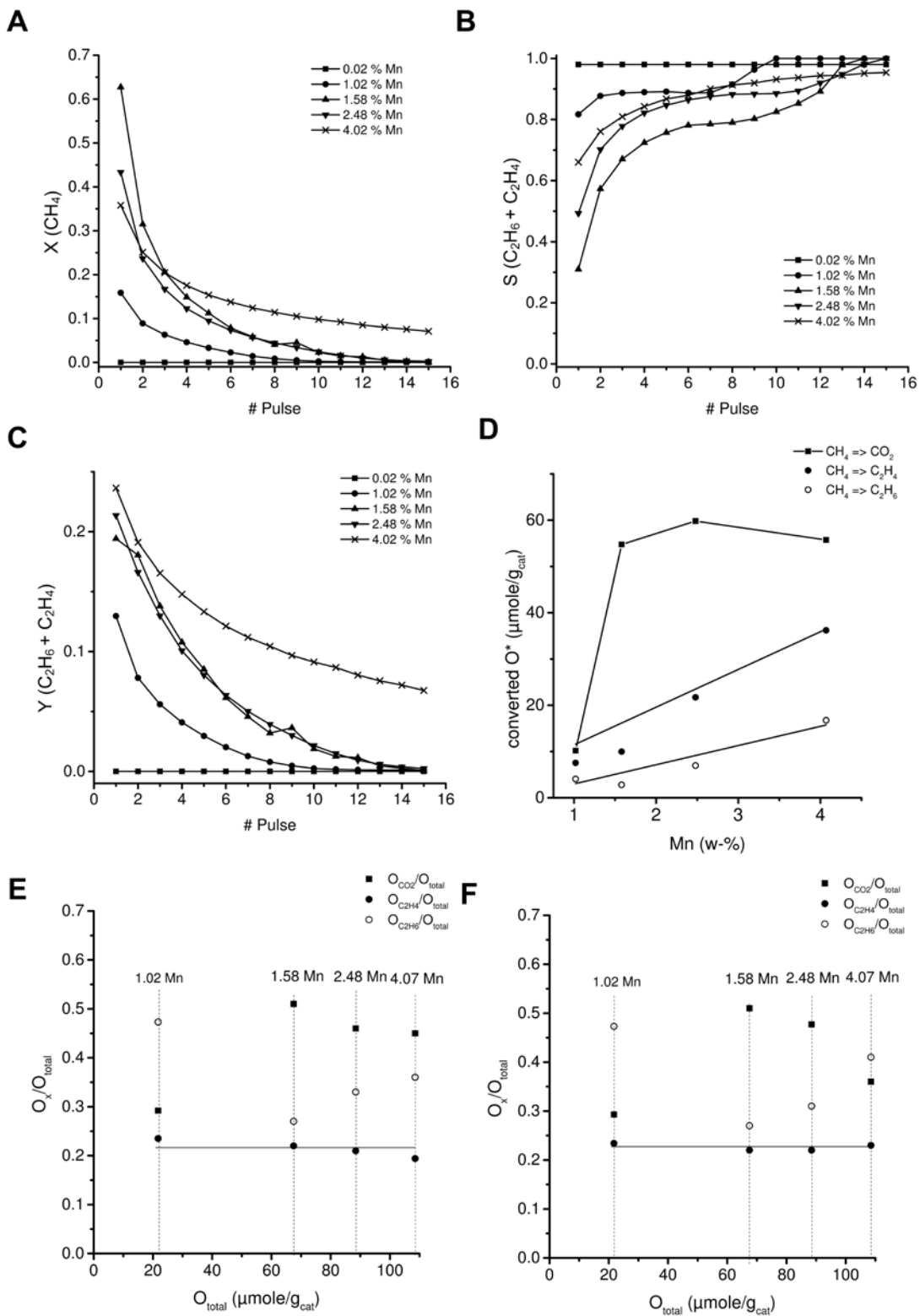


Figure 24: Results of repetitive methane pulse experiments on Na_2WO_4 (5 wt-%)/Mn (var. wt-%)/ SiO_2 at different manganese loadings, 30Nml/min, 775 °C, 1 g catalyst; **A-C:** methane conversion, selectivity and C_2 yield for each pulse; **D:** oxygen balance (methane based), **E:** oxygen balance (molecule specific, $k_3/k_4 = 7$), **F:** oxygen balance (molecule specific, $k_3/k_4 = 2$) ([Paper 5](#))

3.7.3 Variation of the support material

The results of different supported $\text{Na}_2\text{WO}_4/\text{Mn}/\text{SiO}_2$ catalysts in chemical looping experiments is presented in Figure 25. We observed lower methane conversions for the quartz supported catalyst compared to the COK-12 supported one, but higher C_2 selectivity. Such difference in activity was also reported by Yildiz et al. [53]. They found similar activity enhancement of the catalyst in steady state experiments at SBA-15 supported catalyst materials and concluded that mainly a better distribution of the active compounds contributes to that improvement. In our study ([Paper 5](#)) we assumed that the enhancement comes not only from a better distribution of the active compounds. It has to be considered that the COK-12 supported catalyst has also a higher SSA and therefore the film thickness and the crystallinity play also an important role, as discussed before.

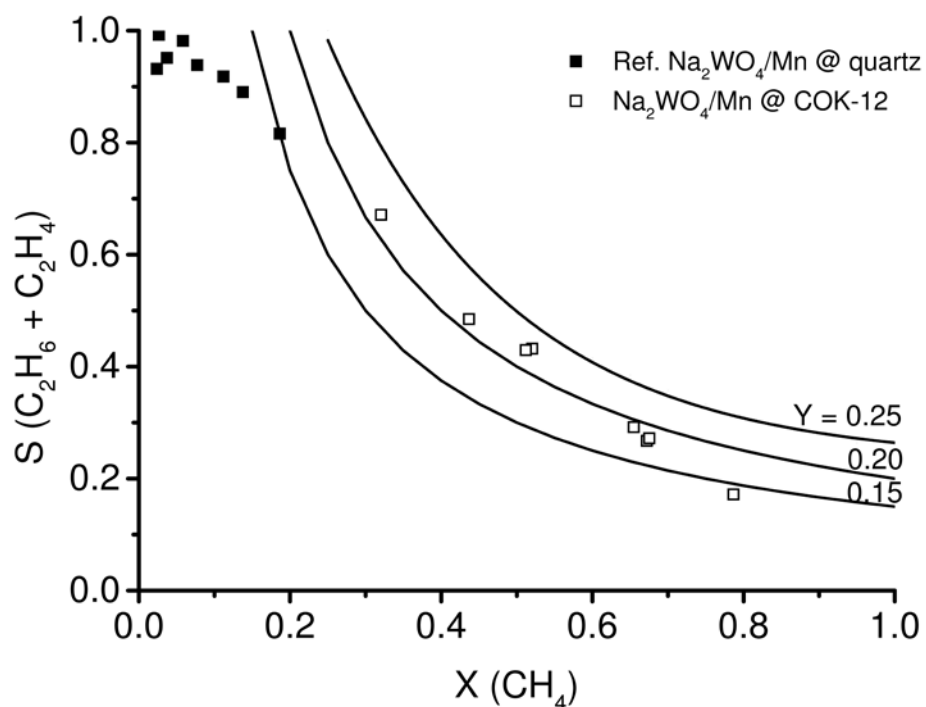


Figure 25: Results of chemical looping experiments on $\text{Na}_2\text{WO}_4/\text{Mn}/\text{SiO}_2$ catalysts at different support materials and temperatures, 1 g catalyst, 700 – 775 °C, 20 Nml/min, 1 ml CH_4 pulse ([Paper 5](#))

The results of our repetitive methane pulse experiments for the two different supported $\text{Na}_2\text{WO}_4/\text{Mn}/\text{SiO}_2$ catalysts are presented in Figure 26. Two effects were observed. The COK-12 supported one is more active and stores higher amounts of oxygen, which can be converted by methane. For the Quartz supported one much more methane pulses were necessary until no methane conversion was observed anymore. These findings support our hypothesis about the influence of the film thickness. The COK-12 supported catalyst had the same weight loadings of Na_2WO_4 and Mn but a much higher SSA than the quartz supported one. Therefore, the $\text{O}_{\text{surface}}/\text{O}_{\text{bulk}}$ ratio must be higher. As discussed before, the higher that ratio, the more active is the catalyst because more oxygen is exposed on the catalyst surface to be converted.

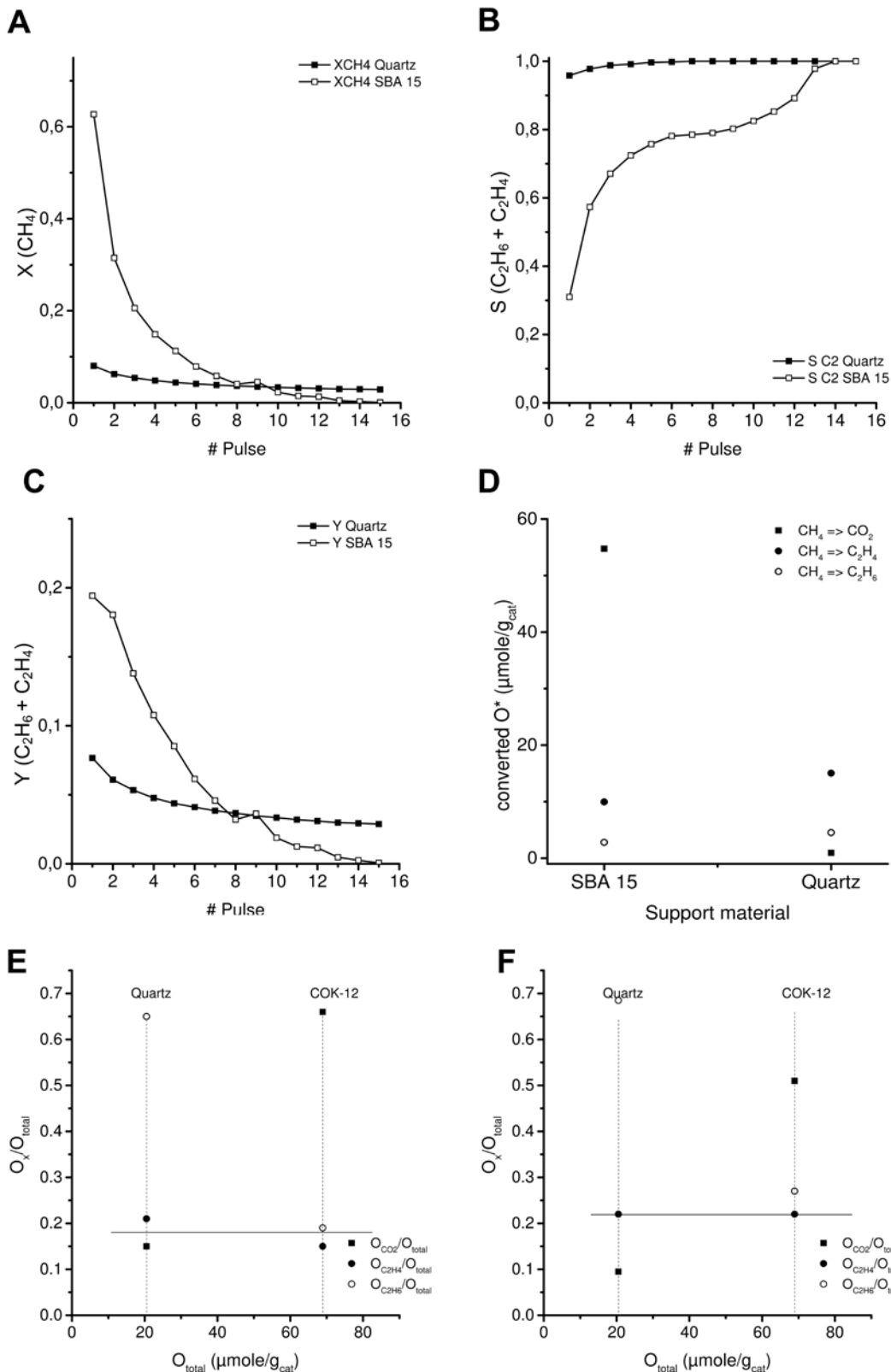


Figure 26: Results of repetitive methane pulse experiments on $\text{Na}_2\text{WO}_4/\text{Mn}/\text{SiO}_2$ at different support materials, 30Nml/min, 775 °C, 1 g catalyst; **A-C:** methane conversion, selectivity and C_2 yield for each pulse; **D:** oxygen balance (methane based), **E:** oxygen balance (molecule specific, $k_3/k_4 = 7$), **F:** oxygen balance (molecule specific, $k_3/k_4 = 2$) ([Paper 5](#))

The findings of all repetitive pulse experiments are summarized in Figure 27. Three theoretical trend lines for different reduction steps of different manganese oxide species were calculated and presented (Figure 27 A). These trend lines consider the Mn_2O_3 , Mn_3O_4 and MnO species, which coexist on the catalyst surface [121]. We also found that the total amount of stored oxygen, which has to be released for reduction of Mn_2O_3 into MnO , was never reached. This could be explained by the fact that the catalyst material cannot be fully oxidized under OCM conditions or a certain amount of oxygen is not available for methane conversion and remains in the lattice of the catalyst active phase. It has to be considered that at higher temperatures (ca. 775 °C) a phase change of Mn_2O_3 to Mn_3O_4 was observed, which also indicates a loss of oxygen [121]. The influence of the film thickness on the oxygen storage capacity is presented in Figure 27 B. We calculated a theoretical film thickness of the active compounds on the support material according to equations (36) and (37).

$$d = \frac{m(\text{Na}_2\text{WO}_4)}{\rho(\text{Na}_2\text{WO}_4) \cdot A_{\text{spec,cat,as prepared}}} + \frac{m(\text{Mn(II)})}{\rho(\text{Mn}_2\text{O}_3) \cdot A_{\text{spec,cat,as prepared}}} \quad (36)$$

$$\# \text{ Layer} = \frac{d(\text{Na}_2\text{WO}_4)}{L(W - O)} + \frac{d(\text{Mn}_2\text{O}_3)}{L(Mn - O)} \quad (37)$$

As discussed before thinner films (below 25 theoretical Layers) lead to lower catalytic performance. The increase of the film thickness showed similar results at 43 Layers, which shows clearly, that the film thickness is a very sensitive parameter for a high performance $\text{Na}_2\text{WO}_4/\text{Mn}/\text{SiO}_2$ catalyst.

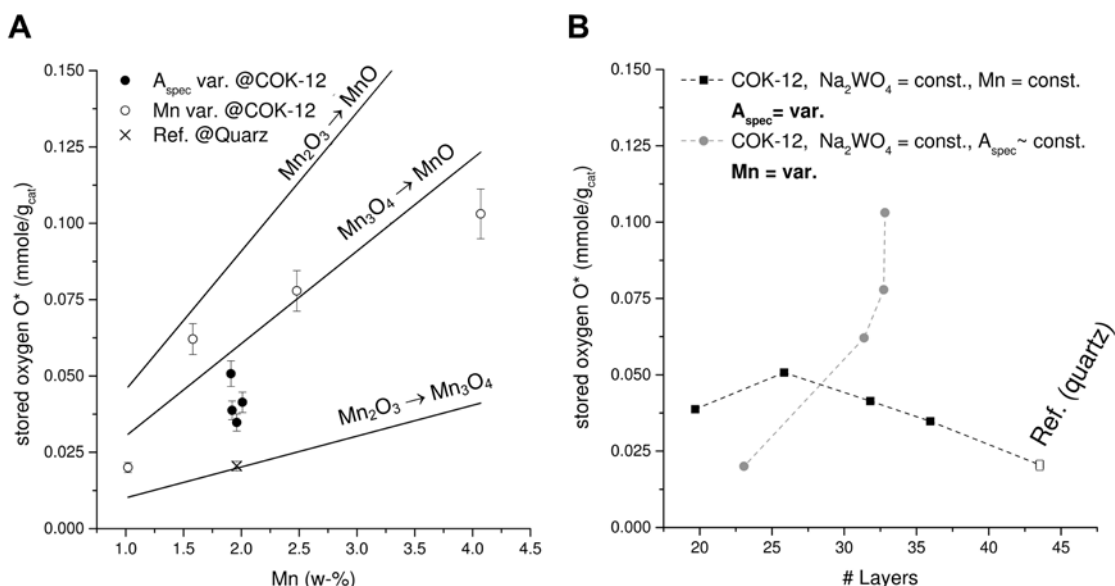
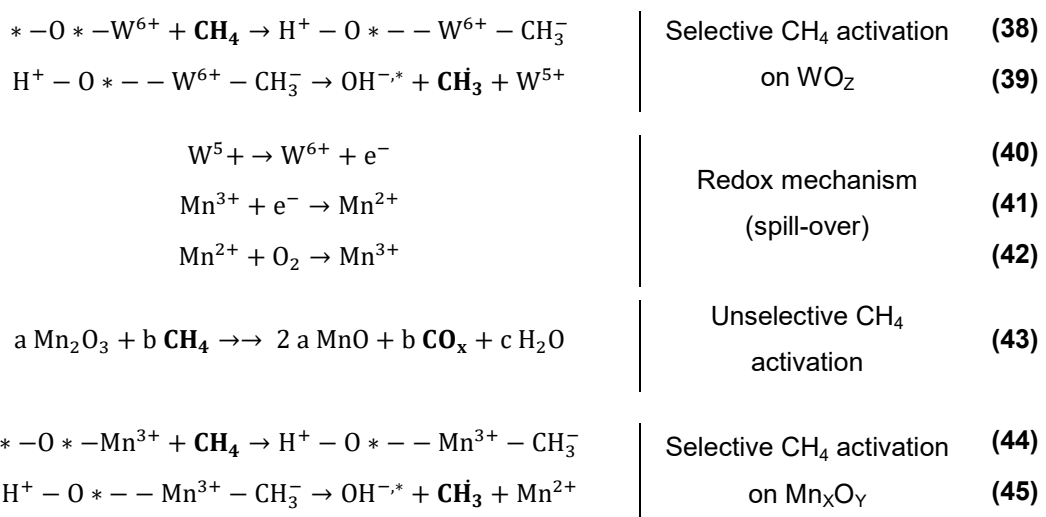


Figure 27: Total stored amount of oxygen at differently prepared $\text{Na}_2\text{WO}_4/\text{Mn}/\text{SiO}_2$ catalyst materials, **A:** correlation between oxygen storage capacity and manganese oxide loading, **B:** correlation between oxygen storage capacity and film thickness of Na_2WO_4 and Mn_2O_3 ([Paper 5](#))

As presented in the introduction, manganese oxide systems are well-known as oxygen storage material in several other chemical looping studies [89]. It is commonly used in methane combustion or synthesis gas production. In the case of the OCM reaction on $\text{Na}_2\text{WO}_4/\text{Mn}/\text{SiO}_2$ the oxidation state of methane changes only from (-IV) to (-III). Therefore, the role of the manganese oxide is similar, but the role as catalyst is very different.

It was demonstrated that Na_2WO_4 rich catalysts are less active in chemical looping experiments, but highly selective for C_2 products. As demonstrated, the oxygen storage capacity depends on the manganese oxide. Therefore, both compounds seem to have a different role. We concluded that on the one hand the tungstate is responsible for the selective activation of methane; maybe by involvement of a redox intermediate W^{5+} . On the other hand, the manganese oxide shows clearly redox activity but with less C_2 selectivity. That was demonstrated by Jones et al. who studied the OCM performance of $\text{Mn}_x\text{O}_y/\text{SiO}_2$ catalysts [122]. The cooperation effect between both compounds was reported as oxygen spill-over by Jiang et al. [50]. They proposed a redox mechanism according to equations (38) - (42). Similar findings were reported by Li [51]. The methane is activated on a tungstate species by C-H bond cleavage. Thereby methyl radicals are formed, which can couple to form ethane, while tungstate is reduced from W^{6+} to W^{5+} . The manganese oxide is able to reoxidize the tungstate, which enhances the catalyst activity. The catalyst reoxidation rate strongly depends on the reoxidation rate of the manganese oxide species. However, the findings of Jones et al. indicate that also the manganese oxide is able to form active sites for the selective activation of methane [122]. As reported by other groups, supported manganese oxides tend to form also deep oxidation products [121,123,112]. Therefore, the proposed redox mechanism of Jiang et al. has to be extended according to equations (43)-(45), which considers further redox activity of manganese oxide, as the total oxidation reaction of methane and also a selective activation. However, due to the fact that even small amounts of Na_2WO_4 enhances the methane conversion and the C_2 selectivity, the reaction rates of equations (38) - (42) must be higher compared to the reaction rates in equations (44)-(45). Another possible explanation is the number of selective, active sites, which could be lower for the manganese oxide system. [46]



We concluded that the proposed oxygen spill-over effect between Na_2WO_4 and Mn seems to be a suitable mechanism to explain our findings. As discussed before, the film thickness of the active compounds triggers mainly the activity and the oxygen storage capacity of the catalyst. The Mn_xO_y species depends on both parameters and therefore tunes the methane activation potential, which could be explained by equations (40)-(42). The thicker the film the more Mn_3O_4 is possibly formed. That effect leads to a lower amount of stored oxygen and may also change the redox potential of the catalyst material. Another point is the phase change of Mn_2O_3 to Mn_3O_4 , which is similar to an auto-reduction step. Such a reaction would also contribute to the catalyst activity.

4 Conclusions

In this work we investigated the influences of gas phase reactions on the catalyst performance of the OCM reaction. That was done by experiments and simulations of different reactor types, which have different mixing properties. In our experimental and also in simulation studies we found that the gas phase reaction network is very sensitive to the mixing properties of the reactor, indicated by different conversions of methane and oxygen in fluidized bed (CSTR), fixed bed (PFTR) and membrane reactor under same reaction conditions. The addition of a semi-empirical model of the catalyst functionality, which only generates methyl radicals showed that the final selectivities of the reaction products depend strongly on the oxygen dosage strategy. High oxygen partial pressures and strong mixing behavior lead to a significant decrease of the amount of C_2 products. Furthermore, the same effect leads to the formation of Hot Spots in the gas phase, which are responsible for a significant increase in the reaction rate. The main reasons are the low heat conductivity and heat capacity of the gases, which leads to heat transfer problems. Thus, a reactor system is required which improves the catalyst oxidation without the presence of high oxygen partial pressures.

To improve the catalyst oxidation rate, the influences of higher pressure in OCM experiments was investigated. Our results indicate that the adsorption process on the catalyst surface was enhanced, which increases the methane conversion and C_2 selectivity. Further, the enhanced oxidation rate of the catalyst material, caused by enhanced oxygen adsorption, decreases the amount of gas phase oxygen. Thus, less gas phase oxidation reactions lead to less formation of deep oxidation products.

In TAP experiments it was demonstrated that weakly bound oxygen, a possible adsorption intermediate of gas phase oxygen, influences strongly the methane activation process. Weakly bound oxygen leads to deep oxidation products, while strongly bound oxygen seems to be responsible for selective methane activation. Therefore, a study of the catalyst under steady state conditions is affected by both oxygen species and the reliability of kinetic studies under steady state conditions is questionable, because the contributions of both species can hardly be resolved.

Thus, dynamic experimental techniques, such as TPSR, were used to investigate the catalyst. By the use of such techniques, the oxidation process of the catalyst material by gas phase oxygen was separated from the OCM reaction. That allowed the investigation of the catalytic surface reaction network without the influences by gas phase oxygen and its adsorption intermediates on the catalyst. In temperature programmed surface reaction experiments, we found that two strongly bound oxygen species are involved in the OCM reaction on the catalyst surface. Electrophilic oxygen seems to be responsible for the selective methane activation, while nucleophilic oxygen is responsible for the formation of deep oxidation products. The formed ethane is quickly converted to ethene in the gas phase by thermal dehydrogenation or oxidative dehydrogenation on the catalyst surface. Both oxygen species may also contribute to unselective ethene activation. By the variation of the heating rates in methane TPSR experiments, an activation energy of 275 kJ/mole for the selective methane activation was derived according to the Redhead method. This high energy barrier reflects that the strongly bound oxygen species have a comparable nature as lattice oxygen. Further, these results indicate a Mars-van-Krevelen like reaction mechanism for the OCM reaction on the $\text{Na}_2\text{WO}_4/\text{Mn}/\text{SiO}_2$ catalyst.

Dynamic experiments at constant reaction temperatures showed that the strongly bound oxygen species are stored at OCM conditions for hours on the catalyst surface. We also found a linear dependence of the methane partial pressure. An oxygen balance of the formed products gave an oxygen storage capacity of 20 O/nm², which indicates the involvement of several sublayers from the $\text{Na}_2\text{WO}_4/\text{Mn}$ phase. As mentioned in the introduction, a structural flexibility of the $\text{Na}_2\text{WO}_4/\text{Mn}$ phase is necessary for a highly active catalyst. Therefore it seems to be possible that such an amorphous, flexible structure allows the involvement of many sublayers for methane activation reactions.

Based on our findings we developed a simulated chemical looping setup, despite of a low oxygen transport capability R_O , which was 0.014 – 0.001. That technique allowed the dosage of defined amounts of methane. The main principle of operation was an oxidation step, followed by a purge step to remove gas phase oxygen from the reactor by the help of a carrier gas. Then, a methane pulse was dosed and unconverted methane and OCM products were transported by an additional purge step to the detector. We could show that the $\text{Na}_2\text{WO}_4/\text{Mn}/\text{SiO}_2$ catalyst has a stable performance in continuous chemical looping operation. In our yield optimization studies we found an apparent C₂ yield maximum of 0.25. That seems to be caused by the contribution of stored electrophilic and nucleophilic oxygen on the catalyst surface to the OCM reaction, which activate methane as well as ethene. A comparison between simulated chemical looping experiments and steady state experiments showed that methane can be converted more efficiently in dynamic experiments due to the higher selectivity than in steady state mode. In Figure 28, we compared the chemical looping results with the literature in order to highlight the advantage of this technique for the OCM reaction. At methane conversions lower than 0.3 more C₂ products are formed in chemical looping experiments than in steady state experiments. That difference reflects the involvement of several oxygen intermediates, which contribute in gas

phase and on the catalyst surface to alkane and alkene activation in steady state operation. Further we demonstrated that also high methane conversions are reachable in chemical looping experiments, which cannot be investigated under steady state conditions. The required ratio of CH₄:O₂ in the feed mixture is higher than 0.5, but for this composition the explosive regime is reached.

Due to the fact that no gas phase oxygen is present in chemical looping experiments, the methane is completely activated by oxygen from the catalyst surface and the most heat is also generated there, which can be much easier removed than in gas phase. It was also highlighted that the use of different reactor techniques and feed strategies improve the OCM performance. According to the findings of Takanabe et al. the addition of water improves the C₂ selectivity at low methane conversions additionally. [71] Increased methane conversions lead to the formation of more water and therefore that effect is not observable anymore. Godini and Coworkers demonstrated the successful operation of a membrane reactor, performing the OCM reaction [86]. They demonstrated that the dosage of low amounts of oxygen along the catalyst fixed bed had a similar, beneficial effect as the simulated chemical looping experiments. Kruglow et al. presented a countercurrent moving bed reactor, where methane is partially converted and the C₂ products were separated from the rest of the feed [84]. Unconverted methane was fed to the next reactor section, which was repeated four times. They reported a C₂ yield of 0.55.

The conversion of low amounts of a reactant at high selectivities is carried out in the production of ethylene oxide in chemical industry. [124] The most important factor is the high price difference between ethene and ethylene oxide, which makes such a process economical. Thus, the chemical looping seems to have the potential for industrial application, due to its potential to increase the selectivity for the desired products.

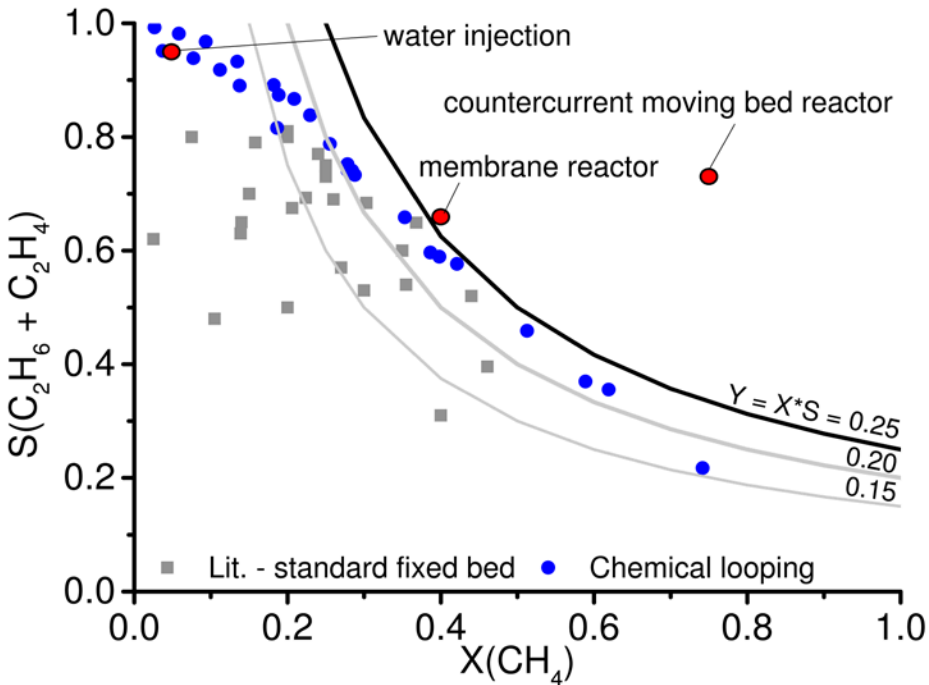


Figure 28: Comparison of literature results for $\text{Na}_2\text{WO}_4/\text{Mn}/\text{SiO}_2$ catalyst in standard fixed bed reactors with simulated chemical looping and other reactor concepts ([Paper 4](#))

One of the most important parameters in chemical looping experiments is the oxygen storage capacity, which was investigated by the synthesis of different $\text{Na}_2\text{WO}_4/\text{Mn}/\text{SiO}_2$ catalysts. We found a relationship between the storage capacity of oxygen and the manganese oxide loading. We also found an influence of the film thickness of $\text{Na}_2\text{WO}_4/\text{Mn}$ on the support material on OCM activity. In addition the formation of ethene seems to be mostly independent from the catalyst and takes place only in the gas phase by thermal dehydrogenation of ethane. A summary about the functionality of the $\text{Na}_2\text{WO}_4/\text{Mn}/\text{SiO}_2$ catalyst in chemical looping experiments are presented in [Paper 5](#) and schematically shown in Figure 29.

The active compounds Na_2WO_4 and Mn_xO_y are deposited on SiO_2 as support material. The sodium ions induce a phase transition of the SiO_2 into α -cristobalite [44]. That phase change allows a structural flexibility of the $\text{Na}_2\text{WO}_4/\text{Mn}_x\text{O}_y$ mixture under OCM conditions [48]. Such amorphous property enables high OCM performance for that material by oxygen spill-over reaction between Mn and Na_2WO_4 [50,51]. During the oxidation of the catalyst material with gas phase oxygen an adsorbed oxygen intermediate is formed, which is able to convert methane into deep oxidation products [72]. The oxidized catalyst stores electrophilic and nucleophilic oxygen species. Those can interact in different ways. Electrophilic oxygen ($\text{O}_{\text{elec.}}$) reacts with methane and leads to methyl radical formation. Those radicals can couple, possibly in gas phase, and form ethane [54]. Afterwards, it is dehydrogenated in the gas phase to ethene, which can be activated by electrophilic oxygen, which forms oxygenates. These oxygenates tend to form deep oxidation products. Nucleophilic oxygen ($\text{O}_{\text{nuc.}}$) interacts with methane and leads to deep oxidation product formation. That species can be reduced by molecular hydrogen

to water and can convert ethene into deep oxidation products by the formation of carbon coke as intermediate, which is further oxidized. The role of Na_2WO_4 seems to be the active site for selective activation of methane. The manganese oxide contributes by its complex redox properties. On the one hand it is able to oxidize the tungstate species, which enhances the formation rate of methyl radicals [50]. On the other hand it also contributes to the formation of deep oxidation products. The film thickness of the active phase is another important factor for a highly active $\text{Na}_2\text{WO}_4/\text{Mn}/\text{SiO}_2$ catalyst in chemical looping experiments. Thick films store more oxygen in the lattice, which is not accessible for methane activation. Under OCM reaction temperatures the Mn_2O_3 could transform also into Mn_3O_4 [121]. That may suppress the catalyst performance. Thinner films show a higher performance, because more oxygen is accessible on the catalyst surface for methane activation. Further decrease of the film thickness may destabilize the structural flexibility, decreasing the oxygen spill-over effect and finally, decrease the catalytic activity. In addition oxygen could be less stable bound and could be more easily desorb into the gas phase, causing again unfavorable reactions.

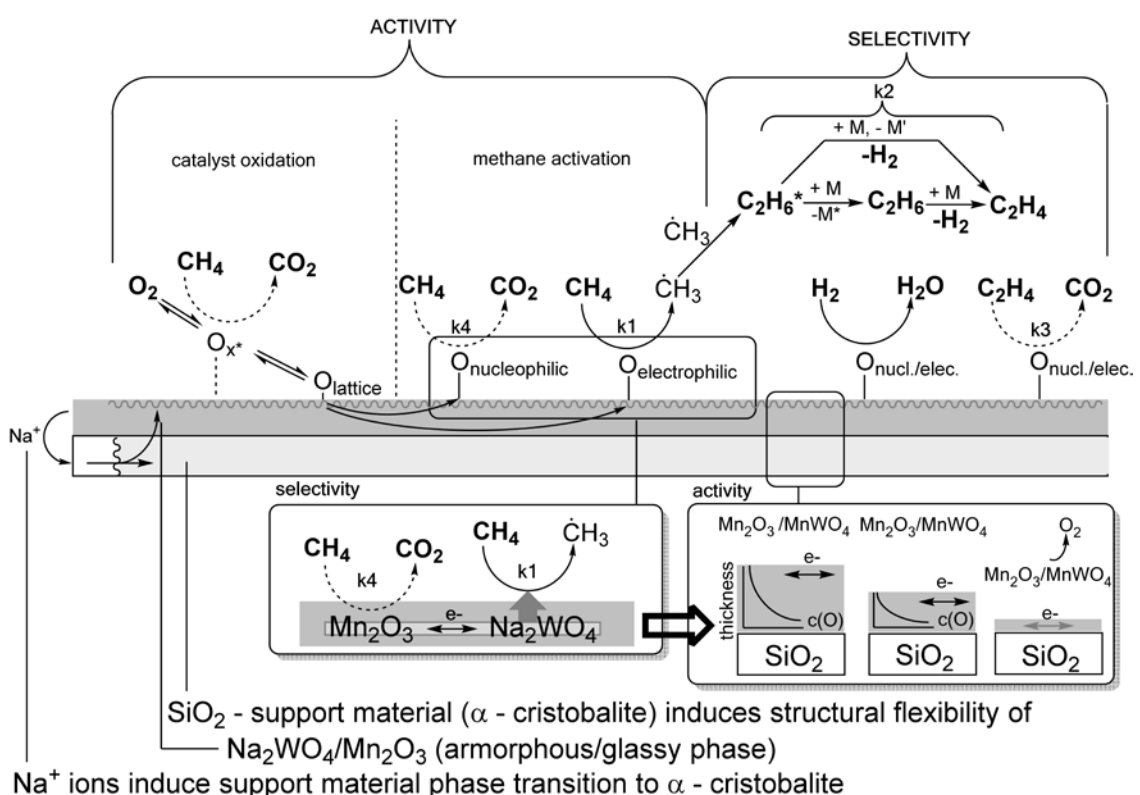


Figure 29: Proposed OCM surface and gas phase reaction network, and working functionality of the $\text{Na}_2\text{WO}_4/\text{Mn}/\text{SiO}_2$ catalyst in simulated chemical looping experiments [44,48,50,54,72] ([Paper 5](#))

5 List of References

- [1] N.A. Owen, O.R. Inderwildi, D.A. King, *Energy Policy* 38 (2010) 4743–4749.
- [2] R. Diercks, J.-D. Arndt, S. Freyer, R. Geier, O. Machhammer, J. Schwartze, M. Volland, *Chem. Eng. Technol.* 31 (2008) 631–637.
- [3] D. Jeremic, *Ullmann's Encycl. Ind. Chem.* (2014) 1–42.
- [4] H. Zimmermann, R. Walzl, *Ullmann's Encycl. Ind. Chem.* 13 (2012) 547–572.
- [5] M. Thiemann, E. Scheibler, K.W. Wiegand, *Ullmann's Encycl. Ind. Chem.* (2006) 177–223.
- [6] G.E. Keller, M.M. Bhasin, *J. Catal.* 73 (1982) 9–19.
- [7] T. Ito, J. Wang, C. Lin, J. Lunsford, *J. Am. ...* 107 (1985) 5062–5068.
- [8] S. Arndt, G. Laugel, S. Levchenko, R. Horn, M. Baerns, M. Scheffler, R. Schlögl, R. Schomäcker, *Catal. Rev.* 53 (2011) 424–514.
- [9] S.J. Blanksby, G.B. Ellison, *Acc. Chem. Res.* 36 (2003) 255–63.
- [10] <http://webbook.nist.gov/chemistry/>, (2011).
- [11] S. Dooley, M.P. Burke, M. Chaos, Y. Stein, F.L. Dryer, V.P. Zhukov, O. Finch, J.M. Simmie, H.J. Curran, *Int. J. Chem. Kinet.* 42 (2010) 527–549.
- [12] H. Schwarz, M. Geske, C. Franklin Goldsmith, R. Schlögl, R. Horn, *Combust. Flame* 161 (2014) 1688–1700.
- [13] S. Mavlyankariev, *Investigation of Oxidative Coupling of Methane in the Gas Phase by Reactor Profile Measurements and Microkinetic Modeling*, Technische Universität Berlin, 2013.
- [14] H. Zanthonoff, M. Baerns, B.A. Ax, *Ind. Eng. Chem. Res.* 29 (1990) 2–10.
- [15] U. Zavyalova, M. Holena, R. Schlögl, M. Baerns, *ChemCatChem* 3 (2011) 1935–1947.
- [16] E. V. Kondratenko, M. Baerns, in: *Handb. Heterog. Catal.*, 2014, pp. 3010–3023.
- [17] J.C.W. Kuo, C.T. Kresge, R.E. Palermo, *Catal. Today* 4 (1989) 463–470.
- [18] G.E. Keller, M.M. Bhasin, *J. Catal.* 73 (1982) 9–19.
- [19] M. Baerns, in: *Methane Convers. by Oxidative Process.*, 1992, pp. 382–402.
- [20] G.J. Hutchings, M.S. Scurrell, J.R. Woodhouse, *Chem. Soc. Rev.* 18 (1989) 251.
- [21] L. Olivier, S. Haag, H. Pennemann, C. Hofmann, C. Mirodatos, A.C. van Veen, *Catal. Today* 137 (2008) 80–89.
- [22] P. Schwach, W. Frandsen, M.-G. Willinger, R. Schlögl, A. Trunschke, *J. Catal.* 329 (2015) 560–573.
- [23] P. Schwach, N. Hamilton, M. Eichelbaum, L. Thum, T. Lunkenbein, R. Schlögl, A. Trunschke, *J. Catal.* 329 (2015) 574–587.
- [24] K. Kwapien, J. Paier, J. Sauer, M. Geske, U. Zavyalova, R. Horn, P. Schwach,

- A. Trunschke, R. Schlögl, *Angew. Chemie - Int. Ed.* 53 (2014) 8774–8778.
- [25] S.J. Korf, J.A. Roos, N.A. de Brujin, J.G. van Ommen, J.R.H. Ross, *Catal. Today* 2 (1988) 535–545.
- [26] R.P. Taylor, G.L. Schrader, *Ind. Eng. Chem. Res.* 30 (1991) 1016–1023.
- [27] T. Levan, M. Che, J.M. Tatibouet, M. Kermarec, *J. Catal.* 142 (1993) 18–26.
- [28] S.L. Kaliaguine, B.N. Shelimov, V.B. Kazansky, *J. Catal.* 55 (1978) 384–393.
- [29] C. Lin, K.D. Campbell, J. Wang, J.H. Lunsford, *J. Phys. Chem.* 90 (1986) 534–537.
- [30] S. Lacombe, C. Geantet, C. Mirodatos, *J. Catal.* 151 (1994) 439–452.
- [31] M.S. Palmer, M. Neurock, M.M. Olken, *J. Am. Chem. Soc.* 124 (2002) 8452–8461.
- [32] C. Louis, T.L. Chang, M. Kermarec, T. Le Van, J.M. Tatibouët, M. Che, *Colloids Surfaces A Physicochem. Eng. Asp.* 72 (1993) 217–228.
- [33] V.J. Ferreira, P. Tavares, J.L. Figueiredo, J.L. Faria, *Catal. Commun.* 42 (2013) 50–53.
- [34] P. Schwach, M.G. Willinger, A. Trunschke, R. Schlögl, *Angew. Chemie - Int. Ed.* 52 (2013) 11381–11384.
- [35] Y. Cui, X. Shao, M. Baldofski, J. Sauer, N. Nilius, H.J. Freund, *Angew. Chemie - Int. Ed.* 52 (2013) 11385–11387.
- [36] R. Ghose, H.T. Hwang, A. Varma, *Appl. Catal. A Gen.* 452 (2013) 147–154.
- [37] X. Fang, S. Li, J. Gu, D. Yang, *J. Mol. Catal.* (1992) 255.
- [38] R. Koirala, R. Büchel, S.E. Pratsinis, A. Baiker, *Appl. Catal. A Gen.* 484 (2014) 97–107.
- [39] D. Wang, M.P. Rosynek, J.H. Lunsford, *J. Catal.* 155 (1995) 390–402.
- [40] H. Liu, X. Wang, D. Yang, R. Gao, Z. Wang, J. Yang, *J. Nat. Gas. Chem.* 17 (2008) 59–63.
- [41] U. Simon, O. Görke, A. Berthold, S. Arndt, R. Schomäcker, H. Schubert, *Chem. Eng. J.* 168 (2011) 1352–1359.
- [42] S. Jašo, S. Sadjadi, H.R. Godini, U. Simon, S. Arndt, O. Görke, a. Berthold, H. Arellano-Garcia, H. Schubert, R. Schomäcker, G. Wozny, *J. Nat. Gas. Chem.* 21 (2012) 534–543.
- [43] J. Wang, L. Chou, B. Zhang, H. Song, J. Zhao, J. Yang, S. Li, *J. Mol. Catal. A Chem.* 245 (2006) 272–277.
- [44] A. Palermo, J. Pedro, H. Vazquez, A.F. Lee, M.S. Tikhov, R.M. Lambert, *J. Catal.* 177 (1998) 259–266.
- [45] Z.-C. Jiang, C.-J. Yu, X.-P. Fang, S.-B. Li, H.-L. Wand, *J. Phys. Chem.* 97 (1993) 12870–12875.
- [46] S. Ji, T. Xiao, S. Li, C. Xu, R. Hou, K.S. Coleman, M.L.H. Green, *Appl. Catal.*

- 225 (2002) 271–284.
- [47] Y. Kou, B. Zhang, J. Niu, H. Wang, T. Tanaka, S. Yoshida, *J. Catal.* 173 (1998) 399–408.
- [48] Z. Gholipour, a Malekzadeh, M. Ghiasi, Y. Mortazavi, a Khodadadi, (2012) 189–211.
- [49] G.D. Nipan, *Inorg. Mater.* 50 (2014) 1012–1017.
- [50] Z. Jiang, H. Gong, S. Li, *Stud. Surf. Sci. Catal.* 112 (1997) 481–490.
- [51] L. Shu-Ben, *Chinese J. Chem.* 19 (2001) 16–21.
- [52] A. Malekzadeh, A.K. Dalai, A. Khodadadi, Y. Mortazavi, *Catal. Commun.* 9 (2008) 960–965.
- [53] M. Yildiz, Y. Aksu, U. Simon, K. Kailasam, O. Goerke, F. Rosowski, R. Schomäcker, A. Thomas, S. Arndt, *Chem. Commun.* 50 (2014) 14440–14442.
- [54] D.J. Driscoll, J.H. Lunsford, *J. Phys. Chem.* 89 (1985) 4415–4418.
- [55] J.H. Lunsford, *Angew. Chemie Int. Ed. English* 34 (1995) 970–980.
- [56] T. Ito, J.H. Lunsford, *Nature* 314 (1985) 721–722.
- [57] M.Y. Sinev, *Russ. J. Phys. Chem. B* 1 (2007) 412–433.
- [58] G.J. Hutchings, M.S. Scurrell, J.R. Woodhouse, *J. Chem. Soc. Chem. Commun.* (1987) 1388–1389.
- [59] G.J. Hutchings, M.S. Scurrell, J.R. Woodhouse, *J. Chem. Soc. Chem. Commun.* (1989) 765–766.
- [60] M. Ghiasi, A. Malekzadeh, S. Hoseini, Y. Mortazavi, A. Khodadadi, A. Talebizadeh, *J. Nat. Gas Chem.* 20 (2011) 428–434.
- [61] Z. Stansch, L. Mleczko, M. Baerns, *Ind. Eng. Chem. Res.* 36 (1997) 2568–2579.
- [62] R. Ghose, H.T. Hwang, A. Varma, *Appl. Catal. A Gen.* 472 (2014) 39–46.
- [63] Y. Simon, F. Baronnet, P.-M. Marquaire, *Ind. Eng. Chem. Res.* 46 (2007) 1914–1922.
- [64] M. Daneshpayeh, A. Khodadadi, N. Mostoufi, Y. Mortazavi, R. Sotudeh-Gharebagh, A. Talebizadeh, *Fuel Process. Technol.* 90 (2009) 403–410.
- [65] S. Lacombe, Z. Durjanova, L. Mleczko, C. Mirodatos, *Chem. Eng. Technol.* 18 (1995) 216–223.
- [66] J. Sun, J.W. Thybaut, G.B. Marin, *Catal. Today* 137 (2008) 90–102.
- [67] M.R. Lee, M.-J. Park, W. Jeon, J.-W. Choi, Y.-W. Suh, D.J. Suh, *Fuel Process. Technol.* 96 (2012) 175–182.
- [68] H. Yamamoto, H.Y. Chu, M.T. Xu, C.L. Shi, J.H. Lunsford, 142 (1993) 325–336.
- [69] K. Langfeld, B. Frank, V.E. Strempel, C. Berger-Karin, G. Weinberg, E. V. Kondratenko, R. Schomäcker, *Appl. Catal. A Gen.* 417-418 (2012) 145–152.
- [70] Y. Liu, R. Hou, X. Liu, J. Xue, S. Li, *Stud. Surf. Sci. Catal.* 119 (1998) 307–311.

- [71] K. Takanabe, E. Iglesia, *Angew. Chem. Int. Ed.* 47 (2008) 7689–93.
- [72] B. Beck, V. Fleischer, S. Arndt, M.G. Hevia, A. Urakawa, P. Hugo, R. Schomäcker, *Catal. Today* 228 (2014) 212–218.
- [73] A.J. Nagy, G. Mestl, R. Schlögl, *J. Catal.* 188 (1999) 58–68.
- [74] P.A. Kilty, W.M.H. Sachtler, *Catal. Rev.* 10 (1974) 1–16.
- [75] A. Kooh, J.L. Dubois, H. Mimoun, C.J. Cameron, *Catal. Today* 6 (1990) 453–462.
- [76] D. Wolf, M. Ho, M. Baerns, *Ind. Eng. Chem. Res.* 36 (1997) 3345–3353.
- [77] M. Daneshpayeh, N. Mostoufi, A. Khodadadi, R. Sotudeh-gharebagh, *Energy & Fuels* 23 (2009) 3745–3752.
- [78] M. Makri, C.G. Vayenas, *Appl. Catal. A Gen.* 244 (2003) 301–310.
- [79] S. Ren, S. Qin, J. Zhu, X. Peng, C. Hu, *Ind. Eng. Chem. Res.* 49 (2010) 2078–2083.
- [80] G. Wozny, H. Arellano-garcia, *Chem. Enginnering Trans.* 21 (2010) 1399–1404.
- [81] H.-R. Godini, S. Jaso, W. Martini, S. Stünkel, D. Salerno, S.N. Xuan, S. Song, S. Sadjadi, H. Trivedi, H. Arellano-Garcia, G. Wozny, *Tech. Trans.* 109 (2012) 63–74.
- [82] P.O. Graf, L. Lefferts, *Chem. Eng. Sci.* 64 (2009) 2773–2780.
- [83] J.H. Edwards, K.. T. Do, R.J. Tyler, *Fuel* 71 (1992) 325–334.
- [84] A. V. Kruglow, M.C. Bjorklund, R.W. Carr, *Chem. Eng. Sci.* 51 (1996) 2945–2950.
- [85] C. Hu, J. Wu, H. Zhang, S. Qin, *AIChE J.* 53 (2007) 2925 – 2931.
- [86] H.R. Godini, A. Gili, O. Görke, U. Simon, K. Hou, G. Wozny, *Energy & Fuels* 28 (2014) 877–890.
- [87] S. Gadewar, S.A. Sardar, P. Gross, A. Zhang, V. Julka, P. Stolmanov, Continuous Process for Converting Natural Gas to Liquid Hydrocarbons, US8921625B2, 2014.
- [88] S. Hurst, *Oil Soap* 16 (1939) 29–35.
- [89] J. Adanez, A. Abad, F. Garcia-Labiano, P. Gayan, L.F. de Diego, *Prog. Energy Combust. Sci.* 38 (2012) 215–282.
- [90] I.M. Dahl, E. Bakken, Y. Larring, A.I. Spjelkavik, S.F. Håkonsen, R. Blom, *Energy Procedia* 1 (2009) 1513–1519.
- [91] F. Petrakopoulou, A. Boyano, M. Cabrera, G. Tsatsaronis, *Int. J. Greenh. Gas Control* 5 (2011) 475–482.
- [92] J. Ströhle, M. Orth, B. Epple, *Appl. Energy* 113 (2014) 1490–1495.
- [93] E. Jerndal, T. Mattisson, A. Lyngfelt, *Chem. Eng. Res. Des.* 84 (2006) 795–806.
- [94] K. Li, H. Wang, Y. Wei, *J. Chem.* (2013).

- [95] P. Gupta, F. Li, L. Velázquez - Vargas, D. Sridhar, M. Iyer, S. Ramkumar, L.-S. Fan, in:, *Chem. Looping Syst. Foss. Energy Conversions*, John Wiley & Sons, Hoboken, 2010, pp. 57–142.
- [96] L.F. de Diego, M. Ortiz, F. García-Labiano, J. Adámez, A. Abad, P. Gayán, *J. Power Sources* 192 (2009) 27–34.
- [97] M. Ishida, H. Jin, T. Okamoto, *Energy and Fuels* 12 (1998) 223–229.
- [98] D.W. Park, S. Ghazali, G. Gau, *Appl. Catal.* 6 (1983) 175–193.
- [99] X. Lang, R.R. Hudgins, P.L. Silveston, *Can. J. Chem. Eng.* 67 (1989) 635–645.
- [100] X. Lang, P.L. Silveston, R.R. Hudgins, *Can. J. Chem. Eng.* 69 (1991) 1121–1125.
- [101] D. Creaser, B. Andersson, R.R. Hudgins, P.L. Silveston, *Chem. Eng. Sci.* 54 (1999) 4437–4448.
- [102] D. Creaser, B. Andersson, R.R. Hudgins, P.L. Silveston, *Appl. Catal. A Gen.* 187 (1999) 147–160.
- [103] N. Ballarini, F. Cavani, A. Cericola, C. Cortelli, M. Ferrari, F. Trifirò, G. Capannelli, A. Comite, R. Catani, U. Cornaro, *Catal. Today* 91-92 (2004) 99–104.
- [104] V. Salehoun, A. Khodadadi, Y. Mortazavi, A. Talebizadeh, *Chem. Eng. Sci.* 63 (2008) 4910–4916.
- [105] S. Brunauer, P.H. Emmett, *J. Am. Chem. Soc.* 59 (1937) 2682–2689.
- [106] S. Pak, P. Qiu, J.H. Lunsford, *J. Catal.* 230 (1998) 222–230.
- [107] C. Shi, M.P. Rosynek, J.H. Lunsford, *(1994)* 8371–8376.
- [108] S. Wauters, G.B. Marin, *Ind. Eng. Chem. Res.* 41 (2002) 2379–2391.
- [109] P.A. Redhead, *Vacuum* 12 (1962) 203–211.
- [110] G.J. Hutchings, M.S. Scurrell, J.R. Woodhouse, *Chem. Soc. Rev.* 18 (1989) 251.
- [111] T. Mattisson, A. Järdnäs, A. Lyngfelt, *Energy and Fuels* 17 (2003) 643–651.
- [112] Q. Zafar, T. Mattisson, B. Gevert, *Energy and Fuels* 20 (2006) 34–44.
- [113] P. Atkins, J. De Paula, in:, *Phys. Chem.*, 8th ed., Oxford university press, 2006, pp. 747 – 757.
- [114] T. Miyauchi, T. Kikuchi, *Ckemicol Eng. Sci.* 30 (1975) 343–348.
- [115] S. Jaso, *J. Nat. Gas Chem.* 21 (2012) 534–543.
- [116] I.E. Wachs, *Catal. Today* 27 (1996) 437–455.
- [117] A.A. Tyunyaev, G.D. Nipan, T.N. Kol'tsova, A.S. Loktev, V.A. Ketsko, A.G. Dedov, I.I. Moiseev, *Russ. J. Inorg. Chem.* 54 (2009) 664–667.
- [118] G.D. Nipan, A.S. Loktev, K. V. Parkhomenko, S.D. Golikov, A.G. Dedov, I.I. Moiseev, *Dokl. Phys. Chem.* 448 (2013) 19–22.
- [119] E.R. Stobbe, B.A. de Boer, J.W. Geus, *Catal. Today* 47 (1999) 161–167.

- [120] Z.-C. Jiang, L.-B. Feng, H. Gong, H.-L. Wang, Methane and Alkane Conversion Chemistry, Springer US, New York, 1995.
- [121] N. Anacleto, O. Ostrovski, S. Ganguly, *ISIJ Int.* 44 (2004) 1615–1622.
- [122] C.A. Jones, J.J. Leonard, J.A. Sofranko, *J. Catal.* 103 (1987) 311–319.
- [123] P. Cho, T. Mattisson, A. Lyngfelt, *Fuel* 83 (2004) 1215–1225.
- [124] S. Rebsdat, D. Mayer, *Ullmann's Encycl. Ind. Chem.* 13 (2012) 547–572.

Paper 1

Thermal Reaction Analysis of Oxidative Coupling of Methane

Hamid Reza Godini^{1,*‡}, Vinzenz Fleischer^{2,‡}, Oliver Görke³, Stanislav Jaso¹, Reinhard Schomäcker^{2,*}, Günter Wozny¹

DOI: 10.1002/cite.201400080

Dedicated to Prof. Dr. Manfred Baerns on the occasion of his 80th Birthday

For more than three decades, the oxidative coupling of methane (OCM) process has been investigated as a promising alternative approach for ethylene production. Simulations of different sets of surface mechanisms over the $\text{Na}_2\text{WO}_4/\text{Mn}/\text{SiO}_2$ catalyst and the gas phase reactions that come along with the OCM reaction were analyzed in a fixed-bed, membrane, and fluidized-bed reactor. The results were compared with the experimental data generated in an OCM mini-plant. It was observed that the gas phase reactions are crucial in reducing the overall selectivity, especially in the fluidized-bed reactor.

Keywords: Gas phase reactions, Oxidative coupling of methane, Reaction kinetic, Reaction network, Reactor design, Thermal reaction engineering

Received: May 28, 2014; revised: August 12, 2014; accepted: August 15, 2014

1 Introduction

Global ethylene production capacity was over 140 million ta^{-1} in 2013 [1]. Depending on the easier access to various hydrocarbon resources and their local prices, different feedstocks are exploited for producing ethylene in different parts of the world. For instance, in Asia-Pacific and in Western Europe, where around half of the world ethylene-production facilities are located, mainly naphtha is used as the feedstock of cracking processes while in North America and the Middle East, accounting for 40 % of the global ethylene production, mainly ethane and natural gas are used as the feed for crackers. In general, ethane and natural gas are becoming the dominant feedstock for ethylene production. This is part of a major trend to substitute the oil-based feedstocks by natural gas for producing chemicals, especially in the US after the shale gas revolution. Oxidative coupling of methane (OCM) uses methane as the main component of natural gas to directly produce ethylene. This highlights the significance of the OCM process in this trend.

The systematic research on the OCM process started in DOW Chemical in the early 80s and the first report was published by Keller and Bhasin [2]. Since then and during the last three decades, several catalysts and reactor concepts have been proposed for OCM [3–5]. Pioneering work by Prof. Baerns and his research groups at Ruhr-Universität Bochum and later at the Institute of Applied Chemistry Adlershof and Fritz Haber Institute of the Max Planck Society Berlin are considered to be fundamental and vital for OCM research in the last three decades [6–8]. UniCat (Unifying Concepts in Catalysis, www.unicat.tu-berlin.de), a research group coordinated by the Berlin Institute of Technology and funded by the German Research Foundation (Deutsche Forschungsgesellschaft), also has the honor of his associated membership and benefits from his expertise in the field of OCM.

Further advancing the understanding of the OCM reaction mechanism and improving the performance of the OCM catalyst, reactor and process have been the main motives of Prof. Baerns and UniCat's OCM research group. In this paper, the issue of the selectivity is addressed in the context of catalyst and reactor performance analysis with the view on the OCM reaction mechanism. The effect of homogeneous gas phase reactions and catalytic activity in different reactors are investigated in details.

1.1 Reaction Mechanisms and Important Aspects

In the early eighties, Lunsford and co-workers showed that the methyl radical formation by hydrogen abstraction and radical coupling are the fundamental mechanisms of the

¹Dr. Hamid Reza Godini (hamid.r.godini@mailbox.tu-berlin.de), Dr. Stanislav Jaso, Prof. Günter Wozny, Berlin Institute of Technology, Chair of Process Dynamics and Operation, Straße des 17. Juni 135, Sekr. KWT-9, 10623 Berlin, Germany; ²Vinzenz Fleischer, Prof. Reinhard Schomäcker (Schomaecker@tu-berlin.de), Berlin Institute of Technology, Institute for Technical Chemistry, Straße des 17. Juni 124, 10623 Berlin, Germany; ³Dr. Oliver Görke, Berlin Institute of Technology, Department of Ceramic Materials, Institute for Material Science and Technologies, Hardenbergstraße 40, 10623 Berlin, Germany.

‡First and second author contributed equally to this paper.

OCM reaction [9]. There are some macro [7, 10, 11] and micro-kinetic models [12–15] that combine methane activation via adsorbed oxygen, methyl radical formation, coupling, oxidation of methane and the products, reforming, and dehydrogenation reactions to represent the OCM reactions network.

An OCM kinetic model should consider the contribution of both gas phase and catalytic reactions in order to predict the methane conversion and product selectivity. The major challenge, however, is to determine the kinetic parameters for the modeling of the surface reactions, which are strongly influenced by the gas phase contribution.

Dooley and co-workers published an extended micro-kinetic mechanism of the methane oxidation in homogeneous gas phases [16]. However, simulations with the Dooley model and comparing the results with the experimental data enable predicting the conversion and selectivity with high accuracy [17]. Therefore, this model was used here in the simulation part of this investigation to represent the gas phase contributions to the OCM reaction [16].

1.2 Limitations of Catalyst, Reactor and Operating Conditions

The OCM net energy balance is highly exothermic and with increasing conversion of methane, the operating temperature continually increases until the temperature gradient between the reaction temperature and the temperature in the external surrounding environment becomes high enough to transfer the excess generated heat out of the catalytic bed. Approaching the reactor end, both methane and oxygen (in reactors with co-feeding structure) are progressively consumed and the operating temperature decreases.

Being able to control the reactor's operating temperature not only secures a safe reactor operation, but also improves the reactor performance in terms of selectivity and yield of ethylene. This is mainly because of the crucial effect of temperature on gas phase reactions. Significance of the effect of gas phase reactions [18–21], however, is different in different reactor feeding policies. Therefore, choosing a proper reactor and set of operating conditions can significantly enhance the OCM reactor performance with respect to all these aspects.

A wide range of the reactor concepts has been proposed for the OCM application. Each type of reactor offers an advantage with respect to one or some of the OCM reactor performance indicators. Usually the fixed-bed reactor is considered to be a standard reactor concept and offers a simple construction and operation in industrial-scale operation. Although this is not completely the case for the OCM reactor, it is reasonable to investigate the performance of a fixed-bed reactor for the OCM reaction. On the other side, fluidized-bed reactors seem to be one of the advantageous and ultimate choices for the OCM reaction unit due to their isothermal performance [22–24].

It is also a fact that low concentrations of oxygen are advantageous for high C₂ selectivity [25–27]. The partial

pressure of oxygen can be reduced by either a diluted gas stream or an inorganic membrane to distribute the oxygen along the bed and keeping its local concentration low. This is the operating concept of the OCM membrane reactor. Among the membrane reactor structures applied for the OCM reaction so far, the porous packed-bed membrane reactor (PBMR) offers a fine oxygen-dosing potential and provides a proper permeation and contact-volume ratio. Therefore, it allows achieving a significant amount of methane conversion which ensures a high level of C₂ yield.

The performance of the fixed-bed [28, 29], fluidized-bed [23, 24] and membrane reactors [29–32] for OCM were experimentally investigated in UniCat's OCM mini-plant. The observed performances will be discussed here based on the mechanisms of the OCM reaction simulated with the detailed micro-kinetic model. Obviously, this analysis will be performed in the context of the whole OCM process analysis. For instance, injecting an inert diluting gas such as nitrogen, which is prescribed to overcome the challenge of hot spot formation in the fixed-bed catalytic reactor, will itself increase the costs of down-stream units markedly.

Performing current experimental and model-based analysis aims to assess the contribution of gas phase reactions on the OCM reactor performance. A simplified catalytic model which represents a solely radical generation mechanism is exploited in this analysis as a key tool.

2 Experimentation

The performed experimental activities in this investigation are briefly reported here. The catalyst preparation and characterization have been described elsewhere in details [33].

The Na₂WO₄/Mn/SiO₂ catalyst has shown a promising potential [34–38] and was used in the experimental part of this project. In most of the reports, this catalyst has been prepared by the incipient wetness impregnation method according to the reported recipe by Wang et al. [35]. Detailed experimental aspects for testing the Na₂WO₄/Mn/SiO₂ catalyst in fluidized-bed, fixed-bed and membrane reactors have also been provided in our previous publications [23, 24, 31].

2.1 Experimental Setup

The original 600 mm long tubular α -alumina microfiltration membrane was purchased from Fraunhofer Institute for Ceramic Technology and has a 7 mm inner diameter (ID), 1.5 mm thickness and 3 μm average pore size. This commercially available membrane was coated with glassy materials (BOTZ) to provide the desired permeation range of 1–15 $\text{cm}^3\text{cm}^{-2}\text{min}^{-1}\text{bar}^{-1}$ [31]. The modified ceramic membrane is implemented inside the metal reactor module and separates the shell side with the inner diameter of 20 mm

and the tube side with the outer diameter (OD) of 10 mm. Inside the ceramic membrane, a WIKA k-type multipoint thermocouple (with 3 mm OD stem) is located along the reactor, which enables measuring the reaction temperature in 10 points.

The temperature of the fluidized-bed reaction zone was also recorded via multipoint thermocouple in 8 points. In the fluidized-bed reactor setup the operating temperature can be controlled in the range of 10 K deviation along the bed. It has a 40 mm inner diameter. The block-flow diagrams of the reactor setups are shown in Fig. 1.

The membrane reactor module was implemented inside an electrical tubular furnace where the operating temperature is varied using a two-zone electrical heating. Two separate thermocouples are located behind the metal shield inside the furnace and measure the temperatures in each zone of the furnace. By assigning the set points to these temperatures and controlling them, the heat duty of each electrical heating element is tuned. Therefore, the applied high-frequency on/off heating/non-heating mechanism in

this furnace allows controlling the temperature along the reactor. A similar split tubular furnace was used for the fluidized-bed reactor. It should be highlighted that the recorded operating temperature inside the catalytic bed is affected mainly by two factors, namely 1) the reaction rate and chemically generated heat, and 2) the value of the set temperature in the surrounding electrical tube furnace (TW) [32]. The second factor also affects the reaction rate inside the catalytic packed bed. The values of the applied temperature of the electrical heaters, the set points and the measured values of the feed flow rates and operating pressures were set and monitored online.

An IR gas analyzer monitors the concentration of ethylene, ethane, methane, carbon dioxide, and oxygen in the reactor outlet gas stream. The precision of the measurements performed using the IR gas analyzer was confirmed using GC sampling. Having considered the precision of the measurements and control devices, the observed selectivity, conversion and yield in average have $\pm 10\%$ margin of error in reference to their reported values in this paper.

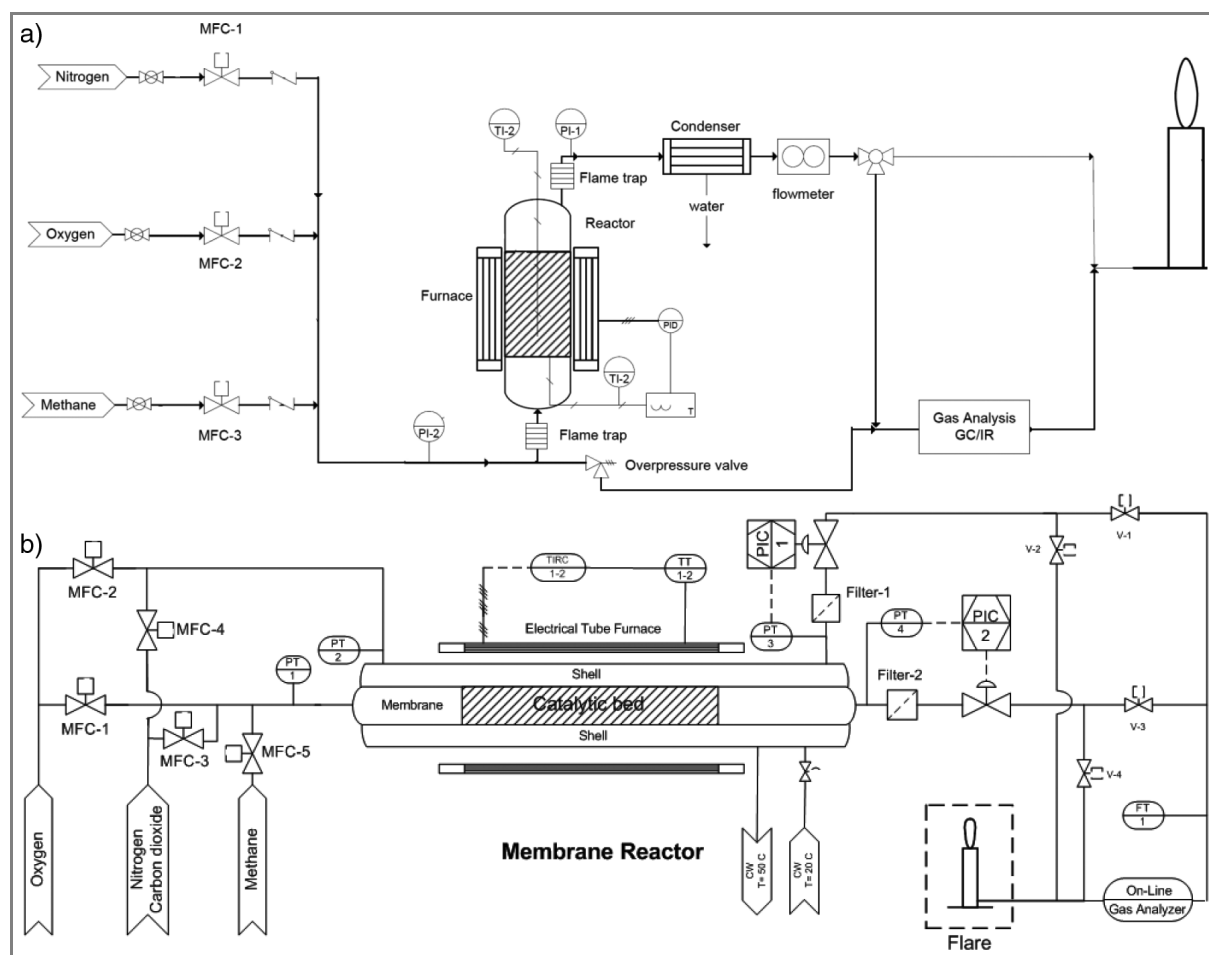


Figure 1. The block-flow diagram of the investigated reactor setups; (a) fluidized-bed reactor setup; (b) fixed-bed and membrane reactor setup.

3 Model-Based Analysis

A comprehensive micro-kinetic model of the $\text{Na}_2\text{WO}_4/\text{Mn}/\text{SiO}_2$ catalyst has been published by Lee and coworkers [39]. This mechanism represents two adsorption steps and 14 surface reactions. However, the residual of each kinetic parameter (uncertainty for calculating the value of parameters) is between 0.33–1. This is due to the fact that not considering the gas phase reactions leads to substantial errors and the conclusion that the effect of gas phase reactions should be included in the kinetic model. On the other hand, the mechanism suggested by Dooley et al. includes 269 species and 1583 reactions and efficiently represents the gas phase reactions.

In this research, a semi-empirical micro-kinetic surface reaction model of three reaction steps (Tab. 1) is proposed as a constant source for methyl radical formation to represent the catalytic surface reaction, which can interact with the gas phase reactions along the reactor.

Table 1. Pseudo micro-kinetic for surface reactions to describe the generation rate of methyl radicals.

No.	Reaction step	$k_{\text{pre}} [\text{s}^{-1}]$	$E_A [\text{kJ mol}^{-1}]$
1	$\text{O}_2 + 2 \text{V}^* \rightarrow 2 \text{O}^*$	$3 \cdot 10^6$	40
2	$\text{CH}_4 + \text{O}^* \rightarrow \text{CH}_3^{\bullet} + \text{OH}^*$	$3 \cdot 10^5$	120
3	$2 \text{OH}^* \rightarrow \text{H}_2\text{O} + \text{O}^* + \text{V}^*$	$3 \cdot 10^6$	40

Considering dummy thermodynamic data and the reaction order of zero for oxygen enable the assumption of the steady state conditions at the catalyst surface and neglecting the influence of the generated heat at the catalyst surface on the adsorption processes. Kinetic properties were chosen in a way that the reoxidation (rate equations 1 and 3 in Tab. 1) is not limited and it is considered to be much faster than the methane activation. This reduced surface model allows the simulation of an ideal catalyst which enables analyzing the effects of gas phase reactions. The relative rates of the gas phase and surface reactions and their dependency on the operating temperature and activity of catalyst has been investigated before [40]. There, it has been reported that the methyl radical generation over the catalyst surface is a strongly temperature-dependent reaction and is dramatically slower than the temperature-independent radical coupling reaction in the gas phase.

Pre-exponential factors and activation energies reported in Tab. 1 were fitted to predict the performance of the fixed-bed reactor. For accurate modeling, both the thermal and reaction performance indicators were exploited to determine the kinetic parameters. For instance, it was tried to capture the observed axial temperature profiles of the fixed-bed and membrane reactor in the simulation. No radial profile was considered, because no adequate experimental data with regard to the radial temperature profile were available. Moreover, enormous amounts of numerical calculations are

required in the case of using two-dimensional models which leads to a long time simulation. Side reactions on the reactor wall and on the quartz granulates were neglected, since they have been found to be negligible also in former experiments [31]. The specific surface area was set to $2 \text{ m}^2 \text{ g}^{-1}$ for the catalyst, which is consistent with the BET analysis of this catalyst [33]. The number of active centers was set to $4 \text{ O}^* \text{ nm}^{-2}$, which is in the range of reported values for various supported oxidation catalysts [41, 42].

The software Reaction design Chemkin was used for the simulation. Pressure drop was calculated by the Ergun equation for the fixed-bed and membrane reactors. The Reynolds number for the reactor was calculated to be around 5700, indicating a turbulent flow regime. Considering these facts makes it possible to simulate the fixed-bed reactor with the PFTR (Plug Flow Tubular Reactor) model.

Simulations of the membrane reactor were carried out by dividing the reactor into a system of 7 equal PFTR's, following the same assumptions as mentioned for the fixed-bed reactor. Between each PFTR pair, a zero dimensional mixer with an oxygen inlet was placed, as oxygen source and for representing the membrane reactor. The fluidized-bed reactor was modeled by a CSTR (Continuous Stirred-Tank Reactor) model which advocates an isothermal performance. All reactor and catalyst properties were kept for simulations as they were in the experimentation.

4 Results and Discussion

In the context of this research, the observed performance of OCM reactors in miniplant-scale operation, especially the effects of methane-to-oxygen ratio and gas dilution in all three reactors, were analyzed.

Increasing the methane-to-oxygen ratio usually increases the C_2 selectivity mainly because of reducing the partial pressure of oxygen in the reaction mixture. Such a trend is typical as shown in Fig. 2 for the co-feed as well as the oxygen dosing reactors. Nevertheless, using inert gas dilution reduces the partial pressure of both oxygen and methane in the gas phase and therefore also reduces the rates of the undesired gas phase reactions. Using a proper amount of gas dilution also can improve the OCM reactor performance as a result of establishing a better thermal operation. Here, it is attempted to distinguish between these thermal and reaction effects. This can be achieved by analyzing the effects of dilution in fixed-bed, membrane, and isothermal fluidized-bed reactor. Special attention is devoted to highlight the effect of dilution on the intensity of gas phase reactions in an OCM reactor. For instance, under the isothermal performance of the OCM fluidized-bed reactor, it has been observed that introducing higher amounts of nitrogen significantly affects the reactor performance by improving the C_2 selectivity and suppressing the undesired gas phase reactions [24].

In all cases, nitrogen dilution significantly enhances the C_2 selectivity. Therefore, usually the lowest C_2 selectivity is

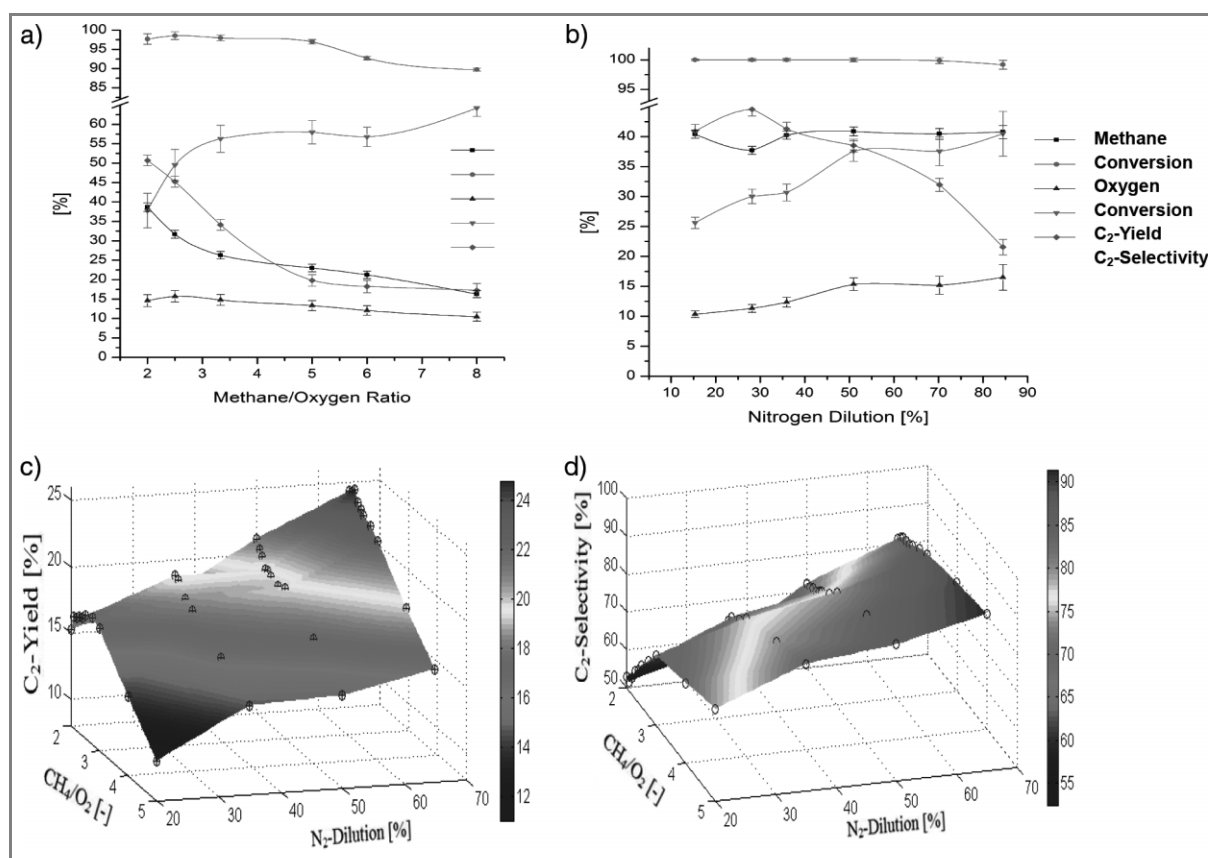


Figure 2. Effect of gas dilution on the performance of the investigated reactors; (a, b) fluidized-bed; (c, d) membrane reactor.

achieved when the lowest nitrogen dilution and methane-to-oxygen ratios are employed. In the case of membrane and fixed-bed reactors, however, the effects of dilution (using excess methane or nitrogen dilution) are coupled with the thermal heat transfer effect.

In an OCM membrane reactor, as is seen in Fig. 2, despite of the observed moderate reduction in methane conversion, C_2 yield usually is improved by increasing the nitrogen dilution. By increasing the methane-to-oxygen ratio in a membrane reactor, C_2 yield usually is decreased due to the reduction in both methane conversion and operating temperature. Therefore, as has been demonstrated in Fig. 2c, due to the thermal effect of gas dilution (using excess methane or nitrogen dilution), the trend of C_2 yield might show a local maximum in membrane reactor operation.

It can be generally concluded that the quantitative impact of the inert dilution on improving the C_2 yield in the OCM reactor depends on the current range of C_2 -selectivity, the intensity of the generated reaction heat and the possibility to control the reaction temperature and maintain the desired level of methane conversion. The last thermal factor is not reflected in the isothermal fluidized-bed reactor.

Similar trends were observed for the performance of the $\text{Sr-La}_2\text{O}_3/\text{CaO}$ catalyst in a fluidized-bed reactor but with

lower C_2 selectivity and yield. Beside these two important stable catalysts, many other types of OCM catalysts have been reported in literature. For instance, LiMgO catalyst has been used in several experimental researches. However, this catalyst and most of other catalysts so far reported for OCM have not proven to be stable enough for continuous industrial application.

4.1 Simulation Results

After reviewing the experimental observations, it is tried to distinguish these aspects in the model-based analysis of the OCM performance in the different reactors based on different sets of catalytic and gas phase reactions. All obtained experimental and simulation results are shown in Tab. 2.

Here, X , Y , S represents the conversion, yield and selectivity, respectively. All experimental data were selected at similar methane conversion for better comparison. Two major differences between these reactor types are the mixing behavior and the oxygen feeding policy. On the one hand, the turbulent gas fraction is responsible for a well-mixed isothermal fluidized bed reactor. On the other hand, a lower void-fraction in the fixed-bed or membrane reactor results in local mixing and non-uniform temperature distribution.

Table 2. Comparing the observed performances of various reactor types and their simulation results to identify the contributions of the gas phase and surface reactions.

Reactor	Parameter	Exp. result	Dooley Mech.	Dooley + Lee	Dooley + semi-emp.
Membrane reactor	X_{CH_4}	0.33	≈ 0	≈ 0	≈ 0
	S_{C_2}	0.65	0.55	0.99	0.99
	S_{CO_x}	0.35	0.45	0.01	0.01
Fixed-bed reactor	X_{CH_4}	0.32	0.01	0.02	0.34
	S_{C_2}	0.53	0.99	0.65	0.56
	S_{CO_x}	0.47	0.01	0.35	0.44
Fluidized-bed reactor	X_{CH_4}	0.35	0.29	0.29	0.30
	S_{C_2}	0.40	0.14	0.11	0.12
	S_{CO_x}	0.60	0.86	0.89	0.88

This also means that more space is available for the gas phase reactions in the fluidized-bed reactor. Furthermore, the initial partial pressure of oxygen is relatively higher for the fixed-bed and fluidized-bed reactor in comparison to its low value in the membrane reactor. These differences can explain the following observations.

The experimental data show a higher C_2 selectivity in the membrane reactor in comparison to the fluidized-bed reactor. All different models describe this trend with different accuracy. Simulations of the fixed-bed and membrane reactor with the Dooley mechanism alone (gas phase) show very low methane conversion in comparison to the fluidized-bed reactor. For the fluidized-bed reactor, significant combustion products were predicted. This is the first indication of dominant gas phase side reactions for this reactor due to its high initial oxygen concentration and a totally mixed system.

The combination of gas phase reactions and the micro-kinetic model for the catalyst surface reported by Lee et al. shows more complicated results. Simulation results for the membrane reactor in this case show no methane conversion. This is mainly due to the presence of high amounts of nitrogen, which results in an extremely low oxygen partial pressure, low space for the gas phase reactions and a short residence time. This is an indication that the membrane reactor model has a strong quenching behavior. The high amount of nitrogen and low oxygen partial pressure prevent any reactions in the gas phase and consequently over the catalyst surface. Testing the initial conditions for the fixed-bed reactor in this case also showed no methane and oxygen conversion. For the fixed-bed reactor the precise prediction of methane conversion and C_2 selectivity was not possible via the model-based analysis using the aforementioned model combination. Moreover, the C_2 selectivity for the simulated fluidized-bed reactor drops slightly in comparison to the case where a pure gas phase model was used. This is due to the effect of catalytically formed ethane and/or ethylene which are less stable than methane and might be oxidized by gas phase reactions. The oxidation of the formed

methyl radicals may also be a plausible reason for these observations.

Implementation of the Dooley gas phase reaction network and the simple micro-kinetic surface reaction model reported in Tab. 1 show a similar situation for prediction of conversion and selectivity in all reactor types. It is seen that the proposed simple micro-kinetic surface reaction model is at least as good as the model which used the detailed gas phase and surface micro-kinetic reported by Lee et al. In case of the membrane reactor, the observed performance indicators are not different from the other model-based analysis. Therefore, it can be concluded that the observed very low values of methane conversion are due to the quenching behavior of this system.

A detailed prediction of the reaction progress in terms of methane conversion and C_2 selectivity for the fixed-bed reactor is shown in Fig. 3. The proposed simplified model predicts the methane conversion and C_2 selectivity for the fixed bed reactor very satisfactorily. Its prediction potential in this case is better than the model proposed by Lee et al. The C_2 selectivity at the reactor inlet is very high and drops constantly as methane and oxygen conversion increase along the reactor, while CO_x selectivity increases. The products of the gas phase reactions in this case determine the performance of the fluidized-bed reactor and the accuracy of the selectivity is not similarly high.

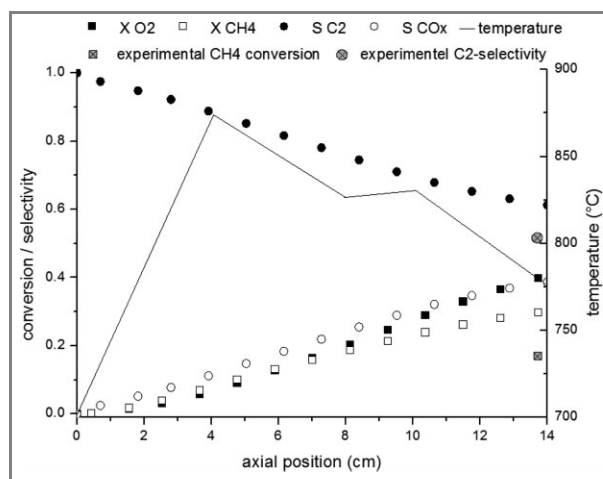


Figure 3. Prediction of the reaction-progress in the fixed-bed reactor using the gas phase model and pseudo surface kinetic model with measured temperature profile ($3 \text{ nmL s}^{-1} \text{ N}_2$; $2 \text{ nmL s}^{-1} \text{ CH}_4$; $1 \text{ nmL s}^{-1} \text{ O}_2$; 3.5 g catalyst; 3.5 g inert quartz).

The fluidized-bed reactor shows significant contribution of the gas phase reactions in all three models. This is especially highlighted in the simulation results based on the

pure gas phase reactions. Including the surface kinetic models into the model also shows similar results. The simulation results of the fixed-bed reactor show relatively low gas phase reactivity. Including the surface reactions in this simulation in the form of the proposed simple micro-kinetic model results in an acceptable prediction of the methane conversion and C₂ selectivity. For the case of membrane reactor, which has the lowest gas phase reactivity, all models fail to predict the experimental results. All these facts lead to the conclusion that there is a very complex situation at the surface of OCM catalysts, which cannot be easily described by a standard model and considering a single active site. In fact, catalytic activity can be divided into two parts. This follows the idea of Ahari et al. [43], which is presented in Fig. 4.

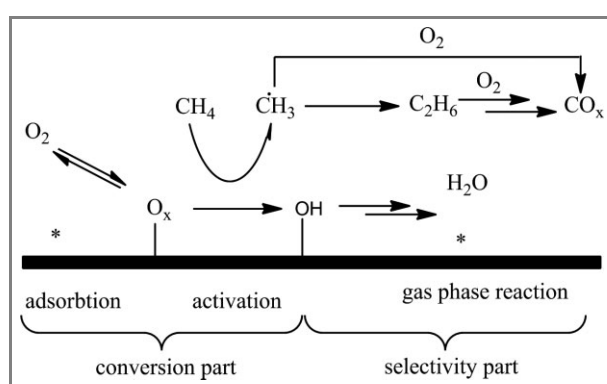


Figure 4. Scheme of the OCM surface reaction mechanism [43].

On one hand, the activity and conversion rates correspond to Eqs. (1) and (2) in Tab. 1. On the other hand, the selectivity is dominated by deep oxidation mechanisms over the catalyst surface and the methyl radical coupling process in the gas phase. Both of these interactive phenomena together are responsible for product formation. After this step, the product is completely decoupled from the catalytic system and follows the basics of thermodynamics and kinetics of gas phase reactions. Improving the yield can only be achieved by controlling these phenomena.

The first part of the catalytic cycle is started by the fundamental phenomenon of adsorption. In all kinetic models, the molecular oxygen is adsorbed and interacts directly with an active center of the catalytic material. The newly formed species are responsible for methane activation as well as deep oxidation processes over the surface. The stoichiometry of the active oxygen species is set to molecular or atomic oxygen, but still unclear. In our previous paper, it was shown that a more complex adsorption phenomenon takes place on the Na₂WO₄/Mn/SiO₂ catalyst. It was shown that two different oxygen species determine the type of catalytic activity. On the one hand, there is a weakly bound oxygen species, which is responsible for deep oxidation reactions. On the other hand, there is a stronger adsorbed species, which activates methane in a selective way [44].

This fact makes it clear that the characteristics of oxygen adsorption play a crucial role on the surface activity. However, another parameter is the number of active sites. It is very difficult to determine this number, since it requires identification as well as the quantification.

The methane activation process follows the properties of the different adsorbed oxygen species at the catalyst surface. Right at this point, each of the investigated reactors will be differently affected by this behavior because of the different oxygen dosing strategies. The membrane reactor has an excess of nitrogen in the axial inlet position. The oxygen partial pressure increases along the axial position and promotes more and more oxygen adsorption. In the fixed-bed reactor, the initial oxygen partial pressure is on its maximum and drops by catalytic and gas phase reactions. At the end of the reactor, the oxygen adsorption limits the catalytic activity. For the fluidized-bed reactor, the situation is totally different. The strong mixing of reactants and products in this reactor provides an almost constant partial pressure of oxygen in the whole volume.

The second point is that the selectivity is controlled in the beginning by the process of coupling of methyl radicals in competition to the methane combustion reaction. This step can later be influenced by the adsorbed oxygen, which leads to deep oxidation of the products. Besides observing these surface phenomena, the same situation is present in the gas phase. In addition to this point, each reactor system influences this sensitive reaction network also by different contributions of void fractions and oxygen dosage. In the membrane reactor the coupling process is the dominant step in the gas phase. The deep oxidation takes place at the catalyst surface. In contrary, the fluidized-bed reactor provides a lot of gas phase oxygen which makes it easier to follow the route of products combustion in the gas phase reactions network. This is clearly shown according to the simulation results reported in Tab. 2 and Fig. 3 where the fluidized-bed reactor model using only Dooley's mechanism, which represents only the gas phase reactions, shows a high level of methane conversion and a very low level of selectivity. The predominant process can be recognized from Fig. 3. Here it can be explained that the formation of ethane is secured via coupling of methyl radicals. This step is later followed by combustion processes as higher conversions and lower selectivity are obtained.

The reaction routes in the fixed-bed reactor change over the length. At the inlet of this reactor, the coupling process dominates to provide a high selectivity at low conversions, which changes with the formation of thermodynamically less stable products like ethane and ethylene. Along with intensive methyl radical coupling, the C₂-products are exposed to the gas phase reaction network. The easier activation of ethane compared to methane plays the major role now and starts facilitating the competitive oxidation. As a result of this situation, further oxidation of ethylene is also encountered, ending with the significant concentration of deeply oxidized products. At this point, the simple micro-

kinetic surface mechanism shows already that the gas phase reactions significantly contribute to the CO_x production since no deep oxidation reactions are included in this model. Beside the effect of oxygen partial pressure, temperature also has the strongest influence on this network (Fig. 5).

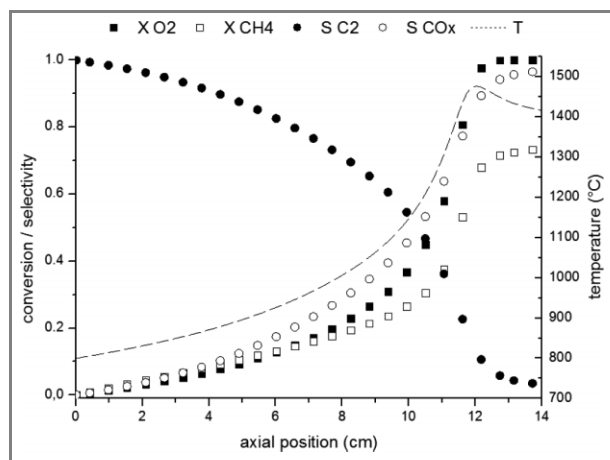


Figure 5. Reaction progress of the fixed-bed reactor with the gas phase model and simple micro-kinetic surface model by solving the free energy equation (hot spot formation) with the initial temperature of 800 °C (3 nmL s⁻¹ N₂; 2 nmL s⁻¹ CH₄; 1 nmL s⁻¹ O₂; 3.5 g catalyst; 3.5 g inert quartz).

The initial feed temperature was set to 800 °C and the heat transfer potential was not considered in the model. This scenario leads to a hot spot formation. The combustion of alkanes strongly increases the local heat formation. At this point, the reaction system favors the combustion routes, which is accelerating itself. It should be emphasized, however, that the selectivity is affected by the level of hot spot and conversion.

The membrane reactor quenches most of the gas phase steps, as shown in the simulation. Reviewing the reported data in Tab. 2 for the model which uses Dooley mechanism shows no gas phase activity, which is due to quenching effect. This is the main explanation for the highest observed C₂ selectivity in the experiments. The fluidized-bed reactor shows significant potential for the gas phase reactivity, which was reflected in the experimental and simulation results as the high selectivity towards deep oxidation products. For the fixed-bed reactor, the fraction of C₂ products causes more combustion products, because the gas phase oxidation has a strong influence at the outlet, but shows a minor oxidation potential at the reactor entrance where more stable reactants exist.

It became clear that oxygen adsorption, activation phenomena, and the gas phase reaction network influence each other strongly, which limits the methane conversion as well as the C₂ selectivity. This becomes most evident by the fact that a simple methyl radical formation mechanism in combination with a comprehensive gas phase model predicts

most of the observed results in three different reactors in a satisfactory way.

It can be clearly concluded that the reactor design has a strong influence on the ratio of gas phase and catalyst contributions. In order to overcome the yield limitation, as a consequence of restricted conversion and declining selectivity, the reactor engineering should clearly be the main focus of the further OCM process development.

4.2 Limitations of Kinetic Modeling

The simplified model implemented in this research consists of an individual surface-activation step and several gas phase reactions and was clearly able to predict the general trends of the reactor performance. As a result, it was highlighted how important it is to consider the contribution of the gas phase reactions and it became clear that the gas phase chemistry is not only a minor side reaction, but an essential part of the main reaction path. However, this is only a first step and further detailed mechanisms and interactive effects should be considered in order to improve the predicting potential of kinetic models.

The used minimal surface mechanism is not complete, but due to the lack of data and considering the nature of consecutive reactions, they have not been included in this simulation. The modeling approach in this manuscript is completely different from the ones reported in literature. Here, it was aimed to see how the contribution of the gas phase reactions can be predicted using this simplified model. Another aim is the identification of missing steps in the surface model.

For instance, the Lee mechanism has several surface species included, but shows only low activity, which indicates the restrictions with regard to predicting the activation of hydrocarbons. This fact makes it clear that this micro-kinetic model does not cover all necessary reactions steps or its kinetic parameters have not been determined adequately.

Moreover, the implemented simplified model in this research fails to predict the performance of the reaction atmosphere with low partial pressure of oxygen because of too low values of oxygen binding parameters of the surface of the catalyst. These values should be properly tuned in order to ensure realistic levels of catalytic activation of all involved species.

Another aspect which should be considered is the formation of hydrogen or carbon deposition, as was observed in our experiments. However, similar to several other available kinetic models [10, 11], these aspects have not been considered in the modeling due to difficulty of establishing the full mass balance of the species in separate streams.

4.3 General Thermal Engineering Observations

In the context of OCM reactor engineering, it is not an exaggeration to claim that the thermal engineering remains to be the main challenging task in designing an efficient OCM reactor. It can be concluded that due to the applied heating/non-heating procedure in the electrical furnace, the cooling effects of the inert gas dilution might not be completely tracked down in the observed experimental trends. Most of the experimental studies reported for the OCM reactors so far have also been performed using electrical furnaces and have exploited similar mechanism to control the thermal performance of the OCM reactors. Therefore, in the reported trends of the reactor performance indicators in these cases, also the effect of changing the reaction temperature is not clearly separable from the effect of introducing the inert dilution. This thermal control mechanism acts like implementing a constant reactor wall policy. In case of implementing a constant heat flux, this effect will be better highlighted and distinguished. However, this procedure also has its own limitations and in any types of the applied control mechanisms using electrical furnaces, there is a need for fine-tuning the frequency of the electrical power to maintain a stable thermal and reaction performance in the OCM membrane reactor.

The procedure of heating also has a crucial impact on the reactor performance. In order to clarify this, the thermal reaction performance of the OCM reactor was investigated under the co-feeding scenario. It was observed that when the operating temperature is rising, the C₂ yield and C₂H₄ yield are also rising up to a certain level. In this experimentation, even a C₂ yield of 29.5 % and a C₂H₄ yield of 23.6 % were temporarily recorded. After a short time, the yield decreases again. This is assumed to be closely related to the rate of methyl radical generation over the surface of the OCM catalyst and the intensifying combustion effect in the gas phase due to temperature rise. This phenomenon was observed repeatedly in numerous experiments.

5 Conclusions

According to the performed experimental and model-based analysis, it was shown that the proposed simple microkinetic surface model coupled with a comprehensive gas phase model is capable of predicting the performance of a fixed-bed and a fluidized-bed reactor with the same precision as a detailed formal kinetic model does.

The fraction of weakly or strongly adsorbed oxygen over the catalyst surface is a crucial factor for the selectivity. Oxygen feeding policy plays an important role in this regard. For instance, in the membrane reactor where the oxygen partial pressure increases gradually along the bed, more oxygen adsorption and possibly stronger adsorption will be observed at the end of reactor. It is opposite to the case of the co-feed fixed-bed reactor. At the front end of the fixed-

bed reactor, weak oxygen adsorption limits the catalytic selectivity. In the fluidized-bed reactor, however, a significant portion of gas phase reactions is responsible for the observed low selectivity.

Acknowledgment

The authors acknowledge the financial support from the Cluster of Excellence „Unifying Concepts in Catalysis“ coordinated by the Technische Universität Berlin and funded by the German Research Foundation (Deutsche Forschungsgemeinschaft).

References

- [1] W. R. True, *Oil Gas J.* **2013**, *111* (7).
- [2] G. Keller, M. Bhasin, *J. Catal.* **1982**, *73*, 9–19.
- [3] E. Kondratenko, M. Baerns, in *Handbook of Heterogeneous Catalysis*, Wiley-VCH, Weinheim **2008**, 3010–3023, Ch. 13.17.
- [4] U. Zavyalova, M. Holena, R. Schlögl, M. Baerns, *ChemCatChem* **2011**, *3*, 1935–1947.
- [5] K. Langfeld, B. Frank, V. E. Strempel, C. Berger-Karin, G. Weinberg, E. V. Kondratenko, R. Schomäcker, *Appl. Catal., A* **2012**, *417*, 145–152.
- [6] M. Baerns, in *Methane Conversion by Oxidative Processes: Fundamental and Engineering Aspects* (Ed: E. E. Wolf), Van Nostrand Reinhold, New York **1992**, 382–402.
- [7] Y. Stansch, L. Mleczko, M. Baerns, *Ind. Eng. Chem. Res.* **1997**, *36*, 2568–2579.
- [8] L. Mleczko, M. Baerns, *Fuel Process. Technol.* **1995**, *42*, 217–248.
- [9] D. Driscoll, J. Lunsford, *J. Phys. Chem.* **1985**, *89*, 4415–4418.
- [10] M. Daneshparyeh, A. Khodadadi, N. Mostoufi, Y. Mortazavi, R. Sotudeh-Gharebagh, A. Talebizadeh, *Fuel Process. Technol.* **2009**, *90*, 403–410.
- [11] T. P. Tiemersma, M. J. Tuinier, F. Gallucci, J. A. M. Kuipers, M. V. S. Annaland, *Appl. Catal., A* **2012**, *433*–434, 96.
- [12] J. W. Thybaut, J. Sun, L. Olivier, A. C. Van Veen, C. Mirodatos, G. B. Marin, *Catal. Today* **2011**, *159*, 29–36.
- [13] P. N. Kechagiopoulos, J. W. Thybaut, G. B. Marin, *Ind. Eng. Chem. Res.* **2014**, *53*, 1825–1840.
- [14] M. Y. Sinev, Z. T. Fattakhova, V. I. Lomonosov, Y. A. Gordienko, *J. Nat. Gas* **2009**, *18*, 273–287.
- [15] Y. Simon, F. Baronnet, P.-M. Marquaire, *Ind. Eng. Chem. Res.* **2007**, *46*, 1914–1922.
- [16] S. Dooley, M. P. Burke, M. Chaos, Y. Stein, F. L. Dryer, V. P. Zhukov, O. Finch, J. M. Simmie, H. J. Curran, *Int. J. Chem. Kinet.* **2010**, *42*, 527–549.
- [17] S. Mavlyankariev, *Ph.D. Thesis*, Technische Universität Berlin **2013**.
- [18] H. Zanthonoff, M. Baerns, *Ind. Eng. Chem. Res.* **1990**, *29*, 2–10.
- [19] P. M. Couwenberg, Q. Chen, G. B. Marin, *Ind. Eng. Chem. Res.* **1996**, *35*, 415–421.
- [20] P. M. Couwenberg, Q. Chen, G. B. Marin, *Ind. Eng. Chem. Res.* **1996**, *35*, 3999–4011.
- [21] O. Korup, S. Mavlyankariev, M. Geske, C. F. Goldsmith, R. Horn, *Chem. Eng. Process.* **2011**, *50*, 998–1009.
- [22] U. Pannek, L. Mleczko, *Chem. Eng. Sci.* **1997**, *52*, 2429–2434.

- [23] S. Jaso, S. Sadjadi, H. R. Godini, U. Simon, S. Arndt, O. Görke, A. Berthold, H. Arellano-Garcia, H. Schubert, R. Schomäcker, G. Wozny, *J. Nat. Gas Chem.* **2012**, *21*, 534–543.
- [24] S. Jaso, *Ph.D. Thesis*, Technische Universität Berlin **2012**.
- [25] A. L. Y. Tonkovich, D. M. Jimenez, J. L. Zilka, G. L. Roberts, J. L. Cox, *Chem. Eng. Sci.* **1996**, *51*, 3051–3056.
- [26] A. Tota, D. Hlushkou, E. Tsotsas, A. Seidel-Morgenstern, in *Modeling of Process Intensification*, Wiley-VCH, Weinheim **2007**, 99–148, Ch. 5. DOI: 10.1002/9783527610600.ch5
- [27] L. Olivier, S. Haag, C. Mirodatos, A. C. van Veen, *Catal. Today* **2009**, *142*, 34–41.
- [28] S. Arndt, T. Otremba, U. Simon, M. Yildiz, H. Schubert, R. Schomäcker, *Appl. Catal., A* **2012**, *425*–426, 53–61.
- [29] H. R. Godini, A. Gili de Villasante, O. Görke, S. Arndt, U. Simon, A. Thomas, R. Schomäcker, G. Wozny, *Catal. Today* **2014**, *236*, 12–22.
- [30] H. R. Godini, H. Trivedi, A. Gili de Villasante, O. Görke, S. Jašo, U. Simon, A. Berthold, W. Witt, G. Wozny, *Chem. Eng. Res. Des.* **2013**, *91*, 2671–2681.
- [31] H. R. Godini, A. Gili de Villasante, O. Görke, U. Simon, K. Hou, G. Wozny, *Energy Fuels* **2014**, *28*, 877–890.
- [32] H. R. Godini, S. Xiao, M. Kim, N. Holst, S. Jašo, O. Görke, J. Steinbach, G. Wozny, *J. Ind. Eng. Chem.* **2014**, *20*, 1993–2002.
- [33] U. Simon, O. Görke, A. Berthold, S. Arndt, R. Schomäcker, H. Schubert, *Chem. Eng. J.* **2011**, *168*, 1352–1359.
- [34] X. Fang, S. Li, J. Lin, J. Gu, J. D. Yan, *J. Mol. Catal. (China)* **1992**, *8*, 255–262.
- [35] D. Wang, M. P. Rosynek, J. H. Lunsford, *J. Catal.* **1995**, *155*, 390–402.
- [36] S. Ji, T. Xiao, S. Li, C. Xu, R. Hou, K. S. Coleman, M. L. H. Green, *Appl. Catal., A* **2002**, *225*, 271–284.
- [37] A. G. Dedov, G. D. Nipan, A. S. Loktev, A. A. Tyunyaev, V. A. Ketsko, K. V. Parkhomenko, I. I. Moiseev, *Appl. Catal., A* **2011**, *406*, 1–12.
- [38] J. Y. Lee, W. Jeon, J.-W. Choi, Y.-W. Suh, J.-M. Ha, D. J. Suh, Y.-K. Park, *Fuel* **2013**, *106*, 851–857.
- [39] M. R. Lee, M.-J. Park, W. Jeon, J.-W. Choi, Y.-W. Suh, D. J. Suh, *Fuel Process. Technol.* **2012**, *96*, 175–182.
- [40] I. Machin, P. Pereira, V. de Gouveia, F. Rosa, *Prepr. Symp. – Am. Chem. Soc.* **1992**, *37*, 173–178.
- [41] M. V. Ganduglia-Pirovano, C. Popa, J. Sauer, H. Abbott, A. Uhl, M. Baron, D. Stacchiola, O. Bondarchuk, S. Shaikhutdinov, H.-J. Freund, *J. Am. Chem. Soc.* **2010**, *132*, 2345–2349.
- [42] B. Beck, M. Harth, N. G. Hamilton, C. Carrero, J. J. Uhrlrich, A. Trunschke, S. Shaikhutdinov, H. Schubert, H.-J. Freund, R. Schlögl, J. Sauer, R. Schomäcker, *J. Catal.* **2012**, *296*, 120–131.
- [43] J. S. Ahari, R. Ahmadi, H. Mikami, K. Inazu, S. Zarrinpashne, S. Suzuki, K. Aika, *Catal. Today* **2009**, *145*, 45–54.
- [44] B. Beck, V. Fleischer, S. Arndt, M. G. Hevia, A. Urakaw, P. Hugo, R. Schomäcker, *Catal. Today* **2014**, *228*, 212–218.

Paper 2



Oxidative coupling of methane—A complex surface/gas phase mechanism with strong impact on the reaction engineering



Benjamin Beck^a, Vinzenz Fleischer^a, Sebastian Arndt^a, Miguel González Hevia^b, Atsushi Urakawa^b, Peter Hugo^a, Reinhard Schomäcker^{a,*}

^a Technische Universität Berlin, Institut für Chemie, Straße des 17. Juni 124, 10623 Berlin, Germany

^b Institute of Chemical Research of Catalonia, Avgda. Països Catalans 16, 43007 Tarragona, Spain

ARTICLE INFO

Article history:

Received 13 July 2013

Received in revised form

14 November 2013

Accepted 23 November 2013

Available online 9 January 2014

ABSTRACT

The oxidative coupling of methane over Mn/Na₂WO₄/SiO₂ has been investigated at reaction conditions suitable for industrial applications up to 10 bar in a fixed bed reactor as well as by temporal analysis of products (TAP) by admitting pulses of methane, ethane and ethene oxygen mixtures. The influence of pressure on selectivity is investigated and a concept for optimizing it is derived. A maximum yield is estimated from the ratios of the involved main reactions of the reaction network assuming that the undesired parallel reactions can be suppressed.

© 2013 Elsevier B.V. All rights reserved.

Keywords:

Mn/Na₂WO₄/SiO₂

Oxidative coupling of methane

High pressure

Temporal analysis of products

Maximum yield

1. Introduction

Oxidative coupling of methane (OCM) to ethylene offers great industrial potential, because it would broaden the feedstock basis for chemical industry. Today crude oil derived olefins and aromatic hydrocarbons via steam cracking of naphtha are still the crucial raw materials for the majority of value added chains in chemical industry. The importance of alternative carbon sources for chemical processes becomes greater as oil price increases [1].

For the development of an OCM process Mn/Na₂WO₄/SiO₂ has been highlighted as catalyst from the rich literature on OCM [2,3], but little is known about its structure and the reaction mechanism at this catalyst. Its reported stability and high yield were the important motivations to select the catalyst for detailed studies [4–6]. However, the obtained yield still needs to be improved for industrial application.

In most reports the focus is mainly directed to the catalyst material, and reactor setups and conditions are designed and selected in a way that no reaction of methane is observed in an empty reactor. One has to mention that for industrial application high pressures are necessary to make the process economically viable, but detailed studies of empty reactors at higher pressures are

missing in literature. Furthermore, the consecutive reactions of the targeted C₂ products has the strongest negative impact on the yield [7–9]. Reactivity data of ethane or ethylene at increased pressures are almost not existent in the literature. At typical OCM conditions of 800 °C virtually no material typically used for these reactors or packing is absolutely chemically inert. For the development of an industrial scale reactor one should expect that these factors contribute even more to the reaction, due to use of materials like stainless steel. The purpose of this paper is to point out important factors which have to be considered for the reaction engineering of OCM including the interaction of gas phase and surface reactions.

The design of an industrial scale reactor requires knowledge about the reaction kinetics. If a reaction network shares strong contributions of gas phase and surface reactions, it is very difficult to derive this knowledge from experimental series at typical reaction conditions with the use of a fixed bed reactor only. This is due to inseparable kinetic data of gas phase and surface contribution. OCM is known to function in a very complex reaction network containing a variety of surface and gas phase reactions, which is depicted in a simplified scheme in Fig. 1. Obviously, the yield of ethane and ethylene is strongly dependent on the parallel and consecutive reactions to carbon oxides. Obtaining more information about the surface catalyzed activation of methane, ethane and ethene requires suppression of the gas phase activation of these components, which can be attained at the very low pressure such as the condition of temporal analysis of products (TAP) reactors.

* Corresponding author. Tel.: +49 30 31424973.

E-mail address: schomaecker@tu-berlin.de (R. Schomäcker).

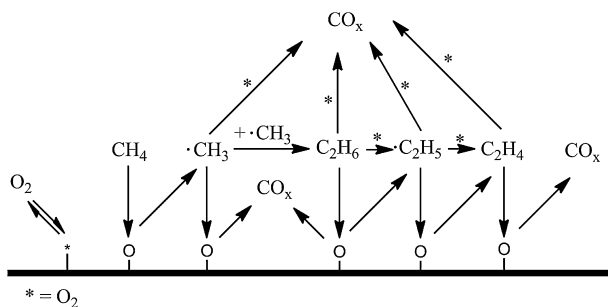


Fig. 1. Simplified reaction network of the oxidative coupling of methane at oxides.

2. Experimental

2.1. Catalyst synthesis

Mn/Na₂WO₄/SiO₂ catalyst material was prepared by fluidized bed processing of the constituent substances as described elsewhere [4]. The final catalyst contains 2 wt% Mn(II) and 5 wt% Na₂WO₄. A detailed characterization was also performed by Simon et al. [4].

2.2. Fixed bed reactor

OCM was investigated in a stainless steel reactor (65 cm length and 4 mm i.d.) equipped with an inlay made of corundum to minimize catalytic reactions at the reactor walls. This reactor can be operated up to 10 bars. The reaction temperature was between 700 and 800 °C. The product gases were analyzed with a gas chromatograph GC-2014 by Shimadzu, which was equipped with a methanizer and thermal conductivity and flame ionization detectors.

The reactor was filled with a fixed bed of quartz granules of 400 to 800 μm diameter up to height of 38 cm to end in the isothermal zone of the reactor. On the top of the quartz bed, a small piece of quartz wool was placed to keep the 100 mg Mn/Na₂WO₄/SiO₂ in position. The feeding mixture contained 95 vol% methane and 5 vol% oxygen with an overall gas flow rate between 50 to 500 N ml/min, in such a way that the residence time is kept constant with varying pressure. The shift of the explosion region to lower oxygen fractions with increasing pressure prohibits the usage of high oxygen fractions.

2.3. Temporal analysis of products

TAP experiments were conducted in a TAP-2 device, which is described in detail elsewhere [10]. In a small reactor (71 mm length and 4.6 mm i.d.) made of quartz, fixed bed 50 mg of catalyst (2–3 mm thickness) was placed, sandwiched by two layers of quartz particles. Both catalyst and quartz particles were in the 200–300 μm range. Before the TAP measurements the catalyst was pretreated for 30 min at 650 °C in oxygen flow. Measurements were performed at temperatures between 500 and 800 °C with pulse sizes large enough to be affected by intermolecular collisions (ca. 10¹⁷ molecules per pulse) due to the absence of desired products at small pulse sizes. Using the large pulse size, the mass transport is generally characterized as molecular diffusion regime.

Two types of experiments were conducted: simultaneous pulsing and sequential pulsing of oxygen and the specific hydrocarbon; i.e. methane, ethane or ethylene. The pulsed gas consisted of a hydrocarbon to oxygen to neon (internal standard) mixture of 2/1/4. In the case of sequential pulsing the methane to oxygen ratio cannot be set accurately due the usage of two pulse valves and is adjusted individually to obtain accurate TAP responses. In the case

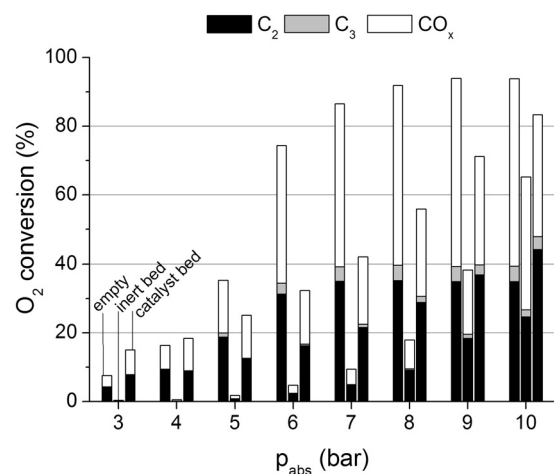


Fig. 2. Oxygen conversion with resulting product distribution at constant residence time at various pressures at 700 °C.

of MgO a methane to oxygen ratio of roughly 6 to 1 is obtained. In the case of Mn/Na₂WO₄/SiO₂ the methane to oxygen ratio was roughly 1 to 1. The response pulses of each component were calculated by averaging ten pulses per investigated atom mass unit (amu). Since carbon monoxide, carbon dioxide, ethene and ethane share some relevant amus, it was necessary to use the fragmentation patterns of these compounds for quantification. For the sake of comparison, we have also investigated magnesia by TAP as reference beside Mn/Na₂WO₄/SiO₂. It is well known that doping magnesia with lithium results in an enhanced catalytic performance, but the instability of this system prevents a closer investigation by TAP experiments.

3. Results and discussion

3.1. Catalyst characterization

A detailed characterization of the used Mn/Na₂WO₄/SiO₂ is given by Simon et al. [4]. The catalyst support was homogeneously coated with Na₂WO₄ and Mn precursors resulting in crystalline phases of Mn₂O₃ and Na₂WO₄. The support is transformed into the stable cristobalite phase with a macroporous surface morphology. The final catalyst contains 2 wt% Mn(II) and 5 wt% Na₂WO₄ and has a surface area of 1.86 m²/g. The catalyst was chemically and mechanically stable during OCM. Magnesium oxide was purchased from Sigma-Aldrich (99.9%) and has a surface area of 78 m²/g.

3.2. Pressure experiments

The results of the OCM reaction at up to 10 bar and 700 °C are shown in Fig. 2. Experiments were performed with an empty reactor (left), a fix bed of quartz granules (middle) and a fixed bed of quartz granules with a layer of catalyst on top of it (right). The tint inside the columns specifies the yield to carbon oxides, C₂ and C₃ components, respectively. The carbon balance for the pressure experiments did not deviate more than 0.5%. Strikingly the empty reactor results in the highest conversion of oxygen over the full range of examined pressure, reaching almost complete conversion at 8 bar. Only a small increase in C₂₊ yield is observed above 5 bar, which is caused by the increasing influence of the total oxidation of the C₂₊ components. The sigmoid characteristic of the oxygen conversion is typical for reactions with orders higher than one. In contrast, the fixed bed of quartz granules results in a reduced residence time that leads to the lowest conversion over the complete range of pressure. The behavior seems to be almost the same as

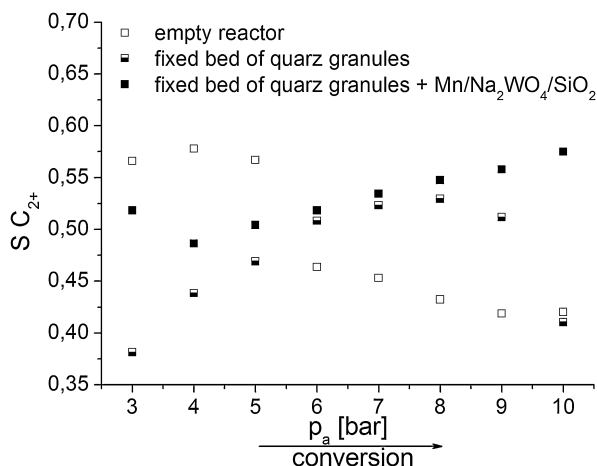


Fig. 3. Influence of absolute pressure on C_{2+} selectivity at constant residence time.

in the empty reactor with a shift to higher pressures. Addition of Mn/Na₂WO₄/SiO₂ on top of the quartz fixed bed regains higher oxygen conversions. The absence of a clear sigmoid behavior with increasing pressure indicates a more surface controlled reaction sequence, with a much higher yield of C_{2+} components compared to the reactor loaded only with quartz.

Fig. 3 shows the corresponding selectivities to C_{2+} at the investigated pressures. The empty reactor as well as the fixed bed of quartz granules passes through a maximum selectivity to C_{2+} at 4 and 8 bar, respectively. In contrast, the addition of Mn/Na₂WO₄/SiO₂ results in a steady increase of selectivity to C_{2+} with increasing pressure. Its maximum is not reached in the investigated range of pressure. The C_2 selectivity in OCM is strongly affected by consecutive reactions. This results generally in a loss of selectivity with increasing conversion due to total oxidation [11]. The observation of a higher selectivity in combination with a higher methane and oxygen conversion implies a clear benefit of higher pressure toward better C_2 selectivity.

For detailed understanding of the homogeneous gas phase as well as the heterogeneous surface catalyzed reactions, it is necessary to quantify their contributions to the overall product mixture in order to maximize the C_{2+} yield. Zanthonoff and Baerns developed a kinetic model for the gas phase contribution including 33 species and 192 elementary steps, which describes the product distribution and conversion at the end of the reactor accurately as long as the reactor temperature is higher than 600 °C [12,13]. A recent investigation of the spatial compositional profile along a reactor has exhibited discrepancies with the simulated profiles with respect to conversion and composition [13]. Better consistency could be achieved by extension of the gas phase model to more species and reactions. Marin et al. [14] coupled a gas phase reaction model to a heterogeneous catalysis one. However, the gas phase part alone of this model does not explain the observed increase in C_{2+} selectivity with increasing pressure at low oxygen conversions with quartz granules packing (Figs. 2 and 3) [15].

Nevertheless, it is necessary to couple the gas phase model to a model describing heterogeneous surface reactions. At typical reaction conditions their kinetic data are obviously compromised by gas phase contributions. This unusual approach is necessary due to the high complexity of OCM. Therefore we employed the TAP technique with the aim to directly obtain kinetic data of the CH bond activation reaction based on the assumption of the reaction as the rate determining step. Gaining the surface reactivity of C_1 and C_2 without the influence of gas phase reactions is expected to reveal factors maximizing the yield of desired products while minimizing the formation of the undesired CO_x by-products.

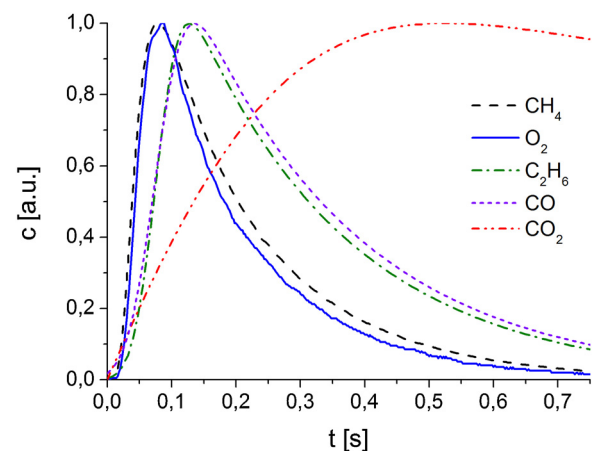


Fig. 4. TAP response of CH₄/O₂/Ne (=4/1/2) pulse over magnesia at 700 °C.

3.3. Temporal analysis of products

Generally TAP measurements are performed with small pulse sizes resulting in gas transport by Knudsen diffusion, in which gas phase intermolecular collisions are negligible [16–19]. As depicted in Fig. 1, the recombination of methyl radicals takes place in gas phase as reported by many authors [20–24]. The fact that we did not detect C_2 products in the Knudsen diffusion regime supports this hypothesis. Figs. 4 and 5 show the time resolved pulse responses at 700 °C and Table 1 provides the quantitative evaluation by the zeroth moment of the pulse response (i.e. integrated area of the pulse) for both catalysts. The product responses except CO₂ are noisier than the reactant responses and were smoothed for better illustration in Figs. 4 and 5. The major differences in the reactivity of the two materials are the lower methane conversion and higher selectivity to ethane of Mn/Na₂WO₄/SiO₂ compared to those of magnesia. The carbon balance for the TAP measurements did not deviate more than 3%.

The positions of the peak maxima give evidence about the reaction sequence. In Fig. 4 one can clearly see that carbon monoxide is formed in parallel to the formation of ethane from methane. The origin of CO formation via a consecutive oxidation of methyl radicals is reasonable (Fig. 1). Methyl radicals are produced from methane at the catalyst surface by direct interaction with surface adsorbed oxygen [16]. They can be oxidized before desorption or by re-adsorption at the catalyst or quartz surface; if not they combine to ethane in the gas phase. The delayed peak maxima observed for magnesia compared to those of Mn/Na₂WO₄/SiO₂ indicate more

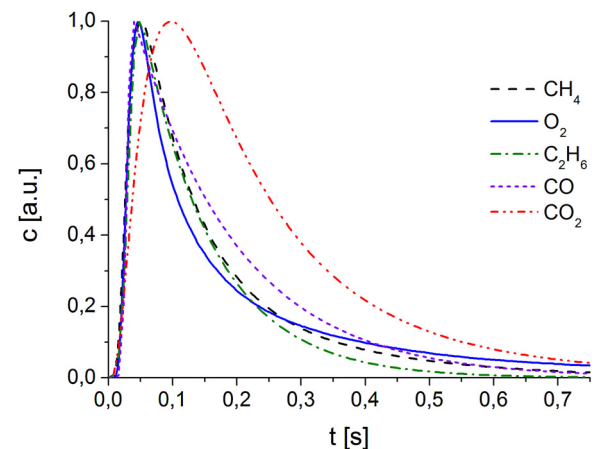


Fig. 5. TAP response of CH₄/O₂/Ne 4/1/2 at Mn/Na₂WO₄/SiO₂ at 700 °C.

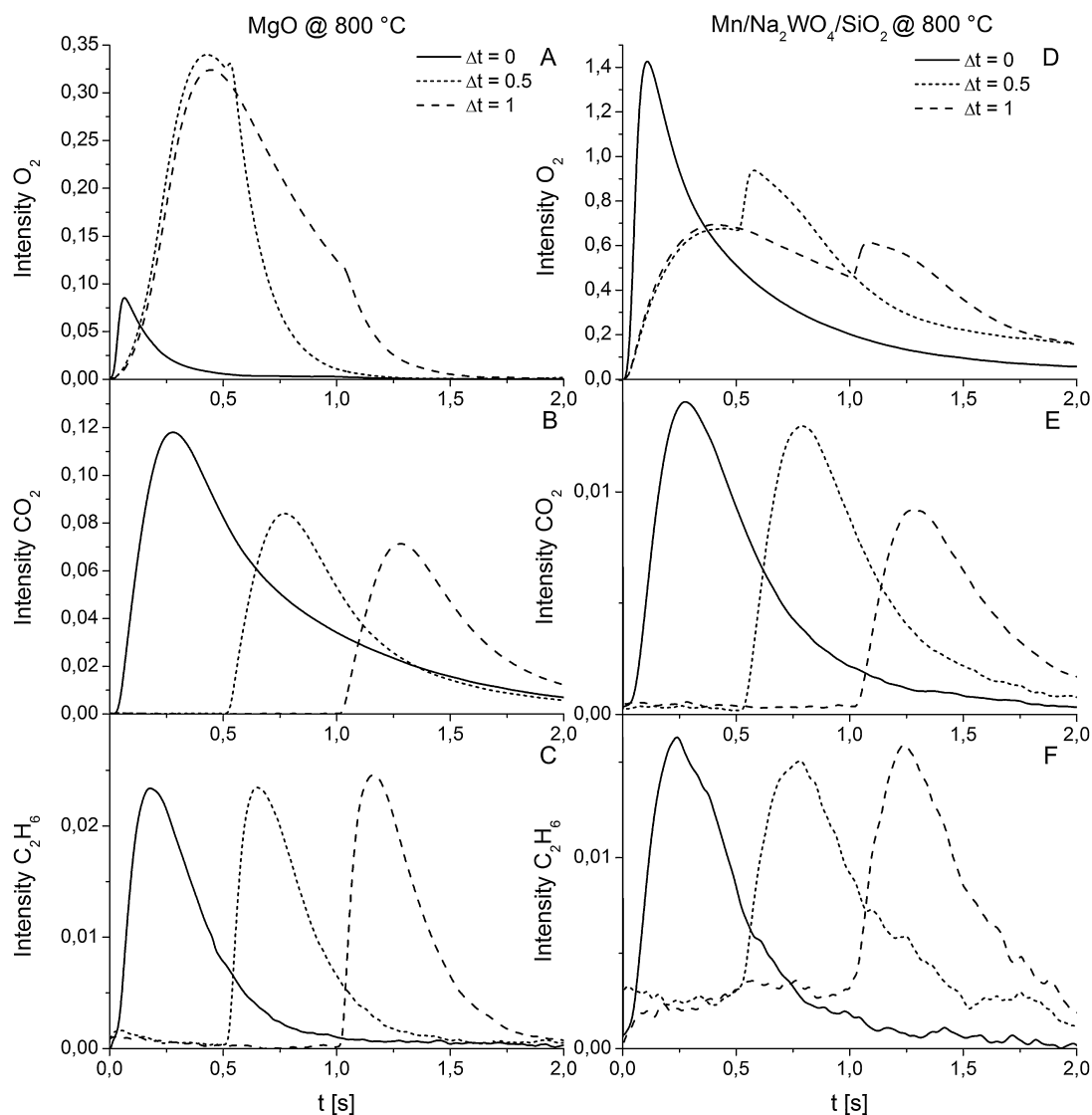


Fig. 6. TAP responses of sequential pulsing of first oxygen and then methane with a delay Δt at $800\text{ }^\circ\text{C}$.

stable surface intermediates over magnesia, easing the consecutive oxidation of methyl radicals, which could be the major reason for the inferior selectivity to C_2 products (Table 1). For magnesia the response time of carbon dioxide is strongly delayed, indicating that it is produced by species strongly adsorbed onto magnesia or simply carbon dioxide interacts strongly with the catalyst surface. Analogous behavior can be observed when using ethane or ethylene as feed gas (not shown). No conversion could be observed by pulsing mixtures of hydrocarbon (methane, ethane or ethene) and oxygen in a reactor only filled with quartz particles. Therefore a gas phase activation of these components can be excluded. Interestingly, the oxygen balance cannot be closed for $\text{Mn/Na}_2\text{WO}_4/\text{SiO}_2$. Pulse experiments with pure oxygen result in a loss of oxygen, which can be explained by the oxidation of the material partially reduced under the TAP vacuum conditions.

Furthermore, sequential pulse experiments were used to investigate the reactivity of adsorbed oxygen at $800\text{ }^\circ\text{C}$. First oxygen is pulsed and next a pulse of methane is given with an offset of 0.0, 0.5 and 1 s. The oxygen response for magnesia is presented in Fig. 6A. The response of the oxygen pulse has a similar shape with an abrupt decay shortly after the pulse of methane. This rapid oxygen consumption is attributed to weakly adsorbed but highly reactive oxygen species. Due to decreasing concentration of these species with time, a decrease of the reaction products with increasing the delay of the methane pulse is expected to be observed. Carbon dioxide is identified as product showing the expected behavior (Fig. 6B). In contrast, in Fig. 6C the pulse intensity of ethane is not decreasing by delayed methane pulses. This indicates that the presence of a second species of more strongly adsorbed oxygen is responsible for the methyl radical formation. It should be mentioned that no

Table 1

Reactivity data of the two catalysts determined from TAP data at $700\text{ }^\circ\text{C}$.

Catalyst	Conversion CH_4 (%)	SCO (%)	SCO_2 (%)	SC_2H_6 (%)	SC_2H_4 (%)
$\text{Mn/Na}_2\text{WO}_4/\text{SiO}_2$	~2	3.6	1.4	95	0
MgO	16.0	83.4	14.6	2	0

Table 2

Integrated MS responses of the components presented in Fig. 6.

Catalyst Δt [s]	MgO			Mn/Na ₂ WO ₄ /SiO ₂		
	O ₂	CO ₂	C ₂ H ₆	O ₂	CO ₂	C ₂ H ₆
0	2.15E–2	8.93E–2	1.15E–2	7.83E–1	8.59E–3	1.33E–2
0.5	1.58E–1	5.28E–2	1.16E–2	1.15	8.23E–3	1.28E–2
1	2.23E–1	4.50E–2	1.16E–2	1.21	6.77E–3	1.38E–2

product formation occurs by pulsing first methane and then oxygen.

The oxygen response for Mn/Na₂WO₄/SiO₂ is shown in Fig. 6D. When the two pulses are made at the same time the total pulse size is bigger, farther from Knudsen diffusion regime, and convective flow is more important, rendering the responses narrower. Immediately after methane enters the reactor, the oxygen response passes through a small maximum, which is not followed by an abrupt decay. The small maximum is an artifact resulting from the pulsing of methane and is also visible in the inert gas response (not shown). The missing fast decay is attributed to the lack of highly reactive adsorbed oxygen species as observed for MgO. The integrated quantities of the sequential pulse experiments are presented in Table 2. Due to the different methane to oxygen ratios the obtained quantities are not directly comparable with the simultaneous pulse experiments.

Nevertheless, Mn/Na₂WO₄/SiO₂ shows a similar response to that of magnesia at varying delay of methane pulse for carbon dioxide and ethane as presented in Fig. 6E and F, revealing the presence of a second species of more strongly adsorbed oxygen. Therefore it is reasonable that the ratio between strong and weak adsorbed oxygen species is responsible for the overall much higher C₂ selectivity of Mn/Na₂WO₄/SiO₂ compared to that of magnesia. Simultaneous pulsing of methane and ¹⁸O₂ was also examined to get closer insight into the nature of the oxygen species responsible for methyl radical formation. Unfortunately, no ¹⁸O containing products were detected unless a very large amount of ¹⁸O₂ was used. Interestingly, the response at amu 36 is almost replaced by responses at the amu's 32 and 34 indicating a very fast exchange between gas phase, adsorbed and lattice oxygen.

Determination of apparent activation energies requires a constant amount of active sites within the studied temperature range. Due to the reduction of Mn/Na₂WO₄/SiO₂ in vacuum, that is temperature dependent, a constant amount of active sites is not provided. A reduction of magnesia in vacuum was not experimentally observed. Therefore the temperature dependence of the surface reactions of methane and the desired intermediates can only be provided for magnesia. Rate constants were determined by the zeroth moment of the reactant response assuming a first order rate expression of the hydrocarbon (methane, ethane or ethene) and oxygen [19]. Therefore, apparent activation energies could be determined from the Arrhenius plot in Fig. 7, as presented in Table 3. A loss of active sites by agglomeration was not observed. Interestingly, the apparent activation energies of methane and ethane are the same within the experimental error. The ratio between the pre-exponential factors of ethane to methane is 1.5, which is in accordance with the ratio of C–H bond quantity. Buyevskaya et al. found a significant difference between methane with 70 kJ/mol and ethane with 29 kJ/mol for samarium oxide, which was assigned to the different strength of the C–H bonds involved in the rate

limiting step [16]. A similar value for the apparent activation energies of methane and ethane could be caused by the conditions, i.e. the bond cleavage is not the controlling parameter.

From the kinetic data it is now possible to estimate the maximum yield which would be achievable assuming that methane, ethane and ethene are only activated by surface catalyzed reaction pathways and each C–H activation successfully leads to the formation of the desired product. We used a simplified reaction network of consecutive reactions assuming a constant oxygen partial pressure as shown below and simulated it by application of a batch reactor model

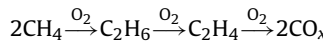


Fig. 8 shows the maximum yield of C₂ components as a function of the methane conversion at 750 °C. The maximum yield of C₂ is around 60%, at a methane conversion of 75%. Additionally, we simulated the C₂ yield at atmospheric conditions and constant oxygen partial pressure including gas phase reactions by application of a

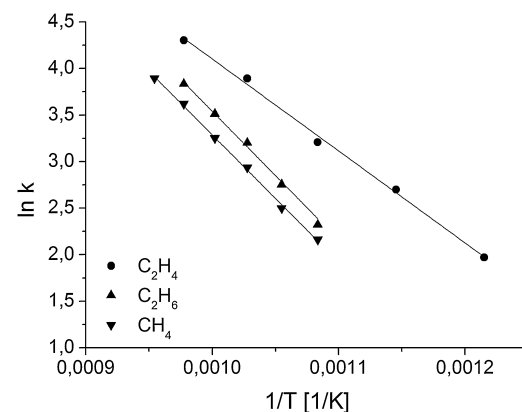


Fig. 7. Arrhenius plot of different substrates from TAP experiments with magnesia.

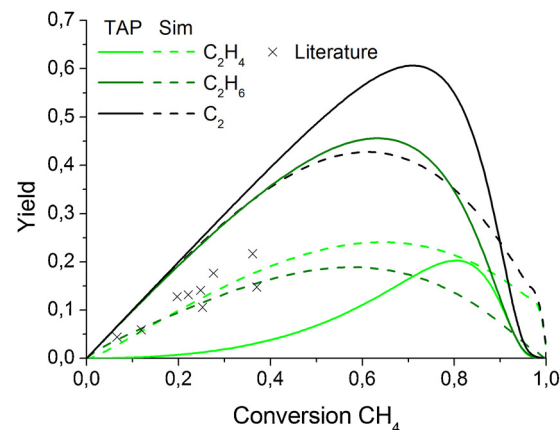


Fig. 8. Simulated yields of C₂ products as a function of methane conversion for magnesia calculated using the kinetic parameters obtained from the TAP measurements (solid line), the micro kinetic model of Sun/Marin [14] (dotted line), in comparison to the reported C₂ yield from literature [26–29] (cross symbol).

Table 3

Kinetic data of magnesia in the TAP reactor.

	CH ₄	C ₂ H ₆	C ₂ H ₄
E _{a,app} [kJ/mol]	113 ± 2	115 ± 6	82 ± 3
k _∞ [mol/l/s]	2.27E + 07	3.40E + 07	1.18E + 06

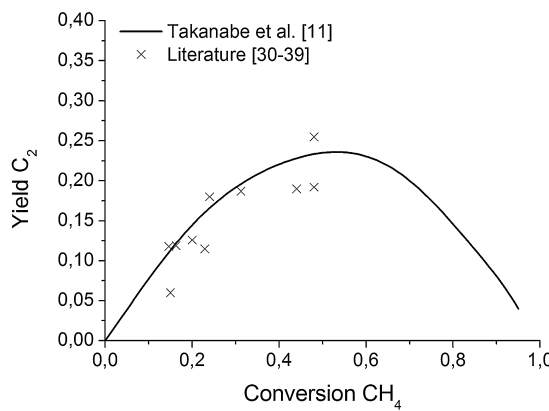


Fig. 9. Simulated yields of C₂ products as a function of methane conversion for Mn/Na₂WO₄/SiO₂ calculated using the kinetic parameters obtained from the OCM reaction in a recirculating batch reactor [11] (solid line) in comparison to singular reported C₂ yields from literature [30–39] (cross symbol).

batch reactor model as predicted by the model of Sun and Marin, which is the only available microkinetic model for magnesia based catalysts [14]. The maximum C₂ yield is predicted to be around 42% at a methane conversion of 60%. A comparison with the experimental data of other research groups with this model leads to a good prediction of the methane conversion, but a large overestimation of the C₂ selectivity [25].

Takanabe et al. [11] simulated the C₂ yield dependent of the methane conversion (Fig. 9) for Mn/Na₂WO₄/SiO₂ in a recirculating batch reactor at atmospheric pressure including direct oxidation pathways form methane and ethane to carbon oxides. The maximum C₂ yield is located around 24% at a methane conversion of 55%. Comparison of the simulated C₂ yield with those available in literature using various reactor setups and reaction conditions exhibits a conspicuous consistency. It is reasonable that suppression of unsselective gas phase activation of methane, ethane and ethene will lead to notable higher C₂ yields as already shown for magnesia.

Independent of the type of reactors, different kinetic models used (TAP or normal pressurized reactor), and the type of catalysts, a methane conversion between 55% and 75% seems to be optimal to maximize the C₂ yield. Due to the explosion limit of methane/oxygen mixtures and the suppression of undesired gas phase reactions, the oxygen partial pressure must be kept at a low level. Therefore, a distributed oxygen feed along the reactor would be a good alternative which could be implemented by means of a membrane or stage-type reactor. Additionally, the formation of hot spots by the strongly exothermic total oxidation reaction has to be prevented.

From this qualitative insight into the reaction mechanism and the thermodynamical data some indication for the reaction engineering and reactor design can be drawn. The complexity of the reaction mechanism prevents accurate simulations of the derived reactor concepts. Therefore these have to be tested and investigated in detail before further upscaling.

3.4. Thermodynamics and reaction engineering aspects

Industrial application of heterogeneous catalyzed gas phase reactions are often realized in tubular reactors. In the case of exothermic reactions the heat production can lead to hot spot formations and in the worst case to a thermal runaway of the reactor. The critical tube diameter is a safety-related parameter giving the upper limit to assure the necessary heat transfer. The thermodynamic data from the NIST database [40] are used to calculate the reaction parameters. The enthalpy of reaction for the OCM in the temperature range of 500 to 1000 °C is –176 kJ/mol

with an equilibrium constant of 1.01E+06. Therefore, OCM is highly exothermic and not thermodynamically limited in practice. The heat capacity of the gas mixture was calculated with Eq. (1).

$$C_p = x_{0,\text{CH}_4} C_{p,\text{CH}_4} + x_{0,\text{O}_2} C_{p,\text{O}_2} \quad (1)$$

For a mixture of 5% oxygen and 95% methane the heat capacity is 71.81 J/(mol K). The adiabatic temperature increase is 507 K under the assumption of a selectivity of 70% ethene and 30% to total combustion products and is calculated with Eq. (2).

$$\Delta T_{\text{ad}} = \frac{-\Delta H_R c_{A,0}}{\nu_A \rho \bar{c}_p} \quad (2)$$

To estimate the critical tube diameter of the fixed bed reactor Eqs. (3) and (4) from [41,42] are used.

$$d_{\text{crit}} = \frac{8 Ge L R T_w^2}{Da E_a \Delta T_{\text{Ad}}} \quad (3)$$

$$Ge = \frac{0.125 d_p / d}{2 - (1 - 2d_p / d)^2} \quad (4)$$

In Eq. (3) the Damköhler number (Da) was added under the assumption of a first order reaction, caused by a quasi stationary methane concentration. The geometry factor (Ge) describes the volume properties of particles in a tube. Typical dimensions of tubular reactors are given by the length/diameter ratio of 100 and a particle size ratio to tube diameter of 0.1. With a wall temperature of 700 °C the critical tube diameter is 8 mm.

An increase of the oxygen mole fraction to 0.15 leads to a reduction of the critical tube diameter to 2 mm. Taking into account that upscaling leads to similar problems, the fixed bed reactor is unsuitable for OCM reactions at industrial conditions. The reason is the fast heat production and the low thermal conductivity of the catalyst bed. The absolute value of the critical tube diameter is dominated by the product distribution. Side reactions resulting in the formation of carbon monoxide and hydrogen will shift it to slightly higher values. Consecutive reactions resulting in the formation of carbon dioxide and water will shift it to lower values.

4. Conclusion

The experiments at elevated pressures point out that the yield of C₂₊ components increases with increasing pressure at the same residence time. Without a catalyst the yield is passing through a maximum, which is caused by the consecutive oxidation of C₂₊. This occurs in homogenous gas phase reaction as well as heterogeneously catalyzed surface reaction at the catalyst itself, the reactor wall, and quartz packing. It is evident that the unselective gas phase reactions are more accelerated by higher pressures than surface catalyzed reactions. Thus it is reasonable that each specific reactor setup will pass through a maximum yield of C₂₊ components with increasing pressure. The methane conversions to maximize the C₂ yield are mostly in the 60–75% range. Sufficient oxygen has to be provided at a constant, but relatively low oxygen partial pressure. Kinetic models for OCM are developed for plug flow reactors with a relatively high oxygen feed fraction. Therefore for reactor simulations it is necessary to extrapolate these models to low fractions of oxygen leading to inaccuracies in the prediction of conversion and selectivity. Nevertheless, it is not possible to prevent the formation of hotspots inside the catalyst bed, due to the strongly exothermic total combustion. Jašo et al. [30] showed that the use of a fluidized bed reactor can overcome this flaw by providing isothermal conditions even at high oxygen to methane ratios. On the other hand, the broad residence time distribution of the gas will favor consecutive reactions, which are lowering the C₂ yield. Additionally, the physical strain could destroy the catalyst material during fluidization, but this was not observed in the case of Mn/Na₂WO₄/SiO₂. Another

potential approach was done by Carr et al. by using a simulated countercurrent moving-bed chromatographic reactor to prevent total oxidation products by continuous separation of the reaction products [43]. C₂ yields of more than 50% were obtained [44,45].

Concerning the different strength of the C–H bonds between methane and ethane one could expect a lower activation energy for ethane, which is obviously negative for the C₂ yield. Interestingly magnesia does not show this behavior indicating a subsequent higher activation barrier to overcome, which could be related to the hydroxyl formation on the catalyst surface due to the C–H bond activation. Even though Mn/Na₂WO₄/SiO₂ was not suited for the determination of apparent activation energies at vacuum conditions due to vacuum-induced surface reduction, it was possible to find some significant differences between this catalyst and magnesia, explaining the higher C₂₊ selectivity observed for Mn/Na₂WO₄/SiO₂. Oxidation to carbon oxides proceeds over magnesia and Mn/Na₂WO₄/SiO₂ mainly by reaction of weakly adsorbed oxygen. The formation of methyl radicals proceeds by a second more strongly adsorbed oxygen species. Mn/Na₂WO₄/SiO₂ provides a much higher ratio of strongly adsorbed oxygen to weakly adsorbed oxygen, which highly improves the selectivity to C₂. Also, very fast oxygen exchange between adsorbed and lattice oxygen was observed for both materials, but at present it was not possible to assign the methyl radical formation to a specific type of oxygen such as lattice or strongly adsorbed oxygen by studies using labeled oxygen. There are still open questions about the nature of the oxygen species responsible for the methyl radical formation and the rate and selectivity determination step. Nevertheless qualitative suggestions for the reactor design and operation can be drawn.

Acknowledgment

We thank the Deutsche Forschungsgemeinschaft for financial support of our work in the cluster of excellence UniCat Berlin.

References

- [1] J. Lunsford, *Catal. Today* 63 (2000) 165–174.
- [2] S. Arndt, T. Otremba, U. Simon, M. Yildiz, H. Schubert, R. Schomäcker, *Appl. Catal. A* 425–426 (2012) 53–61.
- [3] X.P. Fang, S.B. Li, J.Z. Lin, Y.L. Chu, *J. Mol. Catal. A* 6 (1992) 427–433.
- [4] U. Simon, O. Görke, A. Berthold, S. Arndt, R. Schomäcker, H. Schubert, *Chem. Eng. J.* 168 (2011) 1352–1359.
- [5] S. Pak, P. Qiu, J. Lunsford, *J. Catal.* 230 (1998) 222–230.
- [6] H. Liu, X. Wang, D. Yang, R. Gao, *J. Nat. Gas Chem.* 17 (2008) 59–63.
- [7] P.F. Nelson, N.W. Cant, *J. Phys. Chem.* 94 (1990) 3756–3761.
- [8] E. Morales, J. Lunsford, *J. Catal.* 5 (1989).
- [9] J. Roos, S. Korf, R. Veehof, *Appl. Catal., A* 52 (1989) 147–156.
- [10] J.T. Gleaves, G.S. Yablonskii, P. Phanawadee, Y. Schuurman, *Appl. Catal., A* 160 (1997) 55–88.
- [11] K. Takanabe, E. Iglesia, *J. Phys. Chem. C* 113 (2009) 10131–10145.
- [12] H. Zanthoff, M. Baerns, *Ind. Eng. Chem. Res.* (1990) 2–10.
- [13] O. Korup, S. Mavlyankariev, M. Geske, C.F. Goldsmith, R. Horn, *Chem. Eng. Process.* 50 (2011) 998–1009.
- [14] J. Sun, J. Thybaut, G. Marin, *Catal. Today* 137 (2008) 90–102.
- [15] Q. Chen, P.M. Couwenberg, G.B. Marin, *AIChE J.* 40 (1994) 521–535.
- [16] O.V. Buyevskaya, M. Rothaemel, H.W. Zanthoff, M. Baerns, *J. Catal.* 146 (1994) 346–357.
- [17] E. Kondratenko, O. Buyevskaya, M. Soick, M. Baerns, *Catal. Lett.* 63 (1999) 153–159.
- [18] G. Yablonskii, S. Shekhtman, *Ind. Eng. Chem. Res.* 5885 (1998) 2193–2202.
- [19] J.T. Gleaves, G. Yablonsky, X. Zheng, R. Fushimi, P.L. Mills, *J. Mol. Catal. A: Chem.* 315 (2010) 108–134.
- [20] T. Ito, J. Wang, C. Lin, J. Lunsford, *J. Am. Chem. Soc.* (1985) 5062–5068.
- [21] D. Driscoll, J. Lunsford, *J. Phys. Chem.* (1985) 4415–4418.
- [22] K.D. Campbell, E. Morales, J.H. Lunsford, *J. Am. Chem. Soc.* 109 (1987) 7900–7901.
- [23] K. Campbell, J. Lunsford, *J. Phys. Chem.* 92 (1988) 5792–5796.
- [24] E. Mallens, J. Hoebink, G. Marin, *J. Catal.* 234 (1996) 222–234.
- [25] S. Arndt, G. Laugel, S. Levchenko, R. Horn, M. Baerns, M. Scheffler, R. Schlögl, R. Schomäcker, *Catal. Rev.* 53 (2011) 424–514.
- [26] J.S.J. Hargreaves, G.J. Hutchings, R.W. Joyner, C.J. Kiely, *Catal. Today* 10 (1991) 259–266.
- [27] C. Chevalier, P.R. de la Piscina, M. Ceruso, A. Choplin, J.M. Basset, *Catal. Today* 4 (1989) 433–439.
- [28] V. Choudhary, *J. Chem. Technol. Biotechnol.* 68 (1997) 177–186.
- [29] V. Choudhary, S. Mulla, *J. Chem. Soc., Faraday Trans.* 75 (2000) 828–834.
- [30] S. Jašo, S. Sadjadi, H. Godini, U. Simon, S. Arndt, O. Görke, A. Berthold, H. Arellano-Garcia, H. Schubert, R. Schomäcker, G. Wozny, *J. Nat. Gas Chem.* 21 (2012) 534–543.
- [31] K. Takanabe, E. Iglesia, *Angew. Chem. Int. Ed.* 47 (2008) 7689–7693.
- [32] A. Malekzadeh, M. Abedini, A. Khodadadi, *Catal. Lett.* 84 (2002) 45–51.
- [33] A. Palermo, J. Vazquez, R. Lambert, *Catal. Lett.* 68 (2000) 191–196.
- [34] A. Malekzadeh, A. Khodadadi, *J. Nat. Gas Chem.* 16 (2007) 121–129.
- [35] S. Ren, S. Qin, J. Zhu, X. Peng, C. Hu, *Ind. Eng. Chem. Res.* (2010) 2078–2083.
- [36] L. Chou, Y. Cai, B. Zhang, J. Niu, *J. Nat. Gas Chem.* 11 (2002) 131–136.
- [37] S.M.K. Shahri, A.N. Pour, *J. Nat. Gas Chem.* 19 (2010) 47–53.
- [38] A. Karimi, R. Ahmadi, H. Zadeh, *Pet. Coal* (2007) 2–6.
- [39] H. Bozorgzadeh, R. Ahmadi, *Pet. Coal* 53 (2011) 84–90.
- [40] U.S. Secretary of Commerce, <http://webbook.nist.gov/chemistry/> (2011).
- [41] D.A. Frank-Kamenetskii, *Diffusion and Heat Transfer in Chemical Kinetics*, second ed., Plenum Press, London, New York, 1969.
- [42] E.U. Schlünder, *Chem. Ing. Tech.* 38 (1966) 967–979.
- [43] M.C. Bjorklund, R.W. Carr, *Catal. Today* 25 (1995) 159–168.
- [44] A.L.Y. Tonkovich, R.W. Carr, R. Aris, *Science* 262 (1993) 221–223.
- [45] A.L.Y. Tonkovich, R.W. Carr, *Chem. Eng. Sci.* 49 (1994) 4647–4656.

Paper 3



Investigation of the surface reaction network of the oxidative coupling of methane over $\text{Na}_2\text{WO}_4/\text{Mn}/\text{SiO}_2$ catalyst by temperature programmed and dynamic experiments

Vinzenz Fleischer, Rolf Steuer, Samira Parishan, Reinhard Schomäcker*

Technische Universität Berlin, Institut für Chemie, Straße des 17. Juni 124, 10623 Berlin, Germany



ARTICLE INFO

Article history:

Received 1 December 2015

Revised 26 May 2016

Accepted 20 June 2016

Keywords:

Oxidative coupling of methane

$\text{Na}_2\text{WO}_4/\text{Mn}/\text{SiO}_2$

Temperature programmed experiments

Dynamic experiments

ABSTRACT

In this work a series of temperature programmed experiments were carried out on a $\text{Na}_2\text{WO}_4/\text{Mn}/\text{SiO}_2$ catalyst. In TPR experiments we tested the reducibility of this catalyst and O_2 desorption behavior was investigated by TPD. TPSR experiments in a flow of methane, ethane or ethene gave information about the reaction network of OCM on the catalyst surface, without the presence of gas phase reactions, induced by gas phase oxygen. We found indications of involvement of two different active oxygen species on the catalyst surface. Furthermore an activation energy of 275 kJ/mole for selective methane activation was determined. Dynamic experiments were performed to determine the amount of available oxygen species for the OCM reaction. Variation of methane partial pressure and flow rate showed a linear correlation between methane partial pressure and surface oxygen conversion in dynamic experiments.

© 2016 Elsevier Inc. All rights reserved.

1. Introduction

A well-established process for ethylene production is the steam cracking process, which cracks naphtha to olefins and other hydrocarbons. Shortage of crude oil reserves has attracted attention toward alternative processes, which use more available feedstocks. The high availability of methane in natural gas makes it a suitable feedstock alternative for short-chain olefins [1,2]. The oxidative coupling of methane (OCM) is a promising reaction for ethylene production. One of the most stable catalysts described for OCM in the literature is $\text{Na}_2\text{WO}_4/\text{Mn}/\text{SiO}_2$, which has good performance and stability as shown in several publications [3–5].

One of the major challenges in experimental studies of OCM is the parallel reaction network of gas phase and surface reactions, which have a strong influence on each other. For gas phase reactions, Dooley and coworkers published an extended micro kinetic model [6]. This micro kinetic model considers a network of 1582 reactions and 269 species, which are mainly radical reactions. Unfortunately this complex reaction network allows only simulation of ideal reactors, because of the large set of reactions. However, the gas phase network is well described by the Dooley model, which was shown by Schwarz and Coworkers [7]. Formal kinetic models of OCM were published by several groups for

different catalysts [8–16]. All of these proposed mechanisms show similar pathways for reactants and products. All groups who carried out these experiments with extensive experimental efforts, were using similar reactors operated in the classical steady state mode.

The surface reaction network, which is not fully explored, is strongly influenced by gas phase reactions, and its kinetic parameters offer several constellations to fit experimental results. Such complexity is caused by the mentioned involvement of various radical species which are formed via gas phase reactions or during reactions on the catalyst surface [17–20]. In addition for several OCM catalysts different oxygen intermediates contribute to selective and unselective activation of methane on the catalyst surface. The presence of these different species is also influenced by gas phase oxygen [21–23].

A micro kinetic surface reaction model for the surface reactions was published by Lee and Coworkers for the $\text{Na}_2\text{WO}_4/\text{Mn}/\text{SiO}_2$ catalyst [24]. Another one is the model published by Sun and Thybaut for a MgO catalyst [25]. Both models were developed for different catalysts but have similar elementary surface reaction steps which are shown in Table 1. Their models assume dissociative adsorption of oxygen on a free site of the catalyst (*), which is in equilibrium with gas phase oxygen. Methane activation occurs by a surface reaction with dissociated oxygen (O^*) and releases methyl radicals to the gas phase. The coupling reaction of the radicals happens in gas phase close to the catalyst surface where excess heat is released, which is not shown in Table 1. The same activation

* Corresponding author.

E-mail addresses: v.fleischer@mailbox.tu-berlin.de (V. Fleischer), schomaecker@mailbox.tu-berlin.de (R. Schomäcker).

Table 1

Comparison of micro-kinetic surface reaction models from Lee et al. and Sun et al. (x, y, z = stoichiometric factors) [24–26].

Lee et al. [24]	Sun et al. [25]	Beck et al. [26]
$O_2 + 2^* \rightleftharpoons 2O^*$	$O_2 + 2^* \rightleftharpoons 2O^*$	$O_2 + * \rightleftharpoons O_{2,ads}$
$CH_4 + O^* \rightleftharpoons CH_3 + OH^*$	$CH_4 + O^* \rightleftharpoons CH_3 + OH^*$	$O_{2,ads} \rightleftharpoons yO_x^*$
$C_2H_4 + O^* C_2H_3 + OH^*$	$C_2H_4 + O^* \rightleftharpoons C_2H_3 + OH^*$	$CH_4 + O^* \rightleftharpoons CH_3 + OH^*$
$C_2H_6 + O^* \rightleftharpoons C_2H_5 + OH^*$	$C_2H_6 + O^* \rightleftharpoons C_2H_5 + OH^*$	$C_2H_4 + O^* \rightleftharpoons C_2H_3 + OH^*$
$CH_3 + 3O^* \rightleftharpoons HCO^* + 2OH^*$	$2OH^* \rightleftharpoons H_2O^* + O^*$	$C_2H_6 + O^* \rightleftharpoons C_2H_5 + OH^*$
$HCO^* + O^* \rightleftharpoons CO^* + OH^*$	$CH_3 + O^* \rightleftharpoons CH_3O^*$	$2OH^* \rightleftharpoons H_2O^* + O^*$
$CO^* + O^* \rightleftharpoons CO_2^* + *$	$CH_3O^* + O^* \rightleftharpoons CH_2O^* + OH^*$	
$2OH^* \rightleftharpoons H_2O + O^* + *$	$CH_2O^* + O^* \rightleftharpoons HCO^* + OH^*$	
	$HCO^* + O^* \rightleftharpoons CO^* + OH^*$	
	$CO^* + O^* \rightleftharpoons CO_2^* + *$	
	$CO_2^* \rightleftharpoons CO^*$	
	$CO_2 + * \rightleftharpoons CO_2^*$	
	$4HO_2 \rightarrow 3O_2 + 2H_2$	
		$xO_{2,ads} + CH_4 \rightleftharpoons CO_y + zH_2O^*$
		$xO_{2,ads} + C_2H_6 \rightleftharpoons 2CO_y + zH_2O^*$
		$xO_{2,ads} + C_2H_4 \rightleftharpoons 2CO_y + zH_2O^*$

may also happen to the formed ethane and even ethene, which leads to the formation of C_2H_5 or C_2H_3 radicals. An interesting fact is that no ethene combustion on the catalyst surface is considered in both literature models. A typical formation route for deep oxidation products is the reaction of methyl radicals and surface bound oxygen which forms a HCO^* radical which is bound on the catalyst surface, which is further oxidized to CO^* and surface bound OH groups (OH^*) in a parallel route to the coupling reaction. The origin of CO_2 on the catalyst surface (CO_2^*) is the oxidation of CO^* by O^* . A new aspect of the catalyst surface reaction network was published by Beck et al. for the $Na_2WO_4/Mn/SiO_2$ as well as for MgO . In temporal analysis of products (TAP) experiments, they could show the presence of two different oxygen species, which exist in parallel on the catalyst surface. Furthermore they could show that both species have different reaction pathways [26]. One of them is weakly bound ($O_{2,ads}$) and opens the route to deep oxidation products. The other, stronger bound oxygen species (O_x^*) is responsible for the selective methane activation. Following these results a plausible surface reaction network is also presented in Table 1.

In addition, there is also a discussion about the formal kinetic mechanistic aspects of oxygen and methane activation described by an Eley-Rideal, Mars-van-Krevelen or dual site Langmuir Hinshelwood mechanism [12,27,28]. On the one hand, in the Eley-Rideal mechanism gas phase oxygen is required for selective activate methane in the OCM process. On the other hand, in a Mars-van-Krevelen type mechanism lattice oxygen is involved during C–H bond cleavage of methane to form a methyl radical. A possible interaction of lattice oxygen with methane offers the opportunity to avoid the presence of gas phase oxygen in temperature programmed experiments and dynamic experiments. During these unsteady state experiments the catalyst oxidation and the methane coupling reaction can be separated into two different steps. One of the first overviews about these techniques and experimental results from several groups was published by Falconer and Schwarz [29]. Another review about these techniques was presented by Niemantsverdriet [30].

One important factor in temperature programmed reduction experiments is the bond dissociation energy of the reactants. For methane (439 kJ/mole) and hydrogen (436 kJ/mole) these energies are similar, and for ethane (423 kJ/mole) it is lower than those of hydrogen and ethene (464 kJ/mole), which has the highest bond dissociation energy in this group of compounds [31]. Therefore it is possible to reduce the catalyst in the same manner as in a H_2 -temperature programmed reduction (TPR) experiments using OCM reactants to study their pathways in the reaction network in absence of gas phase oxygen. These types of experiments were

introduced as temperature programmed surface reactions (TPSR) by McCarty and Wise some decades ago [32]. Heating rate variations in TPSR experiments allow the determination of the activation energy of desorption or surface reaction steps. This is known as the Redhead method [33]. In this work we want to study the OCM surface mediated reaction network in absence of gas phase oxygen, to understand the role of surface bound oxygen on the $Na_2WO_4/Mn/SiO_2$ catalyst material. Temperature programmed reaction experiments utilizing methane, ethane and ethene as reactant give qualitative insights to their interaction with the surface bound oxygen species. In addition we performed a series of kinetic TPSR studies for the selective activation of methane. The focus of further dynamic experiments at constant temperature is to quantify the converted amount of strongly surface bound oxygen, the stability of the oxygen intermediates on the catalyst surface and the nature of active sites for that material.

2. Experimental

2.1. Catalyst preparation

The details of the preparation and the characterization of the catalyst are described elsewhere [34]. The final catalyst contains 5 wt.% Na_2WO_4 , 2 wt.% Mn(II) ions and has a specific surface area of $1.86\text{ m}^2/\text{g}$. The catalyst material was analyzed by nitrogen adsorption and X-ray diffraction analysis after oxidation pretreatment and after dynamic experiments. The results are presented and discussed in the supporting information.

2.2. Experimental setup and mass spectrometer

All experiments were carried out in a fixed bed reactor made of quartz. The catalyst was placed on a quartz frit (200 μm pore size) in the isothermal zone. The isothermal zone is above the frit and has a length of 5 cm. A scheme of the reactor, a construction plan of the setup and analysis of temperature profile aspects are shown in the supporting information. The inner diameter is 9 mm. The type K thermocouple (NiCrNi) is covered by a quartz-made capillary ($d_{in} = 4\text{ mm}$), which seals the reactor on top. The reactants come through the upper inlet. The bottom part of the reactor shrinks in diameter and is connected to a mass spectrometer or thermal conductivity detector. The feed composition was controlled by mass flow controllers (MFC) and switching valves were installed, enabling the ability to interrupt reactant flow immediately. Detection was carried out with a quadrupole mass spectrom-

Table 2

Calibrated masses for compound detection in dynamic experiments.

Molecule	<i>m/e</i>
CO ₂	44
CO	28
He	4
H ₂	2
H ₂ O	18; 17
CH ₄	16; 15
C ₂ H ₆	30; 29; 28
C ₂ H ₄	28; 27; 26
O ₂	32

eter (QMS, IPI GAM 200) with channeltron detector. The QMS was equipped with yttriated filaments. For O₂ detection in temperature programmed desorption experiments *m/e* = 32 was chosen and data points were recorded each 5 s. The *m/e* values for OCM compound calibration are listed in Table 2. Each compound was calibrated by utilization of a calibration gas bottle filled with 5 ± 0.005 vol.% of one compound and the rest was filled with Helium. The calibration of *m/e* = 28 for ethane and ethene was necessary to prevent false-signals for CO or other compounds. As indicator for ethane the *m/e* = 30 and for ethylene *m/e* = 27 were chosen, while the other listed masses were calibrated by their specific, relative intensities for these molecules. Therefore the feed compositions of these compounds were determined by three calibration factors for ethane and ethene to enhance detection accuracy.

The final mole fraction (*x_i*) of each compound was calculated according to Eq. (1):

$$x_{\text{compound}}(x \dots z) = \frac{S_{\frac{m}{e}, i}(i \dots j)}{\gamma_i} \quad (1)$$

S_{m/e,i}(i) – relative intensity matrix of compound *i*, *γ(i)* – calibration factor matrix for compound *i*.

The relative intensity was derived by

$$\begin{pmatrix} S_{\frac{m}{e}, i} \\ \vdots \\ S_{\frac{m}{e}, j} \end{pmatrix} = \begin{pmatrix} S_{\text{compound}_X}\left(S_{\frac{m}{e}, i}\right) & \dots & S_{\text{compound}_Z}\left(S_{\frac{m}{e}, i}\right) \\ \vdots & \ddots & \vdots \\ S_{\text{compound}_X}\left(S_{\frac{m}{e}, j}\right) & \dots & S_{\text{compound}_Z}\left(S_{\frac{m}{e}, j}\right) \end{pmatrix} \cdot \begin{pmatrix} x_{\text{compound}_X} \\ \vdots \\ x_{\text{compound}_Z} \end{pmatrix} \quad (2)$$

S_{m/e,i} – Sensitivity for a specific *m/e* ratio;

S_{compound_x}(S_{m/e,i}) – Signal of compound *x* on *m/e, i*;

x_{compound,x} – molefraction of compound *x*.

2.3. Temperature programmed reduction (TPR)

The fresh catalyst (60 mg) was placed in the reactor, which was heated up under synthetic air (N₂:O₂ – 4:1, 99.9%, 30 sccm/min) with a temperature-ramp of 10 K/min to 1023 K, keeping this temperature for an hour and cooling down over night under constant air flow. To remove gas phase and adsorbed oxygen, a constant flow of nitrogen (30 sccm/min) purged through the reactor at room temperature for 30 min. The catalyst reduction was carried out by a feed stream of N₂:H₂ (9:1, 60 sccm/min) with a heating rate of 2 K/min, heating up until 1093 K. The analysis of the effluent gas was done with a thermal conductivity detector (Messkonzept, FTD 200) monitoring the stream composition each 0.5 s.

2.4. Temperature programmed desorption (O₂-TPD)

For temperature programmed desorption of oxygen, 1 g of fresh catalyst was used. The catalyst was heated up in a flow of He (99.99%, 20 sccm/min), with a temperature ramp of 5 K/min to

1093 K. In a second experiment 1 g of fresh catalyst was oxidized according to the method as mentioned in the TPR experiment. After the oxidation, the catalyst was treated as in the first O₂-TPD experiment. The detection was carried by mass spectrometer, which was described before.

2.5. Temperature programmed surface reaction (TPSR)

Each TPSR experiment was carried out with 1 g Na₂WO₄/Mn/SiO₂ fresh catalyst. The catalyst oxidation in all experiments was the same procedure as described in the TPR experiment. To remove gas phase and adsorbed oxygen, the catalyst was purged for 30 min by a constant flow of He (99.999%, 30 sccm/min) at room temperature. For methane-TPSR, a flow of 30 sccm/min methane (99.99%) was chosen. Ethane and ethylene-TPSR were carried out in a flow of He:C₂H_X (95:5, 30 sccm/min, 99.98% C₂H_X). All TPSR experiments had an initial temperature of 298 K and the catalyst material was heated up under the reactant feed with a temperature ramp of 1 K/min with a final temperature of 1073 K. Each TPSR experiment was repeated by variation of the temperature with 3, 4 (only for methane) and 5 K/min. For product detection a QMS was used, as described above.

2.6. Dynamic experiments

The reactor, filled with 1 g fresh catalyst, was heated up to 1023 K under a constant flow of He:O₂ (9:1, 30 sccm/min). The final temperature was kept constant during the whole experiment. After 10 min at constant reaction temperature, the oxygen flow was stopped by deactivation of the mass flow controller (MFC) and closing the switching valve. A flow of Helium (20 sccm/min) was used as purging step to remove gas phase and weakly adsorbed oxygen for 5 min at constant temperature. Helium feed was immediately replaced by CH₄ (20 sccm/min) for the reaction mode, keeping the temperature constant. That was done by closing and opening of the switching valves, simultaneously. The methane flow reached the reactor after pressure fluctuation had already been compensated for in the feed tube. In the first series of dynamic experiments the purge time was varied from 10, 180 min to 300 min without using new catalyst material for each run. The methane step time was 10 min. After these experiments the catalyst material was not reoxidized and cooled down in a stream of He (30 sccm/min). The catalyst materials were analyzed by nitrogen adsorption (BET) and XRD. This was followed by a series of experiments reducing the purge time interval from 5 min down to 15 s, using fresh catalyst material again. During these set of experiments, the methane flow rate was 30 sccm/min and the methane time step was 10 min.

In addition, we also varied the methane partial pressure during the reaction sequence in another experimental series with fresh catalyst material. That was realized by a lower flow rate of purge gas down to 10 sccm/min or 15 sccm/min, while methane flow rate was set in parallel to 20 sccm/min or 15 sccm/min. In total a feed of 30 sccm/min reached the reactor. Here the reaction step for methane was set to 5 min.

2.7. Steady state experiment

The reactor was filled with 1 g fresh catalyst and heated up to 1023 K under He:O₂ (8:2, 30 sccm/min). The feed was changed to CH₄:O₂ (95:5, 180 sccm/min) for 1 h, reaching the steady state conditions. The analyses of products were carried out with a QMS.

3. Results and discussion

3.1. TPR

The result of the H₂-TPR experiment is presented in Fig. 1. The oxidized catalyst showed one reduction pattern at 950 K. Furthermore the reduction curve shows early reduction by a slight decrease of the H₂ signal with respect to the baseline. This is also observed in the work of Shahri et al. [35]. They proposed that the early reduction is related to manganese oxide.

Peak integration was carried out and the amount of converted hydrogen was calculated according to Eq. (3). For the integration an adapted baseline was set to the corresponding hydrogen signals before and after the reduction pattern. The hydrogen consumption is equivalent to 17 O-atoms/nm², which is an astonishing high value. Typically expected monolayer coverages of transition metal oxides on various support materials are between 0.1 and 10 atoms/nm² [36]. It was found that various manganese oxide species and supported manganese oxides on silica can be reduced to MnO under hydrogen atmosphere [37,38]. Furthermore it was shown in EPR experiments that only manganese ions are reduced at 1073 K in the Na₂WO₄/Mn/SiO₂ catalyst, while tungsten ions had a constant valency of +VI [39]. In addition, the active phase of this material has a very flexible structure [40]. Therefore it is possible that also sublayers are involved in the reduction reaction during TPR experiments, considering the small specific surface area of that catalyst.

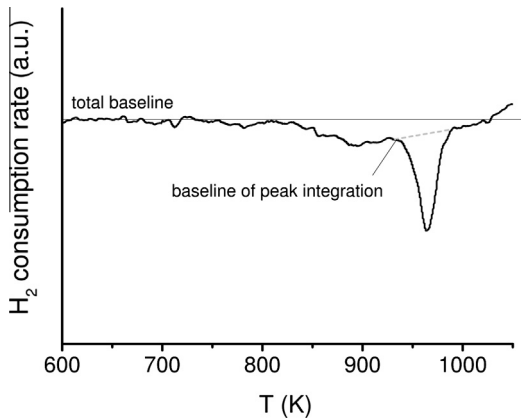


Fig. 1. H₂ TPR of oxidized Na₂WO₄/Mn/SiO₂ catalysts. 60 mg catalyst, N₂:H₂ (9:1, 60 sccm/min), 2 K/min.

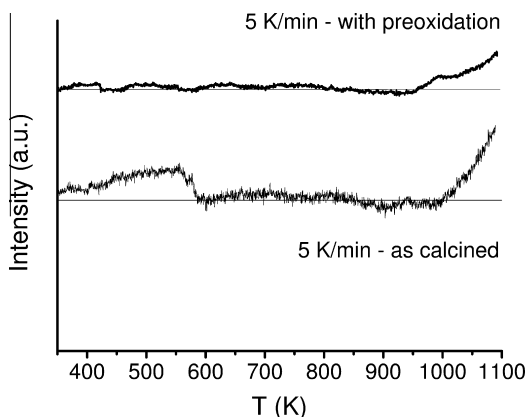


Fig. 2. O₂ TPD of different pretreated Na₂WO₄/Mn/SiO₂ catalysts. 1 g catalyst, He (99.999%, 20 sccm/min), 2 K/min.

$$n_{H_2} = \frac{A_{H_2,\text{peak}}[\% \text{ S}] \cdot \dot{V}\left[\frac{\text{m}^3}{\text{s}}\right] \cdot p[\text{Pa}]}{R\left[\frac{1}{\text{mol K}}\right] \cdot T[\text{K}]} \quad (3)$$

3.2. O₂-TPD

Experimental results of O₂-TPD experiments are depicted in Fig. 2. The “as calcined” catalyst, without further oxidation treatment, shows an O₂ peak at 550 K. For the oxidized catalyst such peak is missing. Radhakrishnan et al. reported such early desorption patterns for different supported Mn_xO_y catalysts [41]. Furthermore this phenomenon is also observed for bulk manganese oxides [42]. This may explain also the early reduction of the catalyst, observed in TPR experiments. However, in both cases stronger O₂ desorption starts at 1000 K. TPD experiments for that catalyst material have already been published by different groups. In the review article by Arndt et al. it is mentioned, that O₂-TPD experiments published by Fang et al. show no oxygen loss of the catalyst [43,44]. This is in clear contradiction to the report by Liu et al. [45]. They observed two oxygen signals at 1070 K and 1150 K, which were interpreted as surface layer oxygen and bulk oxygen. Especially the desorption peak at high temperatures in our experiments is in good agreement with their results.

3.3. TPSR

The results of the TPSR experiments are shown in Fig. 3. Different symbols represent different compounds. Symbols do not represent data points, which are too many, to show due to the fast detection rate. They represent an interpolation of the recorded data. The results of methane feed TPSR experiments are shown in Fig. 3A–C, with increasing temperature ramps.

Only CO and ethane formation is observed in this set of experiments. In each case first ethane is formed and followed by detection of CO. Both peaks shift at higher heating rates to higher temperatures. The ethane formation shifts slightly and forms no clear peaks at heating rates above 4 K/min. Such spectra can be interpreted in different ways. The most important step for the formation of ethane is the selective activation of methane by C–H bond cleavage. These radicals combine and form an ethane molecule. Na₂WO₄/Mn/SiO₂ catalyst material was verified by Jiang et al. [46]. According to the results of Lee et al. these radicals are also converted by surface bound oxygen into deep oxidation products [47]. On the other hand methane or ethane can be activated by another surface side, which leads also to the formation of deep oxidation products. We assume a short lifetime for the methyl radicals and therefore an immediate coupling or adsorption process on the catalyst surface. As mentioned before, in our TPSR experiments CO is formed much later and therefore the coupling process seems to be preferred. Furthermore the CO formation has to be observed parallel to ethane formation, when the oxidation of ethane is the origin of CO formation. Thus, the unselective activation of methane by another oxygen species on the catalyst surface is responsible for the formation of CO.

To analyze that situation in more detail, a series of simulations with the discussed reaction mechanisms in TPSR experiments were carried out and are presented in the supporting information. Our simulation results confirm that two active oxygen species on the catalyst surface in absence of gas phase oxygen contribute to OCM activity. Therefore not only gas phase and oxygen adsorption intermediates contribute to unselective methane activation. The nature of these species could be electrophilic and nucleophilic. On the one hand electrophilic oxygen is responsible for selective methane activation, which forms methyl radicals. On the other hand the nucleophilic species contributes to deep oxidation

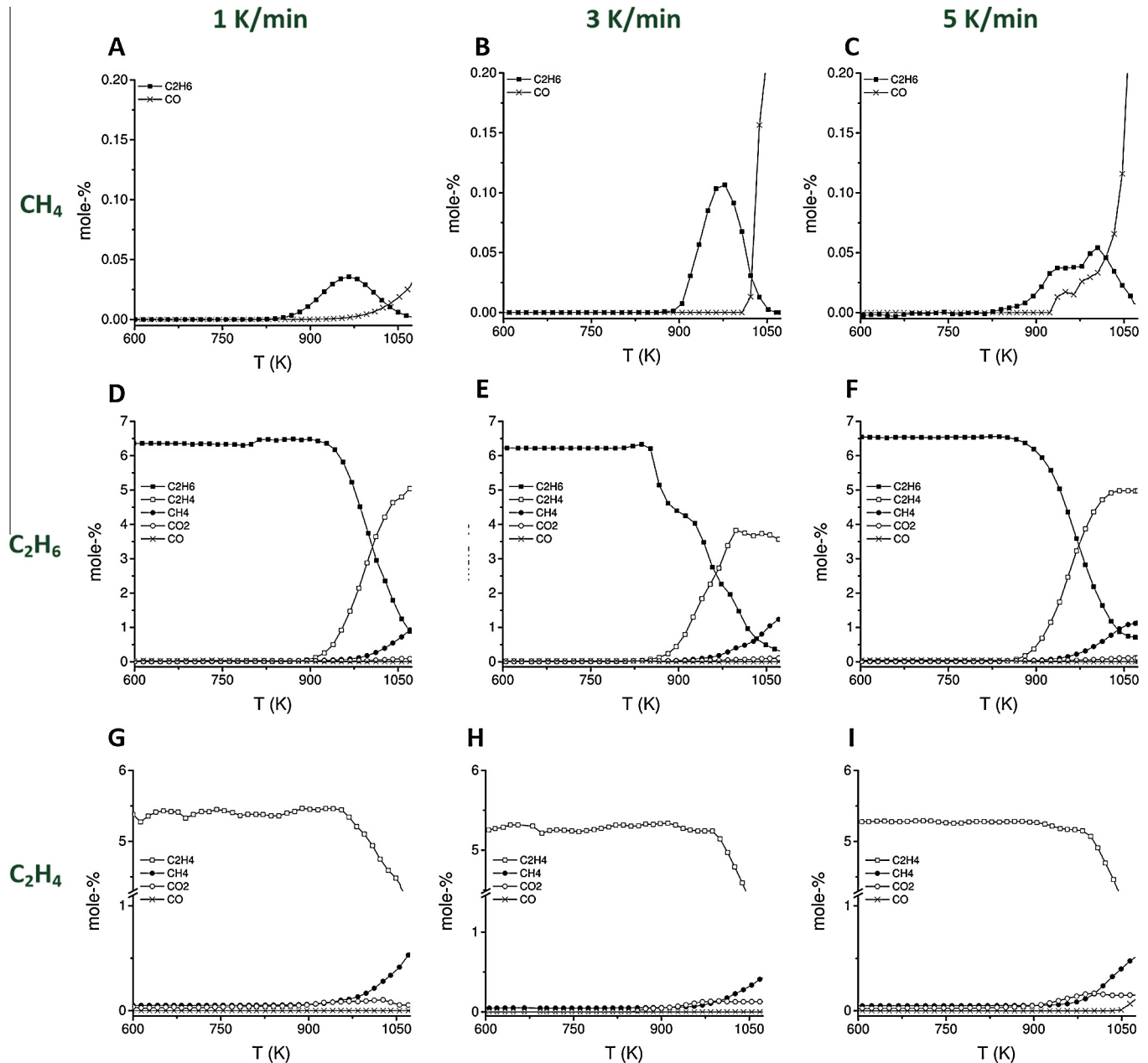


Fig. 3. TPSR product formation peaks of methane, ethane and ethene TPSR experiments at heating rates from 1 to 5 K/min, 1 g Na₂WO₄/Mn/SiO₂, A–C: methane TPSR, D–F: ethane TPSR (He:C₂H₆, 95:5), G–I: ethene TPSR (He: C₂H₄, 95:5), 1 g Na₂WO₄/Mn/SiO₂, 30 sccm/min.

product formation. In the literature similar TPSR experiments were carried out with Sr_xTi_yMgO, confirming our results [48]. The peak shift at different heating rates in TPSR experiments correlates with the slowest reaction in the reaction network. For OCM, this is assumed to be the methane activation reaction [49,50]. That effect is used in the next section to calculate the activation energy of selective methane activation.

It has to be noted that the variations in the peak areas in these experiments are caused in two different ways. On the one hand slow heating rates result in a longer reaction time for oxygen consumption for each temperature during the experiment. Therefore low amounts of methane can be converted already at lower temperatures. Thus, the peak amplitude is different for slow heating rates, because less oxygen is available on the catalyst surface at that time step. In addition, fast heating rates shift the methane activation by oxygen to higher temperatures and therefore the

reaction rate is much higher, because of higher temperature and more oxygen which was not converted so far. On the other hand, as shown in the last section, oxygen can desorb during the experiment. Therefore it is also possible that oxygen is released in gas phase, while methane adsorbs on the catalyst surface.

In the same manner as methane TPSR experiments, a series of TPSR experiments for ethane are shown in Fig. 3D–F. We observe ethane conversion to ethene starting at 890 K in all experiments. At 1050 K most of the ethane in the feed has been converted to ethene but conversion does not change further. The initial temperature of ethane consumption is higher than for methane activation in TPSR experiments. According to the different C–H bond strengths of methane and ethane, a lower activation temperature would be expected. However our TPSR experiments indicate a different activation mechanism for this molecule, which is not effected by C–H bond cleavage on the catalyst surface, which will

be discussed later. Furthermore, the formation of CO_2 and CH_4 can be observed at 950 K. These products indicate deep oxidation reaction steps as well as cracking reactions. Some carbon deposition as consecutive reaction product is also observed during reactor purging.

In TPSR experiments utilizing ethene as reactant only CO_2 and CH_4 formation at 920 K can be observed. That is in good agreement with our results of ethane TPSR experiments. CH_4 is a typical cracking product, which is formed from ethene during coke formation on the catalyst surface [51,52]. Carbon deposition was verified by oxidation of the catalyst subsequent to the TPSR experiment. Interestingly the formation of CO_2 and CH_4 starts in these experimental sets at the same temperature, which indicates a fast consecutive reaction from ethene to carbon deposition followed by CO_2 formation. Another possible explanation is a parallel reaction of ethene to cracking products and to carbon dioxide. The formation of deep oxidation and cracking products from ethene in absence of gas phase oxygen and the adsorption intermediate confirms our hypothesis that two active oxygen species seem to be responsible for ethene activation. On the one hand electrophilic oxygen can interact with the double bond of ethene, which could form ethylene oxygenates. These intermediates are further oxidized to deep oxidation products. On the other hand nucleophilic oxygen can activate ethene by C–H bond cleavage, which results into the formation of deep oxidation and cracking products. Such effect is well-known for ethylene oxide synthesis and for OCM on silver catalysts [53,54].

In Fig. 4A the product formation from ethane TPSR is presented in more detail for further discussion, than in Fig. 3. At 890 K small amounts of ethene can be observed, while water and hydrogen formation starts at the same temperature. At 950 K the amount of water decreases, while the amount of hydrogen still increases. As mentioned before, with increase of ethane conversion, CO_2 and methane signals can be observed. For monitoring the water formation in a consecutive reaction, the detailed product signals for ethene TPSR are shown in Fig. 4B. We observe at 920 K small amounts of water and CO_2 formation. At 1050 K the water amount decreases to the baseline level, while the CO_2 signal stays constant and methane formation can be observed. We observe also hydrogen formation at this temperature and much stronger ethene decomposition. Both product spectra show that the oxygen rich surface provides enough potential for oxidative dehydrogenation reaction steps, indicated by water formation. When that surface oxygen species is consumed, the reaction pathway changes to thermal decomposition reactions. For ethane TPSR experiments it is not

Table 3

Calculated free energy for oxidation and coking reactions from ethane and ethene at 1073 K.

No.	Reaction	ΔG (kJ/mole)
A	$\text{C}_2\text{H}_6 + \frac{1}{2} \text{O}_2 \rightarrow \text{C}_2\text{H}_4 + \text{H}_2\text{O}$	-187.4
B	$\text{C}_2\text{H}_6 \rightarrow \text{C}_2\text{H}_4 + \text{H}_2$	6.9
C	$\text{C}_2\text{H}_6 \rightarrow 2 \text{C} + 3 \text{H}_2$	32.0
D	$\text{C}_2\text{H}_6 + \text{H}_2 \rightarrow 2 \text{CH}_4$	-79.0
E	$\text{C}_2\text{H}_4 \rightarrow 2 \text{C} + 2 \text{H}_2$	-107.4
F	$\text{C}_2\text{H}_4 \rightarrow \text{C} + \text{CH}_4$	-118.9

clear whether thermal and oxidative dehydrogenation follows consecutive or parallel reaction routes.

To analyze this situation we calculated the free reaction energy for different coking and oxidation reactions at 1073 K by Eq. (4). The thermodynamic data for each compound was presented by McBride et al. [55]. The results are shown in Table 3.

$$\Delta G_R = \sum_i v_i \cdot \Delta H_{f,i} - T \cdot \sum_i v_i \cdot \Delta S_{f,i} \quad (4)$$

The oxidative dehydrogenation (ODH) is preferred compared to the thermal dehydrogenation (TDH) (Table 3, reaction A and B). Our ethane TPSR experiments in an empty reactor show thermal dehydrogenation in the same temperature range. According to that result we conclude that this phenomenon is a parallel route in the gas phase. The coupling process of two methyl radicals in gas phase at that temperature has a free energy of -328 kJ/mole. Thus, the energy must be transferred from the ethane intermediate for stabilization. Typically, that could be done by a collision with another molecule or the splitting of ethane into new molecules as ethene and hydrogen [6]. Decomposition of ethane to coke and hydrogen is not favored, but the backward reaction to methane by reduction may happen in the gas phase (Table 3, reaction C and D). The splitting reaction of ethane to methane hydrogen is necessary. As main hydrogen source the TDH of ethane may be responsible. Finally the ODH reaction of ethane is thermodynamically preferred but limited to the amount of stored oxygen on the catalyst surface. For TDH no adsorption of ethane on the catalyst surface is required.

The ethene decomposition to carbon and methane is slightly preferred, compared to the route of carbon and hydrogen formation only (Table 3, reaction E and F). The formation route of carbon dioxide cannot be resolved exactly, because the TPSR method is not sensitive enough for this reaction and the thermodynamic data for the $\text{Na}_2\text{WO}_4/\text{Mn}/\text{SiO}_2$ catalyst are unknown. Isotopic labeling

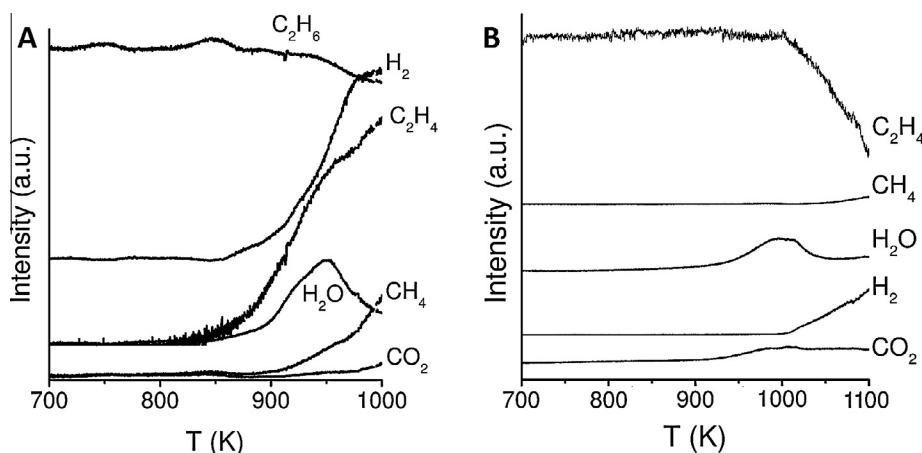


Fig. 4. Detailed ethane and ethene TPSR spectra, A: Ethane, B: Ethene, 3 K/min, 1 g $\text{Na}_2\text{WO}_4/\text{Mn}/\text{SiO}_2$, 30 sccm/min flow (He: C_2H_X , 95:5).

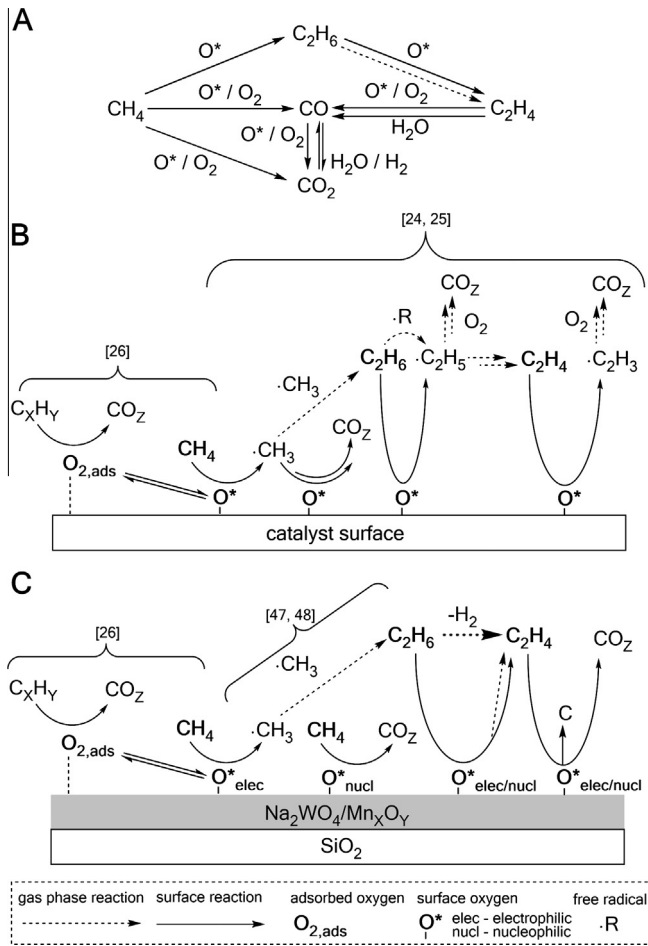


Fig. 5. A: Classical OCM reaction mechanism, including gas and surface reaction steps [8,9]. B: OCM reaction network according to Table 1. C: Proposed reaction route for OCM surface reaction based on TPSR experiments for Na₂WO₄/Mn/SiO₂ catalyst.

experiments with ¹³C in cofeed for that catalyst material are required to understand the origin of deep oxidation products.

To compare our findings, a well-established reaction network for the OCM is shown in Fig. 5A. It must be considered that the reaction network combines oxygen induced gas phase reactions, further gas phase activity by water and oxygen containing products, gas phase interactions of short lifetime intermediates as radicals and surface reactions in each step. Methane undergoes a parallel reaction to ethane or the deep oxidation product CO. The first route leads to ethane which can be converted to CO₂, which is in equilibrium with CO [56]. There are some modifications of this model, which were used for formal kinetic fitting procedures for the Na₂WO₄/Mn/SiO₂ catalyst [8,9].

The micro kinetic model from the introduction part is presented in Fig. 5B for further comparison. Interpretation of the TPSR results leads to a similar reaction model which is presented in Fig. 5C. The methane activation on the catalyst surface is followed by coupling process or by methyl radical absorption and the formation of oxy-genes. In contrast, our TPSR results indicate that methane activation is performed by two different surface oxygen species. Similar to the results of Sun et al. the ethane molecule is activated by oxygen on the catalyst surface or in gas phase by different radical species, which is common for the TDH reaction. The absence of gas phase oxygen leads to hydrogen production instead of water formation. Similar findings in these models show that the TDH is a serious parallel reaction route in the oxidative coupling of

methane. Such information is typically not obtainable in co-fed studies [57]. Furthermore this route reveals the complexity of different gas phase contributions to OCM, considering that the TDH is also a radical chain mechanism, as the selective methane activation on the catalyst surface is. Both reactions are initialized by methyl radical formation [50,58]. The mechanism of ethane activation on the catalyst surface by TPSR experiments cannot be revealed. In contradiction to the literature model, which requires gas phase oxygen for the formation of deep oxidation products by ethene oxidation, the TPSR results for the Na₂WO₄/Mn/SiO₂ catalyst reveal that also lattice oxygen is able to form such kind of products. Therefore it is possible that a Mars-van-Krevelen type mechanism should be considered for ethylene oxidation. In addition, it must be considered that also the cracking mechanism of ethylene is based on radical reactions and coke formation is preferred at higher ethene partial pressures [59].

However, the proposed model is similar to the key steps of the reaction network for the MgO catalyst. It shows that the MgO catalyst and the Na₂WO₄/Mn/SiO₂ catalyst have several similarities, despite their chemical difference.

3.4. Arrhenius parameter of methane TPSR

In the last section we pointed out, that the rate-determining step in TPSR experiments is strongly influenced by the heating rate. Redhead showed that desorption or the rate-determining reaction step follows an Arrhenius type function [33]. The rate constant of the surface reaction is proportional to the ratio of heating rate (β) and peak amplitude temperature (T_A) of the formed product, which is shown in Eq. (5). Following this method an Arrhenius plot can be constructed. Therefore we carried out methane TPSR experiments with heating rate variation from 1 to 4 K/min. Higher heating rates show no clear ethane peak as can be seen in the last section. For a more exact determination of the peak temperature from the observed ethane peaks, each peak was fitted to an empirical amplitude of the Gaussian function, which is shown in Eq. (6). All fits had an accuracy of 0.85 or better. The peak temperatures T_A , derived by this method are shown in Table 4.

$$k \sim \left(\frac{\beta}{T_A^2} \right) \quad (5)$$

$$x_i = x_{i0} + A \cdot \exp \left(-0.5 \cdot \left(\frac{T - T_A}{w} \right)^2 \right) \quad (6)$$

Fitting parameters:

- A – peak amplitude (ordinate).
- T_A – temperature of peak (abscissa).
- x_{i0} – offset of compound baseline.
- w – half width of peak signal.

The inverse temperatures of the ethane peaks were plotted to the Napierian logarithm of heating rate divided by the square of

Table 4

Ethane peak temperatures from methane TPSR experiments with heating rates from 1 to 4 K/min fitted by an empirical Gaussian function, 1 g Na₂WO₄/Mn/SiO₂, 30 sccm/min methane.

Heating rate β (K/min)	Temperature of ethane peak amplitude T_A (K)
1	964 ± 3
2	983 ± 1
3	985 ± 1
4	1003 ± 1

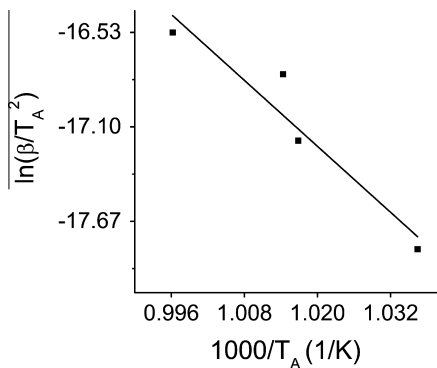


Fig. 6. Arrhenius type diagram of methane TPSR experiments using the ethane peak amplitudes, with heating rate of 1–4 K/min, 1 g $\text{Na}_2\text{WO}_4/\text{Mn}/\text{SiO}_2$, 30 sccm/min methane.

temperature of the peak amplitude, following the Redhead method [33]. The result is shown in Fig. 6.

Deriving the activation energy from this plot results in 275 ± 29 kJ/mole. The error of this astonishingly high value is strongly influenced by the ethane peak amplitude temperatures and the fitting results. Especially slow heating rates show a noisy and weak ethane signal. Other influences are CO formation and carbon deposition, which can block surface sites.

Comparing this activation energy to other apparent formal kinetic model parameters shows a high discrepancy between these values. The apparent activation energy for methane activation in steady state experiments varies from 133 kJ/mole up to 212 kJ/mole [35,60,61]. The different results show clearly that the derivation of a reliable result for this step is very challenging, considering that different oxygen species with different lifetime contributes to methane activation on the catalyst surface. However, Lunsford and Coworkers found similar value of 270 kJ/mole [62].

One reason for such a difference is the assumptions for the derivation of the reaction rate laws. In formal kinetic models, which were discussed in the last section, the activation of oxygen undergoes direct dissociation to an adsorbed species (O_x^*), which is shown in Eq. (7). In our work, we assume an involvement of strongly bound oxygen which may also be lattice oxygen (O_x^*). This may happen by an adsorption process ($\text{O}_{2,ads}$) and a consecutive dissociation reaction, which is shown in Eqs. (8) and (9).



To discuss this situation in more detail, a possible energy profile of the OCM consecutive reaction network is constructed in Fig. 7. We assume a two step activation process for oxygen, starting by adsorption ($\text{O}_{2,ads}$) followed by dissociation (O_x^*), which was postulated by Beck et al. [26]. The difference between these two species is their interaction with the surface. The adsorbed, electrophilic oxygen species $\text{O}_{2,ads}$ is responsible for deep oxidation products and is weakly bound on the catalyst surface. The dissociation of this species to the nucleophilic O_x^* involves the catalyst material, which causes a strong interaction. Both oxygen species must have different energy levels, because of their binding situation. The activation of methane to deep oxidation products undergoes a transition state with $\text{O}_{2,ads}$ (Fig. 7, E_{A1}) in steady state experiments. Assuming that the conversion of methane, ethane and ethene is initialized by C–H bond cleavage at the same oxygen species results in similar activation energies in the range of 120–180 kJ/mol. The much higher activation energy obtained from the TPSR experiments (Fig. 7, E_{A3}) clearly indicates the presence of the strongly bound, presumably dissociated oxygen species at a much lower energy level. Since this species is already formed during the pretreatment of the catalyst, a higher activation barrier has to be overcome. Due to the course of the experiments such a more stable species is required that survives the pretreatment of the catalyst. In addition this is supported by the findings of dynamic experiments, which are discussed in the next section. Similar findings and conclusions were made by Sofranko et al. and Jones et al., who carried out several dynamic experiments with catalyst materials including alkali promoted Mn/SiO_2 catalysts of different compositions [63–65]. They concluded that different surface oxides are involved in the OCM process, which confirms our results. Furthermore they have mentioned that non acidic oxide species are responsible for unselective methane activation. Several methane activation mechanisms were reviewed and discussed by Sinev [66]. He showed that a heterolytic proton or hydride ion abstraction of a C–H bond has similar energy expenditures as the molar energy of the lattice for stable oxides such as MgO or Al_2O_3 .

3.5. Dynamic experiments at constant temperature

3.5.1. Comparison of dynamic and steady state experiments

The results of our steady state experiment are shown in Table 5. Comparing the selectivities of both experimental sets, steady state and dynamic experiment (Table 6) shows similar selectivities of C_2 and deep oxidation products. It has to be noted that gas phase oxygen contributes to the results of steady state experiments, but not to the dynamic ones. The major difference in selectivities is the ratio of ethane to ethene. In the steady state experiment, ethane is the major product while in dynamic mode ethene dominates. The low methane conversion and high C_2 selectivity in the steady state experiment indicate less gas phase activity, compared to the catalytic activity. Therefore we determined the initial reaction rate of methane conversion from Eq. (10):

$$r_{\text{CH}_4} = \dot{n}_{\text{CH}_4} \cdot \frac{X_{\text{CH}_4}}{m_{\text{cat}}} \quad (10)$$

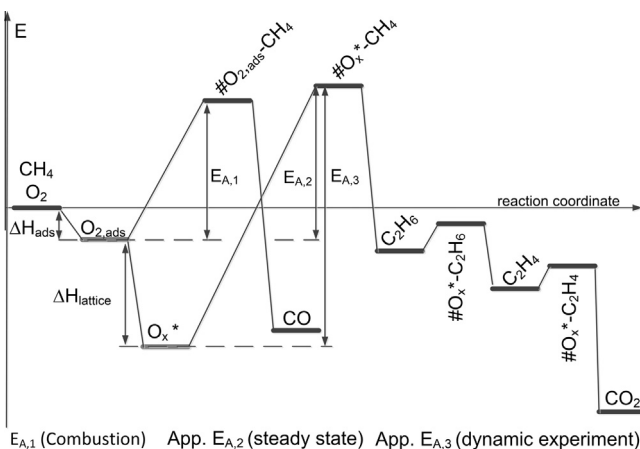


Fig. 7. Proposed energy profile for the OCM reaction at the $\text{Na}_2\text{WO}_4/\text{Mn}/\text{SiO}_2$ catalyst at 1073 K.

Table 5
Results of steady state experiment, $\text{CH}_4:\text{O}_2$ 95:5, 180 sccm/min, 1023 K, 1 g catalyst.

X CH ₄	X O ₂	S C ₂ H ₆	S C ₂ H ₄	S CO ₂	Y
0.032	0.393	0.676	0.114	0.210	0.025

Table 6

Species based oxygen balance for the dynamic experiments of methane at purge process duration from 10 min to 300 min, 1023 K, 20 sccm/min CH₄ for 10 min, 1 g Na₂WO₄/Mn/SiO₂.

Purge interval	10 min				180 min				300 min			
	CO ₂	CO	C ₂ H ₆	C ₂ H ₄	CO ₂	CO	C ₂ H ₆	C ₂ H ₄	CO ₂	CO	C ₂ H ₆	C ₂ H ₄
Aver. S	0.08	0.03	0.44	0.45	0.14	0.01	0.48	0.37	0.12	0.01	0.50	0.37
Aver. S	0.11		0.89		0.15		0.85		0.13		0.87	
#O/nm ²	7.2	5.4	1.8	3.6	10.4	0.6	4.5	7.1	8.8	0.58	4.6	6.8
#O/nm ²	18.00				21.66				20.66			

For the dynamic experiment, we assume that the activation of methane is the rate determining step. All reaction steps should have a reaction order of one, because of the activation by adsorption on the catalyst surface. We calculated the formation rates of all products during the first 20 s, using Eq. (11). It has to be noted that the methane partial pressure is not constant and still increasing in this time span. The experimental conditions and results for the dynamic experiment, with a purge time of 10 min, are shown in Table 6. A detailed discussion for the dynamic experiment follows in the next section.

$$r_{\text{CH}_4} = \sum_{\text{products}, i} \left(\frac{n_{\text{CH}_4}(dt)}{m_{\text{cat}}} \cdot v_i \cdot \frac{dx_i}{dt} \right) \quad (11)$$

n_{CH_4} – Moles of methane in 20 s.

x_i – Mole fraction of detected compound.

v_i – Stoichiometric factor.

In the steady state mode (242 μmol/g_{cat} min⁻¹), the rate is much higher compared to the dynamic mode (5.19 μmol/g_{cat} min⁻¹). The difference of almost two orders of magnitudes between both reaction rates indicates several effects.

On the one hand, in steady state mode the methane partial pressure is constant at 0.95 bar, while in the early period of the dynamic experiment methane partial pressure reaches only 0.1 bar. On the other hand, in steady state the major product is ethane, while in dynamic mode ethane and ethene have the same ratio. Therefore the formed ethane, which is even more reactive, competes in the dynamic experiment with the fed methane for the oxygen and therefore has also a substantial effect on the measured rate of methane consumption. We assume, that the low flow of 20 sccm/min in the dynamic experiment compared to 180 sccm/min in the steady state experiment allows more consecutive oxidative dehydrogenation of ethane. In addition the catalyst in steady state mode is continuously reoxidized by gas phase oxygen, which also enhances the reaction rate. Therefore not only the strongly bound oxygen intermediate is present on the catalyst surface. The weakly bound intermediate contributes also to the reaction rate. The reoxidation rate of the catalyst is fast compared to methane activation. Thus, the catalyst activity is not limited by the available amount of oxygen [47].

In contradiction, in dynamic experiments only small amounts of oxygen are stored on the catalyst surface, which are rapidly consumed. Further effects may limit the reaction rate by mass transport limitation. Possible is the formation of OH groups on Na₂WO₄/Mn/SiO₂, which can even block sites for methane adsorption. An additional limiting effect is the formation of coke, which can also block or convert active sites. All these effects cannot be fully excluded.

However, the large difference in methane partial pressures in steady state and dynamic experiments and the big differences in availability of oxygen in both experimental modes seem to have

the strongest effects on the reaction rate. Thus, we assume to observe comparable initial activity of the active oxygen sites in both types of experiments.

3.5.2. Influence of purge time and flow rate in dynamic experiments

In the first series we carried out a variation of the purge time with Helium from 10 min to 5 h. The results for these experiments are shown in Fig. 8. At time 0 s, the methane flow reached the catalyst bed after purging with inert gas for different time intervals. In all experiments we obtained a C2 selectivity of 85% or better. The amplitudes of the product peaks are much higher compared to the TPSR experiments. In the TPSR experiments the time span between oxidation and reaction is dependent on the heating rate. Furthermore, in TPSR experiments the oxygen conversion starts at lower temperatures and the amount of stored oxygen decreases in a longer time span. Slow increase of temperature enhances this effect. Reaching high temperatures, most of the oxygen will be converted and the peak amplitude is low. In the TPD experiment we could observe an oxygen loss at these temperatures, which may also contribute.

During the first minute in all dynamic experiments we observe deep oxidation products, indicated by CO and CO₂ formation. In this time interval the partial pressure of methane is still increasing, because it replaces the He from the purging process. At high methane partial pressures and reaching the ethene peak amplitude, the CO signal vanishes. The same phenomenon is observed for the CO₂ signal, which has a longer time span than CO. The early decrease of the CO₂ signal indicates that the available amount of oxygen for OCM reaction decreases rapidly and only small amounts are consumed for ethane and ethene formation. The preferred route of deep oxidation product formation, from methane or ethene, during dynamic experiments cannot be revealed. Isotopic labeling experiments for the Na₂WO₄/Mn/SiO₂ catalyst reveal no kinetic isotope effect (KIE) of CH₄/CD₄ for deep oxidation product formation [67]. It was concluded, that a different site on the catalyst surface is responsible for CO_x formation, which was suggested to be MnO_x.

To quantify our results an oxygen balance for each compound was calculated. To do so, the peak areas for each compound ($A_{i,\text{peak}}$) were integrated with respect to the baseline level. The amount of each product was calculated as shown in Eq. (12) and the corresponding moles of consumed oxygen with respect to the stoichiometry were determined. We assume that surface bound oxygen (O*) is an atomic species and quantitatively converted to water. The corresponding reactions are shown in Eqs. (13)–(16).

$$n_i = \frac{A_{i,\text{peak}} [\% \text{ s}] \cdot \dot{V} \left[\frac{\text{m}^3}{\text{s}} \right] \cdot p [\text{Pa}]}{R \left[\frac{\text{J}}{\text{mol K}} \right] \cdot T [\text{K}]} \quad (12)$$



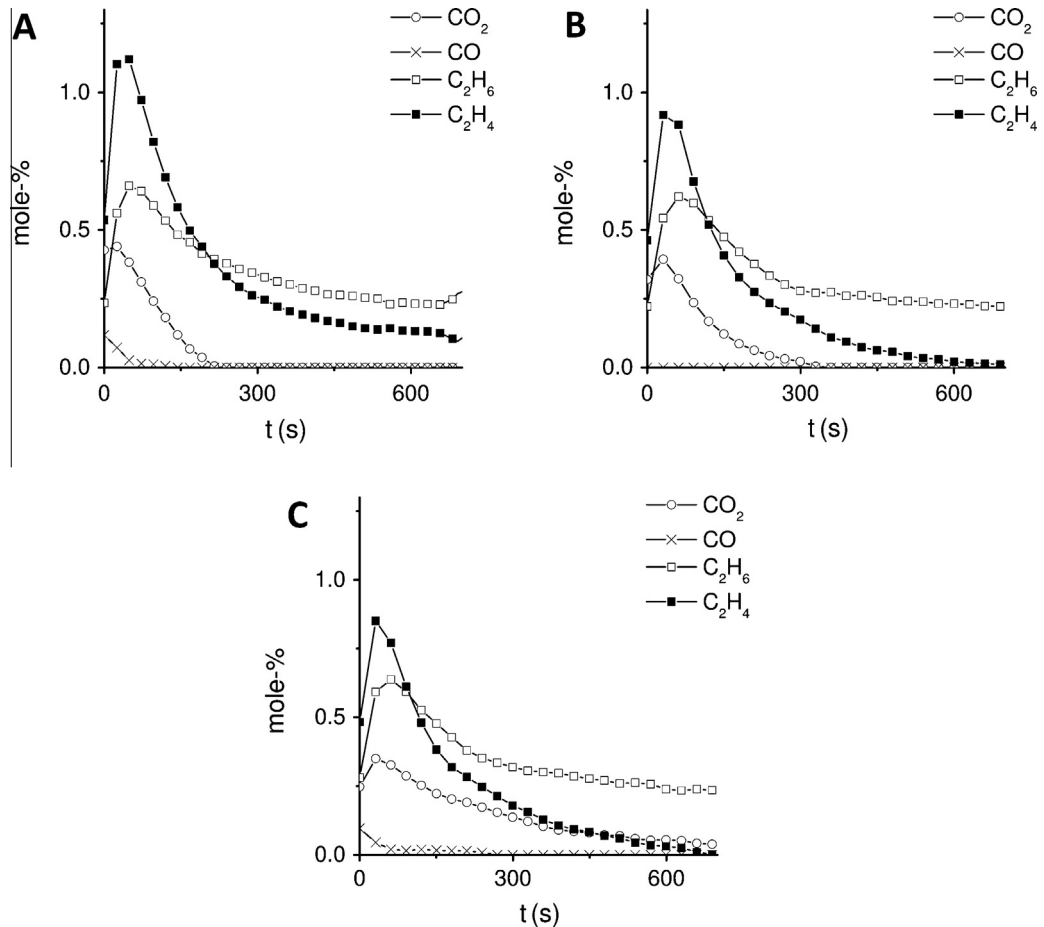


Fig. 8. OCM product signals from dynamic experiments with methane with increasing of purge duration at 1023 K, 20 sccm/min CH₄ for 10 min, 1 g Na₂WO₄/Mn/SiO₂, A – 10 min He purge, B – 180 min He purge, C – 300 min He purge.



The results of these oxygen balances are listed in Table 6. The calculated oxygen amounts are similar to those from the H₂-TPR experiment. Increasing the purge time has no substantial influence on the available oxygen amount. As mentioned before, most oxygen was converted to form deep oxidation products. Only increasing of the purge time interval to 5 h decreases the peak amplitudes of all formed products slightly. Another effect is the decrease of the peak tailing of ethene, whereas the tailing of CO₂ is increased. This implies that the catalyst structure could have changed. As demonstrated in our TPD experiment the catalyst material desorbs oxygen at high temperatures. That could lead to a change of the oxidation state of manganese oxide from Mn₂O₃ to Mn₃O₄, for instance. Both species have different activity for unselective methane activation [38].

With this experiment, we can show that the provided oxygen is stored under harsh conditions even for hours. This implies that the active center on the Na₂WO₄/Mn/SiO₂ for OCM is bound or integrated oxygen in the lattice structure, because simply adsorbed oxygen species should not survive such treatment without additional stabilization. From the mechanistic point of view these results support the theory of a Mars-van-Krevelen like mechanism for the OCM reaction on Na₂WO₄/Mn/SiO₂.

Similar step-change experiments in the OCM with this material were carried out by Salehoun and coworkers [68]. They could show an increase of the ethane peak by an increase of reaction

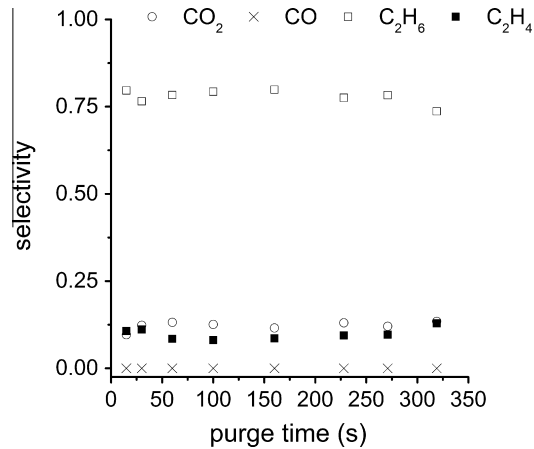


Fig. 9. Selectivity for purge time reduction of dynamic experiments from 5 min to 15 s, 1 g Na₂WO₄/Mn/SiO₂, 1023 K, 30 sccm/min CH₄ for 10 min.

temperature, indicating larger amounts of available oxygen. An interesting difference is the observed ratio of ethane and ethene, because their results show strong ethane formation and less ethene formation, but overall C₂ selectivity is close to our results. They also concluded that C₂ products may come from lattice oxygen by selective methane activation, where CO is formed by unselective reaction of methane with gas phase oxygen. Both interpretations confirm our results. They mentioned also that the

Table 7

Compound based oxygen balance for short He purge times in dynamic experiments from 300 s down to 15 s, 1 g Na₂WO₄/Mn/SiO₂, 1023 K, 30 sccm/min CH₄ for 10 min.

Purge time (s)	CO ₂ (#O/nm ²)	CO (#O/nm ²)	C ₂ H ₆ (#O/nm ²)	C ₂ H ₄ (#O/nm ²)	Σ (#O/nm ²)
300	10.70	0	7.33	2.57	20.60
270	9.41	0	7.64	1.89	18.94
230	9.77	0	7.27	1.77	18.81
160	8.94	0	7.72	1.66	18.32
100	9.14	0	7.19	1.47	17.80
60	9.46	0	7.02	1.52	17.99
30	9.74	0	7.55	2.19	19.47
15	8.27	0	8.55	2.30	19.11

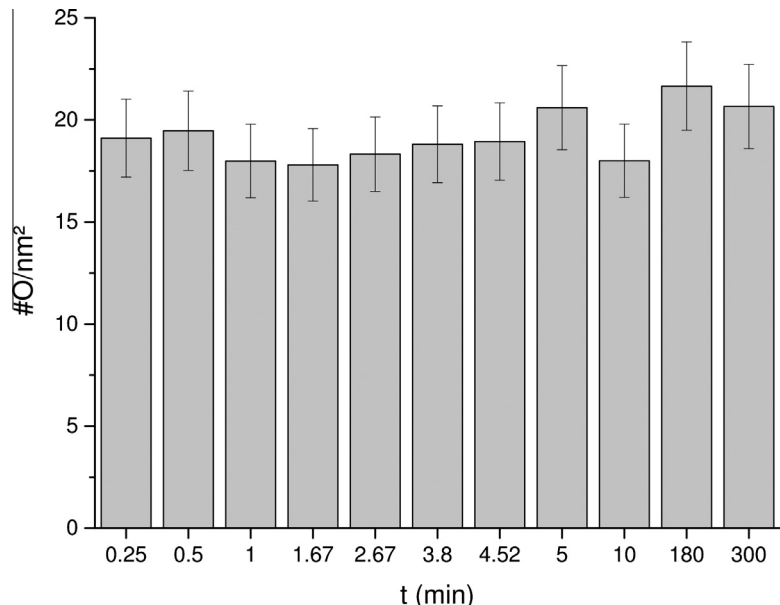


Fig. 10. Total number of oxygen atoms per nm² at different purge time durations in dynamic experiments, 1 g Na₂WO₄/Mn/SiO₂, 1023 K, 20–30 sccm/min CH₄ for 10 min.

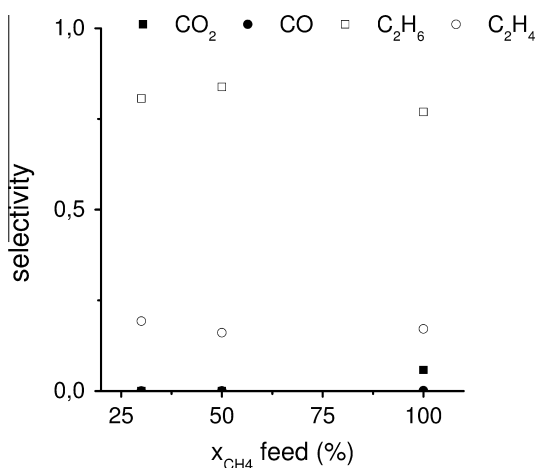


Fig. 11. Selectivity of the varied methane feed concentration in dynamic experiments, 1 g Na₂WO₄/Mn/SiO₂, 1023 K, 30 sccm/min CH₄ for 5 min.

reduced catalyst will be reoxidized by gas phase oxygen, while the catalyst reoxidation rate is much faster than its rate of reduction by bond cleavage of alkanes or alkenes.

The selectivities observed in short purge time experiments are shown in Fig. 9. A detailed oxygen balance for each compound can be found in Table 7. The C2 selectivity changes substantially.

The major product is ethane, whereas ethene decreases and is in the range of the CO₂ signal, which is a minor product. During these experiments no CO was detected by decrease of residence time. On the one hand that could be interpreted, that no methane was activated in an unselective way and the CO₂ results from ethene activation, according to the discussed reaction network before. On the other hand it must be considered that CO could be also oxidized to CO₂ on the catalyst surface. Therefore it is not possible to distinguish between methane and ethene activation to form deep oxidation products.

The number of available oxygen atoms stays constant at 20 O/nm². A more or less constant number of converted oxygen atoms from the catalyst surface indicate that no significant coke formation from ethene disproportionation blocks available surface oxygen for the OCM reaction, in both sets of experiments. These experiments imply that the feed contact time with the catalyst bed has a strong influence on the C2 product ratio, but not on deep oxidation products. That supports our statement from the TPSR section that a different oxygen species must be responsible for deep oxidation product formation, which can interact with methane and ethene in a different, independent route. In our TPSR experiments we discussed that the parallel reactions ODH on the catalyst surface and TDH in gas phase are responsible for C₂H₄ formation. It has to be noted that we cannot reveal how strong these routes are involved in product formation.

Another observed phenomenon is that there is still no influence of the purge interval on the OCM itself. Even for 15 s purge

Table 8

Compound based oxygen balance for reduced methane partial pressure in the reactant feed of dynamic experiments, 1 g Na₂WO₄/Mn/SiO₂, 1023 K, 30 sccm/min CH₄ for 5 min.

CH ₄ feed ratio	CO ₂ (#O/nm ²)	CO (#O/nm ²)	C ₂ H ₆ (#O/nm ²)	C ₂ H ₄ (#O/nm ²)	Σ (#O/nm ²)
1.00	5.22	0.03	4.31	1.45	11.01
0.50	1.75	0.01	2.87	0.85	5.48
0.33	1.24	0.00	2.00	0.80	4.03

duration, there is no shift in the selectivities observed. This result is only plausible, when short purge processes are sufficient for removing all gas phase and adsorbed oxygen from the catalyst surface and the reoxidation rate of the catalyst is fast. A sum of the available oxygen on the Na₂WO₄/Mn/SiO₂ is shown in Fig. 10 that shows no significant change in the available oxygen amount on the catalyst surface for purge time variation.

3.5.3. Methane partial pressure variation in the reactant feed of dynamic experiments

The response of the selectivities to methane partial pressure variation in the reactant feed is shown in Fig. 11. The ethene selectivity increases slightly when reducing the methane partial pressure. CO₂ is only observed for pure methane feed and only small traces of CO appear. Therefore the C2 selectivity is around 0.9. A decrease of the methane partial pressure shifts the overall C2 selectivity for these experimental conditions to 0.96. By reducing the methane fraction in the feed, the converted oxygen amount from the catalyst surface decreases in the same ratio (Table 8). These numbers indicate that less oxygen is consumed, compared to the dynamic experiments before, which showed 20 O/nm². In addition, reducing the reactant feed duration from 10 to 5 min leads to a decrease of the converted oxygen, in pure methane feed experiment, too.

This indicates again, that there is linear methane partial pressure dependence for the overall OCM process on Na₂WO₄/Mn/SiO₂ catalysts. Our results are in good agreement with isotopic labeling experiments of Burch et al., who found a similar correlation [67].

4. Conclusion

In our H₂-TPR experiments we found reduction of Na₂WO₄/Mn/SiO₂ catalyst at 950 K. The O₂-TPD shows weak early oxygen desorption at 540 K and a clear oxygen desorption peak at 1070 K. Both experiments show that the catalyst structure provides oxygen which interacts with different oxidation potentials.

In TPSR experiments we found that methane can be converted into CO or ethane. That is caused by two different oxygen species according to our simulation results. The formed ethane can be oxidized further to ethene in a parallel reaction, by oxidative or thermal dehydrogenation on the catalyst surface or in gas phase. This process is dependent on the available oxygen amount at the catalyst surface and a serious route in the OCM reaction. Ethene undergoes disproportion to coke and methane formation. We also observe CO₂ formation in a parallel pathway. All these pathways were only obtainable in non-cofeed experiments. Methane TPSR experiments at heating rates of 1–4 K/min result in an activation energy of 275 kJ/mole for methane activation and ethane formation by catalyst bound oxygen. This value is common by the assumption that lattice oxygen or a strongly adsorbed oxygen species is involved in the rate determining step of the OCM process on the Na₂WO₄/Mn/SiO₂ catalyst. The higher activation energy obtained from a TPSR experiment compared to methane activation energies from steady state experiments in the literature can be explained by an energy profile including such an activated oxygen species, which is shown in Fig. 7. We conclude that strongly

adsorbed or lattice oxygen is responsible for methane activation, which has a much lower energy level, compared to adsorbed molecular oxygen. In our dynamic experiments we found that around 20 O/nm² are available on the catalyst surface for the OCM process. This number is independent of purge times between 15 s and 300 min and even of the flow rate of methane, which has a strong effect on C2 selectivity but not on the total product amount. Such a high number of available oxygen atoms per surface area indicate involvement of lattice oxygen and may be from sublayers of the catalyst material, caused on its flexible structure properties. A linear decrease of the converted oxygen atoms on the catalyst surface is only observed when reducing the methane feed duration. Partial pressure variation of methane showed a linear dependence on the converted number of oxygen atoms, too.

Finally, the nature of oxygen adsorption and conversion by that catalyst material has strong similarities with other well-known partial oxidation reactions as the synthesis of formaldehyde or ethylene oxide from methanol or ethene on silver catalysts [53,54,69,70]. The function to store a selective oxygen species for chemical reactions under harsh conditions for different periods of time might be useful for dynamic reactor concepts, such as chemical looping. Such a concept has the advantage of excluding oxidation reactions in gas phase. Typical material properties for such a concept are fast storage of oxygen and fast oxygen release for chemical reactions [71]. In our work we could show that a reoxidation of the material is fast compared to the OCM reaction. A direct conversion of the strongly bound oxygen species on the catalyst surface by methane might be a proper manner for a modified chemical looping concept. Such a concept was already successfully tested for propane dehydrogenation and is reviewed in detail elsewhere [72,73].

Acknowledgment

This work is part of the UNICAT excellence cluster, which is coordinated by the Technische Universität Berlin. The funding of this cluster by the German Research Foundation (DFG) is gratefully acknowledged.

Appendix A. Supplementary material

Supplementary data associated with this article can be found, in the online version, at <http://dx.doi.org/10.1016/j.jcat.2016.06.014>.

References

- [1] T. Ren, M.K. Patel, K. Blok, Energy 33 (2008) 817.
- [2] J.J.H. Lunsford, Catal. Today 63 (2000) 165.
- [3] H. Zhang, J. Wu, B. Xu, C. Hu, Catal. Lett. 106 (2006) 161.
- [4] A.V. Kruglow, M.C. Bjorklund, R.W. Carr, Chem. Eng. Sci. 51 (1996) 2945.
- [5] H.R. Godini, A. Gili, O. Görke, U. Simon, K. Hou, G. Wozny, Energy Fuels 28 (2014) 877.
- [6] S. Dooley, M.P. Burke, M. Chaos, Y. Stein, F.L. Dryer, V.P. Zhukov, O. Finch, J.M. Simmie, H.J. Curran, Int. J. Chem. Kinet. 42 (2010) 527.
- [7] H. Schwarz, M. Geske, C. Franklin Goldsmith, R. Schlögl, R. Horn, Combust. Flame 161 (2014) 1688.
- [8] T.P. Tiemersma, M.J. Tuinier, F. Gallucci, J.A.M. Kuipers, M.V.S. Annaland, Appl. Catal. A Gen. 433–434 (2012) 96.
- [9] K. Takanabe, E. Iglesia, J. Phys. Chem. C 113 (2009) 10131.

- [10] J.S. Ahari, R. Ahmadi, H. Mikami, K. Inazu, S. Zarrinpashne, S. Suzuki, K. Aika, *Catal. Today* 145 (2009) 45.
- [11] Y. Nakisa, G.M.H. Reza, *J. Nat. Gas Chem.* 18 (2009) 39.
- [12] N. Razmi Farooji, A. Vatanai, S. Mokhtari, *J. Nat. Gas Chem.* 19 (2010) 385.
- [13] M. Ghiasi, A. Malekzadeh, S. Hoseini, Y. Mortazavi, A. Khodadadi, A. Talebzadeh, *J. Nat. Gas Chem.* 20 (2011) 428.
- [14] P.K. Kundu, A.K. Ray, A. Elkamel, *Can. J. Chem. Eng.* 90 (2012) 1502.
- [15] Z. Taheri, N. Seyed-Matin, A.A. Safekordi, K. Nazari, S.Z. Pashne, *Appl. Catal. A Gen.* 354 (2009) 143.
- [16] N. Yaghobi, M.R.H. Ghoreishy, V. Eslamimanesh, *Asia-Pac. J. Chem. Eng.* 3 (2008) 202.
- [17] H.R. Godini, V. Fleischer, O. Görke, S. Jaso, R. Schomäcker, G. Wozny, *Chemie Ing. Tech.* 86 (2014) 1906.
- [18] A. Ekstrom, R. Regtop, S. Bhargava, *Appl. Catal.* 62 (1990) 253.
- [19] G. Lane, E. Wolf, *J. Catal.* 113 (1988) 144.
- [20] G.J. Tjatjopoulos, I.A. Vasalos, *Appl. Catal. A Gen.* 88 (1992) 213.
- [21] M.S. Palmer, M. Neurock, M.M. Olken, *J. Am. Chem. Soc.* 124 (2002) 8452.
- [22] V.J.V.J. Ferreira, P. Tavares, J.L.J.L. Figueiredo, J.L. Faria, *Catal. Commun.* 42 (2013) 50.
- [23] Q.J. Yan, Y. Wang, Y.S. Jin, Y. Chen, *Catal. Lett.* 13 (1992) 221.
- [24] M.R. Lee, M.J. Park, W. Jeon, J.W. Choi, Y.W. Suh, D.J. Suh, *Fuel Process. Technol.* 96 (2012) 175.
- [25] J. Sun, J. Thybaut, G.B. Marin, *Catal. Today* 137 (2008) 90.
- [26] B. Beck, V. Fleischer, S. Arndt, M.G. Hevia, A. Urakawa, P. Hugo, R. Schomäcker, *Catal. Today* 228 (2014) 212.
- [27] L. Shu-Ben, *Chinese J. Chem.* 19 (2001) 16.
- [28] M. Sohrabi, B. Dabir, A. Eskandari, *J. Chem. Technol. Biotechnol.* 67 (1996) 15.
- [29] J.L. Falconer, J.A. Schwarz, *Catal. Rev. – Sci. Eng.* 25 (1983) 141.
- [30] J.W. Niemantsverdriet, in: *Spectrosc. Catal. An Introd.*, 3rd ed., Wiley-VCH Verlag GmbH & Co. KGaA, Weinheim, 2007, pp. 11–31.
- [31] S.J. Blanksby, G.B. Ellison, *Acc. Chem. Res.* 36 (2003) 255.
- [32] J. McCarty, H. Wise, *J. Catal.* 57 (1979) 406.
- [33] P.A. Redhead, *Vacuum* 12 (1962) 203.
- [34] U. Simon, O. Görke, A. Berthold, S. Arndt, R. Schomäcker, H. Schubert, *Chem. Eng. J.* 168 (2011) 1352.
- [35] S.M.K. Shahri, S.M. Alavi, *J. Nat. Gas Chem.* 18 (2009) 25.
- [36] I.E. Wachs, *Catal. Today* 27 (1996) 437.
- [37] N. Anacleto, O. Ostrovski, S. Ganguly, *ISIJ Int.* 44 (2004) 1615.
- [38] E.R. Stobbe, B.A. de Boer, J.W. Geus, *Catal. Today* 47 (1999) 161.
- [39] Z. Jiang, H. Gong, S. Li, *Stud. Surf. Sci. Catal.* 112 (1997) 481.
- [40] S. Sadjadi, S. Šašo, H.R. Godini, S. Arndt, M. Wollgarten, R. Blume, O. Görke, R. Schomäcker, G. Wozny, U. Simon, *Catal. Sci. Technol.* 5 (2015) 942.
- [41] R. Radhakrishnan, S.T. Oyama, J.G. Chen, K. Asakura, *J. Phys. Chem. B* 105 (2001) 4245.
- [42] H.C. Genuino, S. Dharmarathna, E.C. Njagi, M.C. Mei, S.L. Suib, *J. Phys. Chem. C* 116 (2012) 12066.
- [43] S. Arndt, T. Otremba, U. Simon, M. Yıldız, H. Schubert, R. Schomäcker, *Appl. Catal. A Gen.* 53 (2012) 425–426.
- [44] X. Fang, S. Li, J. Gu, D. Yang, *J. Mol. Catal.* (1992) 255.
- [45] Y. Liu, R. Hou, X. Liu, J. Xue, S. Li, *Stud. Surf. Sci. Catal.* 119 (1998) 307.
- [46] Z.-C. Jiang, L.-B. Feng, H. Gong, H.-L. Wang, *Methane and Alkane Conversion Chemistry*, Springer, US, New York, 1995.
- [47] M.R. Lee, M.-J. Park, W. Jeon, J.-W. Choi, Y.-W. Suh, D.J. Suh, *Fuel Process. Technol.* 96 (2012) 175.
- [48] K. Tomishige, X. Li, K. Fujimoto, *Phys. Chem. Chem. Phys.* 1 (1999) 3039.
- [49] G.E. Keller, M.M. Bhasin, *J. Catal.* 73 (1982) 9.
- [50] D.J. Driscoll, J.H. Lunsford, *J. Phys. Chem.* 89 (1985) 4415.
- [51] H. Zimmermann, R. Walzl, *Ullmann's Encycl. Ind. Chem.* 13 (2012) 547.
- [52] S.H. Khodamorad, D. Haghshenas Fatmehsari, H. Rezaie, A. Sadeghipour, *Eng. Fail. Anal.* 21 (2012) 1.
- [53] A.J. Nagy, G. Mestl, R. Schlögl, *J. Catal.* 188 (1999) 58.
- [54] R.B. Grant, R.M. Lambert, *J. Catal.* 92 (1985) 364.
- [55] B.J. McBride, S. Gordon, M.A. Reno, *NASA Rep. TM-4513*, 1993.
- [56] Z. Stansch, L. Mleczko, M. Baerns, *Ind. Eng. Chem. Res.* 36 (1997) 2568.
- [57] E. Morales, J. Lunsford, *J. Catal.* 5 (1989).
- [58] V.N. Snytnikov, T.I. Mishchenko, V.N. Snytnikov, S.E. Malykhin, V.I. Avdeev, V. N. Parmon, *Res. Chem. Intermed.* 38 (2012) 1133.
- [59] S. Wauters, G.B. Marin, *Ind. Eng. Chem. Res.* 41 (2002) 2379.
- [60] M. Daneshpayeh, A. Khodadadi, N. Mostoufi, Y. Mortazavi, R. Sotudeh-Gharebagh, A. Talebzadeh, *Fuel Process. Technol.* 90 (2009) 403.
- [61] M. Daneshpayeh, N. Mostoufi, A. Khodadadi, R. Sotudeh-gharebagh, *Energy Fuels* 23 (2009) 3745.
- [62] S. Pak, P. Qiu, J.H. Lunsford, *J. Catal.* 230 (1998) 222.
- [63] C.A. Jones, J.J. Leonard, J.A. Sofranko, *J. Catal.* 103 (1987) 311.
- [64] J.A. Sofranko, J.J. Leonard, C.A. Jones, *J. Catal.* 103 (1987) 302.
- [65] C.A. Jones, J.J. Leonard, J.A. Sofranko, *Energy Fuels* 1 (1987) 12.
- [66] M.Y. Sinev, *Russ. J. Phys. Chem. B* 1 (2007) 412.
- [67] R. Burch, S.C. Tsang, C. Mirodatos, J.G. Sanchez, *Catal. Lett.* 7 (1990) 423.
- [68] V. Salehoun, A. Khodadadi, Y. Mortazavi, A. Talebzadeh, *Chem. Eng. Sci.* 63 (2008) 4910.
- [69] A. Nagy, G. Mestl, T. Uhle, G. Weinberg, R. Schi, *J. Catal.* 179 (1998) 548.
- [70] P.A. Kilty, W.M.H. Sachtler, *Catal. Rev.* 10 (1974) 1.
- [71] E. Jerndal, T. Mattisson, A. Lyngfelt, *Chem. Eng. Res. Des.* 84 (2006) 795.
- [72] D. Creaser, B. Andersson, R.R. Hudgins, P.L. Silveston, *Chem. Eng. Sci.* 54 (1999) 4437.
- [73] A. Adesina, H. Budman, J. Brandner, G. Bumimovich, W. Epling, J. Hanika, K. Hashimoto, P. Haure, R. Hudgins, M. Kawase, C.-Y. Li, Y. Matros, G. Meira, M. Petkovska, M. Pritzker, A. Renken, A. Rodrigues, H. Sapoundjiev, J. Scharer, A. Seidel-Morgenstern, P. Silveston, *Periodic Operation of Reactors*, 2005.

Investigation of the surface reaction network of the oxidative coupling of methane over $\text{Na}_2\text{WO}_4/\text{Mn}/\text{SiO}_2$ catalyst by temperature programmed and dynamic experiments - Supporting information

1. Experimental

1.1. Setup for TPSR and Dynamic experiments

The setup for dynamic experiments is illustrated in Figure 1. Different gases can be transported by mass flow controllers (MFC). In front of each MFC a switching valve (SV) was installed. The connection pipe between these valves and the reactor entrance has a length of 2 m to handle pressure fluctuation by switching the two way valves. All connections were tested by leakage spray to test for micro gas leakages. That was verified by mass spectroscopy to ensure that even no traces of gas phase oxygen by air leakage contribute to dynamic experiments. The methane MFC has two inlets, which can be selected by a three way valve. That allows the dose of ethane and ethylene. All MFC's were calibrated by an external flow meter (Gilian, Gilibrator-2 Calibrator) considering the different gases. A detailed analysis about the furnace temperature profile is reported in the next section. Finally the outlet of the reactor was connected to a quadrupole mass spectrometer (IPI QMS, GAM 200).

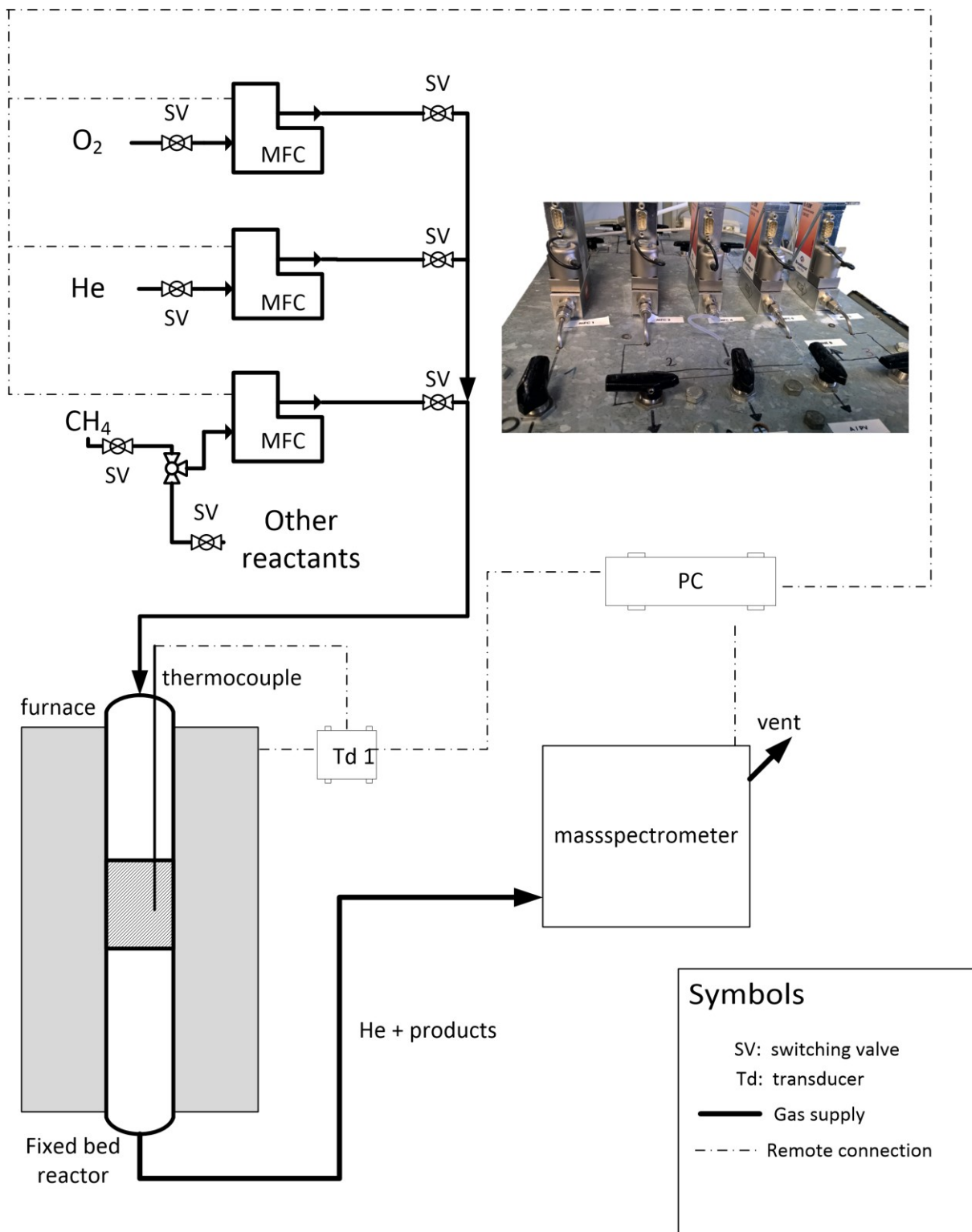


Figure 1 - Construction scheme of the dynamic setup

1.2. Reactor and Furnace

The quartz made reactor is presented in Figure 2. The type K thermocouple is placed in a quartz channel. The tip position of that channel is inside of the catalyst bed. That position was used for temperature control. The catalyst material is placed on a quartz frit, which is in the isothermal zone of the reactor.

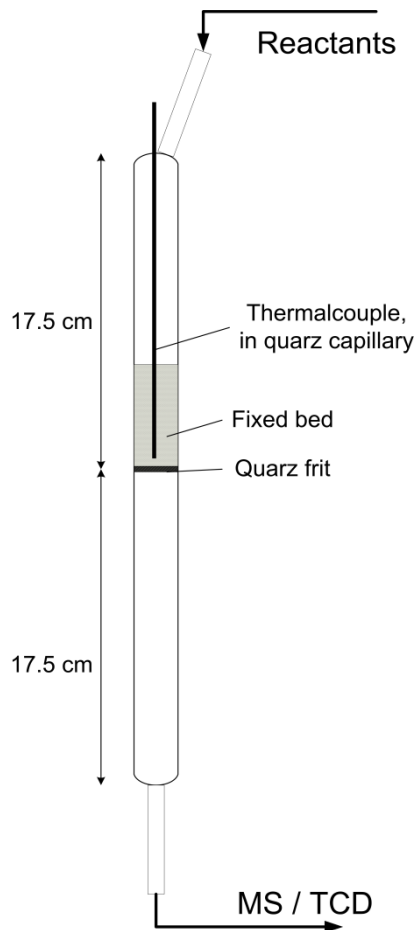


Figure 2- Detailed scheme of the fixed bed reactor ($d_{in} = 9 \text{ mm}$, $d_{capillary,thermocouple} = 4 \text{ mm}$).

A series of axial temperature profiles of the heated parts of the reactor were measured by an additional, movable type K thermocouple. The reactor was placed in the furnace and heated up to a fixed temperature. After reaching that temperature a movable thermocouple was introduced at the inlet or the outlet of the reactor to measure the local temperature on several positions. At this time, no gas was send through the reactor. The results are presented in Figure 3. The position of the catalyst bed ($2 \text{ g Na}_2\text{WO}_4/\text{Mn/SiO}_2$) is also presented. It can be seen, that the catalyst bed is clearly in the axial isothermal zone of the reactor. The radial temperature profile was neglected because of symmetric geometry of the reactor and temperature control inside of the catalyst bed. During dynamic experiments no temperature increase was observed. Calculation of the adiabatic temperature increase results in 33 K, assuming the total oxidation of methane in gas phase according to equation (1). The concentration for oxygen was set to the presented value in the manuscript, considering the fictive free space of the catalyst material as reaction volume.



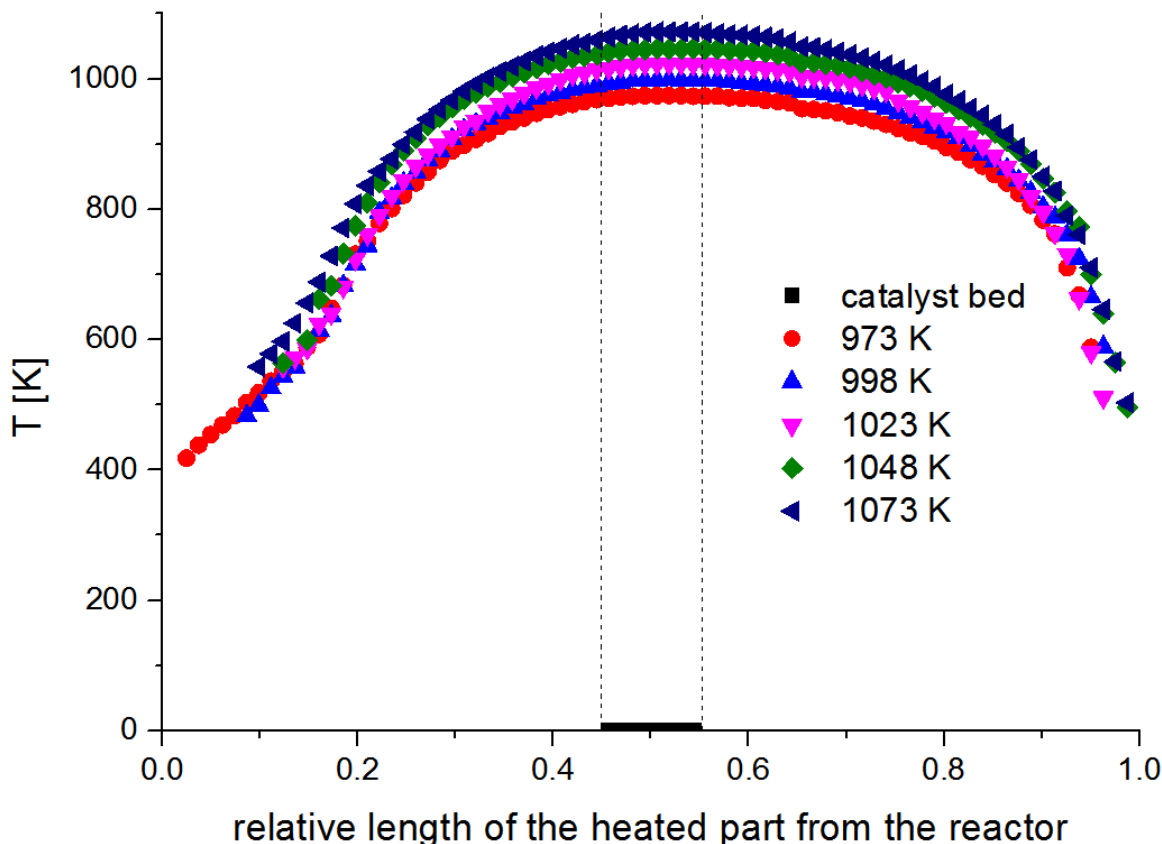


Figure 3 – Axial temperature profile of the heated reactor section at constant set temperature.

2. Catalyst characterization

2.1.BET

The nitrogen adsorption apparatus and sample preparation was described elsewhere. [1] Selected results are presented in Table 1. The enumeration of some experiments follows the experimental plan in Table 2. After the oxidation pretreatment procedure the catalyst material shows only small shrinkage of the specific surface area (SSA). After performing dynamic experiments only small deviation of the SSA is observed. That is a common effect for that material. [2,3]

Table 1 - Results of nitrogen adsoption experiment of pretreated and spent catalysts in dynamic experiments

Experiment	Initial specific surface area (m^2/g)	After oxidation pretreatment of the catalyst material (m^2/g)	After dynamic experiments (m^2/g)
TPR 1	1.86	X	1.68
TPR 2	1.86	1.72	1.70
TPD 1	1.86	X	1.70
TPD 2	1.86	1.75	1.68
TPSR (CH_4 3 K/min)	1.86	1.69	1.76
TPSR (C_2H_4 3K/min)	1.86	1.80	1.68
Dynamic experiment (purge time 10 min)	1.86	1.77	1.70
Dynamic experiment	1.86	1.72	1.70

(purge time 300 min)		
Dynamic experiment	1.86	1.74
(purge time 5 sec)		1.69

2.2. X-ray diffraction analysis

The experimental details were described elsewhere. [1] The xray diffraction patterns of different treated $\text{Na}_2\text{WO}_4/\text{Mn}/\text{SiO}_2$ catalysts are presented in Figure 4. The fresh catalyst shows diffraction patterns for Cristobalit, Tridymite, Na_2WO_4 and Mn_2O_3 . After the mentioned peroxidation method the XRD pattern reveal additional peaks for quartz and very weak signals for MnWO_4 . No other phases were identified for the catalyst material after dynamic experiments. These results are in good agreement with other groups. [2–6]

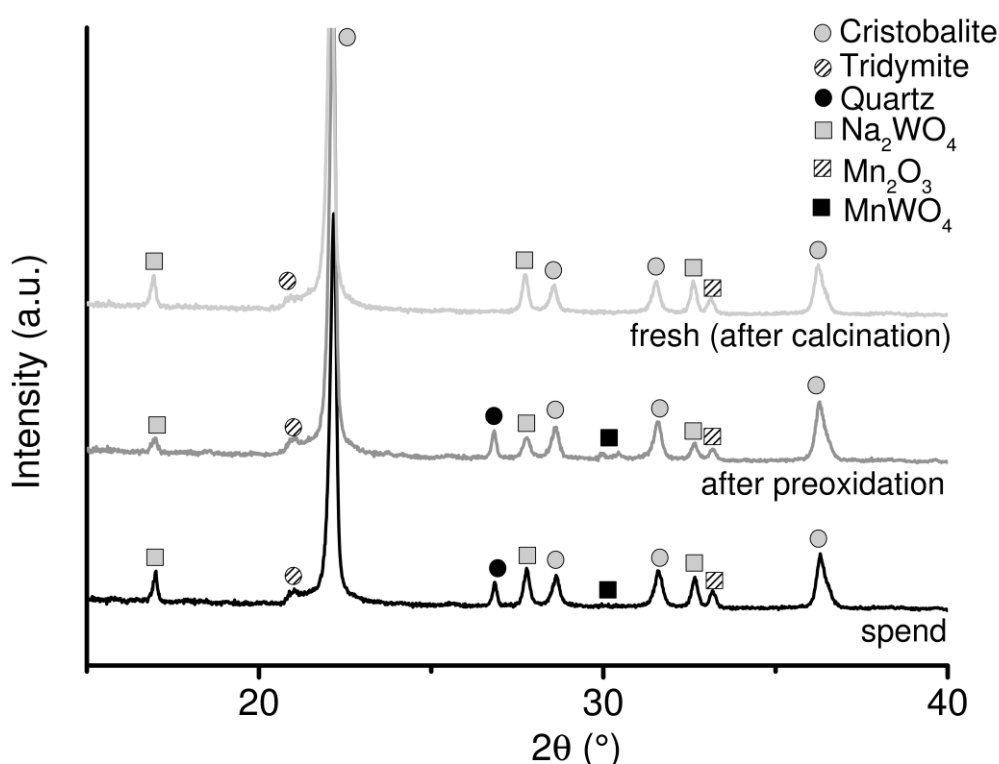


Figure 4 - XRD patterns of fresh, pretreated and spend $\text{Na}_2\text{WO}_4/\text{Mn}/\text{SiO}_2$ catalysts

3. Experimental plan

An experimental plan of all experiments is listed in Table 2.

Table 2- Experimental plan of all temperature ramp and dynamic experiments

Experiment	Catalyst pretreatment	Catalyst Amount (g)	Temp. ramp (K/min)	Max. Temp. (K)	Reduction Feed composition	Total time of reduction Feed (min)
TPR 1	Purge He, no heating	0.06	2	1093	N ₂ :H ₂ (9:1, 60 sccm/min)	400
TPR 2	Oxidation 10 K/min – 1023 K for 1 h, Purge He	0.06	2	1093	N ₂ :H ₂ (9:1, 60 sccm/min)	400
O ₂ TPD	Purge He, no heating	1	5	1093	He (99.999 %, 20 sccm/min)	160
O ₂ TPD	Oxidation 10 K/min – 1023 K for 1 h, Purge He	1	5	1093	He (99.999 %, 20 sccm/min)	160
TPSR – CH4	Oxidation 10 K/min – 1023 K for 1 h, Purge He	1	1	1073	30 sccm/min methane (99.99 %)	800
TPSR – CH4	Oxidation 10 K/min – 1023 K for 1 h, Purge He	1	2	1073	30 sccm/min methane (99.99 %)	400
TPSR – CH4	Oxidation 10 K/min – 1023 K for 1 h, Purge He	1	3	1073	30 sccm/min methane (99.99 %)	265
TPSR – CH4	Oxidation 10 K/min – 1023 K for 1 h, Purge He	1	4	1073	30 sccm/min methane (99.99 %)	200
TPSR – CH4	Oxidation 10 K/min – 1023 K for 1 h, Purge He	1	5	1073	30 sccm/min methane (99.99 %)	160
TPSR – C ₂ H ₆	Oxidation 10 K/min – 1023 K for 1 h, Purge He	1	1	1073	He:C ₂ H ₆ (95:5, 30 sccm/min, 99.98 % C ₂ H ₆)	800
TPSR – C ₂ H ₆	Oxidation 10 K/min – 1023 K for 1 h, Purge He	1	3	1073	He:C ₂ H ₆ (95:5, 30 sccm/min, 99.98 % C ₂ H ₆)	265
TPSR – C ₂ H ₆	Oxidation 10 K/min – 1023 K for 1 h, Purge He	1	5	1073	He:C ₂ H ₆ (95:5, 30 sccm/min, 99.98 % C ₂ H ₆)	160

	for 1 h, Purge He				C ₂ H ₆)	
TPSR – C₂H₄	Oxidation 10 K/min – 1023 K for 1 h, Purge He	1	1	1073	He:C ₂ H ₄ (95:5, 30 sccm/min, 99.98 % C ₂ H ₄)	800
TPSR – C₂H₄	Oxidation 10 K/min – 1023 K for 1 h, Purge He	1	3	1073	He:C ₂ H ₄ (95:5, 30 sccm/min, 99.98 % C ₂ H ₄)	265
TPSR – C₂H₄	Oxidation 10 K/min – 1023 K for 1 h, Purge He	1	5	1073	He:C ₂ H ₄ (95:5, 30 sccm/min, 99.98 % C ₂ H ₄)	160
Dynamic Long purge time	Oxidation 1023 K for 10 min, He purge 10 min	1	-	1023	20 sccm/min methane (99.99 %)	10
Dynamic Long purge time	Oxidation 1023 K for 10 min, He purge 180 min	1	-	1023	20 sccm/min methane (99.99 %)	10
Dynamic Long purge time	Oxidation 1023 K for 10 min, He purge 300 min	1	-	1023	20 sccm/min methane (99.99 %)	10
Dynamic Short purge time	Oxidation 1023 K for 10 min, He purge 300 s	1	-	1023	30 sccm/min methane (99.99 %)	10
Dynamic Short purge time	Oxidation 1023 K for 10 min, He purge 270 s	1	-	1023	30 sccm/min methane (99.99 %)	10
Dynamic Short purge time	Oxidation 1023 K for 10 min, He purge 230 s	1	-	1023	30 sccm/min methane (99.99 %)	10
Dynamic Short purge time	Oxidation 1023 K for 10 min, He purge 160 s	1	-	1023	30 sccm/min methane (99.99 %)	10
Dynamic Short purge time	Oxidation 1023 K for 10 min, He purge 100 s	1	-	1023	30 sccm/min methane (99.99 %)	10
Dynamic Short purge time	Oxidation 1023 K for 10 min, He purge 60 s	1	-	1023	30 sccm/min methane (99.99 %)	10
Dynamic Short purge time	Oxidation 1023 K for 10 min, He purge 30 s	1	-	1023	30 sccm/min methane (99.99 %)	10
Dynamic Short purge time	Oxidation 1023 K for 10 min, He purge 15 s	1	-	1023	30 sccm/min methane (99.99 %)	10
Dynamic Partial pressure variation	Oxidation 1023 K for 10 min, He purge 300 s	1	-	1023	30 sccm/min methane (99.99 %)	10
Dynamic	Oxidation 1023	1	-	1023	15 sccm/min methane	10

Partial pressure variation	K for 10 min, He purge 300 s		(99.99 %) + 15 sccm/min He (99.999 %)
Dynamic Partial pressure variation	Oxidation 1023 K for 10 min, He purge 300 s	1 - 1023	10 sccm/min methane (99.99 %) + 20 sccm/min He (99.999 %) 10

4. Simulation of TPSR experiments

4.1. Modell and conditions

For TPSR experiments we assumed a large difference between methane feed concentration and the stored oxygen amount on the catalyst surface. That type of in-stationary process was modeled as batch-type reactor system. Furthermore the adsorption and desorption of educts and products do not contribute to the reaction progress, because the selective or unselective activation of methane is the rate limiting step. We considered different scenarios of one (O^*) or two (O_α^* , O_β^*) different oxygen species on the catalyst surface. The relative, initial concentration of methane was set to 0.999 and for O^* to 0.001 in the case of one oxygen species. In the case of two different oxygen species the relative methane concentration was set to 0.998, for $O_\alpha^* = 0.001$ and $O_\beta^* = 0.001$. Furthermore it is possible that methane is converted by a parallel reaction to ethane and CO or due to a consecutive reaction, where ethane is an intermediate. The corresponding balances for each mechanism are presented in Table 3 as hypothetical scenario. Initial reactant A simulates methane, while B stands for ethane and C for CO. The rate constant for each reaction was derived by equation (2).

In all cases the pre exponential factor was set to $10^9 \text{ l}/(\text{mole}\cdot\text{min})$. In literature it is assumed that methane activation is the rate limiting step and deep oxidation reactions are favored. That was considered by two different activation energy barriers ($E_{A1} > E_{A2}$). Because of big differences for these parameters in several kinetic models we assumed $E_{A1} = 150 \text{ kJ/mole}$ and $E_{A2} = 100 \text{ kJ/mole}$. [7–11] Please note, that such a model is only valid for fundamental demonstration aspects of heating rate variation experiments!

$$k_i = k_{oo,i} \cdot \exp\left(-\frac{E_{A,i}}{R \cdot (T_{ini} + \beta \cdot t)}\right) \quad (2)$$

β = heating rate (K/min), t = simulation time (min), $T_{ini} = 298 \text{ K}$

Table 3 - Mass balances for different reaction mechanism in simulated temperature programmed experiments A – CH₄ B – C₂H₆, C - CO

Parallel reaction – 1 oxygen species	Consecutive reaction – 1 oxygen species
1. $A + O^* \rightarrow B + H_2O$ 2. $A + O^* \rightarrow C + 2 H_2O$	1. $A + O^* \rightarrow B + H_2O$ 2. $B + O^* \rightarrow C + H_2O$
$\frac{dc_A}{dt} = -k_1 \cdot c_A \cdot c_O^* - k_2 \cdot c_A \cdot c_O^*$	$\frac{dc_A}{dt} = -k_1 \cdot c_A \cdot c_O^*$
$\frac{dc_O^*}{dt} = -k_1 \cdot c_A \cdot c_O^* - k_2 \cdot c_A \cdot c_O^*$	$\frac{dc_O^*}{dt} = -k_1 \cdot c_A \cdot c_O^* - k_2 \cdot c_B \cdot c_O^*$
$\frac{dc_B}{dt} = k_1 \cdot c_A \cdot c_O^*$	$\frac{dc_B}{dt} = k_1 \cdot c_A \cdot c_O^* - k_2 \cdot c_B \cdot c_O^*$
$\frac{dc_C}{dt} = k_2 \cdot c_A \cdot c_O^*$	$\frac{dc_C}{dt} = k_2 \cdot c_B \cdot c_O^*$
Parallel reaction – 2 oxygen species	Consecutive reaction – 2 oxygen species
1. $A + O_\alpha^* \rightarrow B + H_2O$ 2. $A + O_\beta^* \rightarrow C + 2 H_2O$	1. $A + O_\alpha^* \rightarrow B + H_2O$ 2. $B + O_\beta^* \rightarrow C + H_2O$
$\frac{dc_A}{dt} = -k_1 \cdot c_A \cdot c_{O\alpha}^* - k_2 \cdot c_A \cdot c_{O\beta}^*$	$\frac{dc_A}{dt} = -k_1 \cdot c_A \cdot c_{O\alpha}^*$
$\frac{dc_{O\alpha}^*}{dt} = -k_1 \cdot c_{AO} \cdot c_{O\alpha}^*$	$\frac{dc_{O\alpha}^*}{dt} = -k_1 \cdot c_A \cdot c_{O\alpha}^*$
$\frac{dc_{O\beta}^*}{dt} = -k_2 \cdot c_A \cdot c_{O\beta}^*$	$\frac{dc_{O\beta}^*}{dt} = -k_2 \cdot c_B \cdot c_{O\beta}^*$
$\frac{dc_B}{dt} = k_1 \cdot c_A \cdot c_{O\alpha}^*$	$\frac{dc_B}{dt} = k_1 \cdot c_A \cdot c_{O\alpha}^* - k_2 \cdot c_B \cdot c_{O\beta}^*$
$\frac{dc_A}{dt} = k_2 \cdot c_A \cdot c_{O\beta}^*$	$\frac{dc_C}{dt} = k_2 \cdot c_B \cdot c_{O\beta}^*$

4.2. Results and Discussion

The simulation results for different kinetic TPSR situation is presented in Figure 5. In all cases a higher temperature ramp shifts product formation signals to higher temperatures. In Figure 5-A a parallel reaction for selective (product B) and unselective (product C) methane activation on the same oxygen species O α is presented. Formation of product C is preferred at lower temperatures and followed by formation of product B. A hypothetical, consecutive reaction for selective methane activation and unselective ethane conversion is shown in Figure 5-B. Product B is converted immediately to product C, which leads consequently to no shift of peak amplitudes. Another situation (Figure 5-C) is found for a parallel reaction of reactant A, activated by two different oxygen species O α and O β on the catalyst surface. It can be seen that both reactions run independently from each other. Therefore peak formation and amplitude shift depend only on activation energy. Another possible situation for methane conversion is presented in Figure 5-D. Reactant A is converted to product B by O α which is followed by an unselective activation by O β forming product C. Therefore product B is formed and converted to product C at higher temperatures.

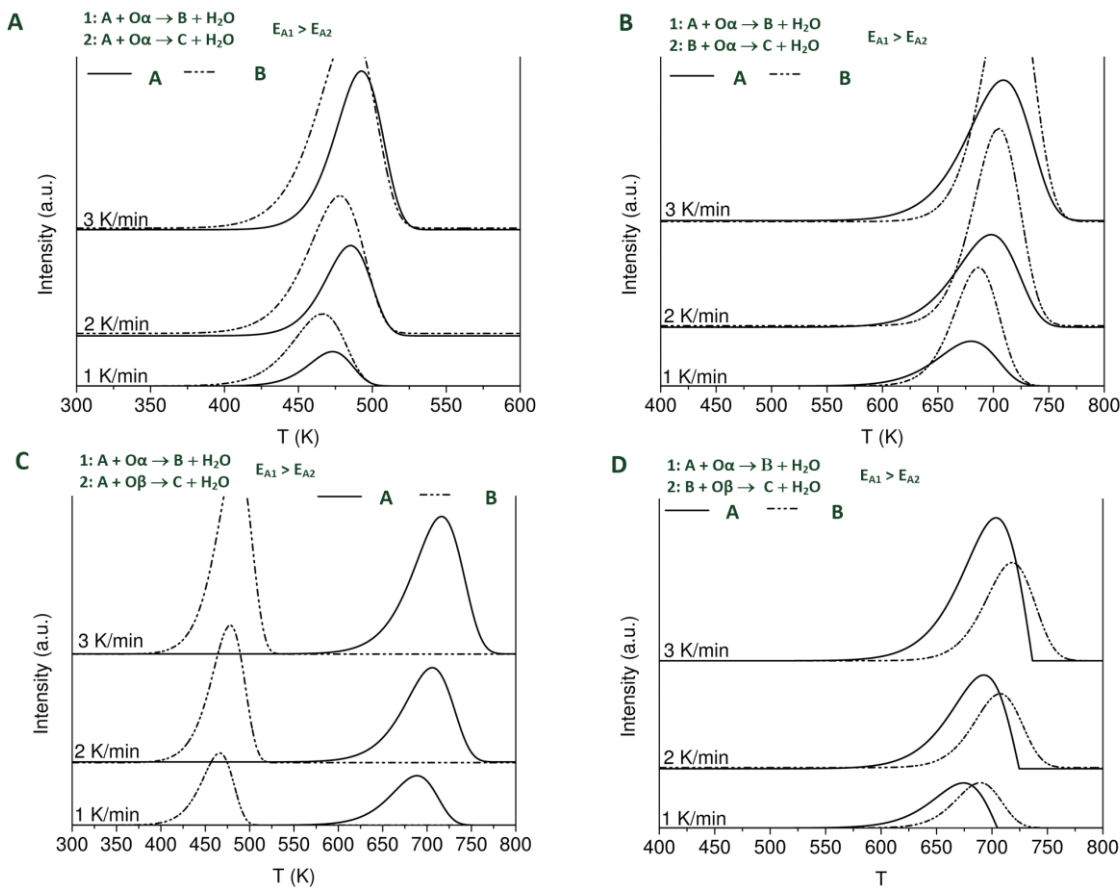


Figure 5 - Simulation results of TPSR experiments

5. References

- [1] M. Yildiz, U. Simon, T. Otremba, Y. Aksu, K. Kailasam, a. Thomas, R. Schomäcker, S. Arndt, Catal. Today 228 (2014) 5.
- [2] U. Simon, O. Görke, A. Berthold, S. Arndt, R. Schomäcker, H. Schubert, Chem. Eng. J. 168 (2011) 1352.
- [3] M. Yildiz, Y. Aksu, U. Simon, K. Kailasam, O. Goerke, F. Rosowski, R. Schomäcker, A. Thomas, S. Arndt, Chem. Commun. 50 (2014) 14440.
- [4] R. Koirala, R. Büchel, S.E. Pratsinis, A. Baiker, Appl. Catal. A Gen. 484 (2014) 97.
- [5] A. Malekzadeh, A.K. Dalai, A. Khodadadi, Y. Mortazavi, Catal. Commun. 9 (2008) 960.
- [6] S. Mahmoodi, M.R. Ehsani, S.M. Ghoreishi, J. Ind. Eng. Chem. 16 (2010) 923.
- [7] M.R. Lee, M.-J. Park, W. Jeon, J.-W. Choi, Y.-W. Suh, D.J. Suh, Fuel Process. Technol. 96 (2012) 175.
- [8] S.M.K. Shahri, S.M. Alavi, J. Nat. Gas Chem. 18 (2009) 25.
- [9] R. Ghose, H.T. Hwang, A. Varma, Appl. Catal. A Gen. 452 (2013) 147.
- [10] M. Daneshpayeh, N. Mostoufi, A. Khodadadi, R. Sotudeh-gharebagh, Energy & Fuels 23 (2009) 3745.

[11] N. Razmi Farooji, A. Vatani, S. Mokhtari, J. Nat. Gas Chem. 19 (2010) 385.

Paper 4



Chemical looping as reactor concept for the oxidative coupling of methane over a Na₂WO₄/Mn/SiO₂ catalyst

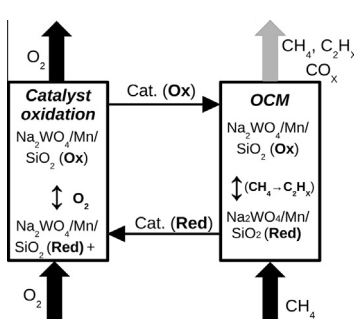
Vinzenz Fleischer, Patrick Littlewood, Samira Parishan, Reinhard Schomäcker*

Technische Universität Berlin, Institut für Chemie, Straße des 17. Juni 124, 10623 Berlin, Germany

HIGHLIGHTS

- Simulated chemical looping experiments were carried out on Na₂WO₄/Mn/SiO₂ methane.
- The absence of gas phase oxygen results in high C2 selectivities (>80%) at moderate methane conversions (<30%).
- High methane conversion (80%) is also reachable, without the risk of explosive regime.

GRAPHICAL ABSTRACT



ARTICLE INFO

Article history:

Received 2 May 2016

Received in revised form 25 July 2016

Accepted 26 July 2016

Available online 28 July 2016

Keywords:

Oxidative coupling of methane

Na₂WO₄/Mn/SiO₂

Chemical looping

Simulated chemical looping

ABSTRACT

In this work we present chemical looping and simulated chemical looping as a new reactor concept for the oxidative coupling of methane over Na₂WO₄/Mn/SiO₂. As a consequence of an alternating feed of oxygen and methane to the catalyst bed side reactions are avoided and the selectivity of the coupling reaction is greatly increased. By variation of methane pulse contact time and temperature a maximum yield of 0.25 is obtained. Although this does not exceed the often discussed yield limitation of OCM, it is achieved from a substantially lower amount of converted methane. A time on stream experiment were carried out at 775 and 800 °C for 150 min and showed stable performance and C2 yield.

© 2016 Elsevier B.V. All rights reserved.

1. Introduction

1.1. Oxidative coupling of methane

The oxidative coupling of methane (OCM) is an attractive alternative concept for ethylene production from methane based feedstocks, as natural gas or bio gas. Major issues for this reaction are high temperatures and therefore competing combustion reactions in the gas phase. Industrial application of OCM is currently not economically viable due to an apparent yield limitation of 0.25 achieved usually at around 0.6 conversion and 0.4 selectivity

[1–3]. Therefore a strong emphasis on reaction engineering is necessary to achieve higher selectivity and yields [4–6].

The basic principle of OCM is the activation of methane by a catalyst material which leads to methyl radical formation by C–H bond cleavage. The methyl radicals can couple to ethane in the gas phase, close to the catalyst surface [7]. A major problem of OCM is the parallel activation of methane and its coupling products in the gas phase. The mentioned components are oxidized to deep oxidation products, what causes a substantial reduction of the selectivity of the process. For improving the selectivity of this reaction a better control of the complex interaction of gas phase and surface reactions is necessary. An apparent yield limitation of 0.25 is an often observed phenomenon for several catalyst materials for OCM, which may be caused from these gas phase reactions.

* Corresponding author.

E-mail address: schomaecker@tu-berlin.de (R. Schomäcker).

The upper yield limit for C₂ products in the absence of gas phase reactions is estimated to be 0.6 [8].

1.2. Chemical looping process and similar concepts

Chemical looping was applied as a reactor concept in the chemical industry for the first time around 100 years ago. This concept was a new route for the synthesis of hydrogen from methane and oxygen by iron particles (syngas chemical looping) [9]. The advantage of chemical looping is the separation of parallel reaction steps during steady state operation into consecutive reaction steps. Disadvantages of this process concept are high costs for capital investment, remote control and maintenance in comparison to

classical steady state reactors. Today, some major research fields are devoted to the utilization of the concept, like chemical looping combustion (CLC) and syngas chemical looping (SLC) or chemical looping hydrogen system (CLH) [10].

A design layout for CLC is shown Fig. 1. Air flows over an oxygen-carrier material ($\text{Me}_x\text{O}_{y-2}$), which contains less oxygen than Me_xO_y . On the outlet of the oxygen adsorption reactor, the air is (partially) depleted of oxygen. The carrier material, with high oxygen content, is transferred to the combustion reactor. The bound oxygen is released into the gas phase, which is achieved by temperature increase or pressure drop. A reactant can thus be oxidized by pure oxygen. The reduced oxygen-carrier is afterwards transferred back to the oxygen adsorption reactor. Such a process has the advantage that the stream of oxidation products contains no nitrogen from the air, which avoids a complex separation process or an air separation unit for the oxygen feed stream. Well-known materials for methane CLC and Chemical looping Reforming (CLR) are CuO, Mn₂O₃ or Co₃O₄ [11–13]. These materials are often supported on silica to increase the specific surface area to optimize oxygen storage and release time. Both, CLC and CLR process operate in the temperature range of 800–1000 °C at ambient pressure.

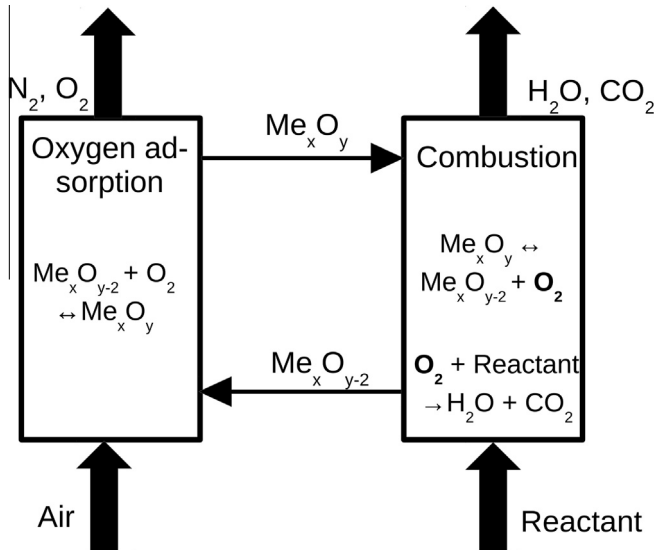


Fig. 1. Principal concept of a chemical-looping process for oxidation reactions.

1.3. Chemical looping concept for the oxidative coupling of methane

A basic concept for a simulated chemical looping process on the lab scale is presented in Fig. 2. It is based on the idea of dynamic experiments, where the feed is switched between different reactants. This is realized by two independently operated six-port pulse valves and a fixed bed reactor, which will be discussed below. The first step serves as the catalyst oxidation process, by dosing oxygen (Fig. 2 – 1), and the second step doses methane (Fig. 2 – 3) for the reduction of the catalyst and methane coupling reaction. The dosing of reactants is always followed by a purging process (Fig. 2 – 2 & 4), which is necessary to avoid mixing of oxygen and methane. A mixed pulse would directly lead to gas phase

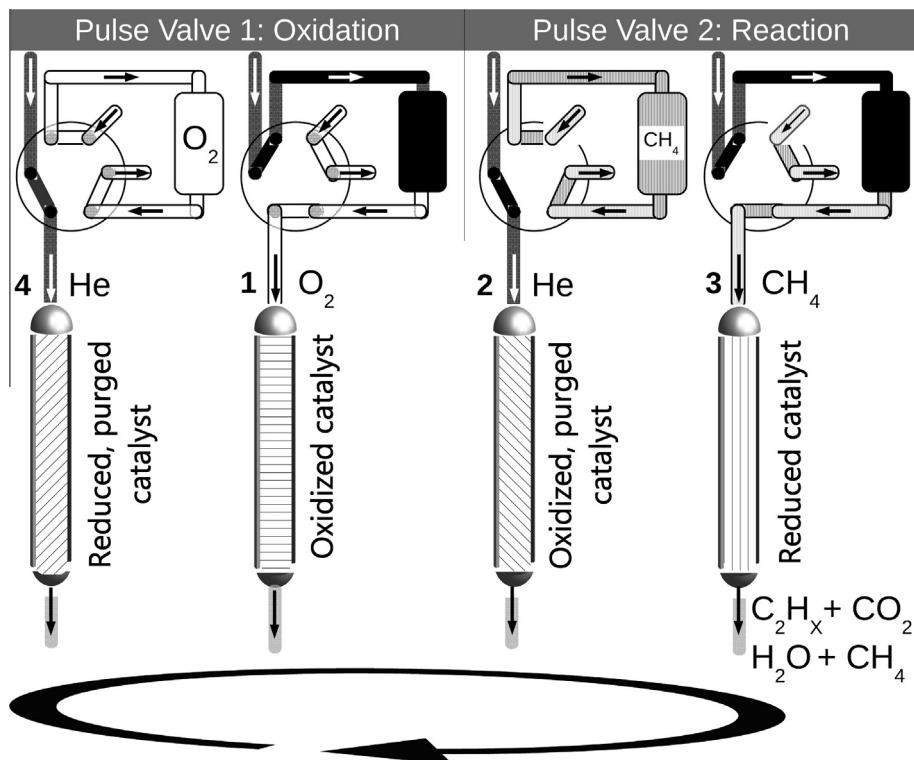


Fig. 2. Principal concept of chemical-looping in the oxidative coupling of methane by pulse valves.

combustion reactions. Beneficially, the purge gas is also the carrier gas for the reactant pulses, which allows dosing of well-defined amounts of oxygen and methane. A proper dosing strategy allows a continuous operation of this process.

The $\text{Na}_2\text{WO}_4/\text{Mn}/\text{SiO}_2$ catalyst material was first introduced by Fang and coworkers and shows a stable catalytic activity for hundreds of hours [14]. Further it showed suitable stability and activity in dynamic experiments, similar to the chemical looping concept [15,16]. In this work we want to take the advantage to investigate the catalyst performance in yield boundary studies without any influences by gas phase combustion reactions. Furthermore this concept was tested in a repetitive continuous operation and compared to classical co-feed operation mode. This will support the investigation of the OCM surface reactions under process relevant conditions for the $\text{Na}_2\text{WO}_4/\text{Mn}/\text{SiO}_2$ catalyst. It has to be noted, that the $\text{Na}_2\text{WO}_4/\text{Mn}/\text{SiO}_2$ material fulfills two functionalities. On the one hand it serves as oxygen carrier material, according to the description before. Thus it will be oxidized to store oxygen, similar to the oxygen carrier materials in the CLC processes. On the other hand the material has also the role of a catalyst material. The stored oxygen is used in a dynamic operation to convert methane into C₂ products by the OCM reaction. Other groups demonstrated that advanced reactor concepts for the OCM reaction showed improved C₂ production performance. Kruglow and coworkers demonstrated the operation of a counter-current moving-bed chromatographic reactor. They separated the C₂ products from unconverted reactants at low conversions and recycle those back [17]. They were able to reach 0.55 C₂ yield. Godini and coworkers presented a membrane reactor with an optimized oxygen dosing strategy [18]. They fed oxygen by use of a membrane in small amounts to the catalyst fixed. Thus, gas phase reactions with gas phase oxygen were minimized.

2. Materials and methods

2.1. Setup design

The chemical looping concept was realized by two pneumatic six-port diaphragm valves (Vichi Valco DV22-2116). The concept of such a valve and its operation is shown in the [Supporting information](#).

A detailed flow chart of the complete setup is shown in [Fig. 3](#). The oxygen and methane supply for both pulse valves is realized by mass flow controllers (MFC, Bronkhorst), which are connected to the first inlet of the pulse valves (PV). It was chosen for purge gas, which is also controlled by a MFC. The pipe is split close to the pulse valves and connected to their second inlet, in order to supply both of them at the same time with carrier gas. Nitrogen supply (6 bar) for the pneumatic impulse is connected to a solenoid for each pulse valve. As mentioned before, the solenoids are connected to transducers (Td, Htronic 191030), which are connected to a PC for data acquisition. Pulse composition can be detected by a quadrupole mass-spectrometer (QMS, IPI GAM 200). Remote control software for the solenoids and the temperature control of the furnace was written in Visual Basic.

A scheme of the tubular fixed bed reactor is in the [Supporting information](#).

2.2. Catalyst preparation and catalytic tests

2.2.1. Catalyst preparation and characterization

A detailed preparation and analysis of the $\text{Na}_2\text{WO}_4/\text{Mn}/\text{SiO}_2$ catalyst is described elsewhere. The catalyst has a composition of 5 wt.% Na_2WO_4 and 2 wt.% Mn(II) and a specific surface area of $1.86 \text{ m}^2/\text{g}$ [19]. The catalyst particle size was 200–300 μm .

2.2.2. Simulated chemical looping experiments

All chemical looping experiments were performed between 700 and 800 °C and at ambient pressure. 2 g catalyst were placed into the isothermal zone of a fixed bed reactor, held by a quartz frit and heated up with 15 K/min under a flow of He:O₂ (95:5, 30 nml/min). To start a series of experiments the reactor was first purged with He, since a constant signal was reached. The total feed flow rate was varied from 15 to 50 nml/min. Methane was dosed from a 1 ml storage loop. The residence time of the gas pulse in the catalyst bed depends strongly on the flow rate, which will be discussed later. After each methane pulse, the catalyst was re-oxidized for 5 min in a flow He:O₂ (95:5, 30 nml/min) during yield study experiments, taking care for a complete reoxidation.

The pulses were detected by a quadrupole mass-spectrometer (QMS, IPI GAM 200). A small amount of the gas flow was sent through a capillary into the QMS high vacuum system, ionized by yttrium filaments and the signal was amplified and detected by a secondary electron multiplier (SEM). All compounds ($Z = \text{CH}_4, \text{C}_2\text{H}_6, \text{C}_2\text{H}_4, \text{CO}, \text{CO}_2$ and O₂) were calibrated with calibration gas bottles ($Z: \text{He} = 5: 95 \pm 0.005\%$, Deute Steiniger). The calibrated m/e ratios for all compounds are presented in the [Supplementary material](#). These one-point calibrations for each compound were repeated 15 times for a precise average value. The calibration was verified by utilization of calibration gas mixtures of ($\text{CH}_4: \text{C}_2\text{H}_6:\text{C}_2\text{H}_4:\text{He}$) and ($\text{CH}_4:\text{CO}:\text{CO}_2:\text{He}$) in the range from (5:5:5:85, $\pm 0.005\%$, Deute Steiniger) to (15:15:15:55, $\pm 0.005\%$, Deute Steiniger).

The measurement of CH₄, C₂H₆, C₂H₄, CO and CO₂ by mass spectroscopy had an interval for each measurement of 5 s. Larger time scales for product detection allow a higher precision for the determination of individual compound concentrations, but has worse resolution for peak detection. Faster methods have a lower accuracy to distinguish ethane and ethene from each other. The number of detected data points for each pulse depends on the flow rate. Therefore the number of data points per detected peak differs from 8 to 34, which is an appropriate resolution for further analysis. The carbon balance for each pulse was between 0.88 (flow = 50 nml/min) and 0.95 (flow = 15 nml/min).

Repetitive continuous simulated chemical looping was carried out at 775 °C for 150 min (50 CH₄ pulses) and further on at 800 °C for another 150 min (50 CH₄ pulses) at 25 nml/min with 2 g catalyst. The experiment was started by an oxygen pulse followed by a time delayed methane pulse. The delay time between dosing of the individual reactants was chosen so that the overlap of methane and oxygen pulses was negligible (120 s). The volumes of the methane and oxygen pulses were set to 1 ml gas at 1 bar. That decision was made to reduce the oxidation time to the same length as the reaction time for the methane pulse.

2.2.3. Steady state experiments

The steady state experiments were carried out in a fixed bed reactor. 250 mg of the catalyst material were placed in the isothermal zone of the reactor. A gas mixture of CH₄:O₂:He (3:1:4) was sent through the reactor at flow rates of 25 and 50 nml/min. This composition allows reduction of the gas phase activity and was chosen also on the mini plant scale in a fluidized bed reactor for a comparison of different reactor concepts [20]. The temperature was set to 800 °C. Detection was carried out by a QMS.

3. Results and discussion

3.1. Yield studies for simulated chemical looping

For a comparison of steady state and looping experiments performing OCM reactions, the characteristic contact time (t) of

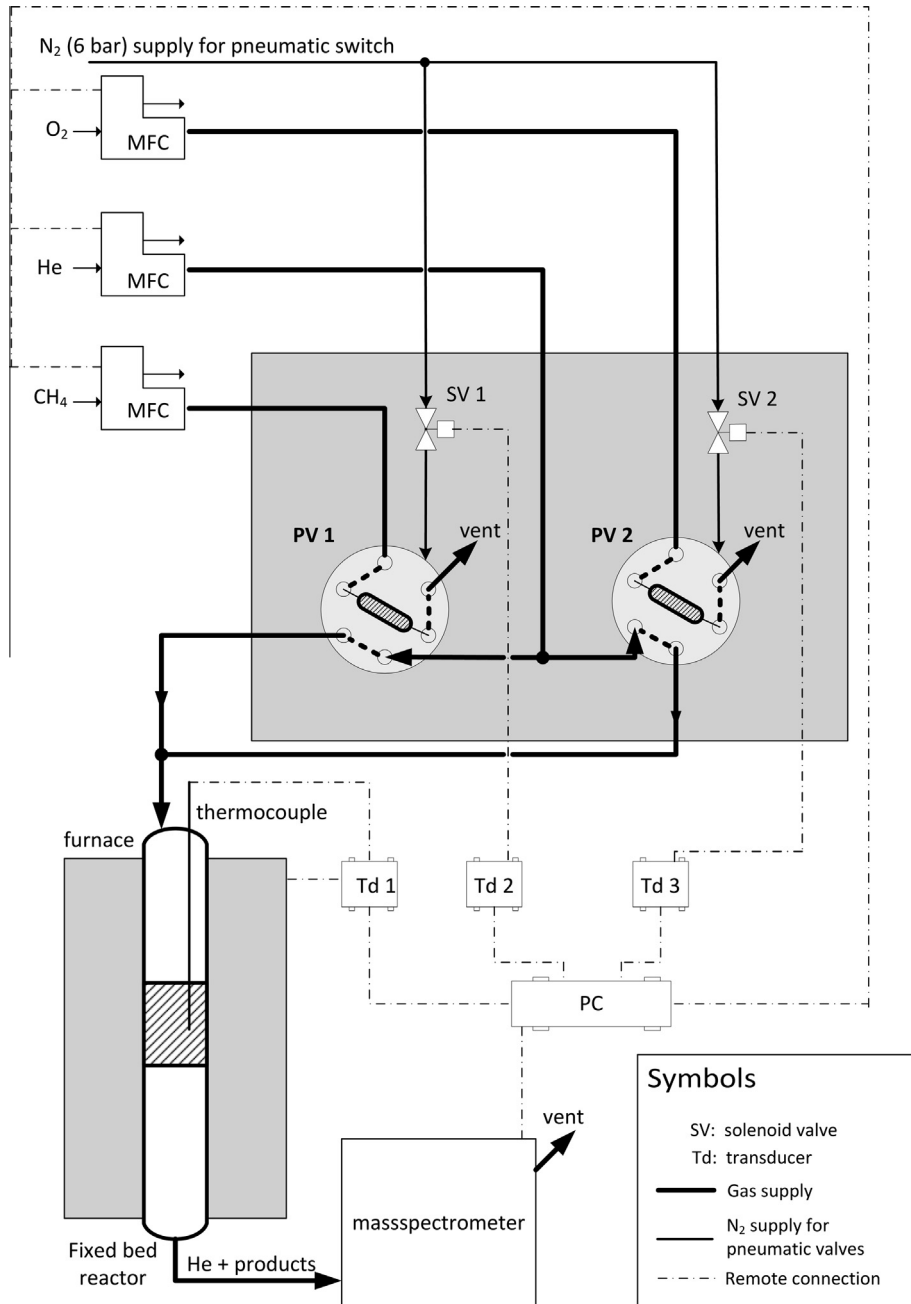


Fig. 3. Flow chart of the chemical looping setup.

each methane pulse was determined by Eq. (1). All pulses were integrated for a detailed carbon balance considering the mole number for each compound as calculated by Eq. (2).

$$t = m_{\text{cat}} \cdot \frac{A_{\text{spec}}}{V} \left[g_{\text{cat}} \cdot \frac{m^2}{g} \cdot \frac{s}{m^3} = \frac{s}{m} \right] \quad (1)$$

m_{cat} = amount of catalyst (g),

A_{spec} = specific surface area of the catalyst (m^2/g),

\dot{V} = flow rate (m^3/s)

$$n_i = \frac{A_{i,\text{peak}} [\% \cdot s]}{R \cdot T} \cdot \dot{V} \cdot p \quad (2)$$

The carbon balance for each methane pulse was 0.88 in all experiments or better. During the oxidation treatment of the catalyst, after each methane pulse, no carbon oxides were detected.

This indicates that there is no carbon deposition on the catalyst surface. All values for conversion (Eq. (3)), selectivity (Eq. (4)) and yield (Eq. (5)) were calculated from the mole number of the detected compounds, derived from a carbon balance of the system.

$$X_{\text{CH}_4} = \frac{C_{\text{CH}_4,\text{in}} - C_{\text{CH}_4,\text{out}}}{C_{\text{CH}_4,\text{in}}} \quad (3)$$

$$S_{\text{C}_2} = \frac{2 \cdot C_2H_6 + 2 \cdot C_2H_4}{2 \cdot C_2H_6 + 2 \cdot C_2H_4 + CO + CO_2} \quad (4)$$

$$Y = X_{\text{CH}_4} \cdot S_{\text{C}_2} \quad (5)$$

The results of methane conversion, C2 selectivity and yield for flowrate and temperature variation are shown in Fig. 4A–C. The surfaces fitted to the data points are only supporting guidelines.

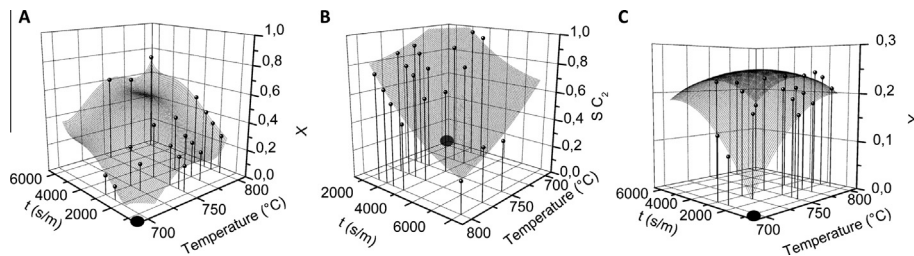


Fig. 4. Results of yield studies, 2 g catalyst, 15–50 nmol/min, 700–800 °C, 1 ml CH₄, A: conversion, B: C2 selectivity, C: C2 yield.

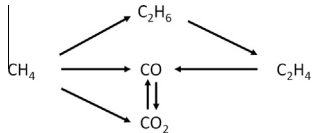


Fig. 5. Reaction scheme of the OCM [24–27].

Methane conversion varies from 0.15 to 0.8, while C2-selectivity is between 0.25 and 1. The highest observed yield was 0.25 at 0.6 C2 selectivity and 0.42 methane conversion. During the experiments CO is only observed at flow rates between 15 and 20 nmol/min at temperatures between 775 and 800 °C. The predominant deep oxidation product is CO₂.

A similar yield limitation was observed for this Na₂WO₄/Mn/SiO₂ catalyst in different other reactor systems, like fixed bed, micro-, fluidized-bed or membrane reactors [20–23]. The absence of gas phase oxygen during the methane pulse in chemical looping experiments allows exclusion of any gas phase deep oxidation reactions. We conclude that the still observed yield limitation is caused by the competition of consecutive surface reactions at this material. This can be explained by a recently proposed surface reaction network, which is shown in Fig. 5 [24–27]. We assume that the activation of methane is the rate determining step for the formation of ethane, while ethene formation and deep oxidation is much faster than this. In our yield studies we analyzed a wide range for the methane conversion and C2 selectivities. The results of this analysis showed a yield maximum of 0.25. The C2 selectivity is strongly controlled by ethene oxidation and methane direct oxidation as can be seen in the reaction network in Fig. 5. We assume that all reaction steps show first order behavior with respect to the hydrocarbon. Therefore all reaction rates are depending on the compound partial pressures and corresponding rate constants. Increasing the methane conversion increases the partial pressures of ethane and ethene, too. This has the consequence that the deep oxidation rate of ethene becomes much faster than the ethene formation rate. At lower methane conversions, the ethene partial pressure is still low. Therefore the formation of deep oxidation products is slow compared to the ethene formation rate.

As mentioned before, the direct oxidation of methane is also possible on the catalyst surface. Lunsford and coworkers found that the formation and coupling of methyl radicals leads to ethane formation [7]. According to their studies, the formation of deep oxidation products and methyl radicals involve two different oxygen species on the catalyst surface. On the one hand there is nucleophilic oxygen which forms carbon oxides. On the other hand there is electrophilic oxygen which leads to methyl radical formation. It has to be noted that these species also may interact with ethane and ethene. Especially the interactions with ethene may lead for both species to the formation of deep oxidation products [28]. These aspects imply that the oxygen species, which is stored on the catalyst surface, contribute to the yield limitation, because one selective route of methane activation competes with three unselective ones.

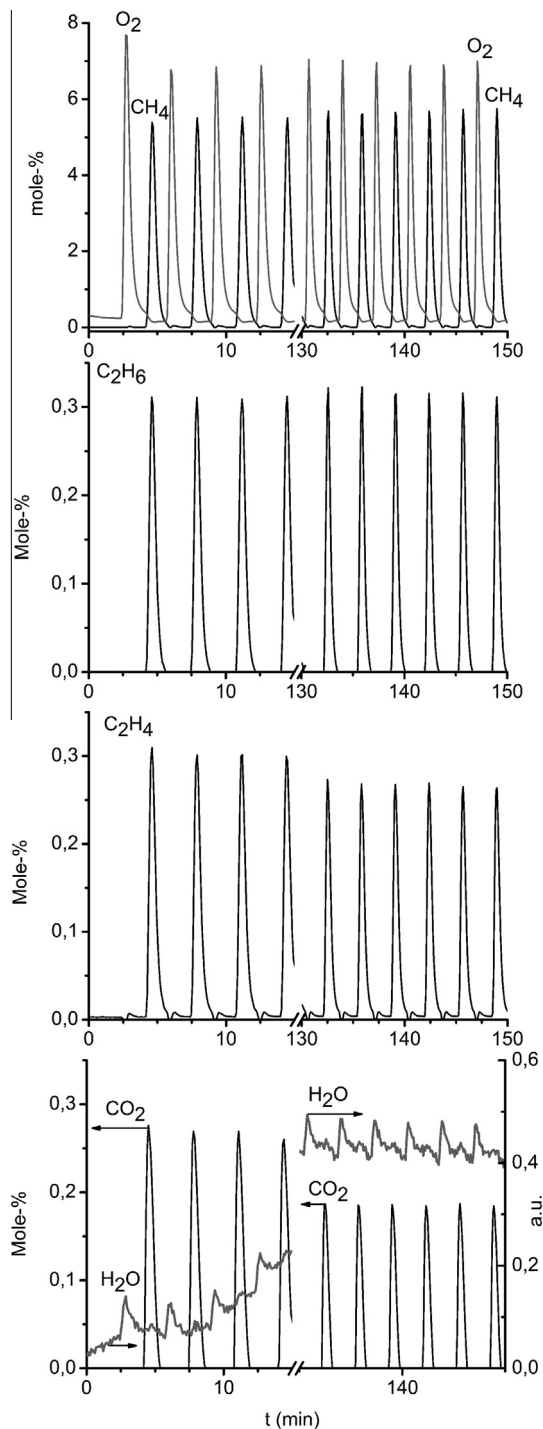


Fig. 6. Early and late reactant and product peaks during continuous simulated chemical looping, 775 °C, 25 nmol/min, 2 g catalyst, pulse of 1 ml O₂ or 1 ml CH₄.

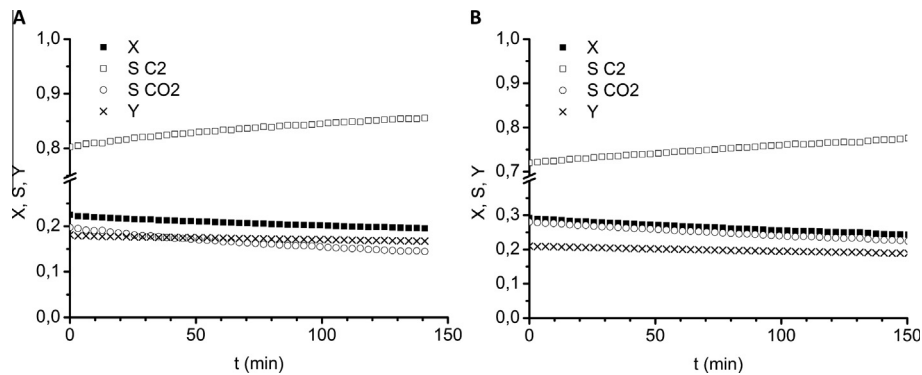


Fig. 7. Observed X, S C2 and Y of continuous simulated chemical looping, 2 g catalyst, 1 ml methane pulse, 25 nmol/min, A – 775 °C, B – 800 °C.

3.2. Simulated chemical looping operation for 150 min

A detailed overview about reactant and product spectra at 775 °C is shown in Fig. 6 (25 nmol/min, t = 2400 s/m). We observed similar results at 800 °C. The first four peaks of all shown compounds represent the initial state of the experiment while the last four were observed after 150 min of operation. The formation of ethane, ethene and carbon dioxide is simultaneous to the methane pulse. Water is constantly removed by the oxygen pulse from the catalyst surface. The increase of the water signal with time is caused by accumulation of water in the detector of the mass spectrometer.

The amount of formed ethane stays constant, as the amount of ethene decreases slightly and carbon dioxide formation decreases clearly. The results for methane conversion, C2 selectivity and yield for both temperatures over the whole period of experiments are presented in Fig. 7. At 775 °C (Fig. 7A) the initial C2 selectivity is 0.8 and increases to 0.85 as CO₂ selectivity decreases. We observe a small decrease in the methane conversion, which is caused by a decrease of CO₂ formation. That is a common effect for that catalyst material in time on stream studies [29,30]. However, the C2 yield is constant at 0.19. The increase of the water signal is based on accumulation of that compound in the mass spectrometer. After this test the temperature was immediately increased to 800 °C and the experiment was continued for another 150 min. At 800 °C (Fig. 7B) the rates of carbon dioxide formation and methane conversion increase, while C2 selectivity decreases. However, the C2 yield increases to 0.21. The catalyst showed reasonable stability during the whole experiment. The space time yield (STY) in our experiments at 775 °C was 20 nmol(C₂)/(s*g_{cat}) and 23 nmol(C₂)/(s*g_{cat}) at 800 °C, respectively. To get an idea about the potential of this reactor concept for the OCM, a comparison with state of the art techniques is necessary.

3.3. Comparison of steady state and simulated chemical looping operation

The results of steady state experiments are shown in Table 1. The characteristic residence time was 300 s/m for 25 nmol/min and 150 s/m for 50 nmol/min. In all cases full oxygen conversion was obtained. The methane conversion was between 0.18 and 0.29 and a C2 yield of 0.18 was obtained. These results are in good agreement with the performance on a mini plant scale with a fluidized bed reactor with 50 g of catalyst [20]. Both experiments operate at similar methane conversions compared to the mentioned chemical looping process, which allows good comparison between both process concepts. Considering a much smaller characteristic residence time under steady state conditions than in chemical looping experiments, and full oxygen conversion, there

Table 1

Results from steady state experiments at different flow rates, 250 mg catalyst, 800 °C, CH₄: O₂: He (3:1:4).

Flowrate (nmol/min)	X (CH ₄)	X (O ₂)	S C2	Y	STY nmol(C ₂)/(s*g _{cat})
25	0.29	1.00	0.63	0.18	147
50	0.18	1.00	0.81	0.15	269

Table 2

Comparison between steady state experiment (800 °C, 25 & 50 nmol/min, 250 mg catalyst) and simulated chemical looping (2 g catalyst, 1 ml methane pulse).

Steady state		S C2	Y
X (CH ₄)	X (O ₂)	0.63	0.18
0.29	1.00	0.74	0.21
0.18	1.00	0.89	0.17
Chemical looping – equal methane conversion			
X (CH ₄)	T (°C)	Flowrate (nmol/min)	S C2
0.29	775	25	0.74
0.18	750	50	0.87
Chemical looping – equal C2 yield			
X (CH ₄)	T (°C)	Flowrate (nmol/min)	S C2
0.21	775	30	0.87
0.19	725	25	0.87

is a much higher reaction rate in steady state experiments. This is also caused by much higher partial pressures of the reactants, compared to the pulses in simulated chemical looping experiments, where the carrier gas diluted the methane pulses. Consequently the STY is much higher compared to our chemical looping experiments as can be seen in the last column of Table 1. The space time yield is one of the most critical parameters for industrial application of a process. The large amount of carrier gas (50 ml per 1 ml of methane) is required for these experiments due to the dead volume of the reactor and the piping connecting it to the analytical equipment. In an industrial scale reactor such volumes are negligible in comparison to the catalyst bed and a carrier gas can be avoided. This should increase the STY of the chemical looping mode substantially. As demonstrated in our recent work, the catalyst reoxidation rate is much faster and therefore much shorter reoxidation times are needed compared to the OCM reaction [31]. We demonstrated also that no temperature swing for the oxidation step is required, as it can be seen from our continuous operation experiments.

For a direct comparison of steady state and chemical looping experiments, similar results for methane conversion should be considered as presented in Table 2. On the one hand, a comparison at the same methane conversion shows clearly that the simulated chemical looping achieves higher C2 selectivities and therefore higher yields.

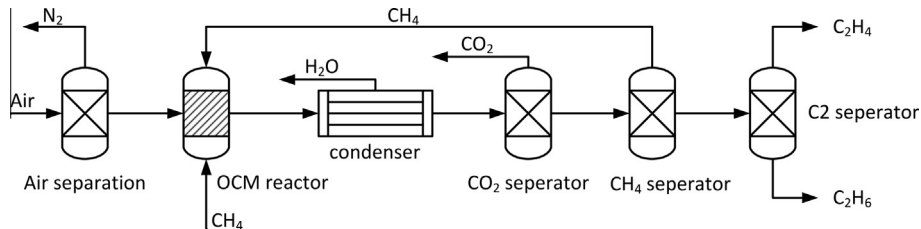


Fig. 8. Scheme of the classic OCM process [32].

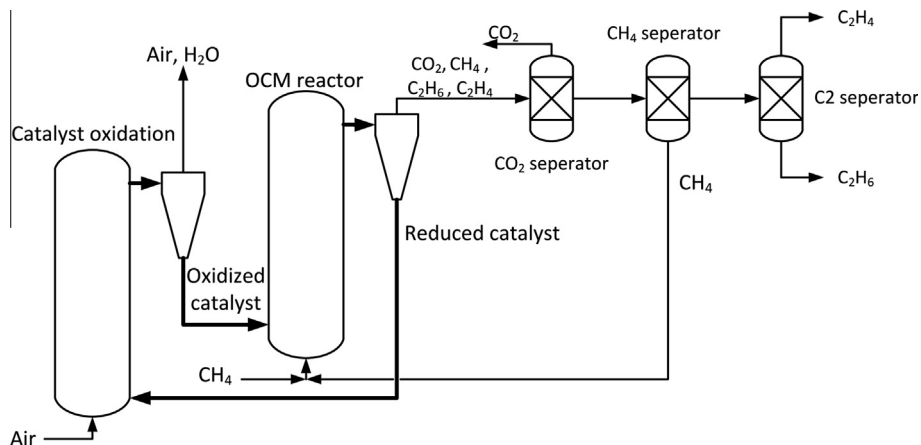


Fig. 9. Scheme of chemical looping of two fluidized bed reactors [32,35].

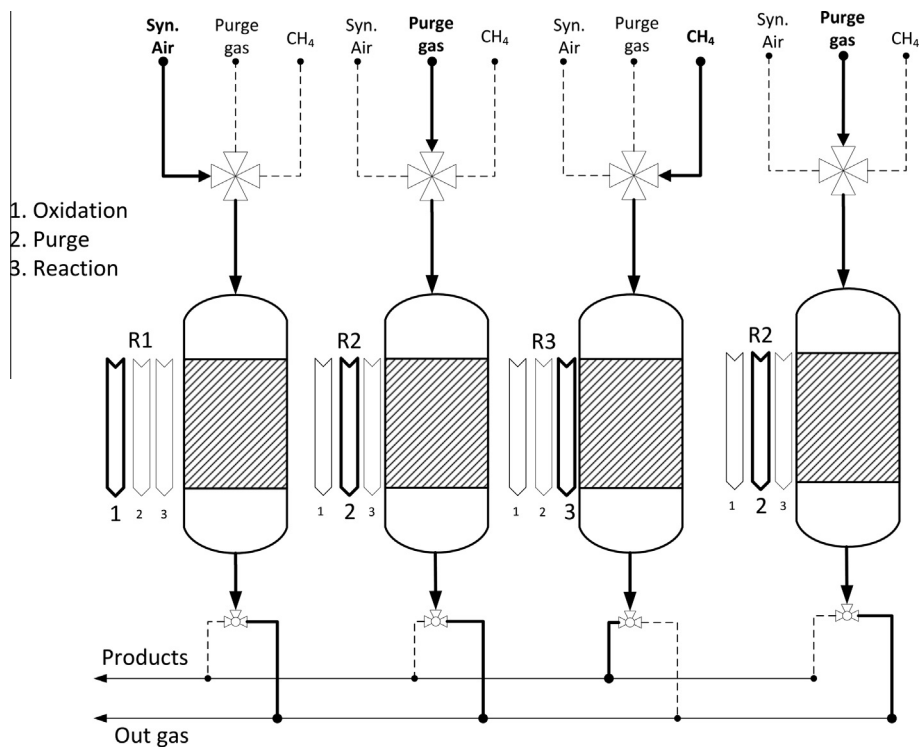


Fig. 10. Scheme of the chemical looping utilizing of fixed bed reactors.

The consequence of these results is that the chemical looping process clearly produces less CO₂. On the other hand, the chemical looping process can be operated at lower methane conversion for the same C₂ yield due to the better selectivity. In both cases, the chemical looping has a better performance and is able to save raw material and energy for the product separation.

This becomes clear by a detailed discussion of the complete OCM process design, which is shown in Figs. 8 and 9. In a classic OCM process an air separation unit removes nitrogen, so that pure oxygen and methane are fed into the reactor. This is required for reducing the total equipment volume. Nitrogen in the feed would increase the total volume and therefore the volume and energy

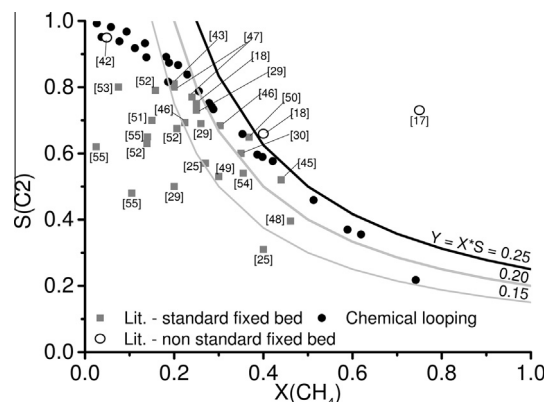


Fig. 11. Conversion/selectivity plot of $\text{Na}_2\text{WO}_4/\text{Mn}/\text{SiO}_2$ catalysts in standard steady state co-feed experiments (Literature, 775–850 °C, Feed: $\text{CH}_4:\text{O}_2:\text{Inert}$), simulated countercurrent moving bed reactor ($\text{Y}_1\text{Ba}_2\text{Zr}_3\text{O}_{9.5}$ catalyst) [17], cofeed experiments with addition of water [42], membrane fixed bed reactor [18] and simulated chemical looping experiments (700–800 °C) [25,29,30,18,43–55]

consumption of each separation unit would be much larger. Especially cryogenic distillation of methane and the C₂ products are very cost intensive separation steps [32]. A proposal for an OCM process based on chemical looping is shown in Fig. 9. As mentioned in the introduction, the state of the art for a chemical looping process is a combination of two fluidized bed reactors. Successful operation of the $\text{Na}_2\text{WO}_4/\text{Mn}/\text{SiO}_2$ catalyst in fluidized bed reactors was shown previously by several groups [32–34]. Therefore two fluidized bed reactors could be utilized for catalyst oxidation and OCM reaction. Based on the observed phenomena, air can be used directly for oxidation and in the same step to remove the water from the catalyst surface. The catalyst should be transported to the OCM reactor with methane atmosphere. Product separation is identical to the separation process shown in Fig. 8. Remembering the better performance of the simulated chemical looping, less CO₂ has to be removed and much more methane can be recycled, saving costs of methane from fresh raw gas.

It has to be noted that the manganese oxide system of the $\text{Na}_2\text{WO}_4/\text{Mn}/\text{SiO}_2$ system is very complex due to different oxidation states (Mn_2O_3 , Mn_3O_4 , MnO). Supported manganese oxides on silica were studied by Stobbe and Coworkers [36]. They have discussed the kinetic and thermodynamic properties qualitatively and summarized that the oxidation rate of MnO to Mn_3O_4 is faster than from Mn_3O_4 to Mn_2O_3 but the Mn_2O_3 species is thermodynamically more favored. Furthermore that system provides the lowest oxygen capacity from all known oxygen storing systems [37].

A well-known problem of fluidized bed reactors is the comminution or abrasion of the catalyst particles [38–40]. An alternative chemical looping concept, utilizing fixed bed reactors, is presented in Fig. 10. Four fixed bed reactors can be operated with alternating gas feed. Such a concept follows the idea which was presented in Fig. 2. Assuming that all procedures in chemical looping operate on similar time scale, continuous operation is possible. Such a concept was reviewed in detail by Kolios et al. [41]. The first reactor can be oxidized by air, while water from the catalyst surface is removed. In parallel, the second and fourth reactors are purged. All of these reactors can be connected to an outgas line. The third fixed bed reactor performs the OCM reaction and is connected to the product line. After this step all feed gases are changed to the next reactor in order to complete the chemical looping process. The outlets of each reactor must be switched to the according line. The separation process for the product line is similar to that discussed above.

4. Conclusion

In our work we tested the $\text{Na}_2\text{WO}_4/\text{Mn}/\text{SiO}_2$ catalyst material in simulated chemical looping experiments. The advantage was that the contributions of gas phase oxygen were avoided, by split of the constant reactant gas feed into separated process steps. We demonstrated that the nature of the oxygen species, which are stored on the catalyst material, limits the C₂ yield. We could demonstrate that the material is stable in a continuous simulated chemical looping experiment under OCM conditions. Finally we compared our dynamic experiment with a standard steady state one. We found that the chemical looping converts methane more efficiently at methane conversions lower than 0.3. Further we presented a hypothetical application of a chemical looping process and its advantages in comparison with the standard process. In addition, our results are compared in a plot of methane conversion and C₂ selectivity with several published results for $\text{Na}_2\text{WO}_4/\text{Mn}/\text{SiO}_2$ catalysts in Fig. 11. On the one hand, methane conversions higher than 0.5 were not possible to realize in standard fixed bed reactors because of the explosive regime of OCM reaction mixtures. On the other hand the chemical looping process concept provides higher C₂ selectivities at methane conversions below 0.25. Furthermore non-standard reactor concepts have shown similar performance improvements which are also presented in Fig. 11. A simulated countercurrent moving bed reactor shows promising C₂ yields by separation of C₂ products and recycling of unconverted methane [17]. Another example for improved performance is a membrane fixed bed reactor with dosing of defined amounts of oxygen to the catalyst bed through a porous membrane [18]. Another option is the modification of the co feed stream by addition of water [42]. In conclusion, it can be seen that new reactor concepts enhance the overall performance of OCM processes.

Acknowledgement

This work is part of the UNICAT excellence cluster, which is coordinated by the Technische Universität Berlin. The funding of this cluster by the German Research Foundation (DFG) is gratefully acknowledged.

Appendix A. Supplementary data

Supplementary data associated with this article can be found, in the online version, at <http://dx.doi.org/10.1016/j.cej.2016.07.094>.

References

- [1] U. Preub, M. Baerns, Chemical technology of natural gas – its present state and prospects, *Chem. Eng. J.* 10 (1987) 297–305.
- [2] M.J. Gradassi, N.W. Green, Economics of natural gas conversion processes, *Fuel Process. Technol.* 42 (1995) 65–83, [http://dx.doi.org/10.1016/0378-3820\(94\)00094-A](http://dx.doi.org/10.1016/0378-3820(94)00094-A).
- [3] T. Setoyama, The contribution of catalysis for the realization of GSC in the twenty-first century, *Catal. Surv. Asia* (2014) 183–192, <http://dx.doi.org/10.1007/s10563-014-9180-0>.
- [4] E.V. Kondratenko, M. Baerns, Oxidative coupling of methane, in: *Handb. Heterog. Catal.*, 2014, pp. 3010–3023.
- [5] Y.S. Su, J.Y. Ying, W.H. Green Jr., Upper bound on the yield for oxidative coupling of methane, *J. Catal.* 218 (2003) 321–333, [http://dx.doi.org/10.1016/S0021-9517\(03\)00043-5](http://dx.doi.org/10.1016/S0021-9517(03)00043-5).
- [6] Y.I. Pyatnitsky, N.I. Ilchenko, M.V. Pavlenko, Kinetic aspects of the methane oxidative coupling at elevated pressures, *Catal. Today* 42 (1998) 233–240, [http://dx.doi.org/10.1016/S0920-5861\(98\)00097-2](http://dx.doi.org/10.1016/S0920-5861(98)00097-2).
- [7] D.J. Driscoll, J.H. Lunsford, Gas-phase radical formation during the reactions of methane, ethane, ethylene, and propylene over selected oxide catalysts, *J. Phys. Chem.* 89 (1985) 4415–4418.
- [8] B. Beck, V. Fleischer, S. Arndt, M.G. Hevia, A. Urakawa, P. Hugo, R. Schomäcker, Oxidative coupling of methane—a complex surface/gas phase mechanism with strong impact on the reaction engineering, *Catal. Today* 228 (2014) 212–218.
- [9] S. Hurst, Production of hydrogen by the steam-iron method, *Oil Soap* 16 (1939) 29–35, <http://dx.doi.org/10.1007/BF02543209>.

- [10] J. Adanez, A. Abad, F. Garcia-Labiano, P. Gayan, L.F. de Diego, Progress in chemical-looping combustion and reforming technologies, *Prog. Energy Combust. Sci.* 38 (2012) 215–282, <http://dx.doi.org/10.1016/j.pecs.2011.09.001>.
- [11] T. Mattisson, A. Lyngfelt, H. Leion, Chemical-looping with oxygen uncoupling for combustion of solid fuels, *Int. J. Greenhouse Gas Control* 3 (2009) 11–19, <http://dx.doi.org/10.1016/j.ijgac.2008.06.002>.
- [12] Q. Zafar, T. Mattisson, B. Gevert, Integrated hydrogen and power production with CO₂ capture using chemical-looping reforming redox reactivity of particles of CuO, Mn₂O₃, NiO, and Fe₂O₃ using SiO₂ as a support, *Ind. Eng. Chem. Res.* 2 (2005) 3485–3496, <http://dx.doi.org/10.1021/ie048978i>.
- [13] Q. Zafar, T. Mattisson, B. Gevert, Redox investigation of some oxides of transition-state metals Ni, Cu, Fe, and supported on SiO₂ and MgAl₂O₄, *Energy Fuels* 20 (2006) 34–44, <http://dx.doi.org/10.1021/ef0501389>.
- [14] X. Fang, S. Li, J. Gu, D. Yang, Preparation and characterization of W-Mn catalyst for oxidative coupling of methane, *J. Mol. Catal.* 255 (1992).
- [15] Y. Liu, R. Hou, X. Liu, J. Xue, S. Li, Performance of Na₂WO₄-Mn/SiO₂ catalyst for conversion of CH₄ with CO₂ into C₂ hydrocarbons and its mechanism, *Stud. Surf. Sci. Catal.* 119 (1998) 307–311, [http://dx.doi.org/10.1016/S0167-2991\(98\)80449-7](http://dx.doi.org/10.1016/S0167-2991(98)80449-7).
- [16] V. Salehoun, A. Khodadadi, Y. Mortazavi, A. Talebizadeh, Dynamics of catalyst in oxidative coupling of methane, *Chem. Eng. Sci.* 63 (2008) 4910–4916, <http://dx.doi.org/10.1016/j.ces.2007.08.013>.
- [17] A.V. Kruglow, M.C. Bjorklund, R.W. Carr, Optimization of the simulated countercurrent moving-bed chromatographic reactor for the oxidative coupling of methane, *Chem. Eng. Sci.* 51 (1996) 2945–2950.
- [18] H.R. Godini, A. Gili, O. Görke, U. Simon, K. Hou, G. Wozny, Performance analysis of a porous packed bed membrane reactor for oxidative coupling of methane: Structural and operational characteristics, *Energy Fuels* 28 (2014) 877–890, <http://dx.doi.org/10.1021/ef402041b>.
- [19] U. Simon, O. Görke, A. Berthold, S. Arndt, R. Schomäcker, H. Schubert, Fluidized bed processing of sodium tungsten manganese catalysts for the oxidative coupling of methane, *Chem. Eng. J.* 168 (2011) 1352–1359, <http://dx.doi.org/10.1016/j.cej.2011.02.013>.
- [20] S. Jaso, S. Sadjadi, H.R. Godini, U. Simon, S. Arndt, O. Görke, A. Berthold, H. Arellano-Garcia, H. Schubert, R. Schomäcker, G. Wozny, Experimental investigation of fluidized-bed reactor performance for oxidative coupling of methane, *J. Nat. Gas Chem.* 21 (2012) 534–543.
- [21] H. Bozorgzadeh, R. Ahmadi, M.M. Golkar, M.R. Khodagholi, Oxidative coupling of methane over different supported Mn/Na₂WO₄ catalysts, *Pet. Coal* 53 (2011) 84–90. <http://www.vurup.sk/sites/default/files/downloads/pc_2_2011_bozorgzadeh_109.pdf> (accessed July 1, 2013).
- [22] J.-L. Dubois, C.J. Cameron, Synergy between stable carbonates and Yttria in selective catalytic oxidation of methane, *Chem. Lett.* 1089–1092 (1991).
- [23] H.R. Godini, V. Fleischer, O. Görke, S. Jaso, R. Schomäcker, G. Wozny, Thermal reaction analysis of oxidative coupling of methane, *Chem. Eng. Technol.* 36 (2014) 1906–1915, <http://dx.doi.org/10.1002/cite.201400080>.
- [24] M.R. Lee, M.-J. Park, W. Jeon, J.-W. Choi, Y.-W. Suh, D.J. Suh, A kinetic model for the oxidative coupling of methane over Na₂WO₄/Mn/SiO₂, *Fuel Process. Technol.* 96 (2012) 175–182, <http://dx.doi.org/10.1016/j.fuproc.2011.12.038>.
- [25] S.M.K. Shahri, S.M. Alavi, Kinetic studies of the oxidative coupling of methane over the Mn/Na₂WO₄/SiO₂ catalyst, *J. Nat. Gas Chem.* 18 (2009) 25–34, [http://dx.doi.org/10.1016/S1003-9953\(08\)60079-1](http://dx.doi.org/10.1016/S1003-9953(08)60079-1).
- [26] S. Lacombe, Z. Durjanova, L. Mleczko, C. Mirodatos, Kinetic modelling of the oxidative coupling of methane over lanthanum oxide in connection with mechanistic studies, *Chem. Eng. Technol.* 18 (1995) 216–223.
- [27] Z. Stansch, L. Mleczko, M. Baerns, Comprehensive kinetics of oxidative coupling of methane over the La₂O₃/CaO catalyst, *Ind. Eng. Chem. Res.* 36 (1997) 2568–2579.
- [28] R.B. Grant, R.M. Lambert, A single crystal study of the silver-catalysed selective oxidation and total oxidation of ethylene, *J. Catal.* 92 (1985) 364–375, [http://dx.doi.org/10.1016/0021-9517\(85\)90270-2](http://dx.doi.org/10.1016/0021-9517(85)90270-2).
- [29] R. Koitala, R. Büchel, S.E. Pratsinis, A. Baiker, Oxidative coupling of methane on flame-made Mn-Na₂WO₄/SiO₂: influence of catalyst composition and reaction conditions, *Appl. Catal. A Gen.* 484 (2014) 97–107, <http://dx.doi.org/10.1016/j.apcata.2014.07.013>.
- [30] H. Liu, X. Wang, D. Yang, R. Gao, Z. Wang, J. Yang, Scale up and stability test for oxidative coupling of methane over Na₂WO₄-Mn/SiO₂ catalyst in a 200 ml fixed-bed reactor, *J. Nat. Gas Chem.* 17 (2008) 59–63, [http://dx.doi.org/10.1016/S1003-9953\(08\)60026-2](http://dx.doi.org/10.1016/S1003-9953(08)60026-2).
- [31] V. Fleischer, R. Steuer, S. Parishan, R. Schomäcker, Investigation of the surface reaction network of the oxidative coupling of methane over Na₂WO₄/Mn/SiO₂ catalyst by temperature programmed and dynamic experiments, *J. Catal.* (2016). accepted.
- [32] H.-R. Godini, S. Jaso, W. Martini, S. Stünkel, D. Salerno, S.N. Xuan, S. Song, S. Sadjadi, H. Trivedi, H. Arellano-Garcia, G. Wozny, Concurrent reactor engineering, separation enhancement and process intensification; comprehensive unicat approach for oxidative coupling of methane (OCM), *CzT* 109 (2012) 63–74.
- [33] A. Talebizadeh, Y. Mortazavi, A.A. Khodadadi, Comparative study of the two-zone fluidized-bed reactor and the fluidized-bed reactor for oxidative coupling of methane over Mn/Na₂WO₄/SiO₂ catalyst, *Fuel Process. Technol.* 90 (2009) 1319–1325, <http://dx.doi.org/10.1016/j.fuproc.2009.06.021>.
- [34] S. Jašo, S. Sadjadi, H.R. Godini, U. Simon, S. Arndt, O. Görke, A. Berthold, H. Arellano-Garcia, H. Schubert, R. Schomäcker, G. Wozny, Experimental investigation of fluidized-bed reactor performance for oxidative coupling of methane, *J. Nat. Gas Chem.* 21 (2012) 534–543, [http://dx.doi.org/10.1016/S1003-9953\(11\)60402-7](http://dx.doi.org/10.1016/S1003-9953(11)60402-7).
- [35] W. Xiang, S. Chen, Z. Xue, X. Sun, Investigation of coal gasification hydrogen and electricity co-production plant with three-reactors chemical looping process, *Int. J. Hydrogen Energy* 35 (2010) 8580–8591, <http://dx.doi.org/10.1016/j.ijhydene.2010.04.167>.
- [36] E.R. Stobbe, B.A. de Boer, J.W. Geus, The reduction and oxidation behaviour of manganese oxides, *Catal. Today* 47 (1999) 161–167, [http://dx.doi.org/10.1016/S0920-5861\(98\)00296-X](http://dx.doi.org/10.1016/S0920-5861(98)00296-X).
- [37] P. Gupta, F. Li, L. Velázquez-Vargas, D. Sridhar, M. Iyer, S. Ramkumar, L.-S. Fan, Chemical looping particles, in: *Chem. Looping Syst. Foss. Energy Conversions*, John Wiley & Sons, Hoboken, 2010, pp. 57–142. doi: 10.1002/9780470872888.ch2.
- [38] F. Scala, A. Cammarota, R. Chirone, P. Salatino, Comminution of limestone during batch fluidized-bed calcination and sulfation, *AIChE J.* 43 (1997) 363–373, <http://dx.doi.org/10.1002/aic.690430210>.
- [39] L. Chou, R. Wollast, Study of the weathering of albite at room temperature and pressure with a fluidized bed reactor, *Geochim. Cosmochim. Acta* 48 (1985) 2205–2217, [http://dx.doi.org/10.1016/0016-7037\(85\)90270-4](http://dx.doi.org/10.1016/0016-7037(85)90270-4).
- [40] X. Yao, H. Zhang, H. Yang, Q. Liu, J. Wang, G. Yue, An experimental study on the primary fragmentation and attrition of limestones in a fluidized bed, *Fuel Process. Technol.* 91 (2010) 1119–1124, <http://dx.doi.org/10.1016/j.fuproc.2010.03.025>.
- [41] G. Kolios, J. Frauhammer, G. Eigenberger, Autothermal fixed-bed reactor concepts, *Chem. Eng. Sci.* 55 (2000) 5945–5967, [http://dx.doi.org/10.1016/S0009-2509\(00\)00183-4](http://dx.doi.org/10.1016/S0009-2509(00)00183-4).
- [42] K. Takanabe, E. Iglesia, Rate and selectivity enhancements mediated by OH radicals in the oxidative coupling of methane catalyzed by Mn/Na₂WO₄/SiO₂, *Angew. Chem. Int. Ed.* 47 (2008) 7689–7693, <http://dx.doi.org/10.1002/anie.200802608>.
- [43] D. Wang, M.P. Rosynek, J.H. Lunsford, Oxidative coupling of methane over oxide-supported sodium-manganese catalysts, *J. Catal.* 155 (1995) 390–402, <http://dx.doi.org/10.1006/jcat.1995.1221>.
- [44] A. Malekzadeh, A.K. Dalai, A. Khodadadi, Y. Mortazavi, Structural features of Na₂WO₄-MO_x/SiO₂ catalysts in oxidative coupling of methane reaction, *Catal. Commun.* 9 (2008) 960–965, <http://dx.doi.org/10.1016/j.catcom.2007.09.026>.
- [45] A. Palermo, J.P.H. Vazquez, R.M. Lambert, New efficient catalysts for the oxidative coupling of methane, *Catal. Lett.* 68 (2000) 191–196.
- [46] J. Wang, L. Chou, B. Zhang, H. Song, J. Zhao, J. Yang, S. Li, Comparative study on oxidation of methane to ethane and ethylene over Na₂WO₄-Mn/SiO₂ catalysts prepared by different methods, *J. Mol. Catal. A Chem.* 245 (2006) 272–277, <http://dx.doi.org/10.1016/j.molcata.2005.09.038>.
- [47] A. Malekzadeh, M. Abedini, A.A. Khodadadi, M. Amini, H.K. Mishra, A.K. Dalai, Critical influence of Mn on low-temperature catalytic activity of Mn/Na₂WO₄/SiO₂ catalyst for oxidative coupling of methane, *Catal. Lett.* 84 (2002) 45–51. <<http://link.springer.com/article/10.1023/A:1021020516674>> (accessed July 1, 2013).
- [48] S. Mahmoodi, M.R. Ehsani, S.M. Ghoreishi, Effect of promoter in the oxidative coupling of methane over synthesized Mn/SiO₂ nanocatalysts via incipient wetness impregnation, *J. Ind. Eng. Chem.* 16 (2010) 923–928, <http://dx.doi.org/10.1016/j.jiec.2010.09.007>.
- [49] G.D. Nipan, Phase states of Na/W/Mn/SiO₂ composites at temperatures of catalytic oxidative coupling of methane, *Inorg. Mater.* 50 (2014) 1012–1017, <http://dx.doi.org/10.1134/S0020168514100112>.
- [50] Z. Jiang, H. Gong, S. Li, Methane activation over Mn₂O₃-Na₂WO₄/SiO₂ catalyst and oxygen spillover, *Stud. Surf. Sci. Catal.* 112 (1997) 481–490.
- [51] H. Zhang, J. Wu, B. Xu, C. Hu, Simultaneous production of syngas and ethylene from methane by combining its catalytic oxidative coupling over Mn/Na₂WO₄/SiO₂ with gas phase partial oxidation, *Catal. Lett.* 106 (2006) 161–165, <http://dx.doi.org/10.1007/s10562-005-9624-2>.
- [52] L. Chou, Y. Cai, B. Zhang, J. Niu, S. Ji, S. Li, Oxidative coupling of methane over Na-Mn-W/SiO₂ catalyst at higher pressure, *React. Kinet. Catal. Lett.* 76 (2002) 311–315, <http://dx.doi.org/10.1023/A:1016592129451>.
- [53] S. Pak, P. Qiu, J.H. Lunsford, Elementary reactions in the oxidative coupling of methane over Mn/Na₂WO₄/SiO₂ and Mn/Na₂WO₄/MgO catalysts, *J. Catal.* 230 (1998) 222–230. <<http://www.ingentaconnect.com/content/ap/ca/1998/00000179/00000001/art02228>> (accessed May 28, 2013).
- [54] S. Hou, Y. Cao, W. Xiong, H. Liu, Y. Kou, Site requirements for the oxidative coupling of methane on SiO₂-supported Mn catalysts, *Ind. Eng. Chem. Res.* 45 (2006) 7077–7083, <http://dx.doi.org/10.1021/ie060269c>.
- [55] M. Yıldız, U. Simon, T. Otremba, Y. Aksu, K. Kailasam, A. Thomas, R. Schomäcker, S. Arndt, Support material variation for the Mn_xO_y-Na₂WO₄/SiO₂ catalyst, *Catal. Today* 228 (2014) 5–14, <http://dx.doi.org/10.1016/j.cattod.2013.12.024>.

Chemical looping as reactor concept for the oxidative coupling of methane over a $\text{Na}_2\text{WO}_4/\text{Mn}/\text{SiO}_2$ catalyst – Supplementary material

1. Experimental – Mass spectrometer

The calibrated m/e ratios for all compounds in mass spectroscopy (QMS, IPI GAM 200) are presented in Table 1.

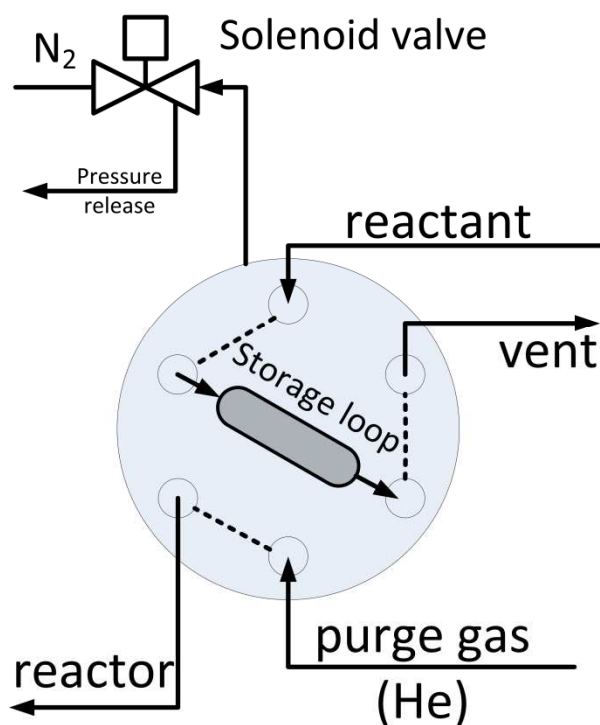
Table 1 - Calibrated m/e ratios for compound detection in chemical looping experiments

Molecule	m/e
CO_2	44
CO	28
He	4
H_2	2
H_2O	18; 17
CH_4	16; 15
C_2H_6	30; 29; 28
C_2H_4	28; 27; 26
O_2	32

2. Experimental – Pneumatic six-port diaphragm valves

A flowchart is presented in Figure 1. A reactant flows in by an inlet, passes through a sample loop and flows to the outlet. In parallel to this, a purge gas flows to the reactor from a second inlet (Figure 1 A). A pneumatic impulse from a solenoid valve switches the connectors to the second position (Figure 1 B). The reactant in the sample loop is conveyed by the purge gas to the reactor, while the reactant from the supply port goes directly to the outlet. The connectors switch back by pressure release. The pneumatic impulse can be controlled by a solenoid valve, which is connected to a 6 bar nitrogen supply line. There is a remote control connection from a computer followed by a transducer to the solenoid for precise realization of time controlled pulses. The sample loop (Vicci Valco CSL250, CSL500, CSL1K, CSL2K) can be varied in its volume from 250 μl up to 2 ml for different amounts of pulsed reactants.

A - Purging / filling sample loop



B – Dosing reactant

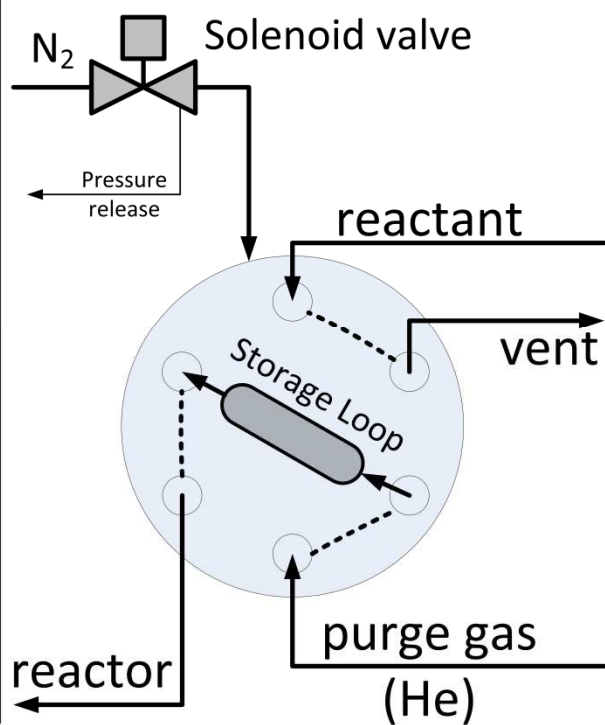


Figure 1 - Schematic function of a 6-port pulse valve, A: storage loop is filled by reactant, while purge gas goes to the reactor, B: purge gas transports the reactant to the reactor

3. Experimental – Fixed bed reactor

The catalyst bed is placed on a quartz frit (200 µm pore size). The reactor inner diameter has a size of 9 mm. The type K thermocouple (NiCrNi) is covered by a quartz-made sheath (din = 4 mm), which also seals the reactor at the top. The fixed bed reactor for chemical looping experiments is presented in Figure 2. The reactants are fed through the upper entrance. The bottom part of the reactor is reduced in diameter and is connected to the analytical system. The isothermal zone is above the frit and has a height of around 5 cm.

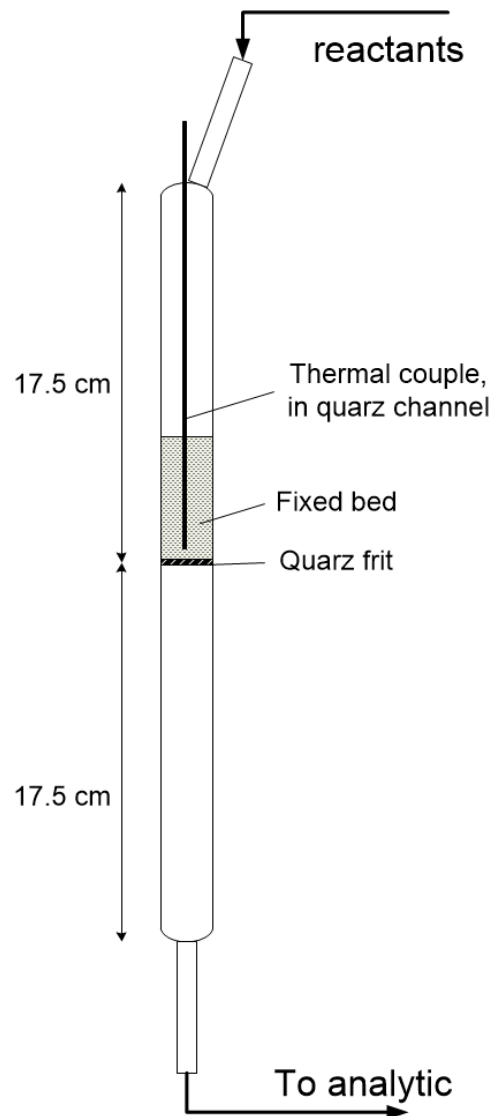


Figure 2 - Detailed scheme of the fixed bed reactor.

Paper 5

Investigation of the role of the Na₂WO₄/Mn/SiO₂ catalyst composition in the oxidative coupling of methane by chemical looping experiments

Vinzenz Fleischer^a, Ulla Simon , Samira Parishan, Maria Gracia Colmenares, Oliver Görke, Aleksander Gurlo and Reinhard Schomäcker^b

Technische Universität Berlin, Institut für Chemie, Straße des 17. Juni 124, 10623 Berlin, Germany

Fachgebiet Keramische Werkstoffe / Chair of Advanced Ceramic Materials, Institut für Werkstoffwissenschaften und –technologien, Technische Universitaet Berlin, Hardenbergstraße 40, 10623 Berlin, Germany

^a v.fleischer@mailbox.tu-berlin.de, ^b corresponding author: schomaecker@mailbox.tu-berlin.de

5.1 Abstract

A series of Na₂WO₄/Mn/SiO₂ catalysts supported on mesoporous silica were prepared and tested for the oxidative coupling of methane in chemical looping experiments. The parameter variations were done for specific surface area, Mn-loading and support material. Chemical looping experiments reveal that highest catalytic activity is observed at 2 wt-% Mn and 5 wt-% Na₂WO₄ on mesoporous silica. Repetitive methane pulse experiments allowed us to determine the oxygen uptake of the Na₂WO₄/Mn/SiO₂ catalyst in chemical looping experiments. We found a correlation between oxygen storage capacity and manganese loading. Furthermore we observed that ethylene formation is independent from the catalyst material in chemical looping conditions.

5.2 Introduction

The mainly utilized process for ethylene production is the steam cracking process, which has naphtha as feedstock. In the last decade the shale gas production came up as an alternative process to provide natural gas from shale formations. Such gas contains different amounts of ethane, methane and propane. [1–3] However, the major compound of shale gas, bio gas and raw gas is still methane which is typically used for heat generation or energy production.[4–6] The oxidative coupling of methane (OCM) is an alternative process to produce ethane and ethylene from methane. This process utilizes the mentioned ressources as an additional feedstock for the formation of C2 compounds. A suitable catalyst material for this process is Na₂WO₄/Mn/SiO₂ which was presented by Fang and Coworkers. [7] This material shows stability at high performance conditions for several 100 hours. [8,9] However, it was reported that the performance of the OCM reaction in various reactor concepts showed an apparent C2 yield maximum of about 0.25. [10–12] To overcome this limitation, it is

necessary to understand the mechanism of the OCM and the functionality of this complex catalyst material.

For a better comprehension of this catalyst material many groups carried out compound variations. Palermo et al. found that the phase transition of the support material from quartz to α -cristobalite is a fundamental step for a high performance catalyst. Furthermore they could show that sodium ions are the inducers for this transition. [13] To understand the role of sodium in more detail it was exchanged against Lithium, Potassium and Cesium. [14] It was found that the $\text{Na}_2\text{WO}_4/\text{Mn}$ film on the support material offers a high structural flexibility during the OCM process, which plays a major role. Such flexible structure allows undergoing the key transition state of methyl radical formation by hydrogen abstraction. The authors suggested that the alkali ion is the key compound which is responsible for such flexibility, which means a kind of amorphous phase on the catalyst surface. A variation of tungsten oxide loading was studied by Mahmoodi and Coworkers. [15] They found a relation between the formation of micro crystals on the catalyst surface and C2 selectivity. This was studied by exchanging the tungsten ion by molybdenum, niobium, chromium or vanadium. The smaller the ion radius of the transition metal ion is the lower is the degree of crystallinity. Therefore the vanadia containing catalyst showed the lowest and the tungstate loaded catalyst the highest C2 selectivity in this constellation. The group of Mortazavi performed catalytic tests by exchanging the manganese ion by other transient metal oxides in their catalysts. [16] They found that this compound is responsible for the redox potential of the catalyst material. Tuning of this potential has a tremendous influence on C2 selectivity and methane conversion. A variation of the support material was shown by Yildiz and Coworkers. [17] They could show that the silica supported catalyst has the best long-time stability and showed the highest performance in catalytic tests. In another study they studied different silica support materials and found that mesoporous structured silica catalyst had the highest performance. [18] Sadjadi et al found that well dispersed active compounds will agglomerate under OCM conditions. [19] Furthermore they observed that the sodium ion is responsible for the formation of an amorphous phase of the active compounds on the catalyst surface, which is in good agreement with the results of the Lambert group. [13] It was reported that the inexpensive analogue of SBA-15, COK-12, showed also good catalytic performance, which is important for industrial application. [20]

From the mechanistic point of view, different oxygen species on the catalyst surface seem to contribute to the OCM reaction. On the one hand there is nucleophilic oxygen, which is involved in deep oxidation reactions. On the other hand there is electrophilic oxygen, which is responsible for hydrogen abstraction reactions. The role of both species for several hydrocarbon oxidation reactions was reviewed by Morooka. [21] The Wang group carried out detailed XPS and Raman spectroscopy studies to understand the role of activation process, which is focused on a tungsten oxide species. [22] EPR studies by Jiang et al. indicate that the manganese ion changes its oxidation state from +III to +II in dynamic experiments. [23] They concluded that manganese is reduced in an electron transfer from C-H bond cleavage induced by tungsten oxide. The reduction of manganese oxide was also reported by other groups. [19,24] They reported a formation of MnWO_4 . Beck et al. found in temporal analysis of products (TAP) experiments on the $\text{Na}_2\text{WO}_4/\text{Mn}/\text{SiO}_2$ catalyst that two different oxygen species are responsible for methane activation during steady state conditions. [25] They found that a

strongly bound oxygen species is responsible for selective methane activation, while weakly bound oxygen leads to deep oxidation products.

In our previous work we investigated the catalyst material by temperature programmed and dynamic experiments [26]. Such experiments revealed that also lattice oxygen seems to be involved in the OCM process on the $\text{Na}_2\text{WO}_4/\text{Mn}/\text{SiO}_2$ material. In addition our results indicated that several oxygen species are stored on the catalyst material even in dynamic experiments. In another work we could show that the involvement of lattice oxygen can be interpreted as oxygen storage function. [27] That functionality was successfully adapted for a chemical looping process. Such reactor concept allows to separate parallel reaction steps in steady state operation into catalyst reduction by methane conversion and catalyst reoxidation in a consecutive step. This has the advantage that gas phase reactions induced by gas phase oxygen are excluded. In chemical looping processes, one of the most important parameters is the oxygen storage capacity. [28] The redox system of Mn(II)/Mn(III) is already known as an attractive oxygen storage system in chemical looping combustion. [29]

In this work we want to study the oxygen storage functionality and its mechanistic aspects for COK-12 supported $\text{Na}_2\text{WO}_4/\text{Mn}/\text{SiO}_2$ catalysts in chemical looping experiments. Furthermore, a non-mesoporous silica supported will be compared. It has to be noted, that the $\text{Na}_2\text{WO}_4/\text{Mn}/\text{SiO}_2$ material acts as oxygen storage material and as catalyst material, simultaneously. An additional feature in simulated chemical looping experiments is the repetitive pulsing of a reactant. Such experiments will give new insights with respect to the involvement of lattice oxygen in the OCM surface reaction mechanism on the $\text{Na}_2\text{WO}_4/\text{Mn}/\text{SiO}_2$ catalyst.

5.3 Experimental

5.3.1 Catalyst Preparation

The preparation of $\text{Na}_2\text{WO}_4/\text{Mn}/\text{SiO}_2$ materials supported on COK-12 follows the procedure described in. [20] The Mn amount was varied from 0 to 4 wt%. In addition, catalysts with a variation in surface area were prepared by varying the annealing temperature between 750°C and 850 °C. The COK-12 catalyst were taken as powders and not pelletized. The reference catalyst, supported on silica gel, was prepared similar to the method described by Simon et al. [30] The final reference catalyst, had a composition of 5 wt.-% Na_2WO_4 and 2 wt.-% Mn(II) and a specific surface area of 1.86 m²/g. The particle size of the SiO_2 support material (Davisil 636, Sigma Aldrich) was 150 -350 μm .

5.3.2 Catalyst characterization

All samples were heated up to 150 °C for 24 h before nitrogen adsorption experiments were performed. The experiment was carried out in an Autosorb (Quantachrome, FL, USA) at 77K. The range of P/P_0 was varied from 0.05 to 0.25.

ICP measurements were carried out in a HoribaScientific inductively coupled plasma spectrometer model Ultima2, to determine the content of Na, Mn and W.

The X-ray powder diffraction was done in a Philips X-ray diffractometer utilizing a Bragg–Brentano geometry with Cu-K α radiation ($\lambda=0.1542$ nm). The angle range of 2θ was 10° to 90° with step time of 0.3 s. The change of angle per step was 0,008°.

5.3.3 Catalytic performance test

5.3.3.1 Single pulse experiments

A detailed description of the chemical looping setup was presented elsewhere. [27] All catalysts were tested at 700 - 800 °C. The absolute flowrate of the gases was 20 or 30 nml/min and the dosed amount of methane was 1 ml for each pulse. For the variation of the specific surface area, 600 mg catalyst for each test was used. The catalyst amount for the manganese and support material variation was 1 g.

The fresh catalyst was heated up at 10 K/min under a flow rate of 30 nml/min O₂:He (1:9). When reaching the reaction temperature, the reactor was purged by a flow of He (30 nml/min) until oxygen partial pressure reached baseline level. The detection of the methane pulse was carried out by a quadrupole mass spectrometer (QMS, IPI GAM 200). The detailed calibration method was described in our previous work. [26] According to equations (46)-(49) methane conversion, C2 selectivity and C2 yield for each methane pulse were calculated and the carbon balance had accuracy between 89-99%.

$$n_i = \frac{A_{i,peak}[\% \cdot s] \cdot \dot{V} \cdot p}{R \cdot T} \quad (46)$$

$$X_{CH_4} = \frac{CH_{4,in} - CH_{4,out}}{CH_{4,in}} \quad (47)$$

$$S_{C2} = \frac{2 \cdot C_2H_6 + 2 \cdot C_2H_4}{2 \cdot C_2H_6 + 2 \cdot C_2H_4 + CO + CO_2} \quad (48)$$

$$Y = X_{CH_4} \cdot S_{C2} \quad (49)$$

This error is caused by the method of the mass spectrometer. The calibration of methane, ethane, ethane, CO and CO₂ shows several overlapping masses for these compounds. Therefore the detection interval for the feed composition was 5 s, each. This value was a compromise between accuracy of compound detection and resolution of pulse signal.

5.3.3.2 Repetitive pulse experiments

Repetitive methane pulse experiments with 1 ml pulses were carried out at 775 °C and a He flow rate of 30 nml/min for each catalyst material. The delay between the methane pulses was chosen that each methane pulse was fully separated from the following one. The experiment was stopped when no methane conversion was detected anymore, which was between 15 – 25 methane pulses.

Oxygen balances were calculated in two different ways. On the one hand we calculated a methane based oxygen balance. All detected products are based on methane molecules which were oxidized.

We assume that all oxygen is finally converted to water or CO₂ molecules. Therefore a specific amount of oxygen atoms (O*) for each product can be calculated as presented in Table 9.

Table 9 - Chemical reactions for a methane based oxygen balance

No.	Reaction
1	$\text{CH}_4 + 4 \text{O}^* \rightarrow \text{CO}_2 + 2 \text{H}_2\text{O}$
2	$2 \text{CH}_4 + \text{O}^* \rightarrow \text{C}_2\text{H}_6 + \text{H}_2\text{O}$
3	$2 \text{CH}_4 + 2 \text{O}^* \rightarrow \text{C}_2\text{H}_4 + 2 \text{H}_2\text{O}$
4	$\text{CH}_4 + 3 \text{O}^* \rightarrow \text{CO} + 2 \text{H}_2\text{O}$

On the other hand we determined a molecule specific oxygen balance. The assumed surface reaction network for all catalysts in this study is presented in Figure 30. This network is based on observations in our previous work. [26] In each reaction step a certain number of oxygen atoms is consumed to form a new molecule. Thus, the number of oxygen atoms were distinguished for each reaction ($\text{O}_{\text{C}_2\text{H}_6}$, $\text{O}_{\text{C}_2\text{H}_4}$, O_{CO_2}) and the consecutive routes were considered, too. For instance, for each ethene molecule one $\text{O}_{\text{C}_2\text{H}_6}$ and one $\text{O}_{\text{C}_2\text{H}_4}$ were converted to water. For all reaction steps we assume a second order behavior. Furthermore we assume that the activity of the oxygen species on the catalyst surface is not limited by mass transport effects. One limitation of this calculation is the ratio of k_3/k_4 . Lunsford and Coworkers carried out isotope labeling experiments with C^{13}H_4 . [31,32] They found that the ratio of k_3/k_4 is between 2 and 7 at different reaction conditions. Therefore both ratios were considered. The detailed calculations and simulation methods are presented in the supporting information.

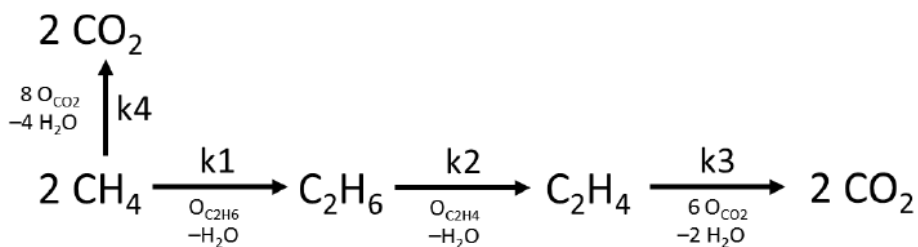


Figure 30 - Surface reaction network of the $\text{Na}_2\text{WO}_4/\text{Mn}/\text{SiO}_2$ catalyst to determine a molecule specific oxygen balance

5.3.4 Simulation in Chemkin

To simulate a pulse experiment in Reaction Design Chemkin we choose a 0-D Batch reactor model, because of the fact that both reactor concepts are non-continuous. All model parameters are listed in Table 10. The corresponding reactor volume was defined as the free gas space in the fixed bed. The residence time was derived from the methane pulse width and the initial mole fraction of methane as mean amplitude of the methane pulse. The specific surface area corresponds to 0.6 g catalyst with a specific surface area of $5 \text{ m}^2/\text{g}$.

Table 10 - Model parameter of Chemkin simulation

Parameter	Value for simulation
Reactor volume (cm ³)	3
Residence time (s)	55
Specific surface area (m ² /g)	3
Temperature (°C)	775
Pressure (bar)	1
Initial molefraction CH ₄ , rest is N ₂	0.05

One well-known model for the gas phase reaction network involved in OCM is the Dooley mechanism. [33] It considers 1582 reactions, 269 species and showed adequate simulation results for profile fixed bed reactor. [34] It must be considered that such a micro kinetic network for gas phase reactions is strongly influenced by a micro kinetic surface reaction model. Therefore only well-tested micro kinetic models for the surface reaction can derive adequate simulation results. Because of lack in such a model for the Na₂WO₄/Mn/SiO₂ catalyst we approximate it by a formal kinetic model. One of the latest models was published by Daneshpayeh and Coworkers, which showed adequate agreement with their experimental results. [11,35] One of the major issues of their network is the poor prediction of methane conversions higher than 0.1. Furthermore, their network contains gas phase and surface reactions in a homogenous model. Therefore we choose only parameters for methane activation in a selective and unselective route, similar to our recent work. [36] Lunsford and Coworkers found that the methane activation and ethane formation is dependent on methyl radical formation and coupling. [37] Furthermore it is widely accepted in micro kinetic models that the unselective reaction route for methane on the catalyst surface proceeds via a CH₃O· species. [38–42] Therefore both reactions were implemented as surface reactions. The pre-exponential factor k_{oo} of Daneshpayeh et al. was adapted with respect to catalyst amount and specific surface area. As thermodynamic data for all species on the catalyst surface dummy values of 0 were set, which is an adequate method if thermodynamic data for such species are not available. The final surface reaction model is presented in Table 11. The number of active sites for this material was set to 1/nm². This results from the fact that transition metal oxides, which are supported on silica, have monolayer coverage between 0.1 – 1 atom per square nanometer. [43]

Table 11 - Micro kinetic reaction routes on the catalyst surface and their parameters [11,35]

Reaction	k _{oo} (1/s)	Ea (kJ/mol)
CH ₄ + O [*] _{electrophile} => CH ₃ · + OH [*]	44.100	212.60
CH ₄ + O ₂ [*] _{nucleophile} => CH ₃ O· + OH [*]	0.614	98.54

5.4 Results and Discussion

5.4.1 Results of catalyst characterization

The results of the catalyst characterization are presented in Table 12. At low manganese loadings higher specific surface areas (SSA) can be observed. ICP-OES results show clearly that manganese loading was successfully varied from 0 to 4 wt%, while the respective other compound loadings are approximately constant. XRD patterns for the fresh catalyst materials showed that similar crystal species can be found. The main phases of the catalyst are cristobalit and Na_2WO_4 crystal structures. XRD patterns indicate Mn_2O_3 might be also explained as braunite ($\text{MnMn}_6\text{SiO}_{12}$) phase, since patterns of Mn_2O_3 and $\text{MnMn}_6\text{SiO}_{12}$ are very similar and overlap. The catalyst with 0.04 w-% Mn showed no manganese oxide reflexes in XRD. The variation of the specific surface area for the $\text{Na}_2\text{WO}_4/\text{Mn/SiO}_2$ catalyst show similar compound loadings in ICP-OES and crystal structures in XRD analysis. This is important for a comparison of this parameter and indicates that only effects by the specific surface area during catalytic test are observed. The shrinkage of the SSA is mainly caused by impregnation with Na_2WO_4 and Mn and the calcination pretreatment, which induces the phase change of the support material. Due to the fact of cristobalit formation the ordered mesoporous structure of the COK-12 support material vanishes.

Table 12 - Analytic results of $\text{Na}_2\text{WO}_4/\text{Mn/SiO}_2$ catalysts, P: fresh, S: spend

Variation	Parameter	BET SSA (m^2/g)	XRD Main phase	XRD Side phases	W (w-%)	Mn (w-%)	Na (w-%)
Mn (COK-12)	0.02 w-%	P: 5.0 S: 3.7	Cristobalit	Na_2WO_4 ; (SiO_2)	2.33	0.04	0.7
	1.00 w-%	P: 3.1 S: 2.6	Cristobalit	Na_2WO_4 ; Mn_2O_3 /Braunite; Quartz	2.18	1.02	0.71
	1.90 w-%	P: 2.6 S: 2.6	Cristobalit	Na_2WO_4 ; Mn_2O_3 /Braunite; Quartz	1.85	1.58	0.66
	2.80 w-%	P: 2.8 S: 2.6	Cristobalit	Na_2WO_4 ; Mn_2O_3 /Braunite; Quartz	2.31	2.48	0.65
	3.70 w-%	P: 3.1 S: 1.1	Cristobalit	Na_2WO_4 ; Mn_2O_3 /Braunite; (SiO_2)	3.53	4.07	0.88
A_{spec} (COK-12)		P: 4.2 S: 3.9	Cristobalit	Na_2WO_4 ; Mn_2O_3 /Braunite	3.26	1.92	0.89
		P: 3.2 S: 3.0	Cristobalit	Na_2WO_4 ; Mn_2O_3 /Braunite	3.26	1.91	0.89

	P: 2.6 S: 2.4	Cristobalit	Na_2WO_4 ; $\text{Mn}_2\text{O}_3/\text{Braunite}$	3.16	2.01	0.84
Ref. (quartz)	P: 2.3 S: 2.1	Cristobalit	Na_2WO_4 ; $\text{Mn}_2\text{O}_3/\text{Braunite}$	3.02	1.96	0.83
	P: 1.9 S: 1.7	Cristobalit	Na_2WO_4 ; $\text{Mn}_2\text{O}_3/\text{Braunite}$	2.57	1.77	0.62

5.4.2 Catalytic tests with different specific surface areas on $\text{Na}_2\text{WO}_4/\text{Mn}/\text{SiO}_2$ catalysts

It has to be noted, that an increase of the SSA keeping the same weight loadings of the catalyst compounds, leads to a decrease the surface concentration. The results for our chemical looping experiments with the SSA variation at constant weight loadings are presented in Figure 31. An increase of the SSA leads to a linear increase of methane conversion, while a decrease of C₂ selectivity can be observed. These results are consistent for different residence times and different temperatures. When the catalyst with the highest SSA was tested opposite trends for methane conversion and C₂ selectivity was observed. BET surface results indicate, that no mesoporous structure can be observed. Calculation of the Weisz-Prater criteria revealed that mass transport limitation can be excluded. [44] In addition ICP measurements showed that the composition of each material has no significant deviation.

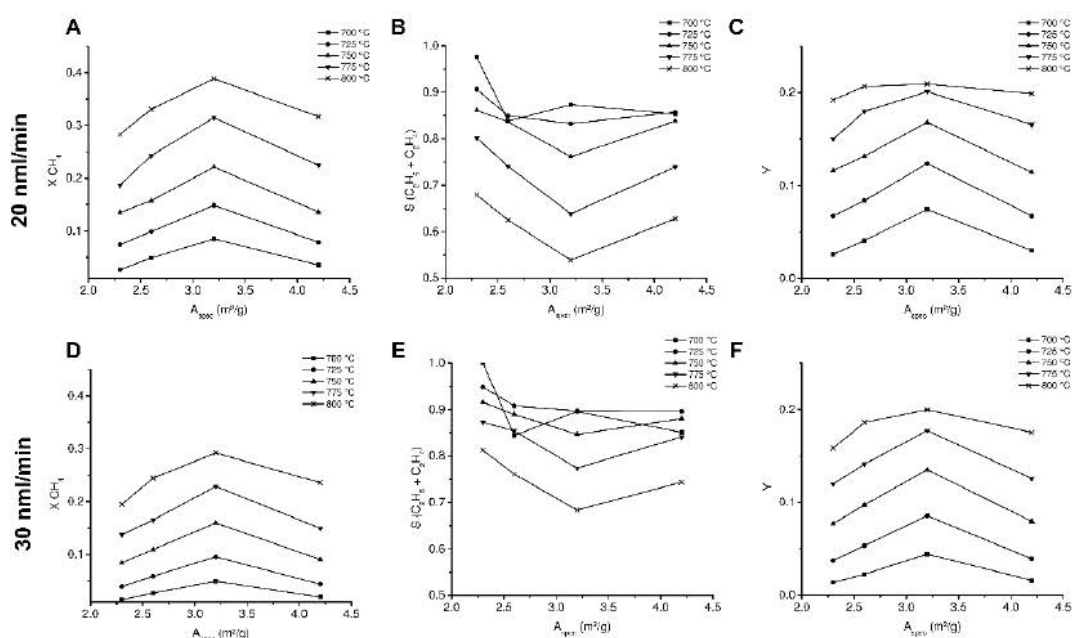


Figure 31 – Results of chemical looping experiments on Na_2WO_4 (5 wt-%)/Mn (2 wt-%)/ SiO_2 catalysts at different specific surface areas and temperatures, 0.6 g catalyst, A – C: methane conversion, C₂ selectivity and C₂ Yield at 20 nmol/min D – F: methane conversion, C₂ selectivity and C₂ Yield at 30 nmol/min, 1 ml CH_4 pulse

In steady state experiments Yildiz et al. showed, that the increase of the SSA raises the catalytic performance. [18] This is caused by more accessible active sites per gram of catalyst. Furthermore a better distribution of the active components on the catalyst surface was reported.

Such activity enhancement was also observed in our simulated chemical looping experiments, but the decline of activity at high SSA indicates that this effect is limited and an optimal surface loading of the catalyst compounds was exceeded. A theoretical film thickness (d) of the active catalyst materials was derived according to equation (38), where the density of the catalyst compounds was assumed to be similar to the bulk material ones.

$$d = \frac{m(\text{Na}_2\text{WO}_4)}{\rho(\text{Na}_2\text{WO}_4) \cdot A_{spec,cat,P}} + \frac{m(\text{Mn(II)})}{\rho(\text{Mn}_2\text{O}_3) \cdot A_{spec,cat,P}} \quad (50)$$

The results of film thickness and surface concentrations are presented in Table 13. The theoretical number of layers (# Layers) was derived according to equation (39). We assumed a constant bond length L(W-O) and L(Mn-O) of 0.1925 nm and 0.1984 nm. [45]

$$\# \text{ Layer} = \frac{d(\text{Na}_2\text{WO}_4)}{L(\text{W}-\text{O})} + \frac{d(\text{Mn}_2\text{O}_3)}{L(\text{Mn}-\text{O})} \quad (51)$$

Calculations of the compound loadings at the highest catalytic activity gives 68 Mn(II)/nm² and 32 W(VI)/nm². The reference catalyst material, which will be compared later, has 115 Mn(II)/nm² and 54 W(VI)/nm², which is much higher.

Table 13 - Calculated theoretical film thickness and surface concentrations of Na₂WO₄ and Mn

	A _{spec} (m ² /g)	d(Na ₂ WO ₄) (nm)	d(Mn ₂ O ₃)(nm)	d (nm)	# Layer	W(VI)/nm ²	Mn(II)/nm ²
A_{spec} (COK- 12)	2,3	5,2	1,9	7,1	36,0	44,6	95,2
	2,6	4,6	1,7	6,3	31,8	39,4	84,2
	3,2	3,7	1,4	5,1	25,8	32,0	68,4
	4,2	2,8	1,1	3,9	19,7	24,4	52,1
Mn (COK- 12)	5,0	2,4	0,0	2,4	12,1	20,5	0,4
	3,1	3,9	0,7	4,6	23,1	33,1	35,3
	2,6	4,6	1,6	6,2	31,4	39,4	80,0
	2,8	4,3	2,2	6,5	32,7	36,6	109,5
Ref. (quartz)	3,1	3,9	2,7	6,5	32,8	33,1	130,7
	1,9	6,3	2,3	8,6	43,5	53,9	115,3

Stobbe and Coworkers studied the reduction and oxidation behavior of supported manganese oxides on silica by temperature programmed experiments. [46] They found in methane oxidation experiments that catalytic performance depends on the degree of manganese oxide crystallinity. An additional dependence was reported for the oxidation state. The crystallinity is strongly dependent on manganese distribution on the catalyst surface. The more manganese oxide is deposited per surface area unit, the higher is the degree of crystallinity. [47] The oxidation state of manganese oxide depends also on dispersion. This was found in Raman spectroscopy studies by Buciuman et al. [48] At low manganese loadings Mn₂O₃ is predominant, while at higher loadings Mn₃O₄ is formed. At OCM reaction conditions both manganese oxide species are equally favored. [46] The transition temperature between these two species is 1100 K. In temperature programmed experiments it was observed that manganese oxides are reduced quantitatively to MnO by methane, but Mn₂O₃ is reduced at lower temperature as Mn₃O₄. Therefore both species should be active on the Na₂WO₄/Mn/SiO₂ catalyst for OCM reactivity. It was reported that also Na₂WO₄ without Mn₂O₃ supported on silica shows good performance in co-feed steady state OCM studies. [13,16] A similar relation between crystallinity and catalytic activity of such catalysts was reported, too. [49] Therefore, the catalytic activity is sensitive for the degree of crystallinity of both compounds. Increasing of the specific surface area at constant weight loadings of both compounds will lead to higher dispersion.

In our experiments the surface concentration of Na₂WO₄ and Mn decreases with increasing the SSA, as mentioned before. Therefore the degree of crystallinity declines and the activity of the catalyst compounds should be higher, but unfortunately the oxidation states of the catalyst compounds can also be changed under reaction conditions. Such change in the oxidation state would explain the results of temperature programmed desorption experiments of O₂. [9,50]

The results of our repetitive pulse experiments are shown in Figure 32 A-C. After six consecutive methane pulses, the methane conversion is more or less constant for each catalyst material. The C₂ selectivities for each material were between 0.8 - 0.9, but decreases with each additional methane pulse. The decrease of the C₂ yield is primarily affected by decrease of methane conversion. The results of the methane based oxygen balances, summarized for all 15 methane pulses for each catalyst in total, are presented in Figure 32 – D. Ethane and Ethene formation show only minor changes for the variation of the specific surface area. CO₂ formation correlates with our findings during chemical looping experiments. The more methane is converted the more CO₂ is formed. In Figure 32 - E the molecule specific oxygen balance is presented for k3/k4 = 7, while Figure 32 - F shows the results for k3/k4 = 2. The more oxygen is stored and converted the more oxygen is consumed by CO₂ formation. This is reflected by an increase of O_{CO₂} and decrease of O_{C₂H₆}. Only a small change for all oxygen ratios can be observed, when the value of k3/k4 is changed to seven. This is caused by high C₂ selectivity of 0.8 - 0.9. Interestingly the ratio of O_{C₂H₄} is more or less constant in both cases.

The most active catalyst material in this set of experiments (SSA = 3.2 m²/g) stores also the highest amount of oxygen. Such effect can be explained by the degree of crystallinity and the film thickness of the active compounds. For low SSA the film thickness of active compounds is high. [46] Furthermore the amount of stored oxygen must correlate with the amount of Mn or Na₂WO₄. A thick film of the active compounds would store most of the oxygen in the lattice, which is heavily accessible for the methane pulse. As consequence the ratio of O_{surface}/O_{bulk} is low. Therefore activity and storage capacity could be lower for that material. A decrease of the film thickness would mean that less oxygen is stored in the bulk and the ratio of O_{surface}/O_{bulk} increases. Thus, more oxygen could be accessible on the catalyst surface and both properties, activity and storage capacity, increase. Further decrease of the film thickness may have a strong impact on the oxidation state of Mn. Wang et al. prepared a series of Na₂WO₄/Mn/SiO₂ catalysts, which had different particle sizes of manganese oxide. [9] They found in O₂-temperature programmed desorption experiments, that small manganese oxide crystal sizes release oxygen at lower temperatures into the gas phase. That means that the oxygen is less stable bound and could be easily released into the gas phase during the experiment or the manganese oxide could not reach a fully oxidized state to Mn(III), forming Mn₃O₄ instead. Therefore the catalyst material could be also reduced under reaction conditions in absence of gas phase oxygen, which may occur at very thin films of the active compounds. Another point is that the activity of the Na₂WO₄/Mn/SiO₂ catalyst material depends drastically on the structural flexibility of the Na₂WO₄/Mn phase. [51,52] If the film thickness decreases, the structural flexibility should decrease, because less amounts of the Na₂WO₄ and Mn are available per surface area unit and the interaction with the support material increases. Thus, the active phase may interact stronger with the support material and the ability to form a flexible structure of Na₂WO₄/Mn decreases. Therefore the activity may decrease, too.

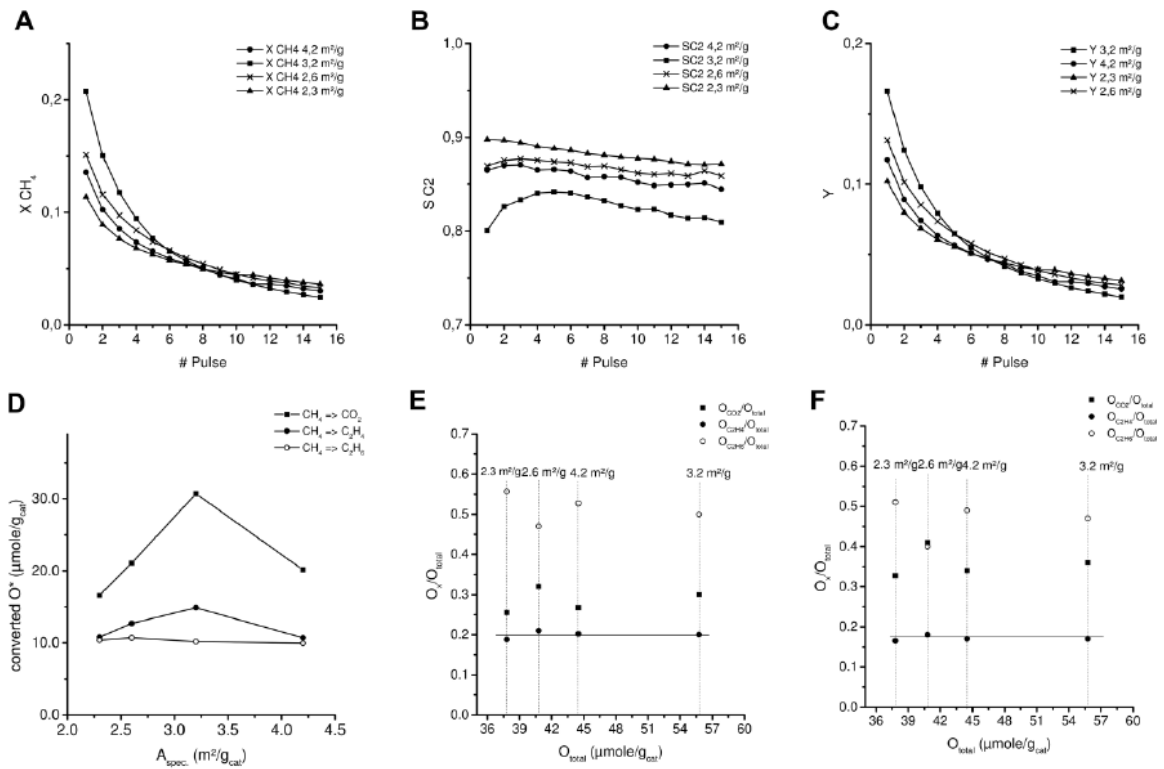


Figure 32 - Results of repetitive methane pulse experiments on Na_2WO_4 (5 wt-%)/Mn (2 wt-%)/ SiO_2 at different specific surface areas, 30 nml/min, 775 °C, 0.6 g catalyst; A-C: methane conversion, selectivity and C2 yield for each pulse; D: oxygen balance (methane based), E: oxygen balance (molecule specific, $k_3/k_4 = 7$), F: oxygen balance (molecule specific, $k_3/k_4 = 2$)

5.4.3 Catalytic tests with different Manganese loadings on $Na_2WO_4/Mn/SiO_2$ catalysts

In Figure 33 the results of the manganese loading variation are presented. For each residence time we observe also a maximum for methane conversion at a certain manganese loading. On increasing of the manganese loading the methane conversion increases drastically. At 2-wt % the highest methane conversion is observed. A further increase of the manganese loading decreases the catalyst activity again. The vice versa trend was observed for the C_2 selectivity. A maximum of 0.25 C_2 yield was observed. As mentioned in the last section, the catalytic activity of the catalyst compounds depends on their crystallinity and oxidation state. An increase of manganese loading leads to higher crystallinity and different oxidation states are possible which results in higher methane conversion. Loadings higher than 2-wt % may shift manganese oxide species from Mn_2O_3 to Mn_3O_4 . Such effect are observed at higher loadings (10-20 wt-% Mn) by XRD and for loadings in the range of 3-10 wt-% by XANES and EXAFS for manganese oxides supported on silica. At loadings below 10 wt-% of Mn, XRD cannot detect the Mn_3O_4 formation. [53] Investigation of the catalyst material by in-situ XRD studies showed $MnWO_4$ formation under OCM reaction conditions. [54] Therefore it would be possible that MnO^*WO_3 instead of Mn_3O_4 is formed. For our catalyst with low manganese oxide loadings, the film on the catalyst surface is thin and an increase of the manganese loading must also increase the film thickness (Table 13). Therefore the coupled effect of oxidation state and film thickness is also relevant in this series of experiments.

Our findings about the catalytic activities are in good agreement with the results of the group of Mortazavi, which were presented in the introduction. [14] Koirala et al. found similar results for methane conversion and C₂ selectivity at such manganese loadings in their co-feed steady state experiments. Exceeding a loading of 2 wt.-% Mn methane conversion and C₂ selectivity are not changing anymore. [55] Ji et al. found similar results to ours in steady state experiments. [56] Further, they found in Raman analyses that the Manganese surface concentration influences the binding situation of tetrahedrally bound WO₄. The typical wavelength for W-O on Na₂WO₄/Mn/SiO₂ catalysts is 910 cm⁻¹. At higher loadings an additional Raman band occurs at 948 cm⁻¹ and the intensity of the band signal at 910 cm⁻¹ decreases. In their XRD results they found at higher Mn loadings that parallel to Mn₂O₃ MnMn₆O₁₂ is formed. Such an effect is in good agreement with our working hypothesis.

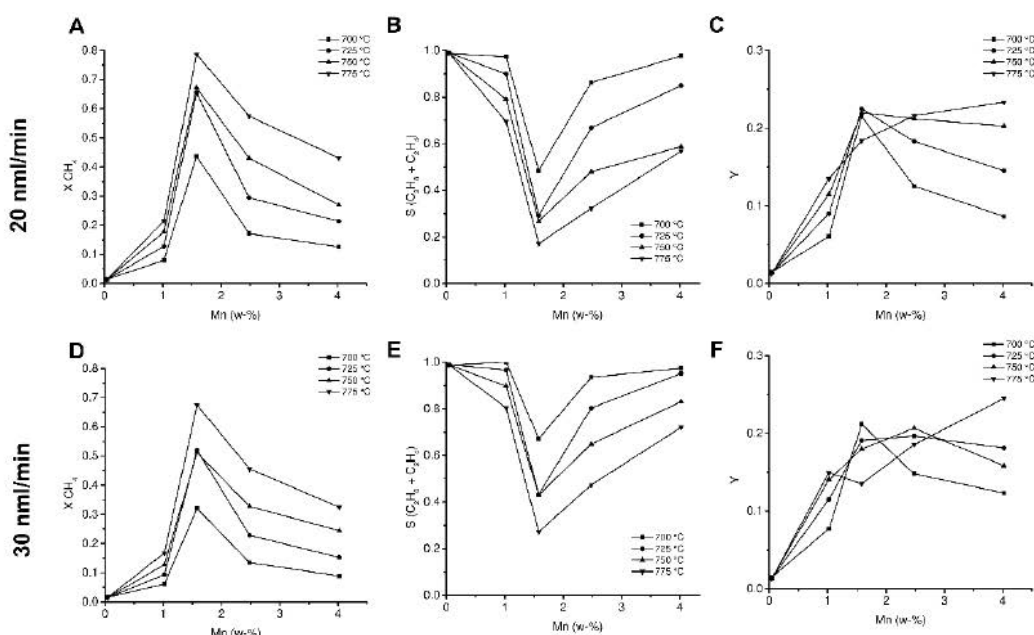


Figure 33 - Results of chemical looping experiments on Na₂WO₄ (5 wt-%)/Mn (var. wt-%)/SiO₂ catalysts at different Mn loadings and temperatures, 1 g catalyst, 1 ml CH₄ pulse A – C: methane conversion, C₂ selectivity and C₂ Yield at 20 nml/min D – F: methane conversion, C₂ selectivity and C₂ Yield at 30 nml/min, 1 ml CH₄ pulse

The results of our repetitive methane pulse experiments for different loadings of Mn are shown in Figure 34. At 0.02 wt-% manganese loading, we cannot observe significant methane conversion. However, it is found that alkaline metal doped tungstate supported on silica shows substantial OCM activity in co-feed steady state experiments. [16,57] The more manganese is loaded the more methane pulses were necessary to reach non catalytic activity in repetitive pulse experiments. The catalyst containing 4 wt-% Mn shows even after 15 methane pulses OCM activity at 0.1 methane conversion and 0.9 C₂ selectivity. This catalyst also shows the highest C₂ yield for each methane pulse. Calculation of the converted oxygen amounts showed that the highest CO₂ formation is observed for a molar ration of W:Mn (1:2), which is the classical composition (5 wt-% Na₂WO₄, 2 wt-% Mn) for this material. This is illustrated in Figure 34 D.

The molecule specific oxygen balances, presented in Figure 34 E & F, indicate similar results as presented in the last section. For O_{C2H4} we observe a constant ratio at different converted oxygen

amounts, while $O_{C_2H_6}$ is high at low oxygen conversion. An increase of the totally converted amount of oxygen shows a drastic increase of O_{CO_2} . The catalyst containing 4 wt-% manganese loadings shows catalytic performance until 25 methane pulses were dosed, which is not presented. The total amount of converted oxygen was at least 105 μ mole/g_{cat}. We conclude that ethene formation is nor dependent on the compound concentration of the catalyst material, neither on the manganese loading. Thus, ethene seems to be formed in gas phase, preferably. Due to the fact that only traces of hydrogen were observed, we assume that this reactant was converted by the catalyst material to water, similar as in temperature programmed reduction experiments with H₂. [23,58]

In order to explain our findings, a switch of the oxidation state of Mn_XO_Y or Na₂WO₄ is necessary. It has to be noted that Na₂WO₄ can switch the oxidation state between W⁺⁶ to W⁺⁵, according to the findings of Jiang et al. [59] Due to the fact, that the Na₂WO₄/SiO₂ catalyst shows only very low activity in our repetitive pulse experiments, but high C₂ selectivity we assume that the switch in the oxidation state of the tungstate would not explain our finding. If Na₂WO₄ would be responsible for the oxygen storage capacity, the stored amount of oxygen would not differ by a factor of five.

Therefore the oxidation potential and oxygen storage function in chemical looping experiments seems to depend on the manganese loadings. Unfortunately, we were not able to detect phases of Mn(II)oxide in our XRD-studies of the spend catalysts. It would be possible, that the formed crystal sizes were to small for reflexes in XRD studies of the spend catalysts or small amounts of oxygen reached the catalyst bed during sample export from the reactor.

However, our hypothesis is supported by the findings of Jiang et al. in EPR spectroscopy studies. [23] They found in dynamic experiments that tungsten oxide has no change in the oxidation state but manganese oxide has. They predicted an electron transfer from C-H bond cleavage by tungsten oxide as active center, while the electron is transferred to the manganese ion. Similar effects of supported manganese oxide catalysts in the OCM were also observed by Jones et al. [60] They tested Mn/SiO₂ catalysts with a variation of the manganese loading in dynamic experiments. Salehoun and Coworkers were able to observe the formation of MnWO₄ after dynamic experiments by XRD. [24]

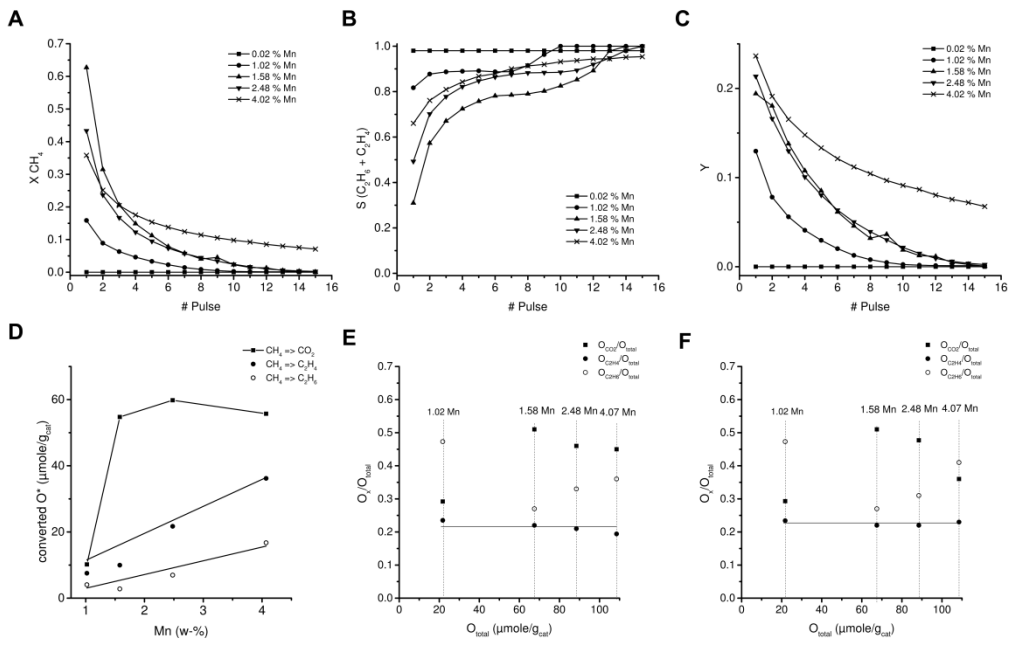


Figure 34 - Results of repetitive methane pulse experiments on Na_2WO_4 (5 wt-%)/Mn (var. wt-%)/ SiO_2 at different manganese loadings, 30nmol/min, 775 °C, 1 g catalyst; A-C: methane conversion, selectivity and C₂ yield for each pulse; D: oxygen balance (methane based), E: oxygen balance (molecule specific, $k_3/k_4 = 7$), F: oxygen balance (molecule specific, $k_3/k_4 = 2$)

5.4.4 Catalytic tests with different silica support materials on Na_2WO_4 /Mn/ SiO_2 catalysts

Figure 35 summarizes the results of chemical looping experiments for Na_2WO_4 /Mn/ SiO_2 catalysts with different support materials. The COK-12 supported catalyst with similar weight loadings of Na_2WO_4 and Mn shows in all cases much higher catalytic activity compared to the silica gel supported catalyst (reference catalyst). Such an activity difference was also observed in the last subsection. The main difference in the support material variation is the SSA and also the dispersion of the catalyst compounds. Such findings reflect our hypothesis of an optimal loading of Na_2WO_4 and Mn on the support material. Therefore the support material has a tremendous effect on catalytic activity, because the SSA of the final cristobalit phase controls the crystallinity and oxidation state of both compounds, Na_2WO_4 and especially the Mn_2O_3 .

Our results are in good agreement with the results of Yildiz and Coworkers, who studied the catalyst on different support materials in co-feed steady state experiments. [18]

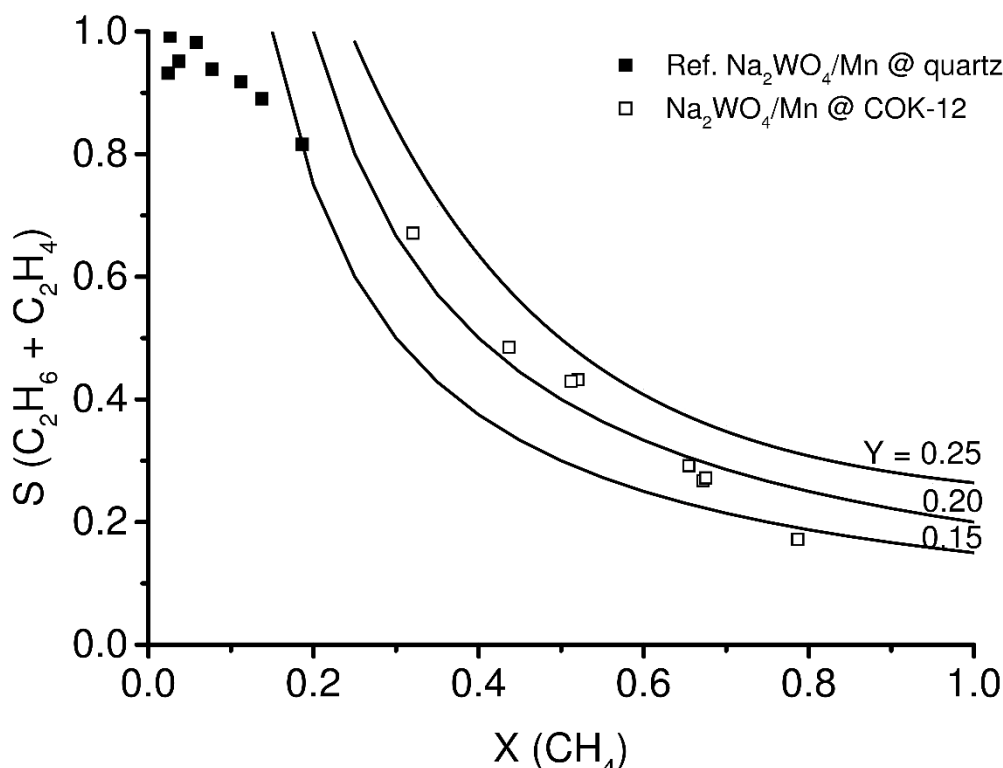


Figure 35 - Results of chemical looping experiments on Na_2WO_4 (5 wt-%)/Mn (2 wt-%)/ SiO_2 catalysts at different support materials, 1 g catalyst, 700 – 775 °C, 20 & 30 nmol/min, 1 ml CH_4 pulse

The results of our repetitive methane pulse experiments are shown in Figure 36 A-C. On the one hand the COK-12 supported catalyst shows much higher activity, which finally ends after 14 methane pulses. On the other hand the silica gel supported catalyst shows still catalytic activity after 15 methane pulses. That difference could reflect the difference of the film thickness for these catalyst materials. In Figure 36 D-F the oxygen balances are presented. The COK-12 supported catalyst stores around three times more oxygen than the silica gel supported one. On the one hand the COK-12 supported has a much thinner film of the active compounds. Therefore the degree of crystallinity of the active compounds is lower and the stored oxygen is more easily available for chemical reactions with the methane pulses. Therefore that material is much more active during the first pulses, but the activity decreases faster, because the stored amount of oxygen is also faster depleted. On the other hand the silica gel supported catalyst has a much thicker film of the catalyst compounds. Therefore the oxygen is much stronger bound on the catalyst surface and in the toplayers, which cannot be removed as easily as for the COK-12 supported catalyst. Thus, less oxygen is removed from the catalyst surface by each methane pulse and therefore more pulses were necessary until no catalytic activity is observed. Such big differences in the oxygen storage capacity were also observed by different groups in different chemical looping experiments. [61–63] The most important factor is the effective oxidation state of the oxygen storage material, which is strongly influenced by the support material, in some cases by a factor up to ten. As discussed before there are several aspects which can influence the oxidation state of the active compounds in our experiments, too.

The C₂ selectivity for the COK-12 supported catalyst is in consequence by higher catalytic activity significantly lower, compared to those of the silica gel supported one. That is because of a competition between methane and C₂H_X activation. At low methane conversion the partial pressure of formed C₂ products is very low and therefore an activation reaction by the catalyst material is very unlikely, assuming a second order behavior and a consecutive reaction route. If the catalyst material is more active, more C₂ products will be formed and therefore the C₂ partial pressure increases. Thus the C₂ activation reaction becomes more relevant and causes to an apparent C₂ yield maximum.

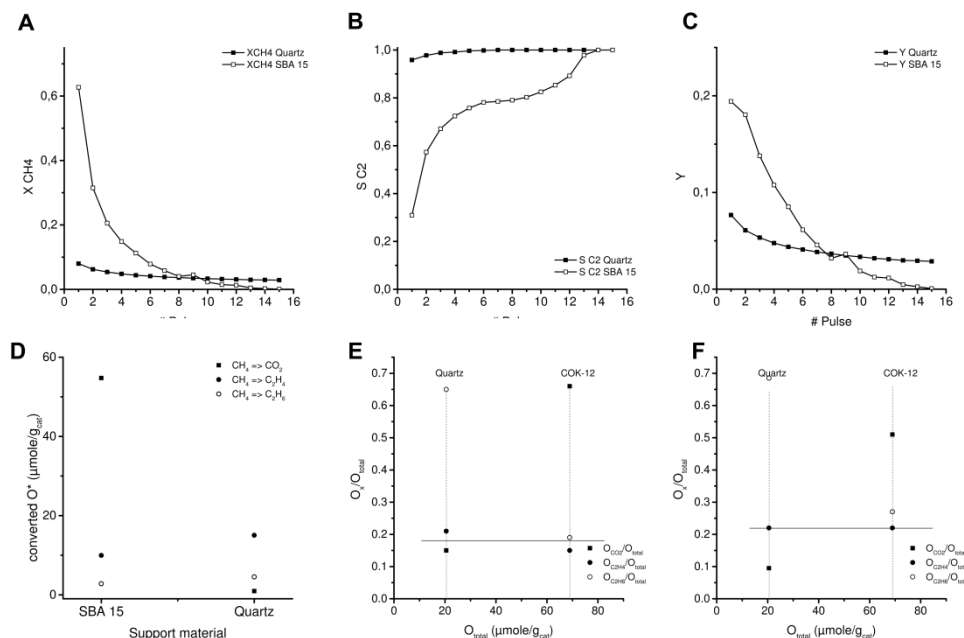


Figure 36 - Results of repetitive methane pulse experiments on $\text{Na}_2\text{WO}_4/\text{Mn}/\text{SiO}_2$ at different support materials, 30nmL/min, 775 °C, 1 g catalyst; A-C: methane conversion, selectivity and C₂ yield for each pulse; D: oxygen balance (methane based), E: oxygen balance (molecule specific, k₃/k₄ = 7), F: oxygen balance (molecule specific, k₃/k₄ = 2)

A direct relation between catalyst compounds and oxygen storage capacity was only found for the manganese system, which is presented in Figure 37 A. We plotted also three theoretical trends which show a projection of the amount of stored oxygen by different manganese oxide species. In all cases the amount of Na_2WO_4 is constant. It has to be noted that MnO is present on the catalyst surface as MnWO_4 , as discussed before. Therefore Mn_3O_4 can also be interpreted as $\text{MnWO}_4 + \text{Mn}_2\text{O}_3$.

In Figure 37 B the correlation between the film thickness and the oxygen storage capacity is presented. A nearly linear dependence was found at constant weight loadings of Na_2WO_4 and Mn, independent from the support material. If the number of layers of the active compounds falls below 25, the catalyst activity decreases dramatically in all cases.

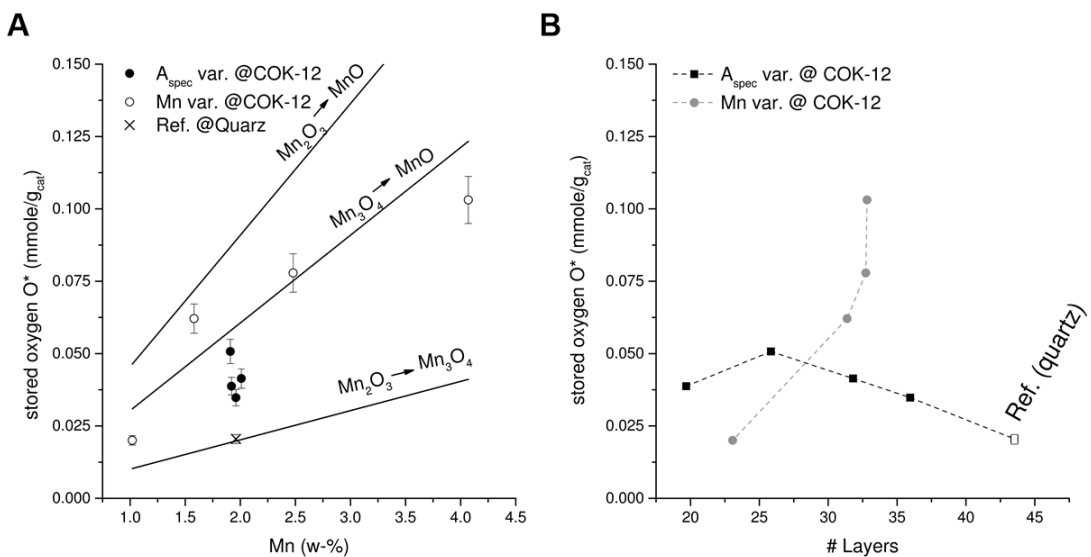
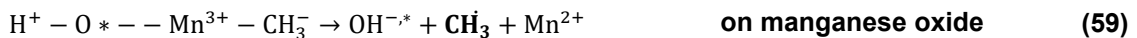
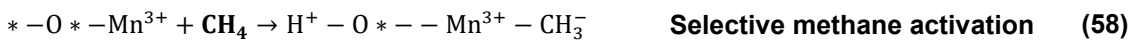
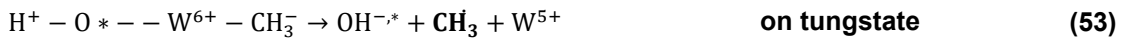
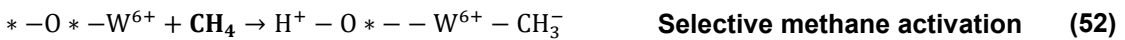


Figure 37 – Total stored amount of oxygen at different prepared $\text{Na}_2\text{WO}_4/\text{Mn}/\text{SiO}_2$ catalyst materials, A – correlation between oxygen storage capacity and manganese oxide loading, B – correlation between oxygen storage capacity and film thickness of Na_2WO_4 and Mn_2O_3

Jiang and Coworkers found by EPR and XANES that only the manganese ions were reduced in dynamic experiments. This phenomenon was discussed as oxygen-spillover effect. [23,64] They postulated a cooperating redox mechanism for selective methane activation according to equations (38)-(42). As mentioned before, Salehoun and Coworkers proposed from dynamic experiments that a new phase (MnWO_4) is observed in their XRD spectra of spent catalysts. [24] This phase contains Mn(II), while on their fresh catalysts Mn_2O_3 is dominating, which is Mn(III). Jones et al. found that also $\text{Mn}_x\text{O}_y/\text{SiO}_2$ is active in OCM, but much less selective for C_2 products. [65] Therefore the proposed redox mechanism of Jiang et al. has to be extended according to equations (43)-(45). Ji et al. demonstrated that even small amounts of tungstate will increase methane conversion and C_2 selectivity dramatically. [56] According to their findings, the reaction rates of equations (38) and (39) have to be much higher compared to the rate of reactions (44) and (45). Therefore the manganese oxide seems to contribute to the selective activation of methane by a redox mechanism via tungstate, but unfortunately it can also activate methane in an unselective reaction and maybe also other alkanes.



We found no change of the amount of O_{C2H4} by use of different catalyst materials, which had different performance during all experiments. Such an effect is only plausible, if ethylene formation is independent from the catalyst material and occurs in the gas phase in chemical looping experiments. To test such hypothesis we simulated a methane pulse with a model that combines gas phase and surface reactions.

5.4.5 Simulation results

The number of active sites was set to $1/nm^2$ in our simulations. This was estimated from the fact that such a number is the monolayer coverage for a supported transient metal oxide on silica. We discussed that a film of several multilayers of the active compounds is present on the catalyst surface. Therefore we assume that around one O atom per squared nanometer is directly available on the top layer of the catalyst surface, while the rest is stored in sublayers.

The result of a simulation of a methane pulse to the catalyst bed in Chemkin is shown in Figure 38. As can be seen in Figure 38 – A the original parameters of Daneshpayeh et al. show only poor methane conversion. [11,35] This is in straight contradiction to our results in the last section. CH_2O is formed as an intermediate species which is formed from $CH_3O\cdot$ decomposition. Further decomposition of CH_2O forms CO and H_2 . It can be seen that ethane and ethene are formed and the C_2 selectivity is in good agreement with our results of the single methane pulse experiments in the variation of the specific surface areas. For a sufficient comparison at same methane conversion both surface reaction rates were increased by factor 300. The results of this simulation are shown in Figure 38 – B. The methane conversion is in the range of our observations in chemical looping experiments, now. CO is dominating the overall selectivity, while ethene is the major product among the C_2 compounds. Ethane shows a typical trend of an intermediate species in a consecutive reaction pathway. This indicates that thermal dehydrogenation is a serious reaction pathway to convert ethane to ethene in oxygen free gas phase. Such a simulation supports our observation of a constant ratio of converted O_{C2H4} as mentioned in the last section.

At this point it has to be noted that the simulation is only a rough estimation for testing our hypothesis. The increase of the surface reaction rates, the lack of an experimental investigation of the number of active sites and a well explored surface reaction network for this material indicate that a lot of important parameters are still missing for an adequate micro kinetic surface reaction model. Due to the fact, that only less amounts of hydrogen were observed in our experiments, we assume that the H_2 reduces also the catalyst material, similar to the results, which were found in temperature programmed reduction experiments. [16,55]

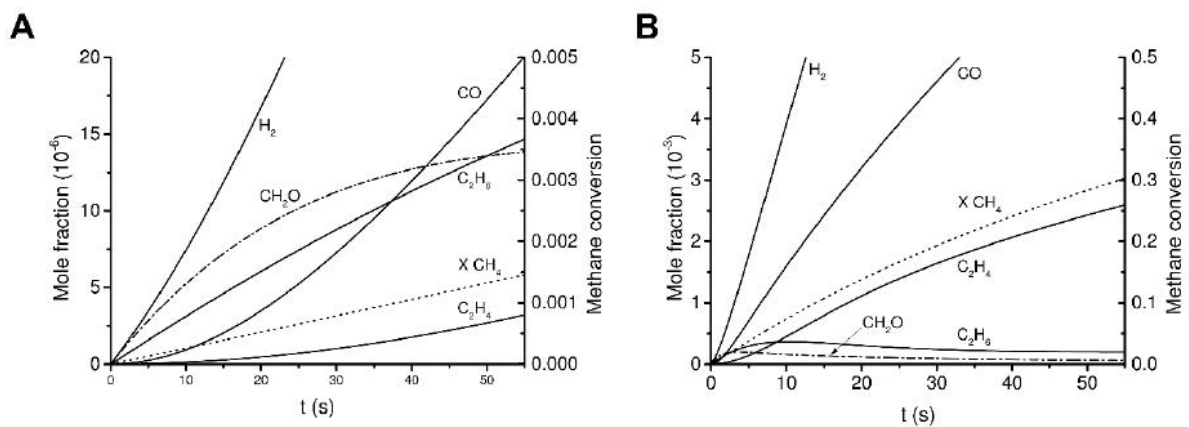


Figure 38 - Results of a methane pulse simulation in chemkin, A: original reaction parameters by Daneshpan et al. [11,35], B: Surface reaction rates increased by factor 300

5.4.6 Mechanistic aspects

A scheme of the catalyst functionality of the $\text{Na}_2\text{WO}_4/\text{Mn}/\text{SiO}_2$ catalyst is presented in Figure 39, which is based on the findings of other groups and ours. Na^+ ions induce a phase change of the support material from SiO_2 to α -cristobalite during the calcination procedure. [13] Such transformation allows for the formation of an amorphous or glassy phase of Na_2WO_4 and Mn_xO_y . The constitution of this phase depends on the amount of both compounds and their dispersion on the support material surface. Furthermore, this phase has a flexible structure under OCM conditions, which is responsible for selective methane activation. [14,52] When the formation of this phase is complete, no crystal structures are detectable by XRD measurements for the impregnated compounds. This film can be oxidized by gas phase oxygen through adsorption (O_x^*) and the conversion to top layer oxygen ($\text{O}_{\text{lattice}}$), which may interact with sublayers, too. [25] We assume two different surface oxygen species, which are stored in chemical looping experiments on the catalyst surface. Electrophilic oxygen seems to be responsible for selective methane activation. [26] On the other hand nucleophilic oxygen seems to be responsible for unselective methane activation. The selective activation of methane by electrophilic oxygen species results in methyl radical formation which couple to ethane. [66] It is unclear whether this coupling process is present on the catalyst surface or in gas phase. However, the combined radicals, which are an energy-rich species from an ethane molecule (C_2H_6^*) which still contains the energy from these radicals. A collision partner (M) in gas phase or a solid phase is necessary to emit this energy to form a stable ethane molecule. [39] We assume from our observations that ethylene is formed in gas phase by thermal dehydrogenation in chemical looping experiments. This reaction is initiated by a collision of ethane and another molecule. [67] Another possible route is the dehydrogenation of C_2H_6^* . During our chemical looping and repetitive pulse experiments we only observed small traces of hydrogen. Therefore we suppose that hydrogen reduces also stored oxygen on the catalyst surface and is converted into water, immediately. The ethylene can be activated by the catalyst to form deep oxidation products by both oxygen species. [68] Thus, the selective oxygen species ($\text{O}_{\text{elec.}}$) for methane activation has a contrary effect on ethene. [68] It has to be noted that methane and ethene C-H bond strength (439 kJ/mole and 464 kJ/mole) have similar stability. [69] It was reported that the ethene double bond has a bond strength of 315 kJ/mole. [70] A highly active catalyst in chemical looping experiments would produce high amounts of ethene if

the residence time would be long enough for the thermal dehydrogenation reaction in gas phase. Therefore the increasing partial pressure of C₂H₄ would enhance the reaction rates for ethene activation by both oxygen species. Assuming that a strong correlation between rate constant and bond strength exists, the activation of ethene by O_{elec.} requires a lower partial pressure for the same activation rate than methane. In sum there seem to be four reaction routes, which contribute to deep oxidation product formation while one route is responsible for selective methane activation. At this point it is unclear, whether the consumption of nucleophilic oxygen is necessary for the re-formation of a new electrophilic active site or if this is a parallel effect. Such constellation indicates a very complex situation for reaching higher C₂ yields by an optimization of the reaction conditions.

However, the role of manganese oxide seems to be manifold, because there seems to be a selective methane activation reaction by a cooperated redox mechanism with tungstate, but also it plays an important role for the formation of deep oxidation products. Further the oxygen storage capacity in chemical looping experiments depends strongly on this compound. One important finding in our experiments is the influence of the film thickness of Na₂WO₄ and Mn_xO_y on the catalytic activity. A thick film provides less oxygen in chemical looping experiments for methane conversion, because the most oxygen is stored inside of the film, which is hard to access for gas phase reactants. Thin films, may feel a less cooperated redox effect between Na₂WO₄ and Mn_xO_y. Also, the oxygen seems to be less stable bound and an auto reduction reaction by oxygen desorption may occur. Both effects decrease the catalytic activity. Therefore an optimal film thickness is required for a performance catalyst in chemical looping experiments.

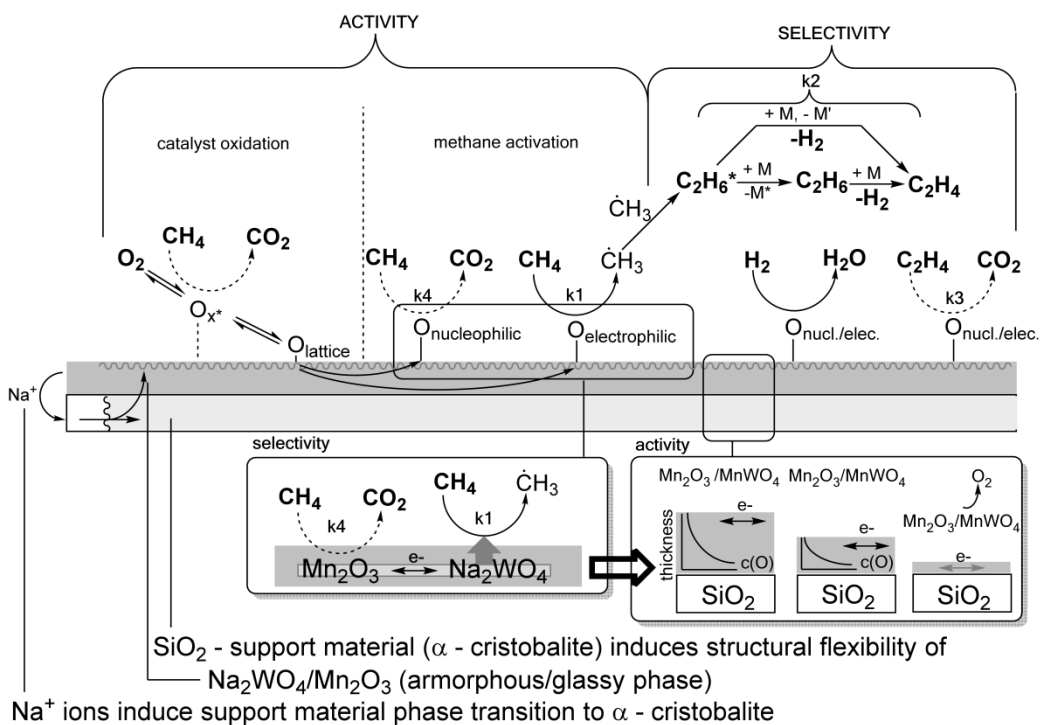


Figure 39 - Proposed OCM surface and gas phase reaction network for the $\text{Na}_2\text{WO}_4/\text{Mn}/\text{SiO}_2$ catalyst in chemical looping experiments [13–19,25,26,39,66,67,71]

5.5 Conclusion

In this work we studied a series of $\text{Na}_2\text{WO}_4/\text{Mn}/\text{SiO}_2$ catalysts in chemical looping and repetitive methane pulse experiments. The variation of the specific surface area of this catalyst material at constant weight loadings indicates that a higher SSA increases the catalytic activity. This effect is limited to SSA's below $4 \text{ m}^2/\text{g}$. Catalysts with higher SSA showed lower catalytic activity in chemical looping experiments. The highest activity for varied manganese loadings was found at 5 wt-% Na_2WO_4 and 2 wt-% Mn in chemical looping experiments. Unfortunately, no C2 yield higher than 0.25 was observed. COK-12 supported catalysts were much more active compared to silica supported one.

In our repetitive methane pulse experiments we found for all catalyst materials by oxygen balances that ethylene formation consumes 25 - 30 % of the total converted oxygen atoms. This indicates that ethylene formation is preferred in gas phase by thermal dehydrogenation in absence of oxygen. That was verified by simulations. The highest amount of converted oxygen was $105 \mu\text{mol(O)}/\text{g}_{\text{cat}}$ for 5 wt-% Na_2WO_4 and 2 wt-% Mn on COK-12. We calculated an optimal surface concentration of $66 \text{ Mn(II)}/\text{nm}^2$ and $33 \text{ W}/\text{nm}^2$, which showed the highest oxygen storage capacity and highest catalytic activity in our experiments. Our results about the variation of the Mn loading indicate that this compound is responsible for the oxygen storage functionality of the $\text{Na}_2\text{WO}_4/\text{Mn}/\text{SiO}_2$ catalyst. A theoretical number of layers for the active phase ($\text{Na}_2\text{WO}_4/\text{Mn}$) was calculated. The highest catalytic performance was observed at about 25 layers and even small deviations from that number result in less performance in

chemical looping experiments for $\text{Na}_2\text{WO}_4/\text{Mn}/\text{SiO}_2$ catalysts. The tungstate contributes by activity enhancement of selective methane activation. We assume that a multilayered redox reaction mechanism of this catalyst material is responsible for the OCM reaction in chemical looping experiments. A scheme about the $\text{Na}_2\text{WO}_4/\text{Mn}/\text{SiO}_2$ catalyst functionalities during the OCM reaction was also presented.

5.6 Acknowledgement

This work is part of the UNICAT excellence cluster, which is coordinated by the Technische Universität Berlin. The financial support of this cluster is gratefully acknowledged. We thank Harald Link for ICP measurements and Jannes Mechler for his support in catalyst preparation.

5.7 References

- [1] A.M. Martini, J.M. Budai, L.M. Walter, M. Schoell, *Lett. to Nat.* 383 (1996) 155–158.
- [2] S. Depa, *Review of Emerging Resources: U.S. Shale Gas and Shale Oil Plays*, Washinton D.C., 2011.
- [3] R. Diercks, J.-D. Arndt, S. Freyer, R. Geier, O. Machhammer, J. Schwartze, M. Volland, *Chem. Eng. Technol.* 31 (2008) 631–637.
- [4] P. Weiland, *Appl. Microbiol. Biotechnol.* 85 (2010) 849–860.
- [5] L.R. Snowdon, *Org. Geochem.* 32 (2001) 913–931.
- [6] P.L. Spath, M.K. Mann, *Life Cycle Assessment of a Natural Gas Combined Cycle Power Generation System*, 2000.
- [7] X. Fang, S. Li, J. Gu, D. Yang, *J. Mol. Catal.* (1992) 255.
- [8] S. Li, *J. Nat. Gas Chem.* 12 (2003) 1–9.
- [9] J. Wang, L. Chou, B. Zhang, H. Song, J. Zhao, J. Yang, S. Li, *J. Mol. Catal. A Chem.* 245 (2006) 272–277.
- [10] H.R. Godini, A. Gili, O. Görke, U. Simon, K. Hou, G. Wozny, *Energy & Fuels* 28 (2014) 877–890.
- [11] M. Daneshpayeh, N. Mostoufi, A. Khodadadi, R. Sotudeh-gharebagh, *Energy & Fuels* 23 (2009) 3745–3752.
- [12] S. Jaso, S. Sadjadi, H.R. Godini, U. Simon, S. Arndt, O. Görke, A. Berthold, H. Arellano-Garcia, H. Schubert, R. Schomäcker, G. Wozny, *J. Nat. Gas Chem.* 21 (2012) 534–543.
- [13] A. Palermo, J. Pedro, H. Vazquez, A.F. Lee, M.S. Tikhov, R.M. Lambert, *J. Catal.* 177 (1998) 259–266.
- [14] Z. Gholipour, a Malekzadeh, M. Ghiasi, Y. Mortazavi, a Khodadadi, (2012) 189–211.
- [15] S. Mahmoodi, M.R. Ehsani, S.M. Ghoreishi, *J. Ind. Eng. Chem.* 16 (2010) 923–928.
- [16] A. Malekzadeh, A.K. Dalai, A. Khodadadi, Y. Mortazavi, *Catal. Commun.* 9 (2008) 960–965.
- [17] M. Yildiz, U. Simon, T. Otremba, Y. Aksu, K. Kailasam, a. Thomas, R. Schomäcker, S. Arndt, *Catal. Today* 228 (2014) 5–14.
- [18] M. Yildiz, Y. Aksu, U. Simon, K. Kailasam, O. Goerke, F. Rosowski, R. Schomäcker, A. Thomas, S. Arndt, *Chem. Commun.* 50 (2014) 14440–14442.
- [19] S. Sadjadi, S. Jašo, H.R. Godini, S. Arndt, M. Wollgarten, R. Blume, O. Görke, R. Schomäcker, G. Wozny, U. Simon, *Catal. Sci. Technol.* 5 (2015) 942–952.
- [20] M.G. Colmenares, U. Simon, M. Yildiz, S. Arndt, R. Schomaecker, A. Thomas, F. Rosowski, A. Gurlo, O. Goerke, *Catal. Commun.* accepted (2016).

- [21] Y. Moro-oka, *Catal. Today* 45 (1998) 3–12.
- [22] Z.-C. Jiang, C.-J. Yu, X.-P. Fang, S.-B. Li, H.-L. Wand, *J. Phys. Chem.* 97 (1993) 12870–12875.
- [23] Z. Jiang, H. Gong, S. Li, *Stud. Surf. Sci. Catal.* 112 (1997) 481–490.
- [24] V. Salehoun, A. Khodadadi, Y. Mortazavi, A. Talebizadeh, *Chem. Eng. Sci.* 63 (2008) 4910–4916.
- [25] B. Beck, V. Fleischer, S. Arndt, M.G. Hevia, A. Urakawa, P. Hugo, R. Schomäcker, *Catal. Today* 228 (2014) 212–218.
- [26] V. Fleischer, R. Steuer, S. Parishan, R. Schomäcker, *J. Catal.* accepted (2016).
- [27] V. Fleischer, P. Littlewood, S. Parishan, R. Schomäcker, *Chem. Eng. J.* submitted (2016).
- [28] J. Adanez, A. Abad, F. Garcia-Labiano, P. Gayan, L.F. de Diego, *Prog. Energy Combust. Sci.* 38 (2012) 215–282.
- [29] T. Mattisson, A. Lyngfelt, H. Leion, *Int. J. Greenh. Gas Control* 3 (2009) 11–19.
- [30] U. Simon, O. Görke, A. Berthold, S. Arndt, R. Schomäcker, H. Schubert, *Chem. Eng. J.* 168 (2011) 1352–1359.
- [31] S. Pak, P. Qiu, J.H. Lunsford, *J. Catal.* 230 (1998) 222–230.
- [32] C. Shi, M.P. Rosynek, J.H. Lunsford, (1994) 8371–8376.
- [33] S. Dooley, M.P. Burke, M. Chaos, Y. Stein, F.L. Dryer, V.P. Zhukov, O. Finch, J.M. Simmie, H.J. Curran, *Int. J. Chem. Kinet.* 42 (2010) 527–549.
- [34] O. Korup, S. Mavlyankariev, M. Geske, C.F. Goldsmith, R. Horn, *Chem. Eng. Process.* 50 (2011) 998–1009.
- [35] M. Daneshpayeh, A. Khodadadi, N. Mostoufi, Y. Mortazavi, R. Sotudeh-Gharebagh, A. Talebizadeh, *Fuel Process. Technol.* 90 (2009) 403–410.
- [36] H.R. Godini, V. Fleischer, O. Görke, S. Jaso, R. Schomäcker, G. Wozny, *Chemie Ing. Tech.* 86 (2014) 1906–1915.
- [37] T. Ito, J. Wang, C. Lin, J. Lunsford, *J. Am. ...* 107 (1985) 5062–5068.
- [38] J. Sun, J. Thybaut, G.B. Marin, *Catal. Today* 137 (2008) 90–102.
- [39] S. Storsæter, D. Chen, A. Holmen, *Surf. Sci.* 600 (2006) 2051–2063.
- [40] Y. Simon, F. Baronnet, P.-M. Marquaire, *Ind. Eng. Chem. Res.* 46 (2007) 1914–1922.
- [41] L. Lehmann, M. Baerns, *Catal. Today* 13 (1992) 265–272.
- [42] P.N. Kechagiopoulos, J.W. Thybaut, G.B. Marin, *Ind. Eng. Chem. Res.* 53 (2014) 1825–1840.
- [43] I.E. Wachs, *Catal. Today* 27 (1996) 437–455.
- [44] P.B. Weisz, C.D. Prater, in: *Adv. Catal. Relat. Subj.*, n.d., pp. 143 – 195.
- [45] R.D. Shannon, *Acta Crystallogr. Sect. A* 32 (1976) 751–767.
- [46] E.R. Stobbe, B.A. de Boer, J.W. Geus, *Catal. Today* 47 (1999) 161–167.
- [47] F. Arena, T. Torre, C. Raimondo, A. Parmaliana, *Phys. Chem. Chem. Phys.* 3 (2001) 1911–1917.
- [48] F. Buciuman, F. Patcas, R. Craciun, D.R.T. Zahn, *Phys. Chem. Chem. Phys.* 1 (1999) 185–190.
- [49] Q.J. Yan, Y. Wang, Y.S. Jin, Y. Chen, *Catal. Lett.* 13 (1992) 221–228.
- [50] Y. Liu, R. Hou, X. Liu, J. Xue, S. Li, *Stud. Surf. Sci. Catal.* 119 (1998) 307–311.
- [51] A.A. Tyunyaev, G.D. Nipan, T.N. Kol'tsova, A.S. Loktev, V.A. Ketsko, A.G. Dedov, I.I. Moiseev, *Russ. J. Inorg. Chem.* 54 (2009) 664–667.
- [52] G.D. Nipan, A.S. Loktev, K. V. Parkhomenko, S.D. Golikov, A.G. Dedov, I.I. Moiseev, *Dokl. Phys. Chem.*

448 (2013) 19–22.

- [53] C. Reed, Y.-K. Lee, S.T. Oyama, *J. Phys. Chem. B* 110 (2006) 4207–4216.
- [54] M. Yildiz, Y. Aksu, U. Simon, T. Otremba, K. Kailasam, C. Göbel, F. Girgsdies, O. Görke, F. Rosowski, A. Thomas, R. Schomäcker, S. Arndt, *Appl. Catal. A Gen.* accepted (2016).
- [55] R. Koirala, R. Büchel, S.E. Pratsinis, A. Baiker, *Appl. Catal. A Gen.* 484 (2014) 97–107.
- [56] S. Ji, T. Xiao, S. Li, C. Xu, R. Hou, K.S. Coleman, M.L.H. Green, *Appl. Catal.* 225 (2002) 271–284.
- [57] a. Erdohelyi, R. Németh, a. Hancz, a. Oszkó, *Appl. Catal. A Gen.* 211 (2001) 109–121.
- [58] A. Malekzadeh, M. Abedini, A.A. Khodadadi, M. Amini, H.K. Mishra, A.K. Dalai, *Catal. Lett.* 84 (2002) 45–51.
- [59] Z.-C. Jiang, L.-B. Feng, H. Gong, H.-L. Wang, *Methane and Alkane Conversion Chemistry*, Springer US, New York, 1995.
- [60] J.A. Sofranko, J.J. Leonard, C.A. Jones, *J. Catal.* 103 (1987) 302–310.
- [61] M.M. Hossain, H.I. de Lasa, *Chem. Eng. Sci.* 63 (2008) 4433–4451.
- [62] T. Mattisson, A. Järdnäs, A. Lyngfelt, *Energy and Fuels* 17 (2003) 643–651.
- [63] Q. Zafar, T. Mattisson, B. Gevert, *Ind. Eng. Chem. Res.* 2 (2005) 3485–3496.
- [64] L. Shu-Ben, *Chinese J. Chem.* 19 (2001) 16–21.
- [65] C.A. Jones, J.J. Leonard, J.A. Sofranko, *J. Catal.* 103 (1987) 311–319.
- [66] D.J. Driscoll, J.H. Lunsford, *J. Phys. Chem.* 89 (1985) 4415–4418.
- [67] M. Frenklach, T. Bowman, G. Smith, Michael Frenklach (2015) <http://combustion.berkeley.edu/gri-mech/>.
- [68] R.B. Grant, R.M. Lambert, *J. Catal.* 92 (1985) 364–375.
- [69] S.J. Blanksby, G.B. Ellison, *Acc. Chem. Res.* 36 (2003) 255–63.
- [70] H. Jacobsen, T. Ziegler, *J. Am. Chem. Soc.* 116 (1994) 3667–3679.
- [71] J.S. Ahari, R. Ahmadi, H. Mikami, K. Inazu, S. Zarrinpashne, S. Suzuki, K. Aika, *Catal. Today* 145 (2009) 45–54.

5.8 supporting information

5.8.1 Experimental - Residence time analyses

The residence time of gas pulses was analyzed by pulse marking experiments. The sample loop (1 ml) was filled with N₂ or Ar, which was used as inert tracer gas. First the pulse was injected to the tube system of the setup, without reactor. After that the reactor was filled with 0.5 or 1 g catalyst material and heated up under He (30 nml/min). Reaching 775 °C, the tracer gas was injected to the setup with installed reactor. The detection of the tracer pulse was carried out by a thermal conductivity detector (Messkonzept 200) which was located directly at the reactor outlet. The detection of the signal was each 0.5 s.

5.8.2 Modelling and simulation

5.8.2.1 Residence time analyses

The residence time distribution function E(t) for each experiment was derived according to equations (14) and (15). The amount of tracer (n_{tracer}) was calculated according to the ideal gas law for 1 ml gas at 298 K and 101300 Pa.

$$E(t) = \dot{V} \cdot \frac{c(t)}{n_{tracer}} \quad (60)$$

$$\int E(t) dt = 1 \quad (61)$$

All residence time experiments were modelled and fitted by Berkley Madonna. The experimental without dispersion effects of the reactor were fitted by an empirical square-pulse function. The function generates a rectangular signal and the fitting parameters were the delay time t_{delay} , the time of square-pulse duration t_{dose} and the amplitude of the square pulse. The delay time represents the time, where no tracer signal was detected and the gas pulse remains in the piping system. The time of square-pulse duration represents the time since the complete tracer gas enters and passed the reactor. The amplitude of the square-pulse was set as the area of the signal is one, according to equation (15).

The heated reactor was modelled by the dispersion model (equation (16), which has as fitting parameters the velocity of the flow (u) and an axial dispersion coefficient (D_{ax}). The axial coordinate is expressed as z. That coefficient is correlated to the Bodenstein number according to equation (17), where L is the length of the reactor.

$$\frac{dc}{dt} = -u \frac{dc}{dz} + D_{ax} \frac{d^2 c}{dz^2} \quad (62)$$

$$D_{ax} = \frac{u \cdot L}{Bo} \quad (63)$$

The model was fitted by implementation of high number (200) of spatial segments M. This is shown in equation (18). The length of each segment is defined according to equation (19). The boundary condition for the M = 0 was the implementation of the squarepulse function (equation (20)).

$$\frac{dc[1..M]}{dt} = -u \frac{(c[i+1] - c[i-1])}{2 \cdot L_i} + D_{ax} \frac{c[i+1] - c[i] + c[i-1]}{(2 \cdot L_i)^2} \quad (64)$$

$$L_i = \frac{L}{M} \quad (65)$$

$$\frac{dc[0]}{dt} = -u \cdot \frac{(-\text{squarepulse}(t_{\text{dose}}, t_{\text{delay}}) \cdot \text{amplitude} + c[i+1])}{L_i} + D_{\text{ax}} \frac{c[i+1] - c[i]}{(L_i)^2} \quad (66)$$

5.8.2.2 Kinetic modelling of repetitive pulse experiments

To understand the reaction routes and the consumption of stored oxygen according to Figure 40 in more detail the repetitive pulse experiments were fitted and simulated in Berkley Madonna. We assumed that each pulse is similar to batch process, where the initial concentration for methane is constant for each methane pulse, while the oxygen concentration decreases with each pulse.

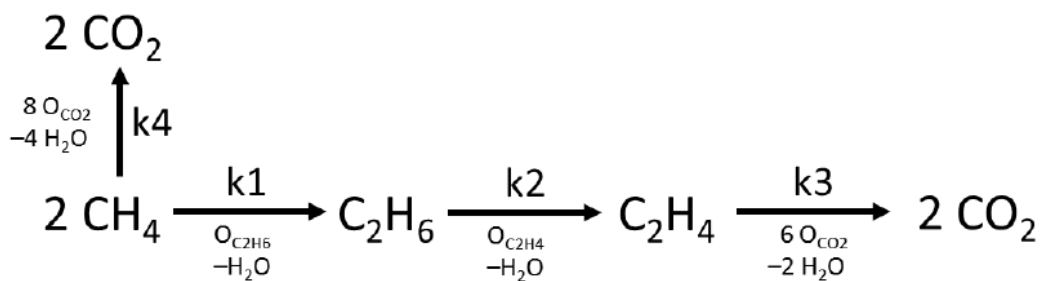


Figure 40 - Surface reaction network of the $\text{Na}_2\text{WO}_4/\text{Mn}/\text{SiO}_2$ catalyst to determine a molecule specific oxygen balance

The reactions were expressed according to equations (67)-(70), where N is the total number of methane pulses, which were 15.

$$R1[1..N] = k1 * \text{CH}_4 * O[i] \quad (67)$$

$$R2[1..N] = k2 * \text{C}_2\text{H}_6[i] * O[i] \quad (68)$$

$$R3[1..N] = k3 * \text{C}_2\text{H}_4[i] * O[i] \quad (69)$$

$$R4[1..N] = k4 * \text{CH}_4 * O[i] \quad (70)$$

The fitting parameters were the rate constants $k1 - k4$. The ratio of $k3/k4$ was set in the first run to 7 and in a second simulation to 2. For each repetitive pulse experiment the first four methane pulses were fitted to the presented parameters, getting a higher model precision. The initial concentration of oxygen was set according to the calculated ones by methane based oxygen balance, which is presented in the manuscript (Table 1). If N is 1 the total amount of stored oxygen was set as initial parameters. That was subtracted for the next pulse by the amount of converted oxygen (equation (71)).

$$O[i+1] = O_{\text{total}} - \sum_i O_{\text{converted}}[i] \quad (71)$$

The amount of methane was derived according to the ideal gas law. We assume 1 ml gas, 298 K and 101,300 Pa. The initial concentrations were set according to equation (72). V_{space} stands for the free gas space in the catalyst bed.

$$c_x = \frac{n_x}{V_{space}} \quad (72)$$

The free space was estimated according to equation (73), where the volume of the catalyst bed (ca. 6 cm³ = 1 g catalyst) were multiplied by the void fraction ϵ which was assumed to be 0.45. That value is common for several fixed beds. [1]

$$V_{space} = V_{catalyst\ bed} \cdot \epsilon \quad (73)$$

The material balances were derived according to equations (74)-(79).

$$\frac{d(CH_4[1..N])}{dt} = -2 \cdot R1[i] - R4[i] \quad (74)$$

$$\frac{d(C_2H_6[1..N])}{dt} = \frac{1}{2} \cdot R1[i] - R2[i] \quad (75)$$

$$\frac{d(C_2H_4[1..N])}{dt} = R2[i] - \frac{1}{2} \cdot R3[i] \quad (76)$$

$$\frac{d(CO_{2;C_2H_4}[1..N])}{dt} = 2 \cdot R3[i] \quad (77)$$

$$\frac{d(CO_{2;CH_4}[1..N])}{dt} = R4[i] \quad (78)$$

$$\frac{d(CO_2[1..N])}{dt} = CO_{2;C_2H_4}[i] + CO_{2;CH_4}[i] \quad (79)$$

5.8.2.3

The residence time was set according to our findings of the residence time analyses experiments, which are discussed in the next section.

5.8.2.4 Simulations of repetitive pulse experiments

According to our fitting results, the kinetic model was used to simulate 15 methane pulses. The decrease of stored oxygen was considered for each methane pulse as presented in the last subsection. The final concentrations for each pulse of the formed products (C₂H₆, C₂H₄, CO_{2;C₂H₄}, CO_{2;CH₄}) were used to calculate the molecule specific amounts of converted oxygen (O_{C₂H₆}, O_{C₂H₄}, O_{CO_{2;C₂H₄}} and O_{CO_{2;CH₄}}), according to Figure 40 for k₃/k₄ = 7 and 2. Finally the amounts of converted oxygen for all 15 pulses were summed up (O_{total}) and the ratio of O_x/O_{total} was derived.

5.8.3 Results

5.8.3.1 Residence time analyses

The experimental results of tracer pulses of the piping system are presented in Figure 41 A. The final fitting parameters are presented in Table 14. These parameters were used to fit the experimental results of the residence time analyses with reactor at OCM conditions. This is presented in Figure 41 B for 1 g catalyst. The final value of the Bodenstein numbers were 26.5 (0.5 g cat) and 26.8 (1 g catalyst), which indicates strong dispersion effects. The pulse width was set as residence time (τ) of the kinetic model, which was 50 s.

Table 14 - Fitting results of residence time experiments

Parameter	Final value
t_{delay}	16.98 [s]
t_{dose}	20.35 [s]
amplitude	0.049

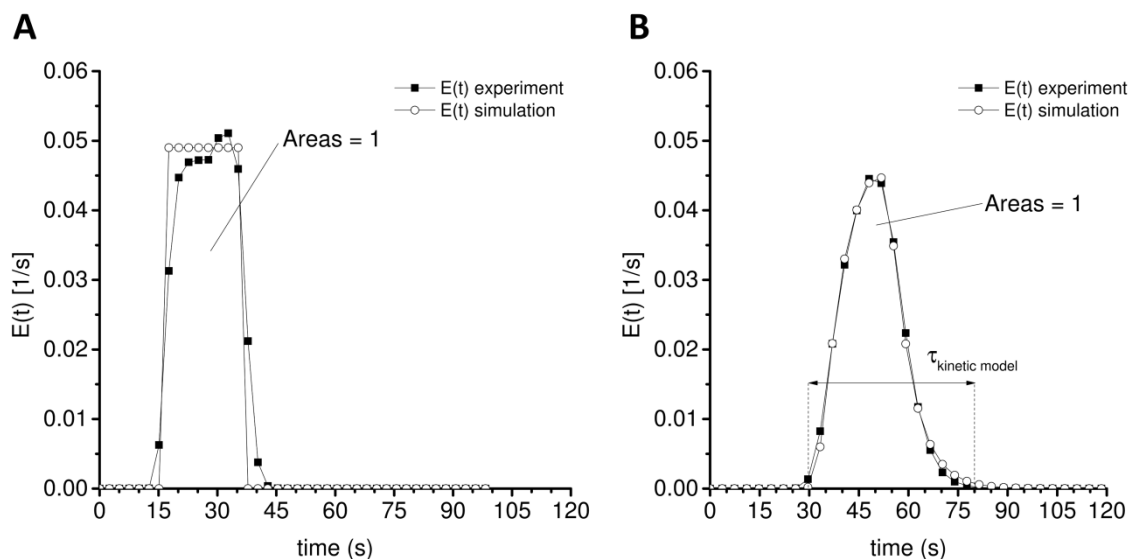


Figure 41 - Results of experimental and simulated residence time distribution functions of 1 ml tracer and 30 nml/min. A – tracer pulse through tube system without reactor, B – tracer pulse through tube system and reactor at 775 °C, 1 g catalyst

5.8.3.2 Modelling of repetitive pulse experiments

The results of the repetitive pulse fitting procedure are listed in Table 15. Variation of the specific surface area of the $\text{Na}_2\text{WO}_4/\text{Mn}/\text{SiO}_2$ catalyst has a smaller influence on the rate constants as the variation of the manganese oxide loading.

Table 15 - Fitted rate constants of repetitive methane pulse experiments

Variation		k3/k4 = 7 [ml/(mole·s)]				k3/k4 = 2 [ml/(mole·s)]			
		k1	k2	k3	k4	k1	k2	k3	k4
Mn (COK-12)	1.00 w-%	3109	2283	12	84	3109	2283	42	84
	1.90 w-%	1183	2997	21	150	1183	2997	75	150
	2.80 w-%	1709	1651	8	54	1675	1616	83,5	167
	3.70 w-%	1246	654	4	30	1278	589	49	98
Aspec (COK-12)	2.3 m ² /g	976	516	4	30	957	501	31	62
	2.6 m ² /g	1375	713	6	40	1349	691	46,5	93
	3.2 m ² /g	1513	814	7	47	1476	787	60	120
	4.2 m ² /g	1335	709	7	47	1358	694	50	100
Reference catalyst		1990	1713	3	21	1939	1647	23	46

5.8.3.3 Simulation of repetitive pulse experiments

The calculated amounts of C₂H₆, C₂H₄ and CO₂ of the first four methane pulses from experiments and simulations are presented in Figure 42 as parity plot. The kinetic model shows adequate reliability to calculate to amounts of each reactant. Based on these models, the amounts of oxygen for each reaction were calculated.

5.8.4 References

- [1] M. Kraume, Einphasig durchströmte Feststoffschüttungen, in: Transportvoränge in der Verfahrenstechnik, 2012: pp. 247–273.

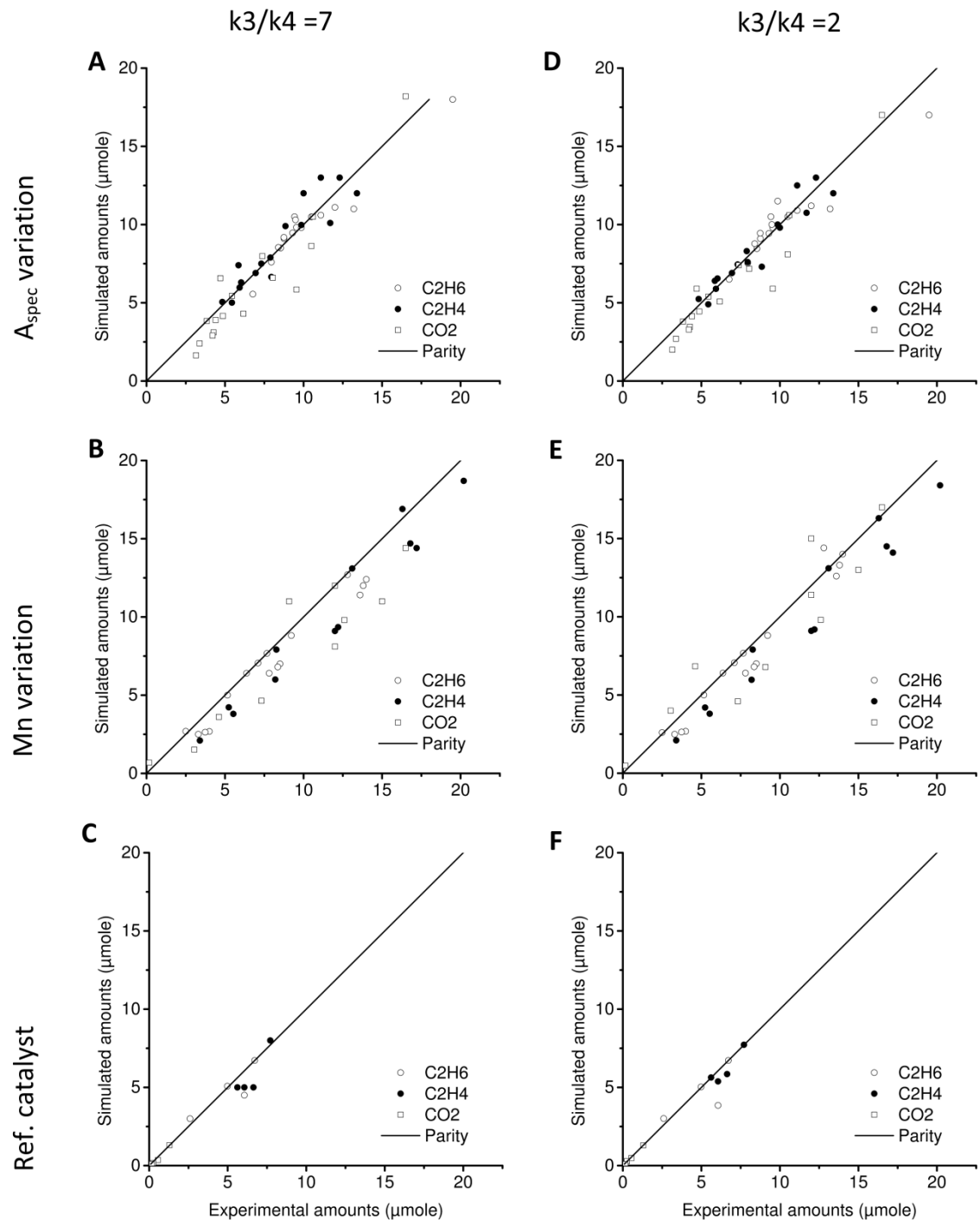


Figure 42 - Parity plot of the initial four 1 ml CH₄ pulses for all catalyst materials in repetitive pulse experiments vs. simulation results at different ratios of k_3/k_4 . A- C $k_3/k_4 = 7$; D-F $k_3/k_4 = 2$